Tampere University

DHANESH KATTIPPARAMBIL RAJAN

Modular Instrumentation for Controlling and Monitoring *In-Vitro* Cultivation Environment and Image-based Functionality Measurements of Human Stem Cells

Tampere University Dissertations 256

Tampere University Dissertations 256

DHANESH KATTIPPARAMBIL RAJAN

Modular Instrumentation for Controlling and Monitoring *In-Vitro* Cultivation Environment and Image-based Functionality Measurements of Human Stem Cells

ACADEMIC DISSERTATION
To be presented, with the permission of
the Faculty of Medicine and Health Technology
of Tampere University,
for public defence at Tampere University,
on 27 May 2020, at 12 o'clock.

ACADEMIC DISSERTATION
Tampere University, BioMediTech, Faculty of Medicine and Health Technology
Finland

Responsible supervisor and Custos
Professor Dr. Jukka Lekkala
Faculty of Medicine and Health Technology
Tampere University
Finland

Pre-examiners
Professor Dr. Gabriel J G Martins
Advanced Imaging Facility
University of Lisbon
Portugal

Professor Dr. Tapio Fabritius
Electronics and Communications Engineering
University of Oulu
Finland

Opponent
Professor Dr. Heinzle Elmar
Department of Biochemical Engineering
Saarland University
Germany

The originality of this thesis has been checked using the Turnitin OriginalityCheck service.

Cover design: Roihu Inc.

ISBN 978-952-03-1568-9 (print)
ISBN 978-952-03-1569-6 (pdf)
ISSN 2489-9860 (print)
ISSN 2490-0028 (pdf)
http://urn.fi/URN:ISBN:978-952-03-1569-6

PunaMusta Oy – Yliopistopaino
Tampere 2020

PREFACE

This thesis embodies application of engineering expertise with cell biology research. I am extremely grateful to my supervisor Professor Dr. Jukka Lekkala for his guidance and endless support. I still cherish the day I joined his 'Sensor Technology and Biomeasurements group' several years ago which was a turning point in my life. I am very thankful for the unwavering support and opportunities I got during these years at the BioMediTech - Institute of Biosciences and Medical Technology and the Faculty of Medicine and Health Technology, Tampere University, and its predecessor, Department of Automation Science and Engineering, at Tampere University of Technology. I would also like to thank 'Business Finland' (former TEKES), for funding the Human Spare Parts 1, 2 and Academy of Finland for funding the 'Centre-of-excellence Body on chip' projects all of which I have worked in. This multidisciplinary research could not have been completed without the efficient cooperation with our biology collaborators. I acknowledge the efforts of Katriina Aalto-Setälä (Group leader, Physiology, Heart Group, Heart Hospital, Tampere University Hospital) and Susanna Miettinen (Group leader, Regenerative Medicine and Adult Stem Cell Group) for organising the projects where I was allowed to carry out the research. I am extremely thankful to my thesis pre-examiners Professor Dr. Gabriel J G Martins, Instituto Gulbenkian de Ciencia, University of Lisbon and Professor Dr. Tapio Fabritius, Electronics and Communications Engineering, University of Oulu, whose positive feedback and valuable comments enabled me to modify the thesis efficiently. I would also like to thank Dr. Heinzle Elmar, Senior Professor of Biochemical Engineering at the Saarland University, Germany for accepting the request to act as an opponent in the public examination of my thesis

I am indebted to Professor Dr. Pasi Kallio for providing me continual opportunities, freedom and guidance for completing the thesis. I want to express my sincere gratitude to Heimo Ihalainen who every so often guided me with encouragements and thought provoking arguments. Many times this has challenged me to push myself to explore new areas. I specially thank Jarmo Verho and Joose Kreutzer for their contributions to the thesis. I am grateful to Hannu Välimäki for

his strong collaboration, and also to all the co-authors of my publications. Special acknowledgements are due to Jouni Niemelä for his huge assistance in system assemblies, and Timo Peltola for his continuous IT support.

I have no words to express the gratitude for the amazing relationship I have with Heikki Jokinen, the interesting conversations we have, the times we share and above all the acceptance I got into his big-hearted family. I also want to thank Markus Karjalainen for his warm friendship, helpfulness and our various travels together and Professor Dr. Jouko Halttunen for his support in the early years of my research. In addition, I am so thankful to my wonderful wife Aveline Meyn for her unconditional support, encouragements and love throughout this journey. My uncle Mohanan PV has played an instrumental role in my life and I am extremely grateful for his companionship. I am blessed to have had great friends and well-wishers throughout my life and would like to extend special thanks to Sudeep, Santhosh, Mathew, Melbin, Bobin, Rahul and Pertti for all the fun times together. I would like to thank my parents, sister and Sobha chitta for their spiritual assistance, all my teachers especially Elisua Benedict and Jessy Sajan for their blessings and last but not the least everyone else in the department for all the support, discussions, banters and conversations that at times inspired me to think out of the box.

Dhanesh Rajan,
17.04.2020, Tampere

ABSTRACT

Artificial animal cell culture was successfully developed by Ross Harrison in 1907. But it was not until the 1940's and 1950's that several developments occurred, which expedited the cell culturing *in-vitro (C-Vitro)* to be a consistent and reproducible technique to study isolated living-cells in a controlled environment. Currently, *C-Vitro* is one of the major tools in cellular and molecular biology both in the academia and industry. They are extensively utilised to study the cellular physiology/biochemistry, to screen drugs/therapeutic compounds, to understand the effects of drugs/toxic compounds and also to identify the pathways of carcinogenesis/mutagenesis. It is also used in large scale manufacturing of vaccines and therapeutic proteins. In any experimental setup, it is important that the *C-Vitro* model should represent the physiological phenomena of interest with reasonable accuracy so that all experimental results are statistically consistent and reproducible. In this direction, sensors and measurement systems play important roles in *in-situ* detection and/or control/manipulation of cells/tissues/environment. This thesis aimed to develop new technology for tailored cell culturing and integrated measurements. Firstly, design and assembly of a portable Invert-upright microscope interchangeable modular cell culturing platform (iuCMP) was envisioned. In contrast to conventional methods, micro-scaled systems mimic the cells' natural microenvironment more precisely, facilitating accurate and tractable models. The iuCMP integrates modular measurement schemes with a mini culture chamber using biocompatible cell-friendly materials, automated environment-control (temperature and gas concentrations), oxygen sensing and simultaneous functional measurements (electrophysiological and image-based). Time lapse microscopy is very useful in cell biology, but integration of advanced *in-vitro*/device based biological systems (e.g. lab/organ/body-on-chips, or mini-bioreactors/microfluidic systems) into conventional microscopes can be challenging in several circumstances due to multiple reasons. But in iuCMP the main advantage is, the microscope can be switched either as an inverted or as an upright system and therefore can accommodate virtually any *in-vitro* device. It can capture images from regions that are otherwise inaccessible by conventional microscopes, for example, cells cultured on physical or biochemical sensor systems. The modular design also allows

accommodating more sensor or measurement systems quite freely. We have demonstrated the system for video-based beating analysis of cardiomyocytes, cell orientation analysis on nanocellulose, and simultaneous long-term *in-situ* microscopy with oxygen and temperature sensing in hypoxia.

In an example application, the system was utilised for long-term temperature stressing and simultaneous mechanobiological analysis of human induced pluripotent stem cell-derived cardiomyocytes (hiPSC-CMs). For this the iuCMP together with a temperature sensor plate (TSP) and a novel non-invasive beating analysis software (CMaN—cardiomyocyte function analysis tool, scripted as a sub-part of this thesis), was applied for automated temperature response studies in hiPSC-CM cultures. *In-situ* temperature sensing is usually challenging with bulky external sensors, but TSPs solved this issue. In the temperature response study, we showed that the relationship between hiPSC-CM beating frequency and temperature is non-linear and measured the Q_{10} temperature coefficients. Moreover, we observed the hiPSC-CM contractile networking, including propagation of the action potential signal between dissociated clusters and their non-invasive measurements. It was the first case where these events were reported in hiPSC-CM clusters and their non-invasive measurements by image processing.

The software CMaN comes with a user-friendly interface and, is equipped with features for batch processing, movement centre detection and cluster finding. It can extract six different signals of the contractile motion of cardiomyocytes (clusters or single cells) per processing. This ensures a minimum of one useful beating signal even in the cases of complex beating videos. On the processing end, compared to similar tools, CMaN is faster, more sensitive, and computationally less expensive and allows ROI based processing. In the case of healthy cells, the waveform of the signal from the CMaN resembles an ECG signal with positive and negative segments, allowing the computation of contraction and relaxation features separately.

In addition to iuCMP, a Modular optical pH measurement system (MO-pH) for 24/7 non-contact cell culture measurements was also developed. The MO-pH incorporates modular sterilisable optical parts and is used in phenol-red medium cell cultures. The modular assembly of MO-pH cassettes is unique and reusable. Measurements are carried out in a closed flow system without wasting any culture medium and requires no special manual attention or recalibrations during culture. Furthermore, a new absorption correction model was put forward that minimised errors caused e.g. by biolayers in spectrometric pH measurement, which improved the pH measurement accuracy. MO-pH has been applied in long-term human adipose stem cells (hASC) expansion cultures in CO_2 dependent and independent

media. Additionally, the MO-pH was also utilised to comprehend the behaviour of pH, temperature and humidity in water jacked incubators as well as to record the pH response as a function of temperature in the presence and absence of CO_2 in the context of stem cell cultures. The resulting plots clearly showed the interplay between measured parameters indicating a few stress sources present all through the culture. Additionally, it provided an overall picture of behaviour of critical control parameters in an incubator and pointed out the need for bioprocess systems with automatic process monitoring and smart control for maximum yield, optimal growth and maintenance of the cells. Besides, we also integrated MO-pH into flasks with re-closable lids (RL-F) and tested its applicability in stem cell cultures. A standalone system around an RL-F flask was built by combining the cell culture, medium perfusion and optical measurements. The developed RL-F system has been successfully tested in ASC-differentiation cultures.

Finally, a few trial experiments for image-based pH estimation aimed for iuCMP have also been carried out. This includes tests with LCD illumination, optical projection tomography, and webcam systems. In reality, the pH is not distributed uniformly in tissues, and has shown a gradient of up to 1.0 pH unit within 1 cm distance. Therefore, producing reliable pH maps also in *in-vitro* can be important in understanding various common pathologies and location of lesions. A reliable and adequately developed long-term pH mapping method will be an important addition into the iuCMP.

CONTENTS

ABBREVIATIONS

ACF	Automated cluster finding
AFOF	Affine optical flow
CAD	Computer-aided design
CM	Cardiomyocytes
CMaN	Cardiomyocytes function analysis tool
CO_2	Carbon dioxide
COPD	Chronic obstructive pulmonary disease
C-Vitro	Cell culturing *in-vitro*
C-VitroS	Cell culturing *in-vitro* systems
DHM	Digital holographic microscopy
DI water	Deionised water
DMEM	Dulbecco's modified eagle medium
ECG	Electrocardiogram
FEM	Finite element model
FOV	Field-of-view
FPS	Frames per second
GUI	Graphical user interface
hASC	Human adipose stem cells
hiPSC	Human induced pluripotent stem cell
hiPSC-CMs	Human induced pluripotent stem cell-derived cardiomyocytes
HOT	Higher-order terms
IHD	Ischemic heart disease
iuCMP	Invert-upright microscope interchangeable modular cell culturing platform
JPEG	Joint photographic experts group (image format)

K	Potassium
LCD	Liquid crystal display
LED	Light emitting diode
MCD	Movement centre detection
MEA	Microelectrode array
mM	Millimolar
MO-pH	Modular optical pH measurement system
MRI	Magnetic resonance imaging
NA	Numerical aperture
Na	Sodium ion
OF	Optical flow
OPT	Optical projection tomography
PDE	Partial differential equations
PDMS	Polydimethylsiloxane
PDMS	Polydimethylsiloxane
pH-FET	pH-field effect transistor
pO_2	Partial pressure of oxygen
PWM	Pulse width modulation
RAW	Minimally processed data from the image sensor
RGB	Red, green and blue
RL-F	Flasks with re-closable lids
ROI	Region of interest
ROM	Ray optics module
SLR	Single-lens reflex
TLM	Time-lapse microscopy
TSP	Temperature sensor plates

SYMBOLS

a	Translation constant along *x* axis
A_{430}	Absorption at 430 nm
A_{560}	Absorption at 560 nm
A_{mx}	Phenol red maximum absorption at 560 nm
A_{dm}^{545}	Fouling layer absorption at 545 nm
A_{dm}^{680}	Fouling layer absorption at 680 nm
$A_{indicator}^{545}$	Phenol red absorption at 545 nm
$A_{indicator}^{680}$	Phenol red absorption at 680 nm
A_{total}	Total absorption
A_{total}^{545}	Total absorption at 545 nm
A_{total}^{680}	Total absorption at 680 nm
b	Translation constant along *y* axis
b_x	Path length
CAS	Chemical abstracts service number
$C_{19}H_{14}O_5S$	Phenol red chemical formula
C_t	Total sum of phenol red concentration in acidic
dm	Fouling layer concentration
ε_{HIn}	Molar absorptivity of phenol red in acid form
ε_{In}	Molar absorptivity of phenol red in alkaline form
ε_{545}	Fouling layer molar absorptivity at 545 nm
ε_{680}	Fouling layer molar absorptivity at 680 nm
GR model	Absorption compensation model
HIn	Phenol red in acidic form

In^-	Phenol red in alkaline form
I_x	Intensity *x* derivative
I_y	Intensity *y* derivative
I_t	Intensity temporal derivative
$I(x,y,t)$	Pixel intensity at location *(x,y)* at time *t*
k_{545}	Light loss constant for the fouling layer at 545 nm
k_{680}	Light loss constant for the fouling layer at 680 nm
m_x	Scaling constant along *x* axis
m_y	Scaling constant along *y* axis
pH	Measure of hydrogen ion concentration
pKa^{In}	Dissociation constant
pKa_T^{In}	Dissociation constant at temperature T
Q_{10}	Temperature coefficient
$s1$	Shear constant along *x* axis
$s2$	Shear constant along *y* axis
t_{545}	Fouling layer optical thickness at 545 nm
t_{680}	Fouling layer optical thickness at 680 nm
Δt	Time difference
T	Temperature
t	Time
V_x	Optical flow along *x* axis
V_y	Optical flow along *y* axis
Δx	Displacement along *x* axis
Δy	Displacement along *y* axis
θ	Angle of rotation about the *x* axis

ORIGINAL PUBLICATIONS

This thesis is based on four publications, which are referenced in the text as **Publications I - IV.** Publications are reproduced with permission from the publishers.

Publication I Rajan DK, Kreutzer J, Välimäki H, Pekkanen-Mattila M, Ahola A, Skogberg A, Aalto-Setälä K, Ihalainen H, Kallio P, Lekkala J. A portable live-cell imaging system with an invert-upright-convertible architecture and a mini-bioreactor for long-term simultaneous cell imaging, chemical sensing, and electrophysiological recording. IEEE Access, vol. 6: pp. 11063–11075, 2018.

Publication II Rajan DK, Mäki, AJ, Pekkanen-Mattila M, Kreutzer J, Ryynänen T, Välimäki H, V Jarmo, Koivumäki JT, Ihalainen H, Aalto-Setälä K, Kallio P, Lekkala J. Cardiomyocytes: Analysis of temperature response and signal propagation between dissociated clusters using a novel video-based movement analysis software. IEEE Access [submitted].

Publication III Rajan DK, Patrikoski M, Verho J, Sivula J, Ihalainen H, Miettinen S, Lekkala J. Optical non-contact pH measurement in cell culture with sterilizable, modular parts. Talanta, vol. 161, pp.755–761, 2016.

Publication IV Rajan DK, Verho J, Kreutzer J, Valimaki H, Ihalainen H, Lekkala J, Patrikoski M, Miettinen S. Monitoring pH, temperature and humidity in long-term stem cell culture in CO_2 incubator. 2017 IEEE International Symposium on Medical Measurements and Applications, MeMeA 2017 - Proceedings. IEEE, pp. 470–474.

THE AUTHOR'S ROLE IN THE PUBLICATIONS AND THE MANUSCRIPT

The author of this thesis is the main author in all the listed publications. Furthermore, the author drafted major parts in each publication. Jukka Lekkala contributed as the supervising author in all the publications. Katriina Aalto-Setälä, Susanna Miettinen and Heimo Ihalainen occasionally acted as supervisors in cellular experiments, experimental planning and software development. The author's own contributions in each publication are described below in more detail.

In Publication I, the author designed and assembled the compact microscope, modular system and the control software. Co-authors developed the PDMS mini-incubator, pO_2 sensor and were responsible for cell culturing and image-based analytical measurements. The author carried out microscopy characterisation, long-term performance measurements and cellular experiments. The manuscript was revised and improved with the co-authors.

In Publication II, the author designed the experimental protocol and scripted the software for automated measurement as well as for video-based movement analysis. The author drafted the first version of the manuscript which was revised by all the co-authors.

The author designed the pH measurement system and developed the absorption correction model presented in Publication III. Long-term pH measurements during hASC culture were carried out under the supervision of Mimmi Patrikoski and Jyrki Sivula. All the authors contributed to the manuscript.

In Publication IV, the author conducted the experiments and drafted the manuscript. The manuscript was improved with the help of all the co-authors.

1. INTRODUCTION

This thesis was aimed to develop new technology for tailored cell culturing and integrated measurements. Design and assembly of a portable *in-vitro* cell culturing platform with a novel interchangeable microscopy architecture was envisioned. In addition, the development of an optical pH measurement system with sterilisable-modular parts for 24/7 non-contact pH monitoring was also envisaged.

1.1. Motivation

Cell culturing *in-vitro (C-Vitro)* is a widely accepted technique both in academia and industry to study biological mechanisms and responses related to human health and disease. One major advantage of *C-Vitro* is its consistency and reproducibility. Culturing systems can vary from simple dishes/slides to more complex and advanced device-based systems such as cells/tissues/organs on chips. Even though a complete abolishment of animal models has not yet been achieved, the systems based on reprogrammed cells, for example, human induced pluripotent stem cell (hiPSC) have generated significant enthusiasm in various fields of life sciences. This is mainly because the hiPSCs can be engineered into other cell types and can overcome the limitations of animal models due to their human origin. Conventionally, hiPSCs and most mammalian cells are cultured in incubators where the environment is usually set to 37 ^{o}C, 5 % CO_2 and 19 % O_2 for the successful growth of the cells. In addition, the relative humidity is maintained nearly at > 95 % to minimise the medium evaporation. These conditions, in principle, should be very stable and not be a source of experimental variations [1]. Correct parameters for the culture medium, in particular, the levels of oxygen (dissolved) and pH are very important in successful cell studies. Oxygen is vital not only for the cell's energy metabolism but is also critical in regulating the cell function and differentiation [2]. Further, with 5 % CO_2, the acid-base homeostatic mechanism (bicarbonate buffering system) in the medium regulates the pH to 7.2-7.4. Fluctuations in pH can have a huge impact, for instance, even 0.1-0.2 pH unit

variation from the setpoint can affect cell growth, function and metabolism. Moreover, as the cells constantly consume oxygen and release wastes (pyruvic acid, lactic acid and CO_2), the pH of the medium may drop further without an appropriate CO_2 control [2]–[5]. Besides, this thermoregulation in cell culture is also very important, for instance, temperature fluctuations (< 2 ^oC) have shown to alter the cardiomyocytes (CM) beating properties and modulate the firing rate in the cortical networks during up states [6]. Temperature can also alter the medium viscosity, density and soften the cells and slower the functions. Lack of proper thermoregulation, apparently, is one of the main reasons in biological variability in cell cultures. Other factors such as pressure and mechanical load are also known to have influence on cell cultures [7].

Measurements have shown that maintaining a uniform environment for each culture container in a conventional incubator is nearly impossible. Cells may also experience intermittent environmental fluctuations at various time points during the culture [8]–[10] Prolonged or repeated environmental fluctuations can have an unhealthy impact, for example, it can affect the cell attachment [11] or trigger stress reactions[12]. If the stress reactions are triggered, cells, depending on the cell type, nature and duration of the stress, respond in various ways ranging from the activation of survival pathways to the initiation of cell death [11]–[14]. The interplay between environmental factors, for instance, the effect of temperature on pH and medium evaporation can also adversely affect the culture output. However, recent developments in microfabrication techniques, microfluidic devices and 3D printers have provided solutions to tackle these problems by devising micro-scaled systems, for instance, microphysiological vessels or microbioreactors. These systems can maintain the culture conditions more precisely and mimic the cell natural environment more accurately. And most importantly, the micro-scaled systems are faster and cheaper to produce, require less electrical power, working volume and supplementary reagents. All these factors, in effect, will enable long-term cost effective and successful cell culturing. Furthermore, the efficient representation of a cell's natural environment can facilitate highly accurate and tractable cell models for advanced studies.

In cell culturing, measurements, including *in-situ* imaging have important roles in activity monitoring, optimization as well as for process control. Reliable measurement systems with good feedback can not only improve the quality of cell culturing but also enhance productivity and reproducibility. But, although cells have been kept alive *in-vitro* and researched for more than a century, the monitoring methods are lagging behind the progress in cell culture techniques[15], [16]. It is an

important issue that needs to be addressed. Not only that, even though several miniaturized bioreactors and device-based biological systems are constantly reported, integration of physiological or chemical sensing systems into them can be challenging in many cases. This can be due to concerns in mechanical incompatibility and practical issues with connectivity (optical, electrical, fluid flow). In this context, we have conceptualised an Invert-upright microscope interchangeable modular cell culturing platform (iuCMP) with a PDMS mini-incubator, a compact digital microscope and an automated environmental control (temperature, oxygen and other gas concentrations). Furthermore, the platform has integrated sensors (fluorometric pO_2 sensor and micro temperature sensor), a microelectrode array amplifier (MEA) and a video-based cardiomyocytes (CM) function analysis software (CMaN-CM function analysis tool). The platform can be used for long-term tabletop cell culturing, cellular response studies and simultaneous functionality assessment (electrophysiological analysis and non-invasive video-based mechanobiological analysis). In addition to the iuCMP, a non-contact modular optical pH measurement system (MO-pH) using sterilisable parts for phenol red (phenolsulfonphthalein) cell culturing medium for 24/7 real-time spectroscopic pH monitoring is also envisioned.

An ideal modular culture platform will be a multifunctional platform that integrates independently created plug and play modules, such as perfusion module, sensor modules, imaging module (3D, fluorescent), MEA module, control module (gas exchange, temperature, pH), stimulation module etc. with the option that the modules can be configured-reconfigured with minimum effort for different biological studies. In addition, it is expected to accommodate various miniaturized *in-vitro* constructs and monitoring devices quite freely. Cultured cells have applications in many areas, for example, in tissue engineering (repair, enhance, or replace biological tissues), in the pharmaceutical industry (drug-dosage screening, side effects-toxicity testing) and in the cosmetic industry (product validation). Furthermore, they are widely used in immunology (antibody, vaccine and therapeutic protein production) and in life sciences' research (future regenerative medicine, cytotoxicity, tissue and organ development). Integrating smart features into culturing systems, for instance, real-time automated image analysis, decision making, tracking, intelligent medium exchange etc. are not typically possible with traditional culture systems without costly, specialised arrangements [17]–[23]. But those can be materialised with modular culturing systems. However, smart systems even with their high potential, are still in the developmental phase, lacking standardised techniques and having still many hurdles to overcome. The research in this area is

fascinating because successful developments can not only boost the academic science but also impact the society, for instance, contribute to reducing the cost of drugs, provide more mechanistic insight into diseases (carcinogenesis, mutagenesis and cancer) and diseases pathogenesis (cardiovascular, epileptic seizures).

As a side note:- Since the focus of this thesis is on methods/technical development with more leverage to engineering aspects, the issues related to intracellular functions, cell-to-cell interactions and stimulation (by chemical, mechanical, optical, and electrical factors) are not considered in detail here.

1.2. Objectives and Research Questions

This thesis has two goals. The first goal is to develop a standalone digital imaging module (compact microscope) for unstained live-cell microscopy together with iuCMP and the CM functionality analysis software CMaN. The iuCMP is intended to enable a highly stable, cell-friendly environment for long-term cellular studies and, if desired, to generate timely environment control to study biological responses. Multiple monitoring and measurement schemes are integrated into iuCMP. The second goal is to develop a non-contact spectroscopic pH measurement system with sterilisable - modular parts. Both the intended goals have been accomplished, and the developed hardware and software are continually being used in different experimental studies. The details of the automated temperature stressing experiments with hiPSC cardiomyocytes (hiPSC-CMs), are also presented in this thesis. To summarise, this work combines 3D modelling and design, ray optics simulations, instrumental assembly and cellular experiments (demonstrative and applied). The specific research questions of the thesis are defined as follows:

1. **How can measurement systems with minimal disturbance to cells and suitable for long-term studies outside a traditional incubator be created?**

2. **Can a mini phase contrast microscope with invert-upright convertibility be developed for good quality imaging of unstained live-cells *in-vitro*?**

3. **Can affine-optical flow be used to reliably analyse multiple beating signals from cardiomyocyte beating videos? If so, does the waveform,**

speed and sensitivity allow the computation of relaxation and contraction features separately? Can it be applied for movement centre detection, batch mode processing and real-time analysis?

4. **Can we carry out long-term automated assessments of the hiPSC-CM contractions to temperature stimuli outside a conventional incubator?**

5. **Can we reliably measure pH, based simply on non-contact optical methods during long-term observations?**

1.3. Thesis Organisation

This thesis comprises of four scientific papers and is divided into five chapters. Chapter 1 presents the motivation, objectives and research questions, and provides a summary of main results. Chapter 2 explains the relevant background for the study and highlights current challenges on the two measurement systems that this thesis aims to develop. Chapter 3 and Chapter 4 present the research work related to this thesis. Chapter 3 details the **Measurement system1: Compact digital microscope, iuCMP and CMaN**. Optical simulations, 3D system design, digital imaging schemes, invert-upright interchangeable system and the theory related to CMaN are outlined in this chapter. The Measurement system1 was applied to multiple studies and four application examples are also included in Chapter 3. Chapter 4 presents the **Measurement System 2: the non-contact optical pH measurement system, MO-pH**. The MO-pH is based on two colour pH measurement whose theory, temperature compensation and absorption correction scheme, as well as the summary of hardware design, are presented in Chapter 4. Measurement results from long term stem cell culture measurements are provided in the Results and discussion section in Chapter 4. Further, a novel pH measurement method using re-closable lid flasks and preliminary ideas for a few image-based pH estimation schemes are also included in Chapter 4. Finally, Chapter 5 concludes the thesis with summarising the results, providing answers to the research questions and discussing the limitations of the study.

2. BACKGROUND

In this chapter, a short overview and the significance of the research in relation to the current knowledge is provided. The purpose is to recall previous studies in the context of the author's work, specifically in the areas of C-Vitro *in-situ* imaging, compact microscopy, iuCMP, CMaN and MO-pH.

2.1. Cell Culturing *In-vitro* and *In-situ* Imaging

Cell culturing *in-vitro* is a well-known technique where the cells are transferred from an organism and placed in a fluid in an artificial *in-vitro* construct/system. Under appropriate conditions, the cells can live, grow, divide (mitosis) or even differentiate into other cell types. Today, cell culturing is widely used in biotechnology, clinical diagnostics, tissue engineering as well as in various areas in life sciences to develop cell and disease models, drug screening, cell-based manufacturing and toxicity testing. Small-scale upstream cell culturing traditionally occurs often in Petri dishes, culture flasks or multi-well plates stored in an incubator. Advances in technology and organotypic cell/tissues models have facilitated microphysiological *in-vitro* systems that can mimic human physiology with great precision [24]–[26]. An *in-vitro* system is usually more complex with a 2D or 3D platform with substrates, fluids (with essential nutrients, growth factors), thermoregulation and usually with an acid-base homeostatic mechanism (eg. by CO_2-bicarbonate buffering). A functional micro-scaled system, compared to conventional methods, emulates the cells' natural environment more exactly where the cells function analogous to their tissues or organs in the whole organism. A broad list of advantages of various *in-vitro* cell techniques have been extensively described elsewhere [27]–[31], but in all cases, it is important that the *in-vitro* model should represent the physiological phenomena of interest with reasonable accuracy so that all experimental results are statistically consistent and reproducible [32]. Sensors and actuators have great potential in *in-vitro* systems for *in-situ* detection and/or manipulation of relevant cells or tissues [33]. Biomarker quantification or methods such as viability assays are frequently used to assess cellular functionalities or cytotoxicity but usually, they are performed off-the-

chip in an endpoint manner. On the other hand, real-time sensing would allow one to avail of the complete advantage of *in-vitro* systems, for example, for efficient control and manipulation. Integrating sensors into *in-vitro* systems usually enables higher sensitivity, temporal and even spatial resolution via integration. Continuous 24/7 real-time measurements have invaluable potential for recapitulating various aspects of human physiology and makes more accurate and tractable models for advanced studies. This can also enhance the efficiency of experiments in human disease modelling, molecular signalling, gene expression and cell-based manufacturing. Besides, this may also help to improve the culturing systems and its environment regulation schemes more effectively. Most importantly, it can further aid in developing miniaturized non-conventional cell culturing systems such as microfluidics cell chips, microphysiological scaffolds and organ/body-on-chips. However, integration of sensors to a culturing systems may not always be easy due to various reasons including issues with sensor physical dimensions (and connectivity), measurement volume requirements, sterilisability, biocompatibility, signal drift and long-term stability. Therefore, not all commercially available sensors can be directly useful for cell culturing applications and development of totally new sensor/measurement systems may be the only alternative in numerous cases. In addition, the measurement location, whether it is for onsite (at the area where the cells grow) or offsite (slightly away from the cell location) monitoring also needs to be sorted out. For offsite measurements, a sampling/flow system may be unavoidable. To sum up, integration of sensors into *in-vitro* systems, in general, requires critical planning, careful studies, including biocompatible tests, and iterations.

For real-time cell culture monitoring, one commonly applied technique is time-lapse microscopy (TLM) which can enable both qualitative and quantitative analyses of important biological information. A TLM system meant for live-cell microscopy is usually equipped with an environment chamber, and utilises a contrast enhancement scheme, for example, differential interference contrast (DIC) or Hoffman modulation contrast (HMC) or phase contrast or fluorescence (by staining) [34]–[37]. The state-of-the-art TLM frameworks such as confocal and super-resolution systems have overcome the barriers of Abbe's classical diffraction-limited resolution, and its novel developments address the problem of photo-cyto toxicity of those techniques [38] and produce high quality-high contrast images. But, it comes with a price; high costs, fairly complicated hardware settings and high upkeep [39]–[43]. High throughput observations can also be difficult with them [44]. Several of today's device based biological systems (e.g. reaction chambers, bioreactors,

microfluidic culture systems, lab/organ/body-on-chips), also require TLM *in-situ*. But integrating them into an off-the-shelf TLM system can be tricky and challenging in many cases due to a multitude of reasons [45]–[54]. Several of recently developed sensor systems [55]–[57] are efficient candidates for accurate process monitoring and environment regulation, however, most of them, unfortunately, are not directly compatible for a conventional TLM system. Research for better/achievable spatial resolution in microscopy is definitely important, but concurrently, the demand for miniaturised case-specific live-cell microscopes with good imaging quality is also constantly increasing. Compact microscopes instead of high-end, large-form-factor systems, are inevitable for obvious reasons, for example, for *in-situ* TLM in a conventional incubator. Several compact microscopes have been reported over the last few years from both academic and commercial endeavours [58], [59]. As new microscope modalities emerge, a trend to miniaturise them can also be seen. For example, the on-chip bright field - fluorescent microscopes offer high resolution, large field-of-view (FOV) and incubator compatibility, but inherently the cells need to be plated on the imaging chip, which makes them somewhat inconvenient for conventional cell culturing workflow [60]–[63]. On the contrary, compact microscopes based on digital holographic microscopy (DHM) facilitate lensless and widefield 2D or 3D imaging. But since it is computational microscopy, numerical image reconstruction from the diffraction pattern of the specimen is inevitable which restricts the immediate visualisation (live-view) of the cells [64]–[68]. On the other hand, Optical projection tomography (OPT), an interesting imaging modality which progressed notably in the last decade can produce 3D cell images, but the cells must be immobilised, which can be problematic for live-cell imaging of certain cell types. The light guide microscopy, for instance, fibre optic endoscopic microscope [69]–[71] has notable advantages, but fibre integration into the cell chamber can be oftentimes cumbersome, in addition to their calibration difficulties [72]–[77].

Alongside the miniaturisation of aforementioned and other emerging microscope modalities, case-specific miniaturisation of conventional modalities can be very useful, especially when they are equipped with features like smart phone compatibility, wireless connectivity, web interfacing, decision making and cloud integration. They can have applications in remote cell microscopy, mobile healthcare, e-health and on-field medical diagnosis [78], [79]. To this end, several mini cost-effective microscopes have been reported recently, but most of them, except for a few employ basic bright-field or fluorescent imaging schemes [60]–[63], [78]–[80]. As live-cells are naturally very transparent for visible wavelengths, the imaging contrast can be a problem in basic bright-field schemes. The contrast is better in

fluorescent systems, but it comes at the cost of fluorescent staining and related photo-toxic limitations in long-term TLM. In some systems, chromatic aberration is noticeable [44]. The webcam-based systems are inexpensive but their lossy image compression schemes and default auto settings limit their applicability in analytical quantifications [44], [81], [82]. Further, the typical webcam frame rates (20-30 frames per second (fps)) are insufficient for certain dynamic studies. To that end, we have also tested two USB 2 microscopes which had several useful features such as a large adjustable magnification, portability and easy computer connectivity [83], [84]. They produced good images of dry surfaces and electrodes, but the performance was not acceptable for wet and transparent samples. In the end, we realised that we need to depend on a microscopy with a contrast enhancement scheme for live-cell imaging in our intended system. The DIC and phase contrast ones were the top priorities, but we were not able to find their miniaturised versions suitable for our systems from any commercial vendor. At this stage, we decided to develop a compact and flexible digital imaging unit suitable for our *in-vitro* systems. The details of the developed system are discussed in Chapter 3. The cost of the system including the invert-upright optomechanics can be around 600-800 Euros.

2.2. Invert-Upright Interchangeable System for *In-vitro* Studies

Recently reported miniaturised microscopes have been developed for a specific application or a system and not necessarily modular or multipurpose for extended applications. They have been explicitly designed to be used either as an inverted or upright system and are mutually exclusive. For most *in-situ* studies, a standard inverted TLM works fine, but in some instances, the room under the cell-substrate may be reserved by other measurement systems (e.g. pH/pO_2 opto-chemical sensors, glucose/lactate biosensors, electrochemical ion sensors), therefore a simultaneous inverted TLM becomes impossible. So after our compact microscope was successfully materialised, we extended the research to devising an invert-upright microscope interchangeable architecture. This lead to the development of the iuCMP. In iuCMP, the microscope can be easily swapped between invert-upright configurations, therefore it is very flexible to integrate additional measurement systems. The iuCMP details and its four possible convertible options (Figure 9) are provided in Chapter 3.3.

While we were designing the iuCMP, no similar system was commercially available. However, a commercial hybrid invert-upright system (Revolve 3/Revolve 4, Echo Laboratories) is currently available [85]. This system has a touch interface, app connectivity as well as accelerometer controlled anti-shake control. But as the commercial one is solely a microscope, the cell culturing incubator chamber, heater stage etc. need to be separately built in order for them to be applied in long-term TLM applications. In addition, a system titled 'The Flexiscope' has been reported very recently in Biorxiv (not peer-reviewed) with multiple claims [86]. The Flexiscope appears to be an interesting system for advanced neurobiology experiments with features for multi-channel fluorescent imaging, 3D scanning and oblique infrared illumination. The system, however, is not very compact or portable due to a large number of optical and opto-mechanical components. But in any case, these recent developments indicate, there is an ever-growing interest in engineering flexible, modular and multipurpose systems to meet diverse needs and the arising new challenges [87]–[94].

The microscopy schemes in iuCMP are not solely for qualitative TLM but also for image-based quantification of cell functionalities, for example, online or offline movement analysis of cardiomyocytes. Image-based or spectroscopic techniques can be implemented as a non-invasive measurement method which is advantageous over traditional invasive analytical methods such as patch-clamp, voltage-sensitive dyes, and Ca transient/sarcomere length profiling [95]–[98]. When traditional methods can be laborious, and occasionally suffer from chemical crosstalk (interplay), the image-based measurements can facilitate label-free, highly localised as well as multipoint measurements.

2.3. Video-Based Cardiomyocyte Non-invasive Contractile Function Analysis

For cardiomyocytes function analysis, methods, such as electrophysiology, fluorescent labelling, Ca2+ transient or impedance measurements or sarcomere length profiling [98] are conventionally used. Advances in digital imaging and image processing methods have facilitated new methods for function analysis. Video-based function analysis is one among them which can be implemented as a fully non-invasive method when the stream of images have enough spatial resolution, magnification and sufficient frame rate matching the CM's contractile timing for lossless movement capture. A number of video-based function analysis software

have recently been reported [99]–[104] with various features. To this end, we have developed an advanced movement analysis software CMaN for offline and online video-based beating analysis. Basic properties of several similar software programs have been compared elsewhere [105]. CMaN was tested against three important programs ([103], [104], [106]) and has been found to have several notable advantages which are summarised in the last paragraph of Chapter 3.4.1. CMaN is an easy-to-use robust tool and available for download with the Publication II. The working principle and algorithm implementations are provided in detail in Chapter 3.4.1.

2.4. Cardiomyocytes and Temperature

Primary CMs are difficult to obtain but the hiPSC-CMs can be produced in laboratories by the differentiation of human iPSC cells. As hiPSC-CM can overcome the limitations of animal models due to their human origin [107], they have been increasingly used in heart research, disease modelling, regenerative medicine, cardiac drug discovery and toxicology [108], [109]. In all these applications, precise control of the experimental environment of O_2, CO_2, pH, osmolarity, temperature are highly important in order to maintain normal cell function and to avoid unexpected experimental variations [1], [56], [110]. In the case of temperature, it can have a mild to acute effect on the cell function. The effect of temperature on cardiomyocyte function is briefly discussed in Publication II. Unfortunately, a complete picture of the underlying mechanism of temperature-induced abnormalities in hiPSC-CM function is still elusive [111]. So it is important to recognise the stress response of hiPSC-CMs to temperature stimuli and quantitatively evaluate it. The acute effect of temperature on hiPSC-CM function has previously been reported, but an automated systematic temperature stressing study has not been reported before. We utilized iuCMP and CMaN together with calibrated temperature sensor plates (TSP, [112]) for this purpose. Measuring temperature from the location where cells grow is usually challenging with traditional methods. But the TSPs have microfabricated meander-type temperature sensors on its surface, so when the CMs are cultured directly on the TSP, the temperature from the exact cell area can be measured precisely. The introduction part of Publication II briefly describes the relevance of hiPSC-CM temperature response study. Our study aimed to precisely understand how the mechanobiology parameters such as, the beating frequency, relaxation time, contraction time, and the beating amplitude respond to temperature stimuli in long-term measurements. Additionally, we reported the Q_{10} temperature coefficients and

the novel results of action potential signal propagation between dissociated hiPSC-CM clusters in Publication II.

2.5. Cell Culturing Environment and pH Measurement

A successful human cell culturing requires a sterile, biocompatible, cell-friendly medium chamber and well regulated gaseous environment. The cell culturing fluid, throughout the culture, should also supply nutrients (e.g. glucose, vitamins, amino acids and hormones), maintain the acid-base homeostatic balance and remove the metabolic waste. Reliable monitoring of culturing environment and metabolic parameters can ensure reproducibility and also give insight into the transient nature of several intra and extracellular processes researched. To this end, there is growing interest in multi-parameter sensing for faster, cheaper, more efficient and less labour-intensive [15], [33], [113], [114] process monitoring. Of all the sensors/monitoring schemes reported, the pH, temperature and dissolved oxygen are the most frequently monitored parameters where the growing interest is perhaps best evidenced by the dramatic increase in the number of papers reported in the last decade. We have also realised how critical these parameters are in our cell culturing applications and therefore quite regularly look for still better sensors. Our own Sensor Technology and Bio-measurement research team actively work for developing various *in-vitro* sensor/measurement systems [115]–[120]. In this context, one of the main focuses of this thesis was to develop the optical pH measurement system the MO-pH.

Being a critical control parameter, pH can have a crucial impact on cell metabolism and proliferation unless it is maintained in a specific narrow range. Tissue functions *in-vivo* and cell viability are a strong function of pH, and a similar pH dependence has been observed in *in-vitro* cell cultures [3], [121], [122]. Most mammalian cells grow at the very narrow range, pH 7.2-7.4 [4], [5], [123], [124]. As cells proliferate and metabolise nutrients during culture, the secreted byproducts (e.g. CO_2, pyruvic acid, lactic acid) tend to lower the pH [3]–[5]. But, the bicarbonate acid-base homeostatic mechanism (bicarbonate- CO_2 buffering system), counteracts to nullify the pH fluctuations. However, the buffering action may not be perfect, especially in prolonged cultures due to reasons including cell confluence (extremely dense/sparse plating), evaporation, environmental fluctuations and lack of periodic medium exchange [125]–[127]. A real-time reliable pH monitoring can probe these changes, as well as provide valuable information on metabolic processes, cell functions and the overall growth[3], [121], [122], [128]. A detailed comparison of

various pH sensors are available elsewhere [129] but of all available systems, the electrochemical and pH-FET (field-effect transistor) sensors [121], [125], [129], [130] are the most commonly applied ones for reliable pH sensing. Both of them are excellent candidates for pH sensing but require frequent calibration, sample physical contact and are prone to significant signal drift in long-term operations[125], [129], [131]–[134]. Frequent sensor calibration always challenges the sterility and increases the risk of contamination. Moreover, they, like any other chemical/biosensors, are extremely difficult to be sterilised [135]. Furthermore, the biofouling and membrane cell clogging are also problematic unless the sensors are coated with antifouling biocompatible materials. In contrast to electrochemical sensors, there is a growing interest in optical pH sensors because they can enable non-contact measurements with very good resolution and accuracy. Moreover, they exhibit very little calibration drift and require minimum maintenance[136]–[140]. Some optical pH sensors are already commercially available (e.g. iTube pH Bioreactor from PreSens, Wavepod II-pHOPT from GE Healthcare, TruFluor®pH from Finesse and OptiSens pH from Sartorius), and a few of them have already been tested in cell cultures.

2.6. Spectroscopic pH Measurements

Optical pH sensors can be of two types, contact sensors and non-contact sensors. A contact sensor, basically, is an optode that consists typically of three components; a chemical transducer (pH dye), a polymer matrix (to embed the dye molecules) and the instrumentation (waveguide such as optical fibre or micropatterned glass plate, light source, detector and measurement electronics). With physical liquid contact, the H^+ ions modify the dye's molecular structure or then the orbital energy levels. This change can be measured spectroscopically, for instance by measuring the light absorption/reflection/luminescence/fluorescence [129][139][140]. A contact optical sensor can measure the pH from extremely small volumes, but the sample physical contact is inevitable. The dye decay (by photobleaching/leaching), associated signal drifts and cytotoxicity/phototoxicity are also other concerns [129], [140]–[142]. On the other hand, a non-contact pH sensor avoids the sample physical contact (partially/fully) with a semi/fully detached chemical transducer and an appropriate optical measurement scheme. One good example is a reflective pH sensor (IDIL non-intrusive sensor from Fibres Optiques and REFLECT-PH-KIT from Ocean optics) that utilises ion-permeable pH membranes. The Smart pH cuvettes (PMMA/quartz, Ocean optics) is another attractive choice, where the inner

walls of the cuvette are sol gel coated with a sensor material (bromocresol green). Smart cuvettes are excellent candidates for many applications but intended for clear-non-turbid media and require a specific spectrometer for pH calibration and measurement. Another interesting possibility is dissolving a biocompatible dye, for instance, a calorimetric pH dye, at a given concentration in a medium of interest and measuring the colour changes qualitatively or quantitatively using a spectroscope or a colour camera [129]. Qualitative pH assessment is very common in cell biology, therefore a wide variety of culture media with phenol red (phenolsulfonphthalein, pH dye) is commercially available these days. Culture medium with phenol red exhibits a gradual colour transition from yellow to red when the pH changes from 6.8 to 8.2. The colour change intrinsically is driven by molecular changes, which is measurable also by spectroscopic means, enabling a quantitative pH estimation. In spectral measurements, phenol red attributes to two characteristic pH-dependent absorptions. This, with appropriate calibration, can be translated into absolute pH [143]. Hence, technically a standalone pH sensor becomes possible by measuring light intensity at one of the characteristic absorption wavelengths and at a neutral (reference) wavelength. This way a true non-contact pH sensor can be materialised, and a few schemes have already been tested elsewhere [121], [136], [138], [141], [144]. However, adapting the previously reported schemes directly into device-based biological systems have some challenges from the hardware integration and calibration perspective. Further, the formulations in previous approaches lack parameters to compensate for the effect of biofouling (biolayer). Also the effect of temperature needed to be corrected in real-time. In this context, we devised the non-contact pH measurement system MO-pH, using 3D printed sterilisable-modular components. For MO-pH, an improvised pH translational model was also developed that accounted for the effect of temperature and non-specific absorptions (eg. by biolayers), resultantly, the measurement accuracy improved notably.

3. PORTABLE SYSTEM FOR CONTROLLING AND MONITORING *IN-VITRO* CULTIVATION ENVIRONMENT AND IMAGE-BASED FUNCTIONALITY MEASUREMENTS

The design details of the compact digital microscope, iuCMP and CMaN (as an-add on tool for iuCMP) are briefly described in this chapter. The imaging module was constructed for both the conventional TLM and image-based analytical measurements. Although this may appear a simple task, our preliminary studies showed, for good quality *in-vitro* live-cell microscopy, the chosen imaging modality and its implementation are important. Otherwise, the imaging contrast and spatial resolution may not be acceptable especially for analytical computations.

Our experiments started with a couple of commercially available portable USB 2 microscopes [83], [84].These devices were rated for their broad adjustable magnification and easy computer connectivity. But, their performance was found not to be sufficient for live-cells and transparent specimens. So we started testing custom microscopy schemes, and at first, tested simple bright-field and dark-field strategies using inexpensive short focal length lenses (ACC-01-4000:4003, f=4 mm:8 mm, M12 microlens) and bare white LED lighting. See Figure 1a-c, for example images of hASCs and hiPSC-CMs, where one can see that the imaging quality and contrast are extremely poor compared to the reference images (AxioCam MRc5). Though these schemes are easy to implement, their performance with live-cells was not adequate mainly because the live-cells are highly transparent and absorb/scatter very little light.

In the next stage, we tested a few custom compact microscopy options, and three feasible digital microscopy schemes are provided in Figure 2.

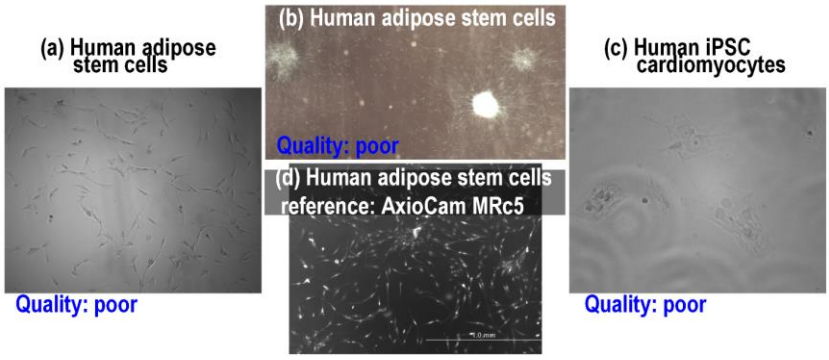

Figure 1. Basic bright and dark-field cell images using inexpensive short focal length lenses, machine vision camera and white LED lighting. (a-b) Human adipose stem cells (c) hiPSC cardiomyocytes. (d) Reference image with a standard microscope (AxioCam MRc 5). Here one can see the image quality and contrast in (a-c) are extremely poor, compared to (d).

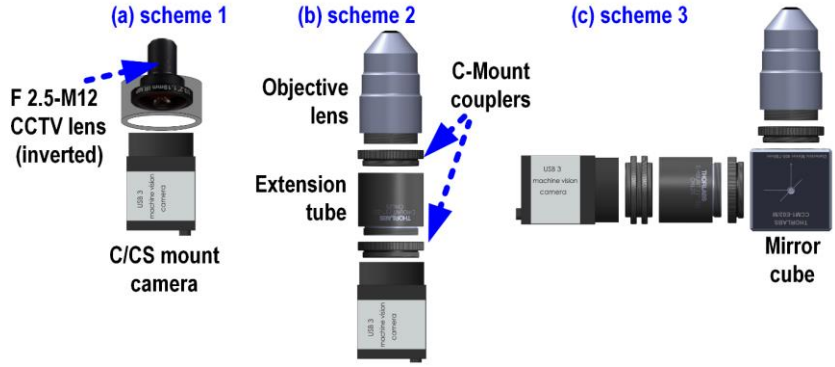

Figure 2. Three compact digital imaging schemes tested. (a) The most compact option (for live-cells) tested so far using an inverted fixed short focal length lens. (b) The option with a conventional objective lens and an extension tube. (c) A further miniaturised scheme using a mirror cube.

Each scheme in Figure 2 has inherent advantages and disadvantages. Figure 2a shows the most compact scheme tested so far that utilises a fixed short focal length lens (e.g. Lyx1.19, Lyxoptics, f=1.19 mm, M12 megapixel fisheye lens) in an inverted manner mounted to a machine vision camera (PointGray, BFLY-U3-13S2M-CS, 1.3 MP, pixel size =3.75 μm in 1/3" sensor) using a 3D printed adapter. Figure 2b shows the option of using a good quality conventional microscope objective lens and extension tubes. An advanced version of this scheme using a mirror cube is shown in Figure 2c. Scheme 1 doesn't allow changing the magnification (or FOV) plus the working distance is very short (4.2 -7.75 mm/EFL=1.19-2.1 mm). But in scheme 2

and 3, the magnification can be adjusted up to a certain extent using various extension tubes. Scheme 3 is the final approved and validated scheme for the iuCMP (Figure 9). In Scheme 3, the objective lens and the camera are implemented at 90^0 to each other through a mirror cube (CCM1-E02/M, Thorlabs). This makes the overall system very compact and, further, facilitates the possibility for installation of additional optics without unmounting the objective lens. Particulars of the Scheme 3 design, as well as results from microscopy characterisation, validation and long-term stability measurements, were presented in Publication I. An illustration together with the required illumination-scheme is shown in Figure 3.

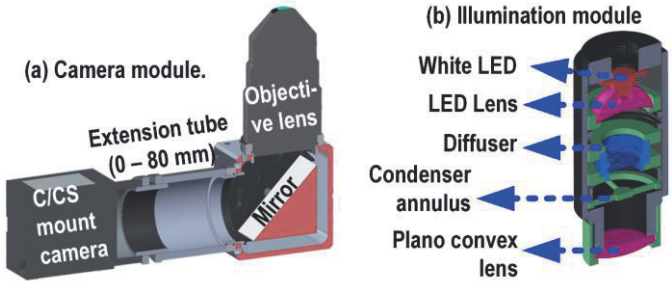

Figure 3. Anatomy of the digital imaging module used in Publication I. Section view of (a) camera module, (b) illumination module. The illumination module has a variable NA of 0.08 - 0.27. In the system, the magnification can be adjusted by changing objectives and/or with extension tubes.

3.1. Optical Simulations and 3D Design.

For the scheme shown in Figure 3, a 3D ray-tracing simulation has also been carried out, mainly to understand the magnifications limits, aberrations and to fine-tune the required illumination and its components. The simulations were solved using Ray optics module [ROM] in COMSOL Multiphysics (Version 4.3b, COMSOL, Inc., Burlington, MA, USA). For the 3D design and assembly, the SolidWorks (Version 2017) computer-aided design (CAD) platform was solely used. Once the suitable optical parts (commercially available) were identified, their 3D models were imported into the SolidWorks assembly and all additional parts were custom designed. The COMSOL-SolidWorks LiveLink delivers efficient interconnectivity for the design, ray-tracing simulations and optimisation. The ROM simulation allows modelling the electromagnetic wave propagation in finite element model (FEM) if the geometry is large compared to ray wavelength. In FEM solving, COMSOL

subdivides the large geometry into smaller parts (finite elements) and partial differential equations (PDE) describing optical propagations (e.g. reflection, refraction and absorption at boundaries) are solved on the generic element using a numerical solver (linear/nonlinear, stationary/time-dependent). PDE can have multiple solutions, so boundary conditions are necessary to constrain the solution. The results from generic elements are then combined to model the whole geometry. ROM-FEM model, therefore, can be used to optimise the geometry for a specific optical application. However, as the model usually represents just a simplified picture of the system, the results should be carefully considered as guidelines to evaluate the effect of multiple parameters [145]. A more meaningful model can be accomplished with appropriate validation typically through experimental investigation. Figure 4a shows the simulated ray trajectories of the digital imaging scheme (Figure 3) with a 10X equivalent objective lens. Here, a total of 2500 unpolarised rays per release were used in the ray tracing, but only just 5 % of them are displayed. The camera position (0-80 mm through the extension tube) is emulated by eight screens (cut planes) in the yz plane. Poincare maps at three selected positions; 1) at the condenser annulus, 2) the specimen and 3) camera locations (0, 40 and 80 mm) are shown in the Figure 4b, c, d. The magnifications simulated as well as experimentally measured (Table 1, Publication I) for a selected objective (10X) are given in Figure 5. The reason the measured and simulated values slightly differ could mainly be due to the difference in the lens train in the model and the actual objective.

In the final assembly, we use machine vision cameras (C or CS mount) and highly corrected objectives (Nikon CFI Achromat ADL 10XF, 20XF and 40XF) to produce good quality live-cell images with a negligibly little halo. The whole optical train is built around Ø1" optics and for a given objective, the FOV is a function of the extension tube length. The microscopy technical specifications are detailed in (Table 1, Publication I). Typical imaging when infinity corrected objectives are used requires the specimen to be at the exact focal point, which sets the image distance to infinity and a tube lens is used to produce the image at the camera. We avoid the tube lens to keep the system very compact but the trade-off is a reduction in the overall magnification but this on the other hand provides some extra working distance. Figure 6 shows a few example images of various cells (hiPSC neurons, hiPSC-CMs, hASCs, MEFs and Giemsa stained human blood smear) imaged with our digital microscope. A few additional cell images captured in different *in-vitro* studies can be seen [55], [112], [146], [147]. See also some example videos captured with our device in Publication I (Supplementary Video 1 and 2) and Publication II (Supplementary material 2 and 3).

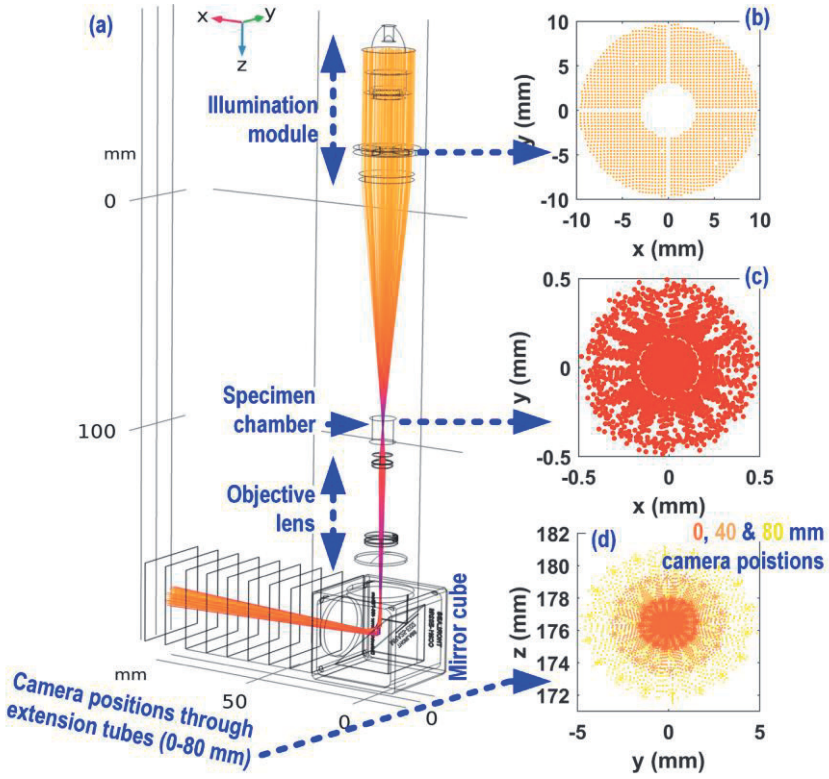

Figure 4. Digital microscope ray tracing simulation. (a) The simulated ray trajectories. Just 5 % of the total rays are displayed here. The camera positions (0-80 mm through the extension tube) are emulated by eight cut planes in the *yz* plane. The Poincare maps at (a) at the condenser annulus (b) at the specimen position and (c) at three camera positions (0, 40 and 80 mm).

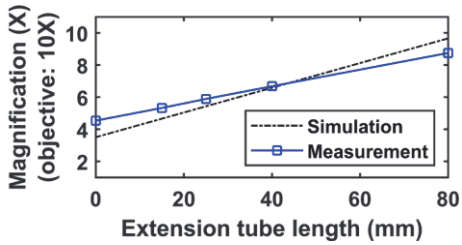

Figure 5. Simulated and experimentally measured magnifications with 10X objective as a function of extension tube length.

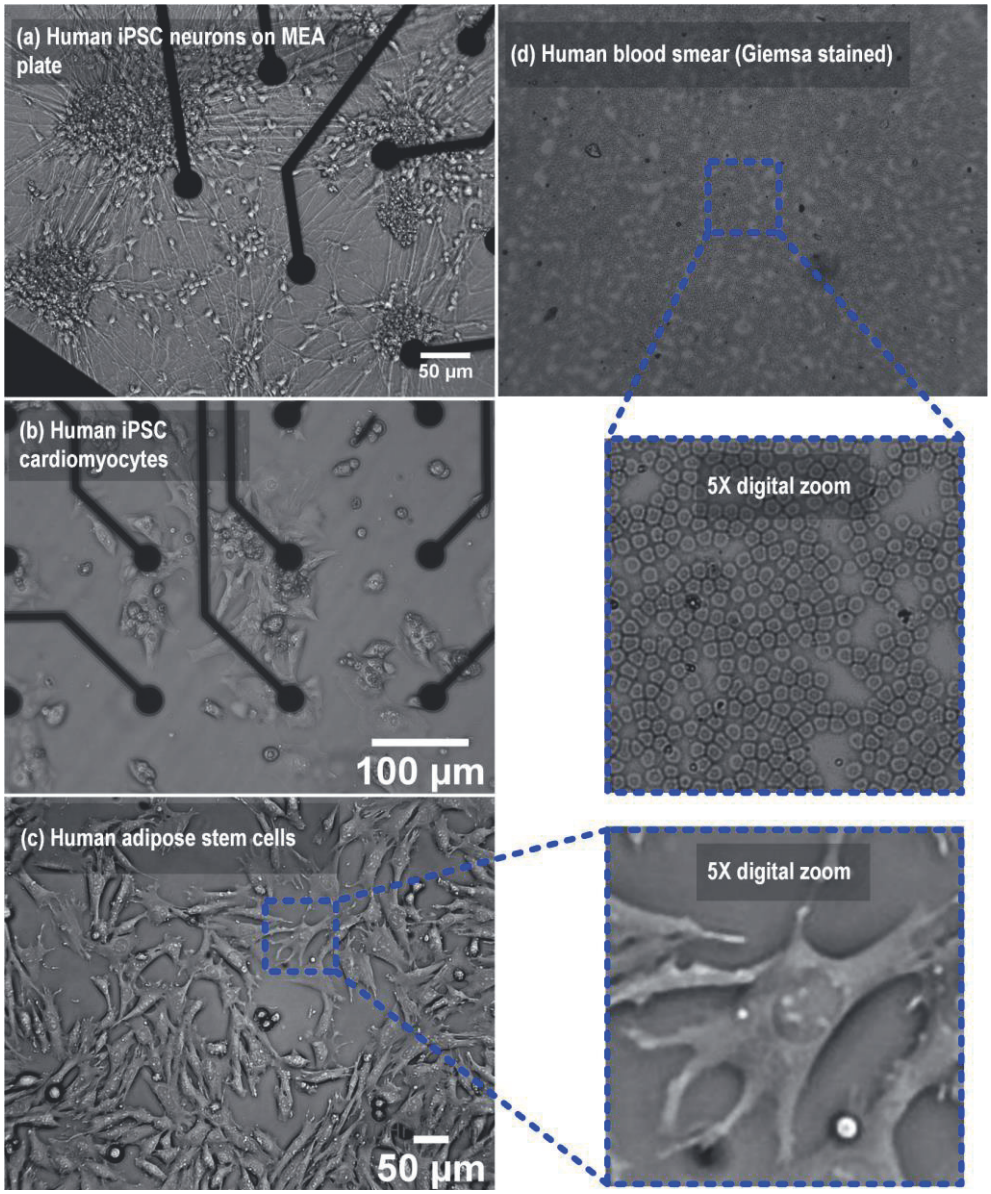

Figure 6. Cell images captured with the modular digital microscope in the iuCMP. (a-d) Various live-cells in the PDMS mini-incubator.

3.2. Digital Imaging Schemes with Programmable Magnifications

In addition to the three schemes presented in Figure 2, two advanced options (see Figure 7) with programmable (via software) magnifications have also been tested. In option 1 (Figure 7a) an inverted motorised varifocal lens (QM-D14-02812IR(3MP)-C-EE, Quanmin) with variable focus, f = 2.8-12 mm is utilised. This lens has two integrated micro-stepper motors to control respectively the focal length and iris. For this lens, the magnification as a function of the focal length measured in the iuCMP is shown in Figure 7c. Here, since the varifocal lens is implemented in an inverted manner, the back focal length (7.1 to 13.6 mm) determines the ultimate NA and spatial resolution. These type of lenses are very compact, customisable and highly cost-effective. Further, the motorised iris can be used to control the amount of light transmitted, thereby the fine focusing. However, tests showed the cell images produced with this lens is somewhat soft (less sharp edges). The second option (Figure 7b) utilises an electrically tunable lens (E-TL, EL-16-40-TC-VIS-5D-1-C-Optotune, f=-50:33 cm, response time = 5 ms) which allows very fast adjustments of the focal length. In its very basic implementation, the magnification measured in our system as a function of E-TL current is shown in Figure 7d. Here, the total change in magnification is not huge, but compared to the varifocal lens scheme, the E-TL can change the magnification very rapidly, hence it can be a good candidate, for example, for high-speed z-stack acquisition, automated focal drift correction and maybe also for CM force characterisation studies. We plan to integrate the E-TL lens (with additional optics), as a standalone module in the near future.

For most *in-vitro* cell experiments, the traditional spatio-temporal inverted TLM is sufficient. But when upright microscopy is to be applied, a long-working distance objective is essential as the cells need to be imaged, for example, from the top of the mini-incubator (7-12 mm tall). For highly corrected optics (e.g. plan fluorite, plan apochromatic), typically, long working distances are seen only with low magnification (and NA) objectives. So for the upright imaging in iuCMP, a low magnification objective is utilised, but, the magnification can be further improved using extension tubes as shown in Table 1, Publication I. The interchangeable architecture in the system enables easy switching between the invert and upright schemes. This is briefly described in the next chapter.

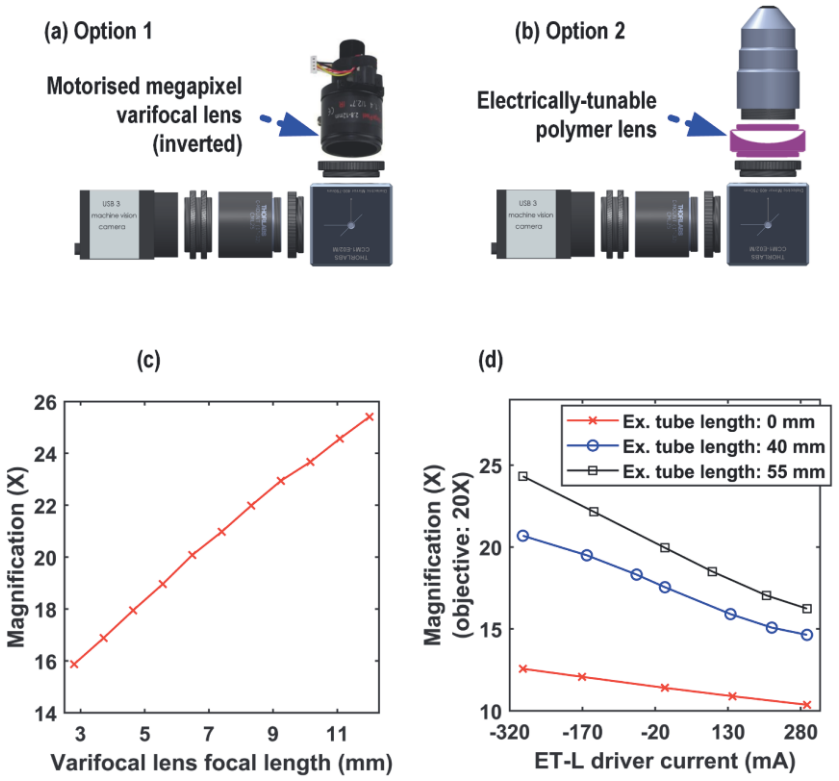

Figure 7. Compact digital microscopes with programmable magnification. (a) The option of using an inverted varifocal lens. (b) A better option of using an electrically tunable (E-TL) polymer lens. (c) Measured magnification against the varifocal lens focal length. (d) Measured magnification versus the driver current in the E-TL scheme.

3.3. Invert-upright Interchangeable Modular System

A brief summary (adapted from Publication I) of iuCMP interchangeability with four convertible options are given in Figure 9. The assembly mainly consists of a narrow motorised translation stage (960-0050, Eksma Optics, z= 50 mm, resolution ≤ 1.25 μm, focusing speed= 5 mm/s) with dovetail heads (rail and carrier). The camera and illumination modules are connected to the carrier heads using custom holders. Additional parts include, a manual xyz-stage (MAXYZ-40R, Optics-focus, x,y = ±6.5mm, z = 10mm, resolution = 10 μm), an ITO (Indium Tin Oxide) stage heater (k-frame, Okolab, H401/in-house-made heater [112]) and a PDMS mini-incubator (Figure 8, see Publication I for specific details)[148]. In addition, gas bottles (with solenoid valves), MEA amplifier (MEA2100-Lite-System, Multi-channel systems)

and the pO_2 sensor [55] are also integrated. The modularity allows the system to be arranged, for example, in an inverted configuration (Figure 9a), an upright configuration (Figure 9b), an upright configuration with pO_2 sensor (Figure 9c), and an upright configuration with pO_2 sensor and the MEA amplifier (Figure 9d). After the system assembly, its long-term mechanical performance (from the focal drift point of view) has been measured and the experimental plots are provided in Publication I (Figure 7). These measurements showed that the system works relatively well and is acceptable for TLM.

In iuCMP, a custom GUI (Figure 10 a-c) is implemented for enabling all the connections (microscope, illumination, pO_2 sensor, MEA, TSP, motorised focusing, ITO heater and its pt100 sensor). The initialisation (LED, camera, live-view, focus and magnification) and the data logging (sensors, camera and TLM) controls can be seen in Figure 10b-c. The LED intensity (0-100% via PWM, resolution 8-bit) and the focusing (Adafruit motor shield V2) are interfaced using ATmega328 (Atmel) based microcontroller (Arduino Uno R2). The GUI shows the plurality of several functions and is constantly being upgraded in line with hardware developments. For example, the integration of automated beating analysis (the modified version of CMaN) is a very recent addition for almost real-time CM functionality analysis. This was developed as part of a subproject (See Chapter: 3.4.4. **Real-Time Closed-Loop Control of hiPSC-CM Beating Frequency**).

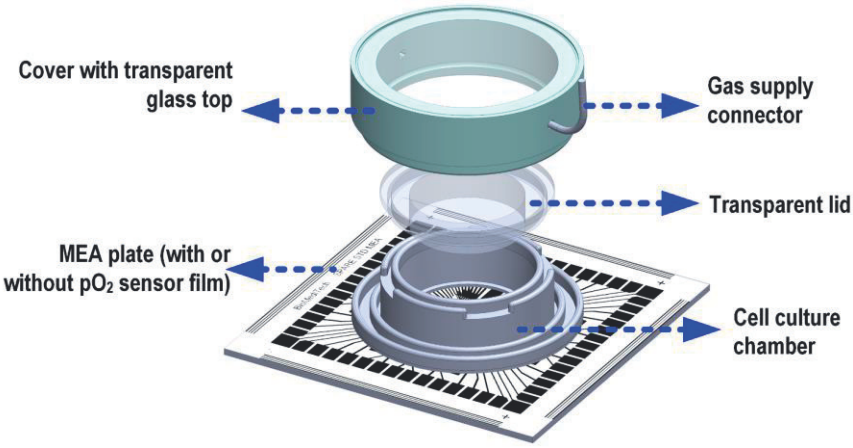

Figure 8. PDMS mini-incubator and its components. See Publication I for the technical details

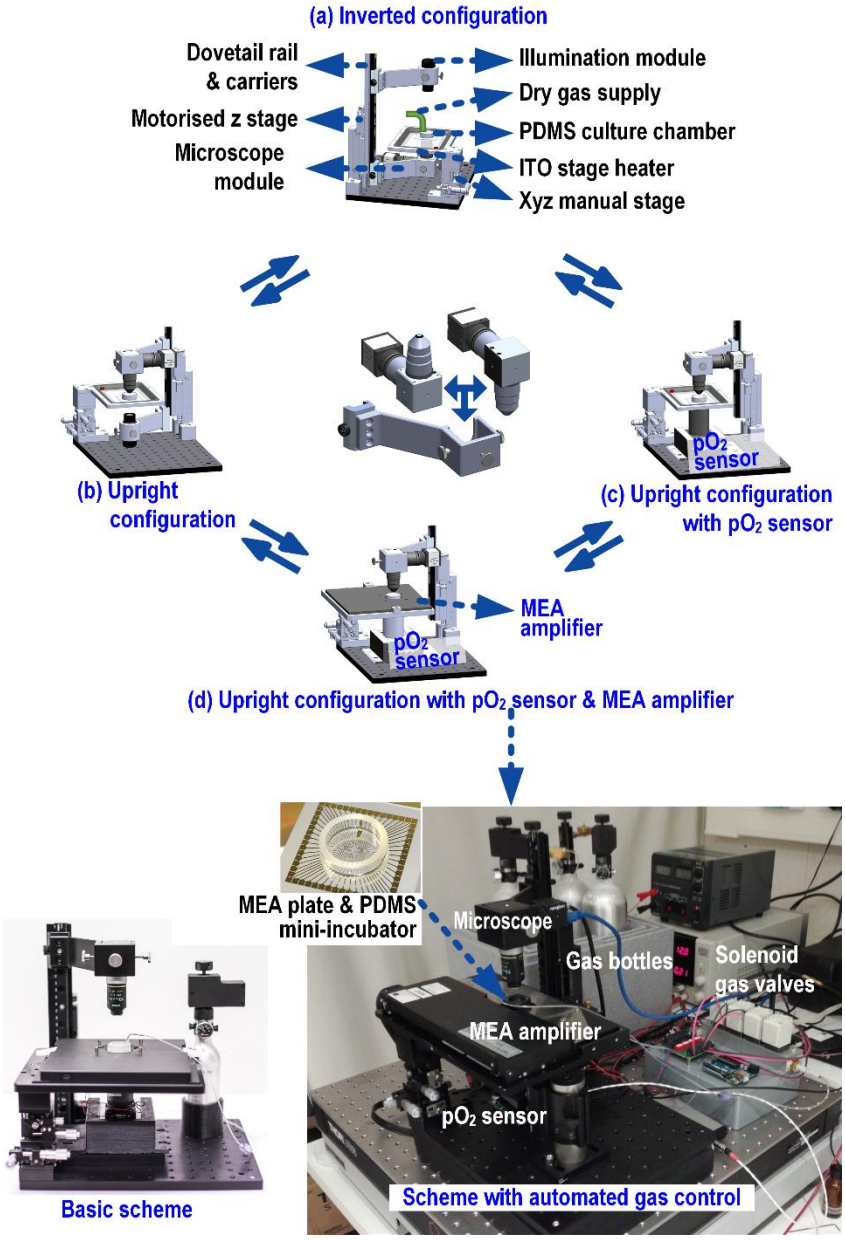

Figure 9. The iuCMP and its Interchangeable architecture. The system configured for (a) inverted microscopy, (b) upright microscopy, (c) upright microscopy with simultaneous pO_2 sensing and (d) upright microscopy with pO_2 sensing and electrophysiological recording (MEA2100-Lite-System, Multichannel Systems). (e) An original photograph and the final system build.

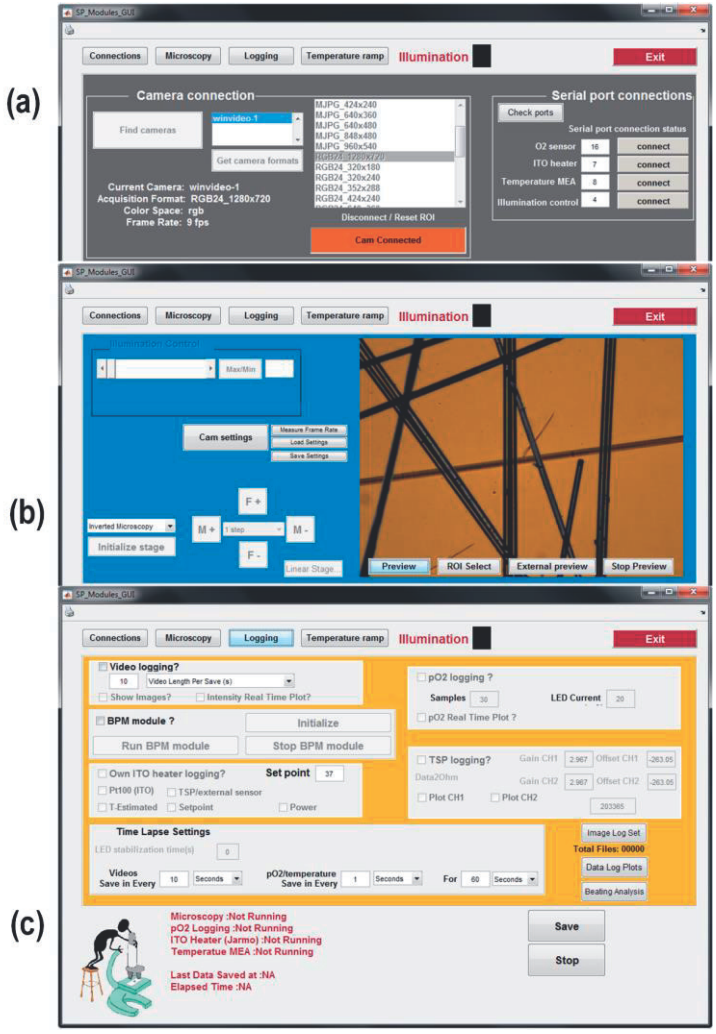

Figure 10. The GUI for iuCMP control. Windows for (a) hardware connections, (b) system initialisation and (c) data logging.

3.4. Results and Discussion

The main results with the iuCMP and CMaN are provided in the following subchapters. Brief discussions are included with each subchapter instead of a common discussion covering all the subchapters in the end.

3.4.1. CMaN - A New Software for Cardiomyocyte Non-invasive Function Analysis

CMaN was scripted (as a GUI software), evaluated and released as part of Publication II. Initially, it was developed as an offline tool, but lately, has been further scripted for almost real-time automated analysis. Figure 11 (adapted from Publication II) shows the user interface of the software. Figure 11b shows the best beating signal automatically selected out of the six signals extracted from a representative single cell cardiomyocyte. The table (Figure 11c) shows the estimated mechanobiological parameters: beating frequency, relaxation time, contraction time, relaxation amplitude, contraction amplitude and beat-to-beat interval. The software details are discussed below.

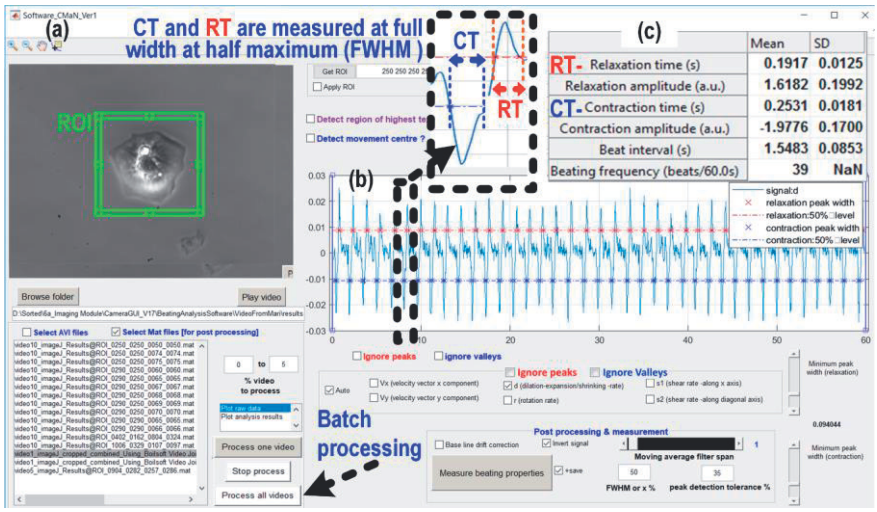

Figure 11. An advanced cardiomyocyte movement analysis software-CMaN. (a) Software user interface. The green rectangle (ROI) shows the region selected around a single cell cardiomyocyte for the beating movement analysis. (b) The best beating signal automatically detected out the six beating signals extracted. (c) The mechanobiological parameters estimated. See also Figure 14.

3.4.1.1. Optical Flow and Affine Optical Flow

In CMaN, the contractile movement is analysed by computing the affine optical flow (AFOF) which is an advanced version of the classical optical flow (OF) [149], [150]. The OF describes the pattern of apparent physical movement of objects in a

scene (eg. digital image) relative to an observer. In the OF computation, the movement is quantified in terms of apparent pixel velocities (magnitude and direction). Computationally, the OF relies on first-order spatiotemporal derivatives of image intensities, as long as the intensity spatial gradient is not too small and varies from point to point [149]. The velocity in OF is parameterised by a two-dimensional flow vector V_x *and* V_y, representing the translations of image features in *x, y* directions. The theoretical formulations of OF are based on the 'brightness constancy assumption' [149]. This assumes the local intensity structure of a time-varying image feature is approximately constant for at least a short duration. This is a reasonable assumption in good fps imaging and the mathematical formulations are discussed below [149].

Let's assume I is the intensity of a pixel at a given location *(x,y)* of a feature in an image captured at time *t*,

$$I(x, y, t) \tag{1}$$

If the feature moves *dx (along the x-axis) and dy (along the y-axis)* in the next frame captured at *t+dt*, the new intensity can be written as,

$$I(x + \Delta x, y + \Delta y, t + \Delta t) \tag{2}$$

If the movement is not very huge and the frames are taken at a very short time apart (e.g. 10 ms in a 100 fps video), with the 'brightness constancy assumption' these two intensities can be treated to be the same, i.e.

$$I(x, y, t) = I(x + \Delta x, y + \Delta y, t + \Delta t) \tag{3}$$

By applying Taylor series expansion to the right hand side, the Equation (3) can be rewritten as,

$$I(x, y, t) = I(x, y, t) + \frac{\partial I}{\partial x}\Delta x + \frac{\partial I}{\partial y}\Delta y + \frac{\partial I}{\partial t}\Delta t + H.O.T. \tag{4}$$

If H.O.T are neglected, the above equation can be rearranged as,

$$\frac{\partial I}{\partial x}\Delta x + \frac{\partial I}{\partial y}\Delta y + \frac{\partial I}{\partial t}\Delta t = 0 \tag{5}$$

Now differentiating Equation (5) with respect to *dt,*

$$\frac{\partial I}{\partial x}\frac{\Delta x}{\Delta t} + \frac{\partial I}{\partial y}\frac{\Delta y}{\Delta t} + \frac{\partial I}{\partial t}\frac{\Delta t}{\Delta t} = 0 \tag{6}$$

$$\frac{\partial I}{\partial x}V_x + \frac{\partial I}{\partial y}V_y + \frac{\partial I}{\partial t} = 0 \tag{7}$$

Where V_x *and* V_y are termed as the optical flow in x and y directions.
If substituting for intensity and temporal derivatives as,

$$\frac{\partial I}{\partial x} = I_x, \qquad \frac{\partial I}{\partial y} = I_y \quad and \quad \frac{\partial I}{\partial t} = I_t$$

Now Equation (7) can be rearranged as

$$I_x V_x + I_y V_y = -I_t \tag{8}$$

Equation (8) is the optical flow constraint equation (OFEq). If we have two images taken at a short time apart, the image x-y derivatives (I_x *and* I_y) and temporal derivative (I_t) can be computed for each pixel. Still, the flow vectors V_x and V_y cannot be solved from Equation (8) since it is under-constrained, i.e. one equation with two unknowns (see Figure 12, the V_x *and* V_y can be anywhere on the constraint line).

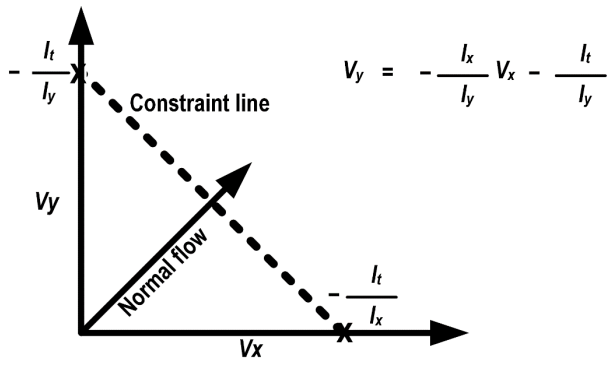

Figure 12. A graphical representation of optical flow constrained equation (Equation (8). The flow vectors V_x and V_y can be anywhere on the constraint line.

Therefore, we need more constraints to solve it and one good approach is considering several pixels in a local neighbourhood (window). For example, with a 9-pixel window (3x3 grid), assuming the OF is the same in this window, 9 separate OFEq equations can be written as,

$$I_{x1}V_x + I_{y1}V_y = -I_{t1}$$

$$I_{x2}V_x + I_{y2}V_y = -I_{t2}$$

….

….

$$I_{x9}V_x + I_{y9}V_y = -I_{t9} \tag{9}$$

Now we have 9 equations and 2 unknowns which is over-constrained and mathematically solvable. In matrix form, we can write Equation (9) as

$$\begin{bmatrix} I_{x1} & I_{y1} \\ I_{x2} & I_{y2} \\ . & . \\ . & . \\ I_{x9} & I_{y9} \end{bmatrix} \begin{bmatrix} V_x \\ V_y \end{bmatrix} = \begin{bmatrix} -I_{t1} \\ -I_{t2} \\ . \\ . \\ -I_{t9} \end{bmatrix}$$

$$AV = I_t \tag{10}$$

But since A is not a square matrix, the method of pseudo inverse (multiply both sides with transpose of A) is applied first to convert it into a square matrix as,

$$A^T AV = A^T I_t$$

$$\text{Now } V = (A^T A)^{-1} A^T I_t \tag{11}$$

Equation (11) can be solved by applying the least square error method by means of minimal

square $\left[min \sum_i \left(I_{xi}V_x + I_{yi}V_y + I_t \right)^2 \right]$.

So when we have two images taken a short time apart, the V_x *and* V_y can be solved from the I_x, I_y and I_t, computed over a window of several pixels. However this basic OF solution provides only the basic translation of features in *x,y*. For more parameters, we applied the method of AFOF computation.

Theoretically, AFOF is based on the affine transformations (see Figure 13) where the flow field need not be constant in the local neighbourhood window. It can be locally affine. The flow is parameterised by a six-dimensional vector to model the image translation (V_x, V_y), dilation-d (rate of expansion/shrinking), rotation-r (rate around z axis) and shears-s1, s2 (rates along x and diagonal axes) [151]–[153].

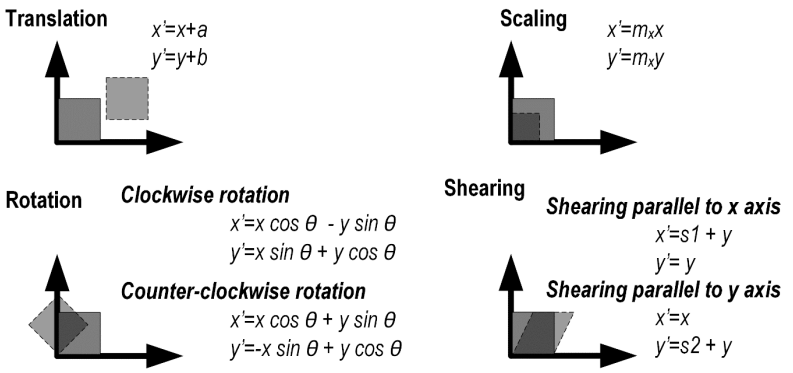

Figure 13. Affine transformations (modified based on [154], [155]). The transformations are modelled by image translation, scaling, rotation and shearing. In all the given plots, the *(x,y)* and *(x',y')* are the co-ordinates before and after the transformation. Other constants: a,b – horizontal and vertical translation constants, m_x, m_y, -scaling constants along *x* and *y* axes; s1, s2, -shear constants along *x* and *y*; θ - angle of rotation about the *x* axis.

All the transformations in Figure 13 can be collectively written as,

$$x' = m_x x + py + a$$

$$y' = m_y x + qy + b \tag{12}$$

where *p* and *q* are combined transformation constants.

Using the previously discussed brightness constancy assumption (Equation (8)), we can now express,

$$I_x(m_x x + py + a) + I_y(m_y x + qy + b) = -I_t \tag{13}$$

With a first-order expansion around a point (x_0, y_0) with flow (V_{x0}, V_{y0}), the affine model can then be expressed [153] as

$$V_x = u_x x + u_y y + V_{x0}$$

$$V_y = v_x x + v_y y + V_{y0} \quad (14)$$

where u_x, u_y (respectively v_x, v_y) are x and y derivative of u (respectively v).

In matrix form, Equation (14) can be arranged as,

$$\begin{bmatrix} V_x \\ V_y \end{bmatrix} = \begin{bmatrix} x \\ y \end{bmatrix} \begin{bmatrix} u_x & u_y \\ v_x & v_y \end{bmatrix} + \begin{bmatrix} V_{x0} \\ V_{y0} \end{bmatrix} \quad (15)$$

This can be equivalently rewritten as,

$$\begin{bmatrix} V_x \\ V_y \end{bmatrix} = \begin{bmatrix} x \\ y \end{bmatrix} \begin{bmatrix} d + s1 & -r + s2 \\ r + s2 & d - s1 \end{bmatrix} + \begin{bmatrix} V_{x0} \\ V_{y0} \end{bmatrix} \quad (16)$$

where *d*-dilation = $(u_x+v_y)/2$; *r*-rotation= $(-v_y+v_x)/2$; *s1=shear along x* = $(u_x-v_y)/2$, *s2=shear along y* = $(u_y+v_x)/2$.

Equation (15) and Equation (16) are implemented in CMaN for the contractile movement analysis. Equation (15) has one linear constraint in six unknowns, therefore a minimum of six pixels will be necessary to solve it. When an ROI (region of interest) in a video is chosen, the AFOF equations (for all the pixels in the ROI) form a system of linear equations, whose solution yields the six AFOM signals (V_x, V_y, d, r, s1 and s2). But usually, as ROI contains a large number of pixels (overdetermined), it is not necessary to calculate the gradients for every pixel. So the ROI may be resampled for fast AFOF processing. See Publication II for the software download link. The image pair extraction and the algorithm flow are schematised in Figure 14a. The six signals extracted from a representative single cell cardiomyocyte video is shown in Figure 14b. The movement centre detection and cluster finding schemes are also illustrated in Figure 14a, which will be discussed in detail in the next chapter.

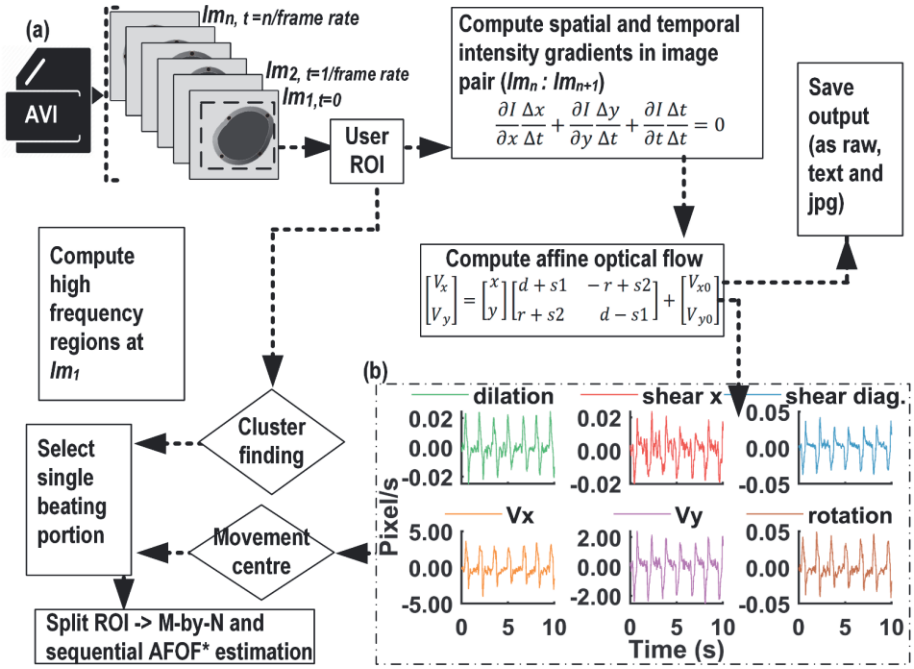

Figure 14. A schematic overview of the CMaN algorithm flow. (a) Extraction of successive image pairs from a beating movie and the principle of affine optical flow computation. The schemes of optional features (movement centre detection and cluster finding) are also shown. (b) The six contractile signal components extracted from a representative single cell beating video.

3.4.1.2. Movement Centre Detection and Cluster Finding

In CMaN, the movement centre detection (MCD) feature identifies the locations of the most energetic movement area by detecting the regions of the highest affine flow amplitude. The process steps are illustrated in Figure 15. Firstly, the AFOF beating signal is analysed from a selected ROI. Secondly, a small portion of the analysed signal containing at least one contraction-relaxation region is selected (see Figure 15a) for the MCD. For processing, the ROI is divided into M-by-N tiles as shown in Figure 15b-c. Then the AFOF signal is computed sequentially in all the tiles and the tile with the highest signal amplitude (movement centre) is identified. Once the movement centre is identified, a better beating signal can be re-analysed by defining a new ROI around it. This feature is illustrated in Figure 16 where the signal from the ROI, and separately from the identified movement centre and its neighbourhood are shown. Here one can see the signal from the region of movement centre is distinctively better than one from its surroundings.

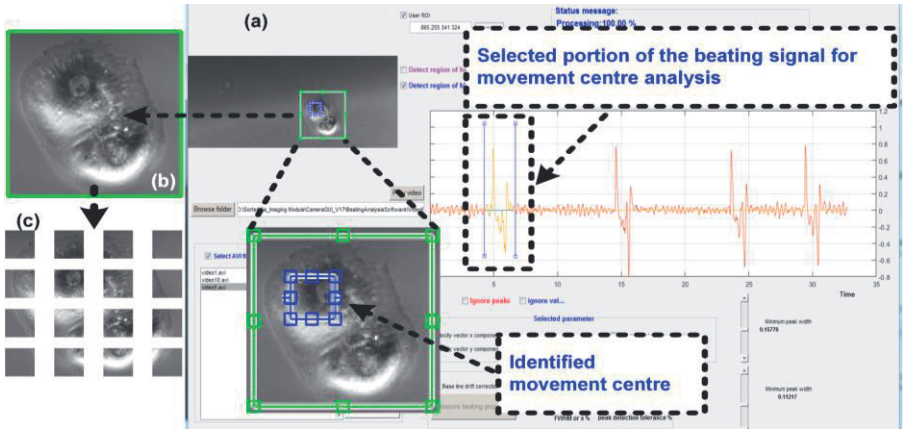

Figure 15. Movement centre detection (MCD) in CMaN. (a) The AFOF-V_y signal and a portion of the signal selected (with the draggable lines) for the MCD. (b-c) The ROI and segmented M-by-N tiles. The identified movement centre is marked with the blue rectangle.

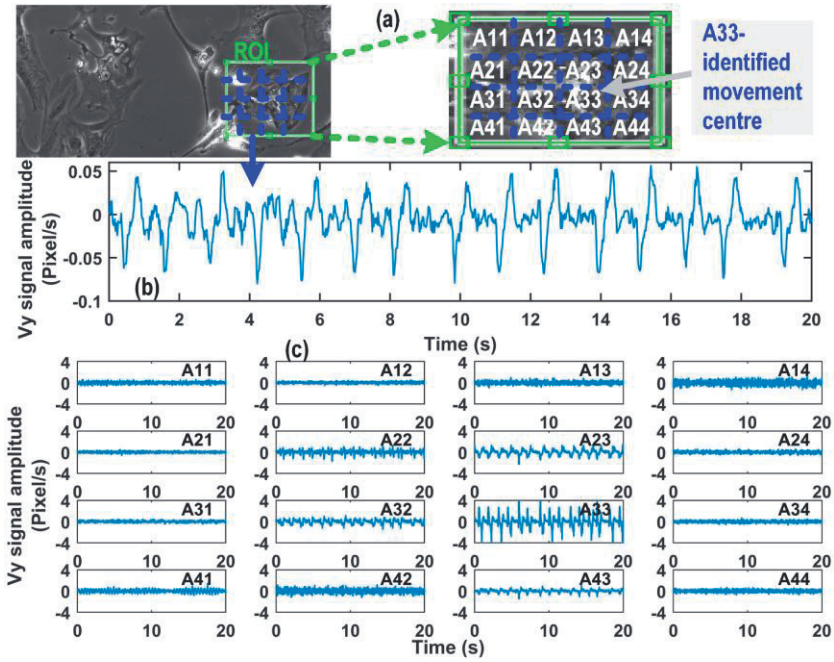

Figure 16. Beating signals at different locations of a contracting hiPSC-CM. (a) The ROI and the segmented tiles for MCD. The AFOF signal (b) from the ROI and (c) from the identified movement centre and in its neighbourhood.

Another added feature is the automated cluster finding (ACF) which is useful especially when the CM movement analysis is implemented with the online

microscopy where the analysis needs to start automatically without human intervention. The ACF is based on identifying the locations of the highest textures (high-frequency components), allowing one to recognise the CM clusters from its surroundings [156]. Usually, the cluster regions (imaged with a good microscope) have textures of high-frequency contents differing from its surrounding. The ACF in two example cases is shown in Figure 17 and Figure 18. After the initial processing (gamma enhancement, smoothing and absolute difference computation to reveal the cluster borders), an image convolution with a template is applied to identify the potential clusters (possible movement area). The histogram plots in Figure 17 and Figure 18 describe the image transformations in each stage. In Figure 17, there are only 3 clusters which are identified correctly with a 50 x 50 pixel template in a 3 stage convolution. But in Figure 18, with a similar 50 x 50 pixel template, an 8 stage convolution was needed to successfully identify all the clusters. But here one can see that instead of six clusters, eight locations (see the red cross marks) were identified. One of the located points (the top most-right hand side blue box) is not actually a cluster but possibly cell debris which happens to be moving with the CM. However, the signals from similar unwanted regions can be discarded later. In short, the ACF feature can be helpful in tracking the clusters for automated analysis even if they would have moved across the FOV during long-term TLM.

CMaN was tested against a tool based on digital image correlation [106] in the development phase, but later was critically tested against [103] and [104]. Table 2 and Figure 19, both adapted from Publication II, show the test summaries. In addition, a comparison of RGB and grayscale video processing times at three ROI sizes is provided in Table 1 . The robustness of automated signal analysis was measured with 114 consecutive TLM videos and found to be 99.12 % successful where 0.88 % failure was due to movement of the cluster outside the ROI (measurement area) over ~ 45 hours of TLM acquisition. See also the software instruction file in Publication II (Supplementary material 1). Based on these tests, CMaN has the following capabilities and notable advantages;

1. Several times faster, more sensitive, computationally less expensive and allows ROI selection.
2. Extracts six separate signal components of contractile motion per processing. This yields a minimum of one useful beating signal even in cases of complex beating videos.
3. Signals correspond to the contractile phenomena more exactly like an ECG signal with both positive (upstroke) and negative (downstroke) segments,

allowing one to compute not only the beating frequency but also the contraction and relaxation features separately.

4. Can detect the movement centre (region of the largest contractile motion) and the cluster locations (the movement area).
5. Suitable for independent or batch wise analysis cardiomyocyte (clusters/single cells) videos.

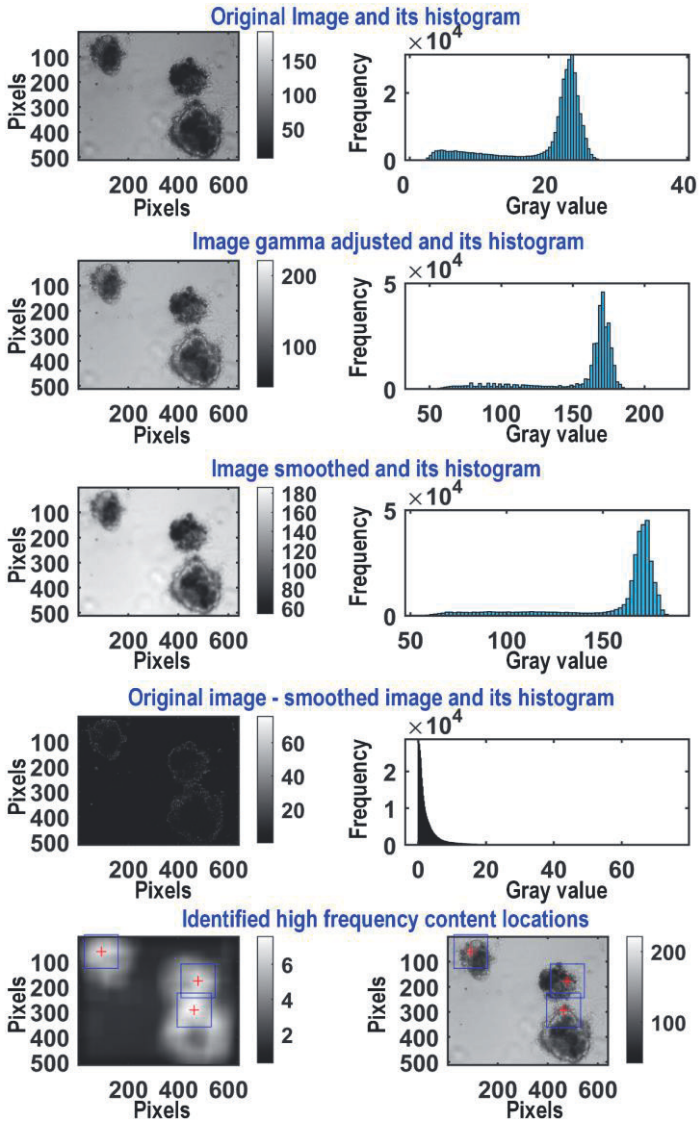

Figure 17. Automated cluster finding, A 3 cluster case: A 50 x 50 pixel template and a 3 stage convolution identified all the three clusters successfully.

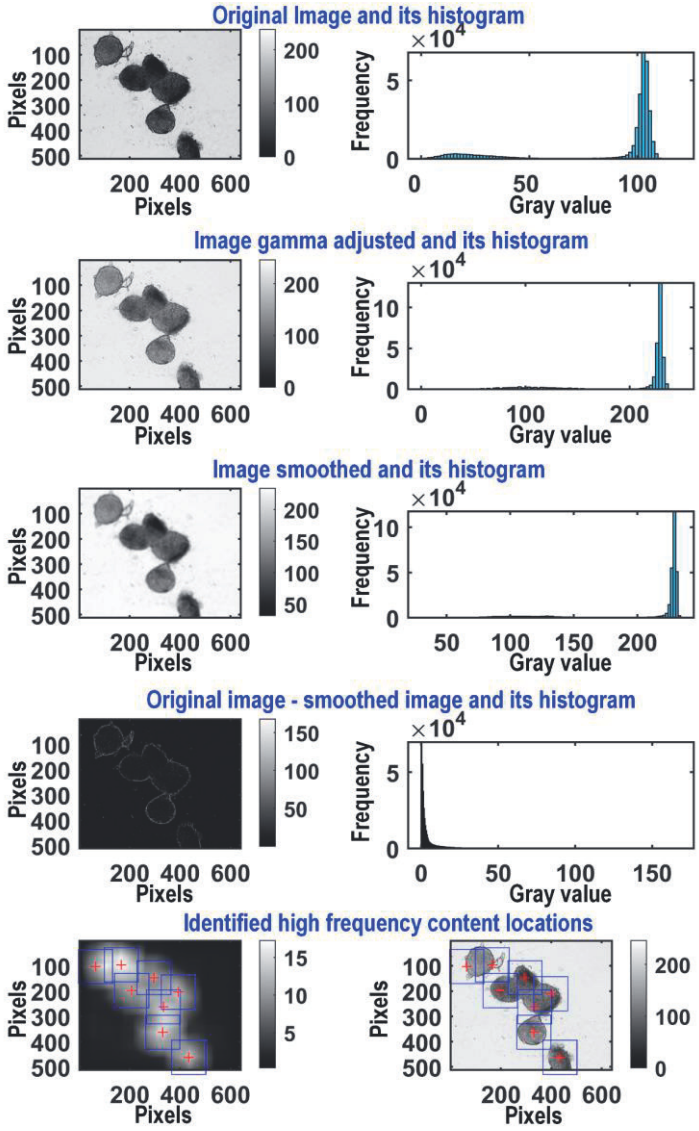

Figure 18. Automated cluster finding, A 6 cluster case: A 50 x 50 pixel template and an 8 stage convolution with 8 movement locations identified out of which 2 are erroneous. Here, certain regions (e.g. the top most-right hand side blue box, bottom plot) are wrongly identified as clusters. This is possibly cell debris that happens to be moving with the host cluster.

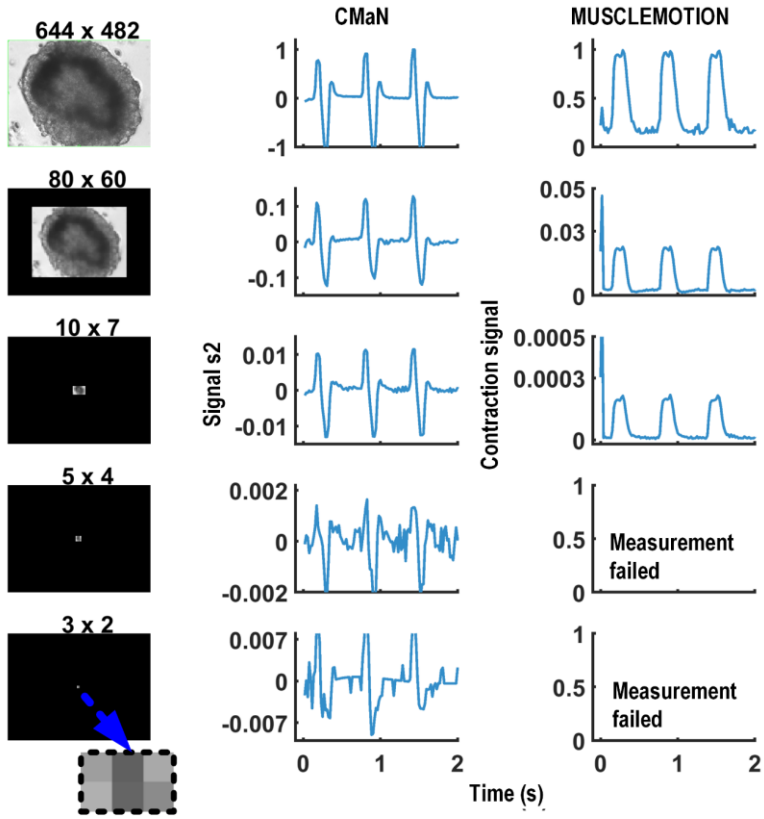

Figure 19. CMaN measurement sensitivity. The 1st column shows the screenshots of 5 videos. Here the original video (1st one) was spatially downsized 1/8, 1/64, 1/128 and 1/256 times to produce subsequent videos with reduced movement area. The next two columns show the signals (normalised, referenced to original signal, ROI: full frame) from corresponding movies using CMaN and MUSCLEMOTION. CMaN displayed better sensitivity.

Table 1. Testing grayscale and RGB video processing times in CMaN. See also Table 2

Bit depth	Fps	Duration (s), total frames		Measurement area (pixels)					
				640 x 512		300 x 300		100 x 100	
				Computer 1	Computer 2	Computer 1	Computer 2	Computer 1	Computer 2
16 / 8 bit (Grayscale)	60	30 s, 1800	**Processing time (s)**	50	62	20	23	17	18
32 bit (RGB)	60	30 s, 1800	**Processing time (s)**	58	80	28	33	21	25

Table 2. CMaN performance comparison against MUSCLEMOTION and SarcTrack using two computers (Computer 1: 2.6 GHz processor and 32 GB RAM, Computer 2: 2.7 GHz processor and 8GB RAM). †30 s long avi (60 fps, 640 x 512 pixels, 32 bit RGB, 1.64 GB size on SSD hard drive). *20 avi files (33 GB size on external SSD drive)

	MUSCLEMOTION	SarcTrack	CMaN	
Platform	Image J	MATLAB	MATLAB	
Algorithm principle	pixel intensity difference	fluorescent tag tracking	affine flow	
User defined ROI	no	no	yes	
Minimum ROI (pixels)	NA	NA	78 x 78	
Number of signals per processing	1	1	6	
Sensitivity	see Figure 19	NA	see Figure 19	
	Computer 1	**Computer 1**	**Computer 1**	**Computer 2**
1 movie† processing time (~minutes)	3 (6 in dynamic mode)	350	1	1.3
Batch* of movies processing time (~ minutes)	129	7390	25	28

3.4.2. Response of hiPSC-CM to Temperature Stimuli

In hiPSC-CM studies, accurate control of the environment, including the experimental temperature is very important to maintain normal cardiac activity and to avoid stress responses such as hyper/hypothermia shock reactions [157]–[161]. We utilised iuCMP and CMaN together with a TSP (glass plate, several micro-patterned resistive sensors) to study the temperature response in hiPSC-CM cultures. Automated temperature stressing and measurements were conducted and the results were reported in Publication II. For the measurements, the CMs were directly cultured on the TSP. This way, accurate temperature sensing from the exact location of cells, which is usually challenging with traditional bulky sensors, became possible. The TSP is coated with 250 nm of Si_3N_4 [112] which is the same insulator material on the commercial MEAs, so the surface properties of a finished TSP guarantees cell viability and harmless measurements. The experimental arrangement is shown in Figure 20 (adapted from Publication II).

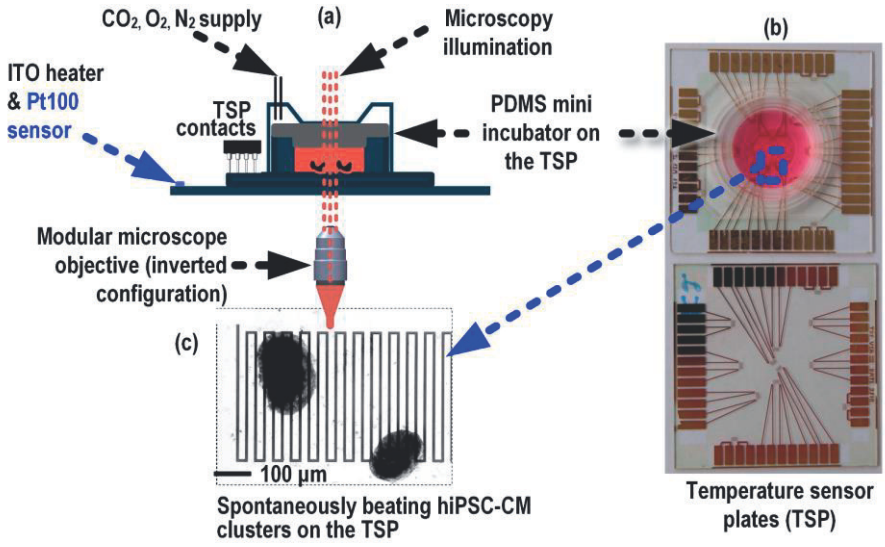

Figure 20. Setup for hiPSC-CM temperature stressing experiments in the iuCMP. (a) The PDMS mini-incubator. (b) Temperature sensor plates (TSP, two different types). (c) Beating clusters on one of the temperature sensors on the TSP.

The twelve spontaneously beating hiPSC-CM clusters used in this study are shown in Figure 21a-e. The middle image (Figure 21e) shows a snapshot from a movie (adapted from Publication II, Supplementary material 2) illustrating the effect of temperature on the hiPSC-CM function. Here one can see how the temperature affects the beating frequency, contraction and relaxation times. The measurements also showed the temperature dependency on the hiPSC-CM beating frequency was non-linear and the hiPSC-CM Q_{10} temperature coefficients were larger than 2. Furthermore, we also observed the signal propagation between dissociated clusters and reported their non-invasive measurements by image processing. Figure 21f shows the signals from six clusters (shown in Figure 21d) at different temperatures. The time delay between the signals indicated there is a clear delay in the signal propagation between the dissociated clusters. This was also made visually observable in the original beating movie by image processing; See Supplementary material 3 in Publication II for an example movie. Detailed measurement results including the calculated propagation velocities are presented in Publication II.

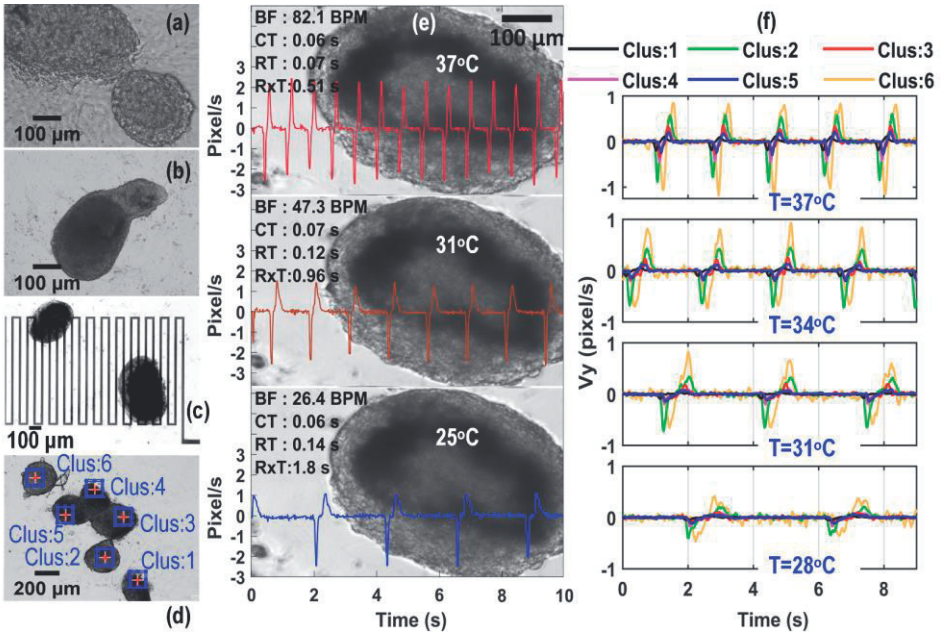

Figure 21. Effect of temperature on hiPSC-CM function. (a-e) Twelve spontaneously beating CM clusters used in the temperature response study. (b) Snapshot from a video displaying the beating signals of a cluster on corresponding movies at three selected temperatures. See Supplementary material 2 in Publication II for the full video. (c) The signals from six clusters (shown in (d)) at different temperatures. Here, the time delay between the signals clearly shows there is a delay in signal propagation between the dissociated clusters. Publication II, shows the computed propagation velocities and an example signal propagation video (made by image processing).

3.4.3. Oxygen Sensing in *In-vitro* Cell Models

Cellular oxygen is highly regulated in mammalian tissues [162]. A similar oxygen level is critical also in *C-Vitro* for the cells to have the same physiological functions as in the human body. A modern *in-vitro* system, ideally, should maintain a stable pO_2 tension similar to that in the corresponding tissue *in-vivo*, and, if needed, generate timely changes to study biological responses. For the pO_2 management in the iuCMP, we have adapted a phase fluorometric sensor as described in [163]. The sensor comprises of an oxygen-sensitive fluorescent dye (platinum(II) octaethylporphyrinketone) embedded in a thin polystyrene film and a fluorescent lifetime readout using a parabolic lens (tailor-made, polystyrene). The oxygen sensor has been applied for the pO_2 control of beating cardiomyocytes cultures to study the

hypoxia responses [55]. In this study, for the microscopy, we used the upright configuration with the Nikon 10x objective. For the special microscopy illumination, a green LED (532 nm) and 3 × 3 x 1 mm glass diffuser were mounted inside the pO_2 sensor head, on the optical axis, just under the parabolic lens. The oxygen levels around the CMs were periodically adjusted by switching the gas flow(5 mL/min) between normoxia (19% of O_2, 5% CO_2, and 76% of N_2) and hypoxia (1 % of O_2, 5% CO_2, and 94% of N_2) and the temperature, pO_2 and beating videos (60 fps, PointGrey FL3-U3-13E4M-C) were recorded. The results showed there is an overall correlation between the hiPSC-CM beating frequency (video analysed) and the oxygen levels. The details can be seen in [55]. However, this study was preliminary, and currently, an improved oxygen sensor (more biocompatible) with better electronics and optics is being utilised in a continued hypoxia project. This project is aimed to model the cardiac ischemia with hiPSC-CMs. Cardiovascular diseases are the leading cause of death worldwide, of which ischemic heart disease (IHD) is the most common one. In IHD, the blood flow to myocardium is blocked (or reduced), causing oxygen and nutrient deprivation and accumulation of metabolic waste. This would damage the myocardial cells (including CMs) and the heart contractions. Since pathophysiology of IHD is not fully understood, new models are needed where the iuCMP is expected to play an important role [164], [165]. Understanding the exact role of pressure and mechanical stress on cardiac ischemia is also important to the study of myocardial infarction [7], [166], [167]. On the experimental side (see Figure 22), automated protocols are enabled for controlling the oxygen levels, simultaneous sensing (pO_2, temperature) and for the functionality measurements (single cell MEA signal [168], video-microscopy and beating signal analysis). The pressure inside the PDMS mini-incubator (on top of single cell MEA) is controlled (1 mbar hydrostatic pressure + ~2-5mbar gas flow pressure). Changing the gas supply (e.g. O_2 from 19 % to 1% for hypoxia screening) does not change the overall pressure but it changes the pO_2 in the medium. With induced hypoxia, the cellular and molecular-level changes in cell functionality, morphology, viability as well as in gene and protein expressions will be studied. According to the preliminary results, hypoxia clearly affects both the hiPSC-CM functionality and the gene expression profiles. Detailed study results are expected to be reported in the near future. The oxygen concentrations used in [55] was mainly to validate the oxygen sensor in hiPSC-CM cultures. Incubators conventionally maintain ~19 % of oxygen level. But for most cells and tissues, this does not provide appropriate physioxia (tissue specific pO_2 in *in-vivo)* for their normal functioning and proliferation. Our group is developing microphysiological systems to control the oxygen in tissue-specific levels for various

cell types including hiPSC-CM. So in the future, the dynamics of physioxia to hypoxia/hyperoxia transfer or the controversial "inhibitory" role of high (~20 %) oxygen levels in CM proliferation etc. can be studied in more detail [169]–[171].

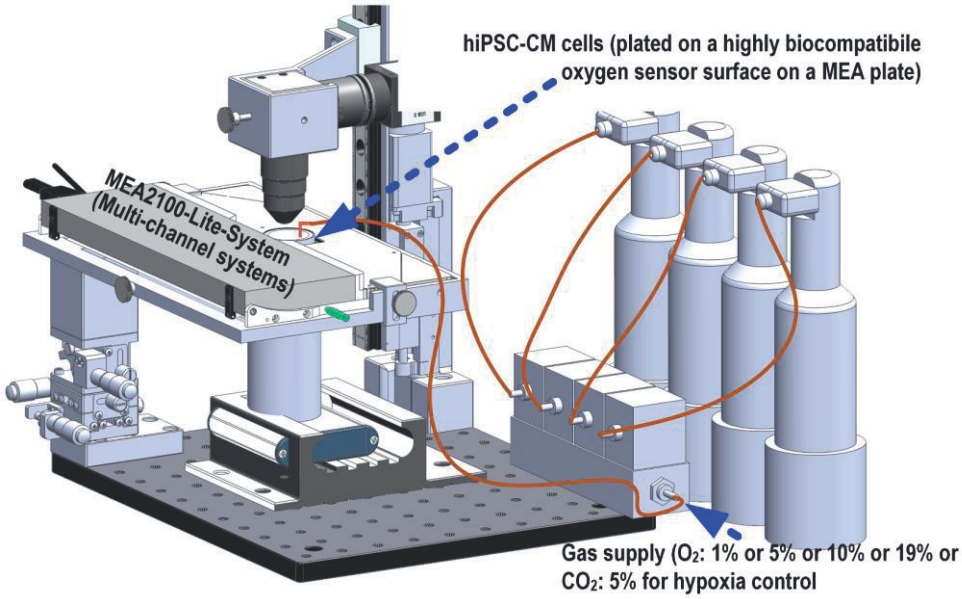

Figure 22. Cardiac ischemia on-a-chip: Experimental arrangement for the timely (automated) regulation of hypoxia, oxygen sensing and hiPSC-CM function (biomechanical and electrophysiological) measurements.

3.4.4. Real-Time Closed-Loop Control of hiPSC-CM Beating Frequency

The temperature response experiments with hiPSC-CM have shown that the beating frequency is clearly a function of the culture temperature [147]. This lead to an engineering question as to whether the beating frequency can be controlled at a required level by precise localised temperature adjustments. For this purpose, AJ Mäki [32] is testing a fuzzy controller based beating frequency control scheme (BPMFuzzy) with the iuCMP and the CMaN (real-time analysis version). See Figure 23 for a flow chart illustrating the BPMFuzzy data flow. In short, the BPMFuzzy records first a few (1 to 3) reference beating videos, analyses them (from the manually selected ROI) and stores the measured beating frequency as the reference. Afterwards, in long-term automated TLM, the BPMFuzzy works as a real-time

closed-loop controller which records videos, analyses them and compares the beating frequency with the reference. If there is a frequency variation, the controller then modulates the cell area temperature in order to adjust the beating frequency, with the frequency difference as a perturbing factor to the controller. For this purpose, we have completed the software editing and preliminary trials (without cells). Technically, BPMFuzzy works nicely but the studies with cells are yet to be scheduled.

3.4.5. Orientation of Fibroblasts on Nano Cellulose Surface

For demonstration purposes, iuCMP has been tested for the orientation analysis of mouse embryonic fibroblasts (MEF, obtained from Hannover medical school, Hannover, Germany) on cationic cellulose nanofibres (c-CNF on glass plate, [172]). The experimental details are presented in Publication I. The expansion of MEF (in DMEM high glucose medium) on the c-CNF surface was imaged in iuCMP for several days to study their orientation outside a traditional incubator. In the captured images, both the cells and cellulose fibres were equally visible with clear cell boundaries which confirmed the applicability of iuCMP also for relatively complex imaging requirements. Later, the degree of MEF orientation (alignment) was computed from TLM images using an orientation analysis tool (CytoSpectre, [173]). Resulting plots exhibited isotropy, indicating a good alignment of all oriented structures along a single line. See Publication I (also Supplementary Video 1 in it) for more details.

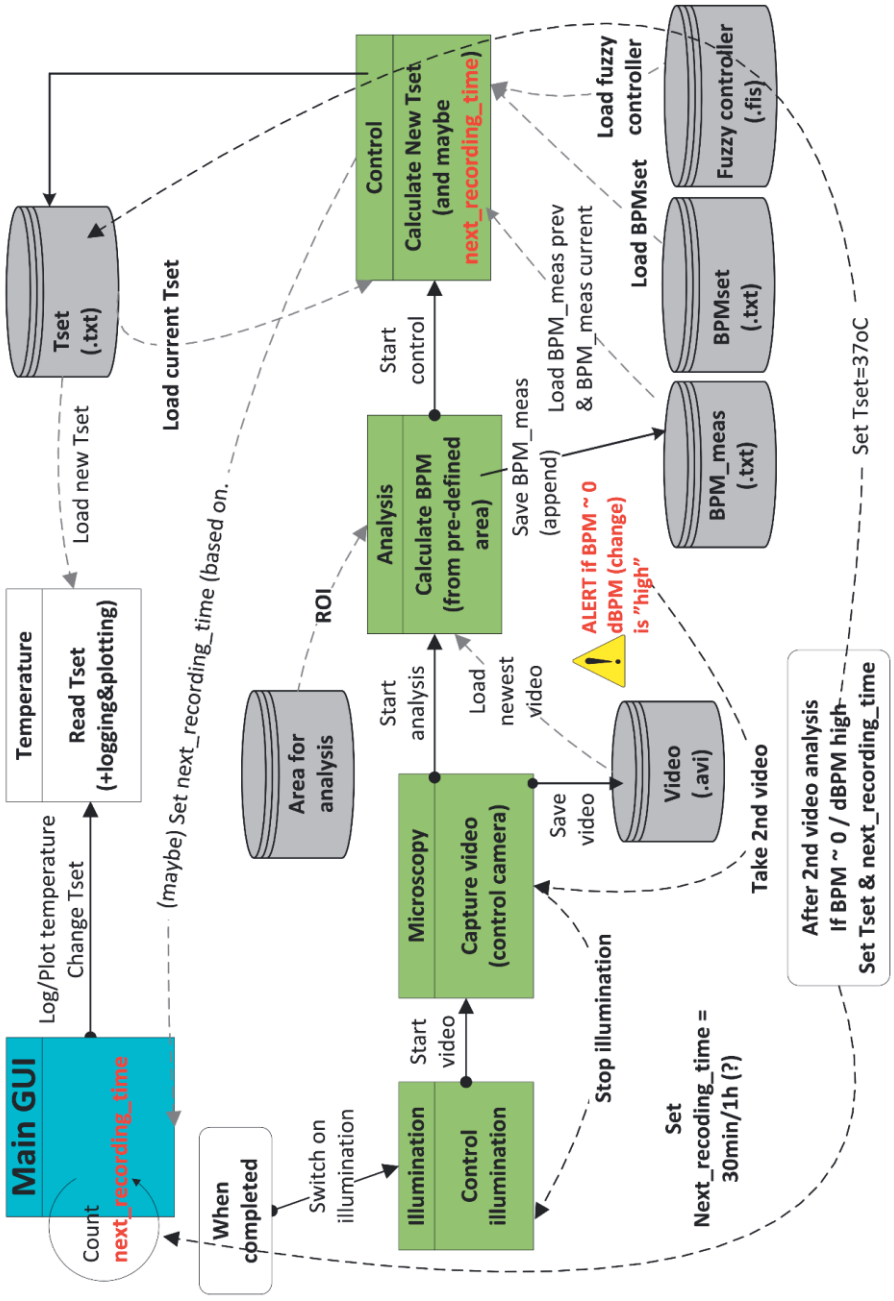

Figure 23. Flow chart illustrating the fuzzy controller based closed-loop control scheme for hiPSC-CM beating frequency.

4. NON-CONTACT OPTICAL pH MEASUREMENT SYSTEM WITH STERILISABLE, MODULAR PARTS

Our pH measurement system, MO-pH quantifies the pH changes of the phenol red (phenolsulfonphthalein -$C_{19}H_{14}O_5S$, *CAS* number 34487-61-1, ~8 mg/L) culture medium using a novel modular read-out scheme. The details of the system and a few application examples are presented in Publication III. This chapter briefly describes the working principle and main components of the MO-pH.

4.1. Two Colour pH Measurement System. Working Principle and Hardware Assembly

Phenol red medium responds to changes in the pH from 6.8 to 8.2 (~ 1.5 pH units) by displaying a gradual colour transition from yellow to red. Spectroscopically, these changes are measurable with absorption spectra (See Figure 1a in Publication III). In the absorption spectrum, an isosbestic point (~470 nm) and two characteristic absorption peaks: one at ~430 nm and the other one at ~560 nm, are visible. The characteristic peaks are due to structural isomerism accounting for the existence of phenol red in two forms: the acidic ([HIn] – yellow) and alkaline ([In^-]- red) forms. Consequently, the colour of the bulk medium (at a given temperature) is decided by the [In^-]/ [HIn] concentration ratio. This ratio can be translated into the absolute pH using the Henderson–Hasselbalch equation[174] as follows,

$$pH = pKa^{In} + log10\left(\frac{[In^-]}{[HIn]}\right) \tag{17}$$

where pKa^{In} - phenol red dissociation constant [175][176] .

In Equation 17, pH will linearly change with concentration ratio, $log10\left(\frac{[In^-]}{[HIn]}\right)$

Using Beer-Lambert's law, Equation 17 can be rewritten as,

$$pH = pKa^{In} + log10\left(\frac{\boldsymbol{\varepsilon}_{HIn}\ \mathrm{A}_{560}}{\boldsymbol{\varepsilon}_{In}\ \mathrm{A}_{430}}\right) \tag{18}$$

where ε_{HIn}, ε_{In} – phenol red molar absorptivity in acidic and alkaline forms. A_{560}, A_{430} – light absorptions at 560 and 430 nm. At a given pH of the solution, the total phenol red concentration (Ct), is the sum of the acidic and alkaline forms,

$$\mathrm{C}_t = [In^-] + [HIn] \tag{19}$$

In highly acidic solutions, phenol red naturally stays exclusively in the acidic form ie. Ct = [HIn]. Similarly in highly alkaline solutions, Ct = [In-]. With this conviction, Equation 18 can be further simplified as,

$$pH = pKa^{In} + \log 10\left(\frac{A_{560}}{A_{mx} - A_{560}}\right) \tag{20}$$

where A_{mx} is the maximum absorption at 560 nm of the highly alkaline state [176][177]. Figure 24 shows an experimental (for DMEM/F-12) plot of A_{560} as a function of pH where one can see the measurement of light intensity at 560 nm can be used for pH sensing with appropriate calibration. We adapted this idea to the MO-pH, but instead of 560 nm, we utilised 545 nm light measurements because 560 nm LEDs with acceptable luminous intensity was not available at the time of system assembly. Figure 24 shows a comparison of absorption at 560 nm and 545 nm as a function of pH where the shift in absorptions is seemingly of static (offset) nature which can be compensated in actual measurements, for example via an appropriate calibration. So in the MO-pH the final pH is estimated using,

$$pH = pKa^{In} + \log 10\left(\frac{A_{545}}{A_{Mx} - A_{545}}\right) \tag{21}$$

where A_{Mx} is the maximum absorption at 545 nm.

Equation 21 can be applied for pH estimation with acceptable accuracy if phenol red is used in its purified form [178]. If not purified, the indicator impurities may cause errors so the Equation 21 without further modifications will not be valid [178].

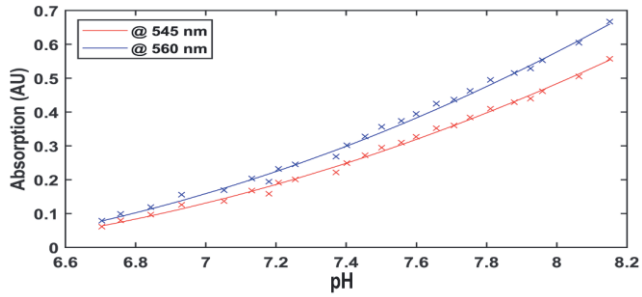

Figure 24. DMEM/F12 absorptions as a function of pH at 545 nm and 560 nm.

Technically, our original idea was to integrate a flow cell (e.g. quartz cuvette) into the *in-vitro* medium circulation tube/channel (e.g. in the perfusion outlet) and monitor the pH in real-time all through the cell cultures. With this aim, we first developed a measurement system suitable for a conventional incubator for long-term cell culture measurements. But in any case, opto-analytical measurements inside the incubator's highly humid environment has some challenges, including sterilisation difficulties, which are briefly discussed in the introduction chapter of the Publication III. As a robust solution, we developed an incubator compatible pH measurement system MO-pH using mostly 3D printed parts. Most importantly, the MO-pH can be sterilised, requires no special sample treatment or sample extraction outside of the incubator. Figure 25 illustrates the MO-pH working principle and shows its major components.

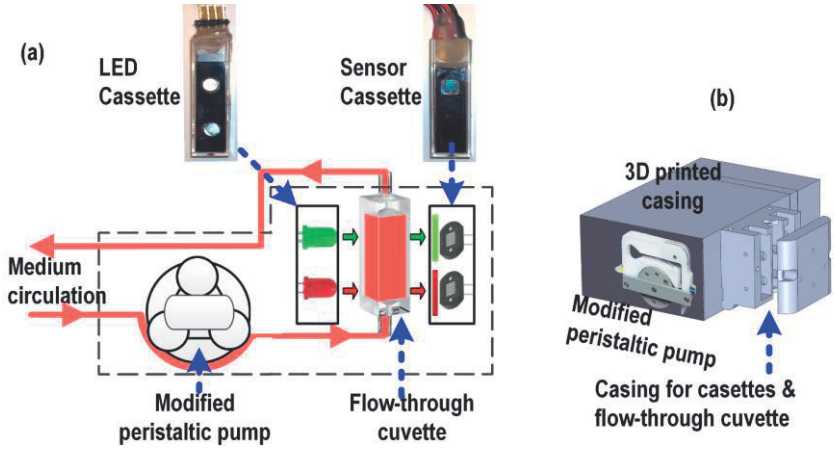

Figure 25. The modular pH measurement system MO-pH. (a) Illustration of measurement principle. (b) The airtight MO-pH casing with holders for LED cassette, sensor cassette and the flow-through cuvette.

The main components are two transparent sterilisable cassettes (custom-built, LED cassette and sensor cassette), a flow-through cuvette (Suprasil® quartz, 10×10 mm pathlength), a closed-loop flow pump (modified peristaltic pump - ISM596D - Ismatec REGLO Digital) and two integrated sensors (for temperature and humidity). The LED cassette comprises of a green LED (545 nm) and a reference red LED (680 nm). The sensor cassette comprises of two photodiodes (with green and red filters for separate green and red light measurements) and integrated transimpedance amplifiers. The measured optical performance of both the cassettes as well as the plots of their long-term performance are given in Figure 2 in Publication III. The cassettes are hermetically sealed, sealing efficacy tested and sterilisable (with 90% ethanol). The measurement medium circulates constantly through the flow-through cuvette via silicone tubing at a very stable rate (5 mL/min) all through the culture. More exact details of all the components can be seen in the Publication III.

Once the system was assembled, the initial pH measurements showed the system works well technically but a few issues were noticed. One immediate observation was Equation 21 solely cannot compensate for the effect of temperature in the pH. Secondly, the biofouling (deposition of proteins or cell debris), on the inner walls of the flow cell in long-term measurements seemingly affect the measurement accuracy. So its influence at the measurement wavelengths need to be carefully studied and a possible compensation scheme has to be figured out. In addition, the system also required a hassle-free calibration scheme reliable enough for several days of unattended pH measurements.

4.2. Temperature Compensation, Calibration and Humidity Monitoring

We figured out the effect of temperature can be compensated by adjusting the dissociation constant (pKa^{In}) in equation 21. Therefore, a good quality temperature sensor (TSic™ 506F/ IST-AG and W-EYK 6 PT100 Platinum temperature sensor, Heraeus Nexensos) was added into the MO-pH and the pKa^{In} was adjusted in real-time using the Van't Hoff's correction (equilibrium constant correction) formulation as,

$$pKa^{In}_{T_2} = pKa^{In}_{T_1} + log\left[e^{-7.5\left(\frac{1}{T_2}-\frac{1}{T_1}\right)}\right] \quad (22)$$

where T_1 - is the calibration temperature, T_2 – the new temperature. Figure 26 shows that the pKa (Equation (22)) as a function of temperatures for CO_2 buffered DMEM/F12 medium. In reality, the effect of temperature can be much higher in the absence of CO_2, which will be discussed in the Results and Discussion chapter. So the temperature compensation is important for accurate opto-analytical pH estimations. Further, the humidity was also constantly monitored mainly to understand/follow its fluctuations in long-term cultures. Humidity sensor (HIH-5031, pre-calibrated,) with a hydrophobic filter was used for condensation-free measurements in the incubator's highly humid environment.

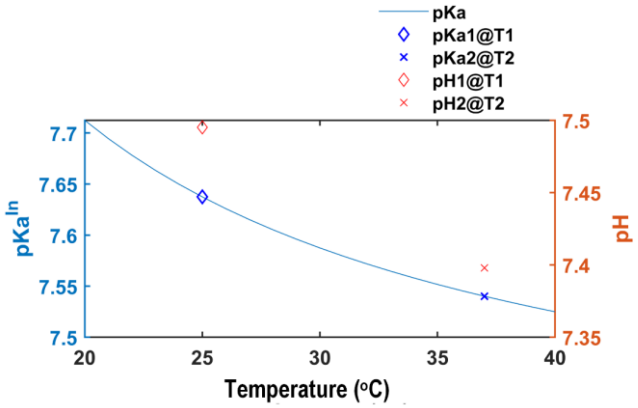

Figure 26. pKa^{ln} versus temperature. The continuous line is the pKa estimated using Equation (22). Two randomly measured pHs (at T1=25 °C and T2=37 °C) are also shown.

4.3. Absorption Correction Model

Equation 21 together with equation 23 is sufficient to estimate the pH when the cell density (confluence) is not very high. But when the cell density is high and/or in long-term continuous cultures, biofouling is very usual. Fouling can be by passivation of the flow cells' inner walls by lipids, proteins and cell debris [122][144][179]. Figure 29a shows an example case of biofouling imaged in ASC culture. Unfortunately, all the biofouling pathways are not yet clearly known. Our tests showed, it is not unambiguously clear how the biofouling affects the pH mainly because of its randomness (spatial and temporal) and consequent light loses (via scattering and absorption). But in any case, it can cause an error in absorption-based pH estimation (in Equation 21). As a reasonable fix, we developed an approximate

absorption compensation model (hereafter named GR model) for the specific instances of biofouling. In the GR model, the core idea is to include the absorptions at 680 nm (A^{680}) also into equation 21 with certain approximations. The hypothesis of the model was that even though A^{680} is not sensitive to the pH and should be constant, its fluctuations if any during the culture, would correspond the non-specific absorptions, for example, by the biofouling. The GR model was presented in the Publication III, but is discussed in detail below.

Optical absorption is an additive phenomenon. So in a mixture/multilayer system with N components, the total absorption,

$$A_{total} = \sum_{i}^{N} A_i \tag{23}$$

Therefore, the total absorptions at 545 nm and 680 nm can be individually written as

$$A_{total}^{545} = A_{indicator}^{545} + A_{dm}^{545} + t_{545}\, k_{545} \tag{24}$$

$$A_{total}^{680} = A_{indicator}^{680} + A_{dm}^{680} + t_{680}\, k_{680} \tag{25}$$

where $A_{indicator}$ – phenol red absorption. A_{dm} – absorption by the fouling layer of thickness *t*. *k* – a constant to account for the light loss by the fouling layer.

In Equation (25), since phenol red molecules do not absorb light at 680 nm,

$$A_{indicator}^{680} = 0 \tag{26}$$

Also
$$A_{dm}^{680} = \boldsymbol{b}_x[dm]\boldsymbol{\varepsilon}_{680} \tag{27}$$

where b_x – path length. [*dm*] and ε – assumed concentration and molar absorptivity of the biofouling layer.

Substituting equation 26 and equation 27 in equation 25 and rearranging it for [*dm*] yields,

$$[dm] = \frac{A_{total}^{680}}{b\boldsymbol{\varepsilon}_{680}} - \frac{t_{680}\, k_{680}}{b\boldsymbol{\varepsilon}_{680}} \tag{28}$$

$$\text{Also } A_{dm}^{545} = b[dm]\boldsymbol{\varepsilon}_{545} \tag{29}$$

Substituting Equation (28) and Equation (29) in Equation (24) yields,

$$A_{indicator}^{545} = A_{total}^{545} - \frac{\boldsymbol{\varepsilon}_{545}}{\boldsymbol{\varepsilon}_{680}} A_{total}^{680} - [t_{545}\, k_{545} - \frac{\boldsymbol{\varepsilon}_{545}}{\boldsymbol{\varepsilon}_{680}} t_{680}\, k_{680}] \tag{30}$$

Equation (30) describes the true phenol red absorption in terms of total measured absorption by avoiding biofouling absorptions. However, since all the terms in this equation cannot be experimentally measured in the context of long-term cultures, a perfect error-free pH measurement is virtually impossible. Nevertheless, mathematically one way to tackle this is by using two approximations (constants) as,

$$\frac{\varepsilon_{545}}{\varepsilon_{680}} = k_{dm} \quad \text{(absolute constant)} \tag{31}$$

$$\left[t_{545}\, k_{545} - \frac{\boldsymbol{\varepsilon}_{545}}{\boldsymbol{\varepsilon}_{680}} t_{680}\, k_{680}\right] \approx k_{bl} \tag{32}$$

With these approximations, equation (30) can be simplified into an empirical equation as,

$$A_{indicator}^{545} = A_{total}^{545} - k_{dm} A_{total}^{680} - k_{bl} \tag{33}$$

In cell culture, endpoint reference measurements (with a traditional pH meter at the beginning, end and at times of medium exchange during culture) can be used with equation 21 and equation 33 to extract approximate values of k_{dm} and k_{bl} by means of non-linear least square fitting. This is just an approximate compensation, but apparently very straight forward and practically possible.

4.4. Results and Discussion

4.4.1. System Calibration and Real Time pH Measurements

The LED timings (on-off cycles), and data acquisitions (16 bit, @ 500Hz sampling rate, 5 second average once in every 60 s) are controlled with a microcontroller (Arduino Uno-R2, a custom GUI). A screenshot of the GUI is shown in Figure 27 where the raw signals and the real-time pH plot can be seen. The 'Direct Green(nA)' and 'Direct Red(nA)' are the measured photocurrents corresponding to the absorptions in the 545 nm and 680 nm channels. Additionally, an extra sensor cassette is also included to measure the light scattered at 90^{o} with respect to incident light. The purpose of this measurement was to test whether the scattered light intensity can be used to estimate (roughly) the detached components (cells, debris, and particles). The signals from the 90^{o} channels are labelled as 'Scatter Green (nA)' and 'Scatter Red (nA)'). The results from these channels are inconclusive and not covered in the scope of this thesis.

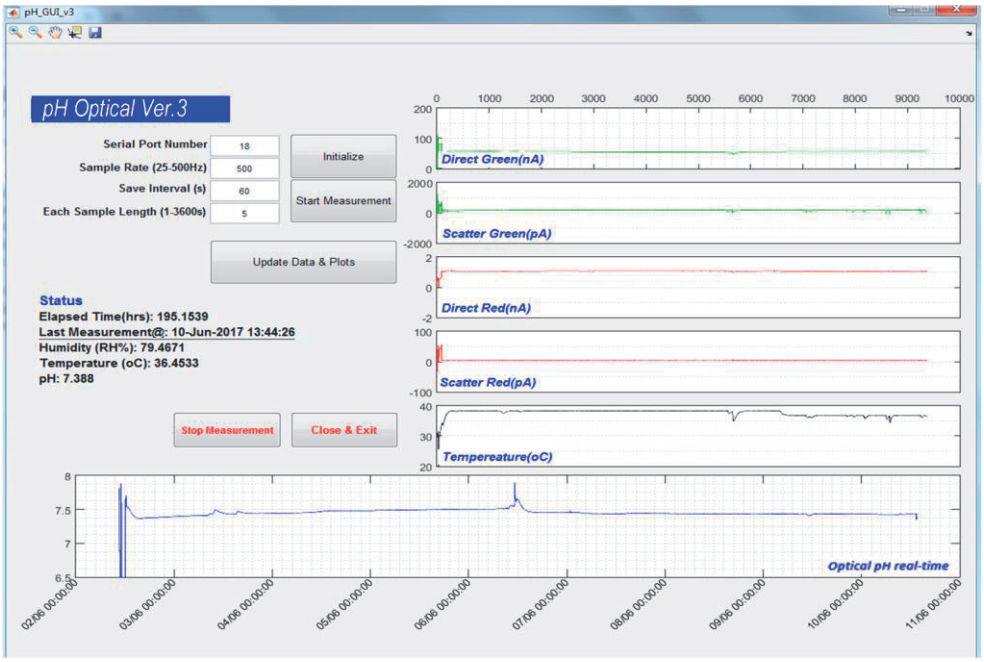

Figure 27. Screenshot of GUI of MO-pH system. The signals marked with 'Direct' are the absorption signals while the ones marked with 'Scatter' are the scatter signals measured at 90^{o} C of the incident light. The real-time pH plot is shown in the bottom axis.

Like any other pH sensor, the MO-pH requires pH calibration for accurate pH prediction. The points/options considered for the calibration are,

Option1: A three-point calibration at the beginning of the culture using custom buffers.

Option2: Option 1 plus supplementary re-calibrations with additional pH samples (the ones removed at times of medium exchange and at the end of the culture).

Option3: Without any calibration with pH buffers. An option to just to follow the pH changes instead of absolute pH. In theory, at a given temperature, pH $\propto$ phenol red absorption, $A=[\varepsilon*b]*C=constant*C$. So a basic absorption measurement can also follow the pH changes roughly.

Figure 28b shows an example calibration curve with three-point calibration. The pH of several samples (Figure 28a) measured with the calibrated system is shown in Figure 28c. On the other hand, when we take into account the biofouling issues and the availability of used-up medium (via medium exchange), the option 2 with re-calibrations improves the measurement accuracy notably. We use this option in long-term cultures and two example plots from hASC expansion cultures (in CO_2 dependent and CO_2 independent medium) can be seen in Figure 4 in Publication III. There, the inset figure shows the error bars with the calibration option 1 (labelled as 'Textbook equation') and option 2(labelled as 'GR model'). Also, original pictures of example biofouling films imaged (Objective 20X, Phase contrast) at the end of a cell culture together with their intensity profiles (horizontal and vertical) are provided in Figure 29a-b. Besides, an additional ~21 days of pH measurement plot in the osteogenic differentiation of adipose stem cells is provided in Figure 4 in Publication IV. All the reference pHs were measured with a glass electrode pH meter (WTW Multi 340i with SenTix 41-3 electrode, Weilheim, Germany) or an ISFET pH probe (Sentron SI600).

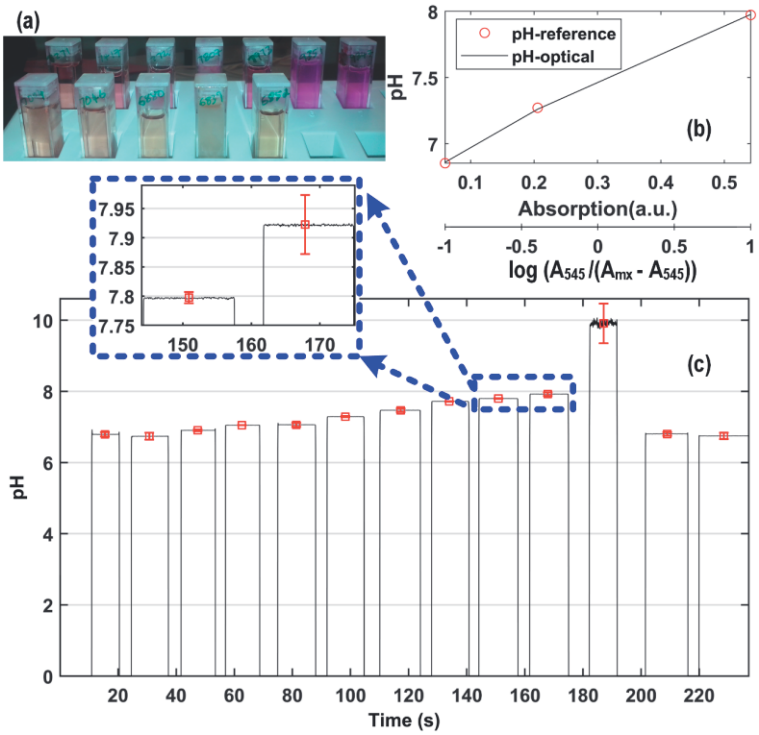

Figure 28. Optical pH measurements. (a) DMEM samples at various pH levels. (b) A three-point pH calibration curve. (c) Optical pH measurements with the calibrated MO-pH.

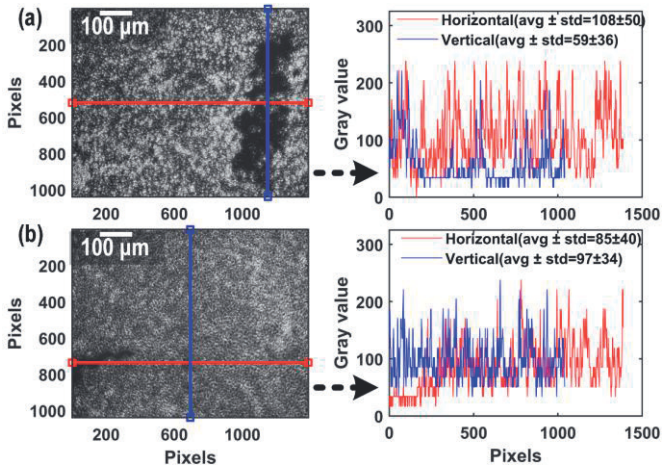

Figure 29. Biofouling in cell culture. (a-b) Original images of biolayer films on the inner wall of the flow-through cuvette after long-term adipose stem cell expansion cultures. The right-hand side images are the horizontal and vertical intensity profiles of the film across the green and blue lines on the left images.

Furthermore, we have also utilised the MO-pH to comprehend the behaviour of pH, temperature and humidity in water jacked incubators as well as to record the pH response as a function of temperature in the presence and absence (supply cut off) of CO_2 in the context of stem cell cultures in it. See Figure 2 in Publication IV for the experimental plots. Here the CO_2 levels were measured with a commercial CO_2 sensor (GC-0016-COZIR/ Factory calibrated). The measurements showed the pH drops ~0.2 and ~1.0 pH units in the absence of CO_2 (in fact it is 0.0995%) and in its presence (5%) respectively when the temperature drops ~ 10^{o}C.

4.4.2. Re-closable Lid System

Cell flasks, conventionally, play a vital role in life science research for the successful growth of cell lines. A wide variety of non-treated and treated (with synthetic or biological surfaces) flasks are commercially available these days for various applications [180], [181]. Out of all, the most commonly applied are the flat-sided flasks, Erlenmeyer flasks and the spinner flasks[182][183]. Some recent advances in the flask technology include, multi-layer flasks (for faster and easier scale-up of the culture), revised flask shaping (to access all corners with a pipette or scraper) and sophisticated flasks (e.g. flasks with sensor spots, rotating wall vessels, spinner flasks with impeller). Another notable technology in recent years is the flasks with re-closable lids (RL-F) and with the peel-off foils [184]. These are very unique flasks with the advantage that they can be opened and re-closed (liquid-tight), allowing total access from above, still without hindering the slip-free multi-flask stacking. Most importantly, they are re-usable with appropriate sterilisation. We have tested the applicability of RL-F flasks in our cell culture research. Then built (re-constructed) a standalone system around an RL-F flask, combining the cell culture, medium perfusion and optical measurements. Figure 30 illustrates the developed system with flow (air and liquid tight) connectors. All the flow fixtures (panel mountable, Qosina OEM) are rated for medical grade and carefully assembled and sterilised with spraying 75% alcohol.

After the assembly and testing, the reconstructed RL-F has been applied in real-time cell culture experiments. Figure 31 shows an example case from the osteogenic differentiation (> 20 days) of hASC and simultaneous pH measurements (Figure 31a, using MO-pH). In Figure 31a, the sharp peaks are at times of medium change, due to sudden temperature and CO_2 drop and addition of fresh medium. Figure 31 b,c

shows the microscope images (captured at the end of differentiation) of hASC in the reconstructed RL-F flask and in a control flask.

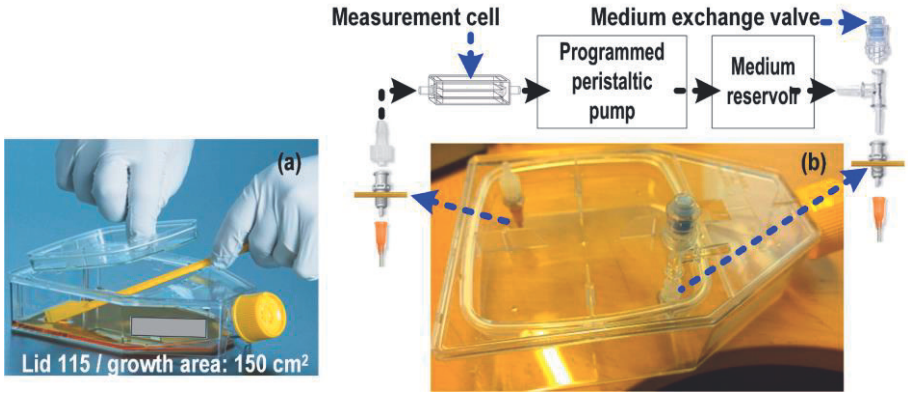

Figure 30. The new type of culture flasks. (a) Culture flask with re-closable lid (RL-F, [184]). (b) A novel standalone system that we constructed around the RL-F, combing the culture, medium perfusion and concurrent optical measurements.

At the end of differentiation, the Alizarin red staining successfully confirmed the mineralisation of cellular extracellular matrices and the formation of bone cell precursors in the reconstructed RL-F system. In the next stage, we plan to integrate simultaneous TLM and an ion sensor into this system.

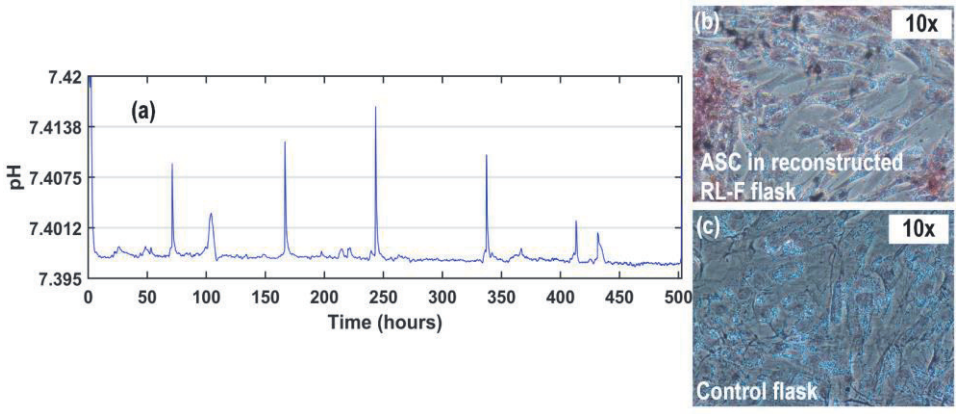

Figure 31. Application of reconstructed RL-F in osteogenic differentiation and simultaneous pH measurements. (a) Real-time pH plot (with MO-pH) during the entire duration of an hASC differentiation. Microscope images of hASC at the end of differentiations, (b) in the reconstructed RL-F flask and (c) in a control flask. Alizarin red staining with RL-F flask sample confirmed the characteristic mineralisation and formation of bone cell precursors.

4.5. Discussion on Spectroscopic pH Measurements

Estimation of pH spectroscopically by measuring the phenol red concentration in cell cultures has previously been utilised. But most of the reported methods have had practical concerns in our measurement requirements. So we developed the MO-pH with a modular and sterilisable architecture. At the moment MO-pH includes also a sample flow scheme (modified peristaltic pump) in order to circulate the medium through a flow-through cuvette (for optical readout). But in due course, the optical readout alone is intended to be added into the inlet/outlet of the perfusion system that would then be a part of the iuCMP.

In practice, compared to fluorescence based pH indicators, phenol red measurements are very stable, non-toxic, and exhibit fast chemical-equilibration, allowing one to achieve good measurement accuracy and short response time. The MO-pH utilises a pH-sensitive 545 nm measurement channel (with 680 nm reference), avoids auxiliary optical components (e.g. lenses and collimators) but still can provide a resolution down to 0.1 pH units. The non *in-situ* pH measurement has some limitations, but on the other hand, it improves cell viability by minimizing the instances of photo-cyto toxicity [185]. If required, pulsed illumination can also be utilised in the MO-pH to reduce the light exposure. In our design, we utilised 3D printed parts for the modular cassettes, casing and the support holders (for cuvette, cassettes and pump rotary mechanism) and demonstrated they can be successfully applied in incubator measurements. Initially, the modular cassettes were encapsulated (and sealed) in transparent cuvettes (Polystyrene, SE-202295, Spectrecology), but later were replaced by more robust quartz cuvettes. Quartz cuvettes are more durable, scratch-resistant and sterilisable by multiple means. Also the effect of sterilisation on the cleaned quartz surface is practically none, but if it happens by any chance, it will be compensated in the calibration. The support structures and cassette parts are 3D printed (TAZ 3/LulzBot) PLA (Polylactic acid)). The cassettes are sealed with hot melt glue and the sealing quality is tested in DI water bath for around 50 h at 38° C. The cassettes can be sterilised with ethanol spray before placing in the incubator. During pH measurement, no sample extraction from the incubator or any special sample treatment is needed and the medium is constantly circulating through peristaltic pump silicone tubing which is biocompatible and suited for life science applications. An integrated temperature sensor (with Van't Hoff's model) compensates the effect of temperature in the pH in real-time. Integrating also a CO_2 sensor in the future could be even better. A new absorption correction model has also been developed and applied in order to

minimise the errors caused by biofouling in long-term cell cultures. Nevertheless, the colorimetric pH measurements, in general, are also prone to salt error (mild displacement of indicator equilibrium by ionic strength, [175], [178]), protein error (by indicator-protein binding [186], [187]) and alcohol error (equilibrium shift in methanolic/ethanolic aqueous system, [188], [189]). But as the concentration of neutral salts in typical stem cell cultures is fairly low (< 150 mM), the salt error correction is unnecessary if it is below 2000 mM. Also, alcohol error is not a concern in an alcohol-free culture. But, the protein error (depending on the type and quantity of proteins present) may have some effect on the measurements. In general, the simpler the protein structure the lesser the error can be [190]. But it can be difficult to address directly in long-term cultures but our absorption correction model indirectly addresses it reasonably well. Needless to say, contamination and microbial growth, for example, bacterial or yeast colonies, can produce huge measurement errors as they usually make the medium very turbid and cause erroneous absorptions [191].

As a future perspective, the possibility of measurement of turbidity without using complex illumination (e.g. laser diodes) is also being considered. With this focus, an additional sensor cassette for 90^{o} scatter measurements at two wavelengths is in operation but the results so far are inconclusive. Another future direction is applying a good quality camera for both turbidity imaging as well as for 2D pH mapping. In this direction, a few image-based schemes have been tested which will be briefly discussed in the next chapter.

4.6. Image Based pH Estimation: Experimental Trials

4.6.1. Measurements with Liquid Crystal Display (LCD) Illumination, Optical Projection Tomography (OPT) and Webcam Arrangement

The distribution of pH in tissue *in-vivo* is not always constant and a pH gradient of up to 1.0 pH unit within 1 cm distance have been verified with MRI images [192]. Static pH measurements can point out systemic problems, but on the other hand, a multipoint pH measurement (e.g. 2D pH map) can pinpoint, for example, the location of a lesion in a tissue or the magnitude of excursion from the normal pH [192]. 2D pH maps can also be helpful to understand a variety of common

pathologies, including COPD, ischemia, renal failure and certain cancers. Therefore various pH mapping methods are constantly being reported for both *in-vivo* and *in-vitro* applications. We have also been testing whether the spectroscopic pH formulations can be applied with imaging sensors for spatial pH maps. With this focus, we have tested three imaging schemes mainly to explore the pros and cons in their implementations in the context of *in-vitro* pH sensing in the iuCMP. The tested schemes are respectively based on 1) a flat illumination, 2) OPT system and 3) a double webcam arrangement which are shown in Figure 32, Figure 33 and Figure 34.

In the flat illumination scheme, several pH samples were placed carefully in-front of an LCD screen (Lenovo P 50) as shown in Figure 32 and RAW images were captured with a colour SLR camera (Nikon D3200, 6016 x 4000 pixels, Exposure 1/8 second).

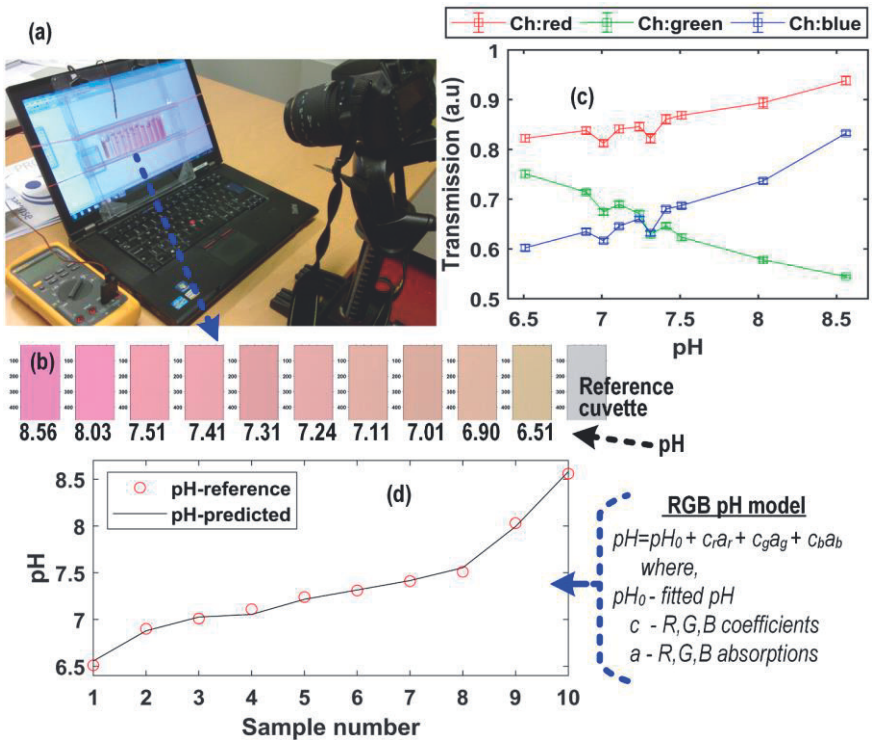

Figure 32. Testing flat illumination for pH imaging. (a) An LCD screen as an illumination source for the pH samples. (b) Images of 10 pH samples and a reference sample (DI water). (c) The computed transmission values in red, green and blue channels versus the reference pH (measured with the glass electrode). (d) Reference pH and the pH predicted using the RGB regression model.

A tiny thermocouple was also attached onto the LCD screen near the cuvettes for the temperature data. The main goal in LCD based imaging was to understand how well the RGB levels with a flat (uniform) background illumination would correspond to the pH changes. Figure 32b shows images of the 10 pH samples (650 x 250 pixels each) and a reference sample (cuvette with DI water, for transmission reference). The computed transmission values in red, green and blue channels are shown in Figure 32c where one can see that the transmissions especially in the green and blue channel change quite proportionally with the pH. Nevertheless, the transmission changes in the red channel were unexpected. A linear regression RGB model with the transmission values from all the three colour channels was applied to predict the pH. Figure 32d shows the pH reference (measured with the glass electrode) and the pH predicted of all the 10 samples with the RGB model.

The second imaging scheme was tested as part of a sophisticated OPT instrument (Figure 33a) with the objective of 2D/3D pH imaging in 3D scaffolds.

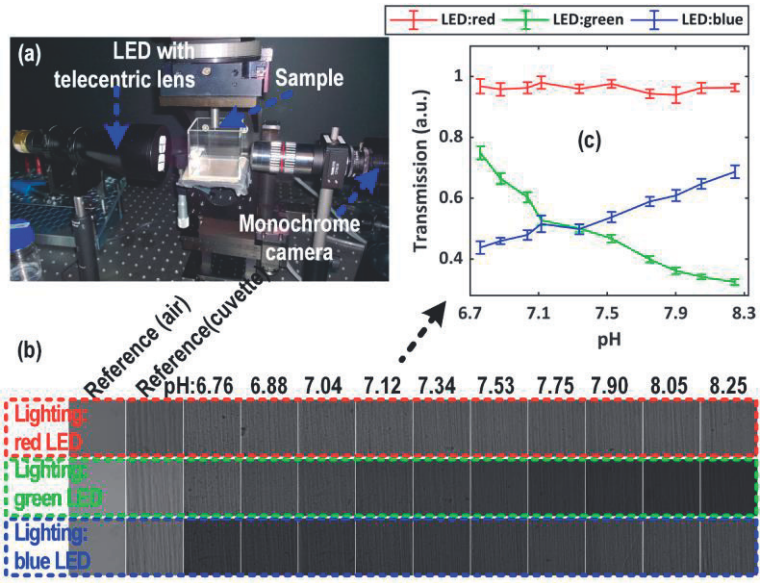

Figure 33. Testing pH imaging in an optical tomographic system. (a) The OPT arrangement. (b) OPT captured images of 10 pH samples and 2 reference samples (empty, DI water) in green, red and blue illuminations. (c) The computed optical transmissions in the three illuminations: Here one can see the green and blue channels show a clear pH dependence.

The OPT instrument comprises of, mainly a monochrome camera (2048 x 2048 pixels, FOV 3 x 3 mm), a telecentric illumination and a small sample holder (typically

a hollow transparent plastic tube) in a water bath. For our pH tests, the OTP's light source was replaced with specific LEDs: green (525 nm-LC503FPG1-15Q-A3, Cree), blue (LED435nm-12-30, Roithner LaserTechnik) and red (630 nm-HLMP-EG1B-Z10DD - Avago). In Figure 33b, the OPT images of 10 pH samples and two reference samples (empty, DI water filled) with green, red and blue illuminations are provided. The computed transmission plots are shown in Figure 33c. As expected, the transmissions with green and blue channels show a clear pH dependence while the red illumination remained insensitive to the pH changes.

The third scheme tested was a direct culture flask imaging scheme with two cameras. In Figure 34a, the constructed arrangement for a T25 type culture flask is shown.

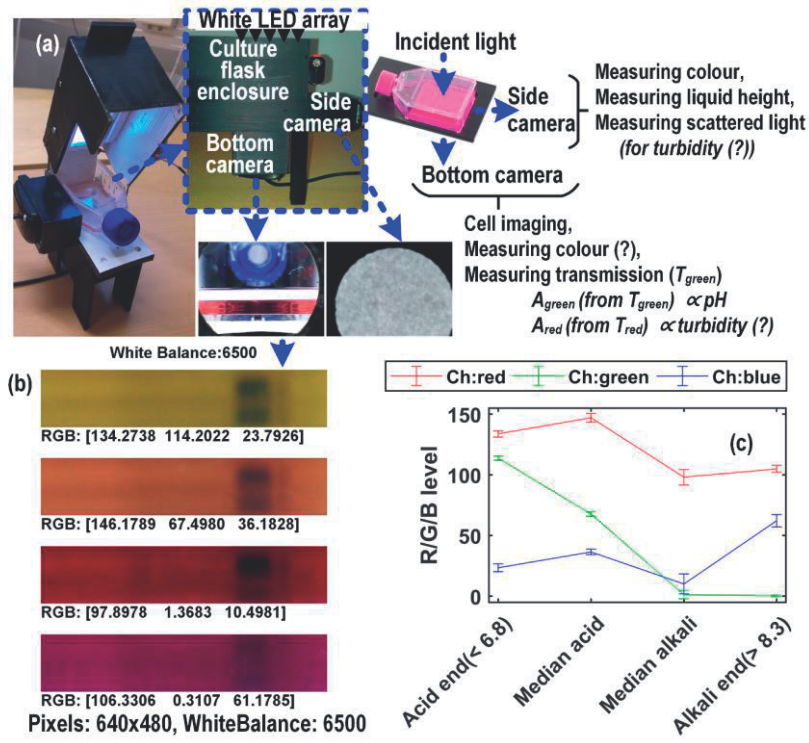

Figure 34. Testing a double webcam system for pH imaging. (a) The imaging arrangement for a T25 type culture flask with two cameras: one for sideway imaging the other one for inverted imaging. A 3D printed closable casing (painted white inside) blocks the background light. For illumination, a LED array with a diffuser glass was used. (b) Images of four pH samples captured with the side camera. (c) Computed mean intensities in red, green and blue channels in the captured images.

There, two cameras (Logitech C920, for vertical-inverted imaging, and for horizontal imaging) and a 3D printed closable lid (painted white inside) can be seen. Example images captured with both the cameras and the research questions under this study are shown in Figure 34a. For the illumination, a LED array (5x5 white LEDs) and a diffuser (DG05-1500-MD, Thorlabs) were mounted on the lid-inside-ceiling for vertically downward illumination. With this type of arrangement, the bottom camera (with selected microscopy lens, e.g. Figure 2a) can capture images of cells and also enable transmission-based pH measurements. The side camera, on the other hand, can image the medium colour more accurately and measure the liquid height (for exact transmission computation). Images (640 x 110 pixels cropped) of four pH samples captured with the side camera and their computed mean intensity levels are shown in Figure 34b and Figure 34c. This scheme too displayed pH-dependent intensity changes as expected in the green and blue channels. With this scheme, the possibility of imaging the turbidity (of culture medium) was also considered.

4.6.2. Discussion on Image-Based pH Measurements

The purpose of our pH imaging trials was to check whether simple-compact schemes in the context of *in-vitro* systems can be applied for pH estimation with acceptable accuracy. For this, we have tested schemes with both colour and monochrome cameras. The webcam schemes, even though are cheap and constantly being tested (by others), may not be the best candidate for the pH imaging. One reason is that their image sensors are too integrated and outputs only the processed images (typically with jpg compression). So the analytical computations based on them might not be very accurate and reliable. Accessing the settings of the webcam sensor for better imaging control is not always straight forward and oftentimes their auto-setting features adjust the scene settings automatically according to the lighting conditions. Further, the webcam lenses are usually basic plastic lenses and not corrected for various aberrations [193]–[195]. The webcam maximum frame rates and the true-pixel-resolution (may differ from the webcam's specifications) can also be limiting factors for certain biological measurements. On the other hand, using a system with a good quality colour camera that outputs RAW images, the colour changes of a colorimetric/fluorescent indicator can be correctly imaged for quantitative analytical measurements. For pH estimation, either RGB models or for better accuracy advance spectroscopic formulations can be applied. For accurate pH estimation, a system with a monochrome machine vision camera and an appropriate

colour illumination may be the best choice. The machine vision cameras permit manual control of all the camera settings which is very important in accurate image based quantitative analyses. In any pH imaging system, the implementation of a proper illumination scheme is very critical. We have tested single LEDs, LED arrays and LCD illumination. An interesting illumination option can be with a mini-LED-projector where the intensity, colour and spatial distribution can be adjusted in numerous combinations. In practical real-time pH imaging, controlling (optically/electronically) the background illumination as well as concurrent temperature monitoring are also essential. If multi-camera systems are appropriately developed for *in-vitro* tabletop systems, it can incorporate TLM (including fluorescent microscopy), as well as, maybe advanced features such as multi-parameter sensing, quantitative phase recovery and movement-free 3D video microscopy.

The pH imaging results presented here are preliminary and the experiments serve as examples highlighting a few possible practical options. More measurements, repetitions, and further equipment development are needed for achieving rigorous results. But the experiments showed non-fluorescent and cost-effective pH imaging schemes could be developed and integrated into portable *in-vitro* systems for pH monitoring and control. In any long-term cell experiments, two challenges any imaging system might face are the medium evaporation (and related issues) and bubble formation. Both of them can hinder accurate imaging, colour capture and transmission measurements. See Figure 35 for a real case of bubble formation in a TLM of MEF experiment and its effect on the pH prediction (Figure 35b).

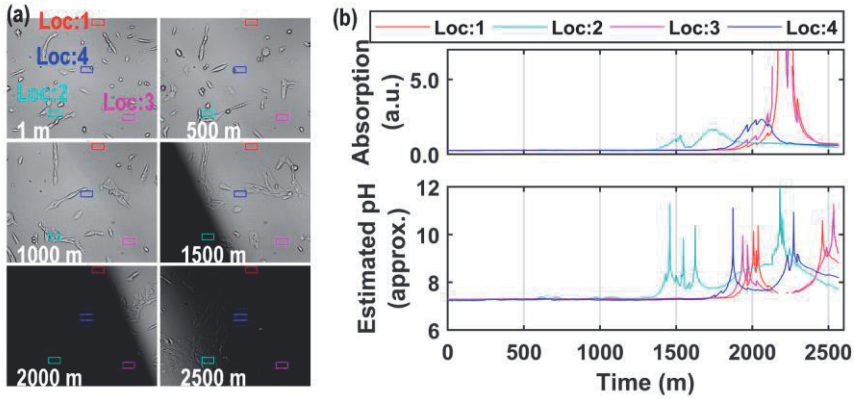

Figure 35. How do bubbles hinder optical measurements? (a) A real case of an air bubble expansion (the black region) during the TLM of an MEF experiment. (b) The computed absorptions and pH from the four spatial locations marked as Loc1:4 at the left image. Here one can see that the bubble in the FOV causes a huge error in the computations.

In Figure 35b, the computed absorptions (and the pH) at four spatial locations (Loc:1, 2, 3 and 4) during the TLM of ~ 2500 minutes are shown. A large bubble gradually blocks the FOV and the light transmission, causing a huge error in the absorption (and the pH commutation). In Figure 35b, the pH estimated are erroneous just from the appearance of bubble onwards. As a matter of fact, a 50 % change in light transmission would report more than 1.0 unit of pH change falsely. Therefore the medium evaporation and bubble formations need to be carefully controlled for accurate *in-vitro* image-based computations unless other ingenious compensation techniques are available.

5. CONCLUSIONS

This chapter summarises the main results, provides answers to the research questions listed in the Chapter 1.2 and discusses the limitations of the study.

5.1. Main Results

The main results and scientific contributions of this thesis are listed below

1. Constructed a good quality compact digital microscope for unstained live-cell imaging. The imaging quality was validated using both stained physiological samples (blood smear, skin section hair follicle and hard-bone grinding section) and live-cells (cardiomyocytes, neurons, human adipose stem cells (hASC) and mouse embryonic fibroblasts (MEF)).

2. Designed and assembled the interchangeable modular cell culturing platform- iuCMP. A graphical user interface (GUI) software for the iuCMP control and data acquisition was also scripted.

3. Scripted the beating signal analysis software CMaN with the following specifications,
    a) Extracts six separate signals of CM contractile motion in a single processing.
    b) Have features for movement centre (region of largest contractile motion) detection and automated cluster finding.
    c) Individual/batch wise processing of CM single cell or cluster videos.
    d) Offline and almost real-time automated video analysis.
    e) Compared to similar tools, it is several times faster, more sensitive, computationally less expensive and allows ROI selection.
    f) The signal waveform resembles an ECG waveform, corresponding to the contractile phenomena more exactly and

allows computation of contraction and relaxation features separately.

4. The iuCMP and CMaN have been used in a few studies/projects. Currently, they are used in experiments to model ischemia with hiPSC-CMs. The results are expected to provide more insight into ischemic heart disease (IHD).

5. Conducted detailed automated temperature stressing experiments with hiPSC-CMs. In data analysis, we showed that the relationship between hiPSC-CM beating frequency and temperature is nonlinear and subsequently computed the Q_{10} temperature coefficients. Further, we reported the novel results of signal propagation between dissociated clusters and their non-invasive measurements.

6. Constructed the optical non-contact pH measurement system MO-pH using 3D printed parts and assemblies. The system is waterproof, modular, sterilisable and suitable for real-time long-term 24/7pH monitoring.
    a. Developed a new absorption correction model to compensate for the effect of biofouling.
    b. Constructed also a new flow-through measurement and perfusion arrangement as part of flasks with re-closable lids (RL-F).

5.2. Answering the Research Questions

Cell culture process monitoring is important to understand the cell functions, metabolic properties as well as to improve the productivity and reproducibility. Monitoring can be helpful not only for physiochemical or metabolite measurements but also for a routine inspection of the substrates, electrodes, contamination and biodegradation. Accurate process monitoring becomes inevitable also for standardisation and regulatory agencies [196]. In many instances, a suitable existing monitoring technology can directly be adopted. But sometimes it becomes apparent the need to develop new methods to meet the specific requirements. Currently, new monitoring technologies, both from the technology-

driven and biology-driven aspects are being developed at an ever-increasing speed. This thesis is also in the direction of developing new technologies for cell culturing.

In a nutshell, there were two specific goals for this thesis. The first goal was to develop an imaging module as part of/together with a tabletop modular cell culturing system for cell experiments outside a traditional incubator. A portable multipurpose system was envisioned. The second goal was to develop a 24/7 non-contact pH measurement system for stem cell cultures. These two goals were pillared on five specific research questions (see Section 1.2). In the following paragraphs, these research questions and the details of how those questions were addressed are discussed.

The first two research questions were

How can measurement systems with minimal disturbance to cells and suitable for long-term studies outside a traditional incubator be created?

Can a mini phase contrast microscope with invert-upright convertibility be developed for good quality imaging of unstained live-cells *in-vitro*?

To this direction, we conceptualised a tabletop, incubator-free 'Invert-upright microscope interchangeable modular cell culturing platform'-iuCMP with a mini-bioreactor, digital microscope, cell-friendly monitoring systems (optical pO_2 sensor, MEA amplifier, TSP sensor) and with a cardiomyocytes functionality analysis software. The iuCMP was first designed and optimised in SolidWorks' 3D CAD platform. The assembled system has been applied in various short-term and long-term cell studies. The details of iuCMP together with the compact microscope design was presented in Publication I. The 3D CAD design files were also published (as Supplementary material) with this publication. In the Publication I, we demonstrated incorporating biocompatible cell-friendly materials, good quality live-cell imaging, a novel convertible microscopy architecture and measurement systems. The convertible architecture enabled the system to be equally useful for both the conventional inverted and upright (for imaging areas otherwise not accessible by conventional microscopes) TLM applications. The imaging quality was validated with histological specimens and with live-cell imaging of neurons, beating hiPSC-CMs, MEFs and hASCs. The suitability of the system for long-term applications has been verified with the orientation analysis of MEF on cellulose fibres and cardiomyocytes imaging and beating signal analysis.

The iuCMP, in fact, is not intended to be a stiff device, but a flexible system that can accommodate various components (*in-vitro* culture constructs, tailored sensor or stimulation units) quite freely. The applications can be but are not limited to cell characterisation, differentiation, chemical sensing, drug screening, electrophysiological recordings, and cell stimulation. See [55], [112] for other published work where the iuCMP was applied for cell experiments. At the moment, two other studies are also in progress. In the first study, the system is used for the experiments to model ischemia with hiPSC-CMs. For this, automated environment control (temperature, oxygen levels) and simultaneous monitoring (oxygen, temperature) and functionality measurements (MEA signals as well as video-microscopy CMaN analysis) are incorporated. The system induces controlled hypoxia and the cellular and molecular-level changes in cell functionality, morphology, viability as well as gene and protein expression are studied. The results are expected to provide more insight into ischemic heart disease. In the second study, the hiPSC-CM beating rate control with localised temperature adjustments by fuzzy control schemes (BPMFuzzy) is being explored.

The third research question was

Can affine-optical flow be used to reliably analyse multiple beating signals from cardiomyocyte beating videos? If so, does the waveform, speed and sensitivity allow the computation of relaxation and contraction features separately? Can it be applied for movement centre detection, batch mode processing and real-time analysis?

The contractile movement analysis of cardiomyocytes videos with the AFOF was tested in detail and subsequently the beating analysis software - CMaN was scripted, validated and reported in Publication II. CMaN is a robust and easy-to-use software (with a GUI) and equipped with features for automated cluster finding and batch processing of single cells and large CM clusters. Importantly, it has features for movement centre detection and the ability to extract six different contractile signals in a single processing. The six signal components are translation velocities-Vx, Vy (along x and y directions), dilation-d (rate of expansion/shrinking), rotation-r (rate around z-axis) and shears-$s1$, $s2$ (rates along x and diagonal axes). This way, CMaN could provide a minimum of one clear beating signal even when the movement is relatively weak or the frames are moderately over exposed or gamma imbalanced. In contrast to similar tools, CMaN is faster, more sensitive, and computationally less

expensive and supports ROI selection. In addition the ECG like signal waveform from CMaN allows the computation of contraction and relaxation features independently. CMaN has been used in analysing the videos recorded in hiPSC-CM temperature stressing studies reported in this thesis. Additionally, CMaN has also been used: 1) In a project : designing gold nanoparticle crosslinked conductive hyaluronan and chondroitin sulfate hydrogels for culturing embryonic stem cells derived human cardiomyocytes (Hanna Kemppi, details not open). 2) In the ischemia project (ongoing) and 3) in the BPMFuzzy (waiting for the cell trials).

The fourth research question was

Can we carry out long-term automated assessments of the hiPSC-CM contractions to temperature stimuli outside a conventional incubator?

This research question was formulated as a demonstrative application of iuCMP and CMaN. In the experimental side, the iuCMP was applied for automated temperature stressing of hiPSC-CMs. A programmable ITO heater, a TSP and the CMaN worked together in the iuCMP for automated temperature adjustments, concurrent TLM and beating signal analysis. The results were presented in Publication II. Since the cells were directly cultured on the TSP, the temperature that the cells experience was measured precisely from the cell area. In the data analysis, we showed that the relationship between hiPSC-CM beating frequency and the temperature was nonlinear and measured the Q_{10} temperature coefficients. Most importantly, the novel results of hiPSC-CM contractile networking (the signal propagation between dissociated clusters) and its non-invasive measurements by means of image processing were also reported in Publication II. Additionally, the software was published as a supplementary material with the same publication.

The fifth research questions was

Can we reliably measure pH, based simply on non-contact optical methods during long-term observations?

The goal here was to develop a real-time optical pH measurement system for the phenol red cell culture medium. Phenol red, being a colorimetric pH indicator, facilitates a colour transition from yellow to red when the bulk pH changes over the physiological range. So technically, the initial plan was to measure the colour directly,

for example, in the medium outlet/inlet of a perfusion channel. For the colour measurements, reflective, transmissive (absorptive) and transflective measurements can be applied. Notably, however, the spectral transmission measurements showed better pH measurement accuracy, repeatability and resolution. So we designed a two-wavelength pH measurement system. The two-wavelength pH measurement technique has previously been applied but we constructed a novel system, MO-pH that is incubator compatible, sterilisable and suitable for long-term unattended measurements. Its modular parts (cassettes) can be sterilised with alcohol. Furthermore, we developed an absorption compensation model which addresses the effect of biofouling in optical pH measurements reasonably well. Consequently, the measurement accuracy improved notably. Currently, the MO-pH can provide a resolution down to 0.1 pH unit in physiological pH range with mean absolute error $\leq$ 0.02. The MO-pH has been applied in 24/7 pH monitoring in several ASC expansion cultures. The details were presented in Publication III. Additional long-term pH measurement result in ASC osteogenic differentiation was presented in Publication IV. The MO-pH has also been used in understanding the overall true environmental (temperature, humidity and pH) behaviour in a water jacked incubator in 2-3 weeks of continuous measurements. These results can also be seen in the Publication IV. These measurements clearly showed the interplay between measured parameters and possible instances of stress reactions at various stages in the stem cell culture. In Publication IV, we also reported the pH changes as a function of temperature in the absence and presence of CO_2. All these measurements provided a comprehensive picture of behaviour of critical control parameters during long-term cell cultures, pointing out the need for bioprocess systems with intelligent features, precise control, and robust cell function analysis. These features will be crucial for maximum productivity in smart-device based systems as well as in future organ-on-chip approaches.

5.3. Limitations of the Study

The iuCMP has been applied in various TLM studies, but the microscopy focus drift is corrected at the moment manually once per day. Technically, z-stack imaging is possible but it still cannot be used for automated focal drift correction at present. Also the E-TL could have been tested for remote focus drift correction. As such the system is a single spot TLM imaging device. For automated multisite imaging, either require a motorised xy stage and/or multiple compact microscopes. Figure 2

(scheme 1 or 2) with multiple CMOS sensors (board level) may be a possible option for this purpose. Fluorescent imaging is important in cell studies but our system lacks it. Extra optics (filters, filter cubes), more sensitive cameras and electronics are essential for this which may come as a separate module. There is no automated medium exchange to remove the waste and replenish the nutrients. Also, we have observed the instances of medium evaporation sometimes, but it may be tackled in future with better incubator geometries or heating schemes. A few times we have noticed the degradation/etching of micro-electrodes, likely by culture medium. In the hiPSC-CM temperature stressing experiments only the video-based functionality analysis was utilised. But since the studies were with cardiac stem cells, measurements of gene or protein expressions could have been incorporated. The phenol red-based pH measurements work only for a very narrow pH range (pH 6.8 to 8.2). One major disadvantage of this method is if the medium is very turbid, the measurements may be unreliable. This scenario is usually associated with contamination (bacterial, yeast etc.)[197] and is highly unlikely in sterile cultures.

REFERENCES

[1] F. Wang, "Culture of animal cells: A manual of basic technique, fifth edition," *Vitr. Cell. Dev. Biol. - Anim.*, vol. 42, no. 5, p. 169, 2006.

[2] P. E. Oomen, M. D. Skolimowski, and E. Verpoorte, "Implementing oxygen control in chip-based cell and tissue culture systems," *Lab on a Chip*. 2016.

[3] A. Sarkar, "Bio Instrumentation," in *Stem Cell Culture*, Discovery Publishing House, Pvt.Ltd, 2009, pp. 29–33.

[4] M. T. Jennie P. Mather, "Expression of cloned proteins in the mammalian cells," in *Large-Scale Mammalian Cell Culture Technology*, V. 10., A. S. Lubiniecki, Ed. Marcel Dekker, 1990, p. 164.

[5] P. Stein, Gary S;Borowski, Maria; Luong, Mai X; Shi, Meng-Jiao; Smith, Kelly P, Vazquez, Ed., "Basic Cell Culture Growth Conditions," in *Human Stem Cell Technology and Biology: A Research Guide and Laboratory Manual*, Wiley-Blackwell, 2011, pp. 34–35.

[6] R. Reig, M. Mattia, A. Compte, C. Belmonte, and M. V. Sanchez-Vives, "Temperature Modulation of Slow and Fast Cortical Rhythms," *J. Neurophysiol.*, 2010.

[7] K. Toischer *et al.*, "Cardiomyocyte proliferation prevents failure in pressure overload but not volume overload," *J. Clin. Invest.*, vol. 127, no. 12, pp. 4285–4296, Dec. 2017.

[8] I. Watanabe and S. Okada, "Effects of temperature on growth rate of cultured mammalian cells (L5178Y)," *J. Cell Biol.*, vol. 32, no. 2, pp. 309–323, Feb. 1967.

[9] F. Triaud, D.-H. Clenet, Y. Cariou, T. Le Neel, D. Morin, and A. Truchaud, "Evaluation of Automated Cell Culture Incubators," *JALA J. Assoc. Lab. Autom.*, vol. 8, no. 6, pp. 82–86, Dec. 2003.

[10] J. E. Swain, "Optimizing the culture environment in the IVF laboratory: impact of pH and buffer capacity on gamete and embryo quality," *Reprod. Biomed. Online*, vol. 21, pp. 6–16, 2010.

[11] J. A. Ryan, "Corning Guide for Identifying and Correcting Common Cell Growth Problems," *Corning Incorporated Life Sciences*, 2019. [Online]. Available: https://beta-static.fishersci.com/content/dam/fishersci/en_US/documents/programs/scientific/technical-documents/technical-bulletins/corning-guide-

identifying-cell-growth-problems-technical-bulletin.pdf. [Accessed: 12-Jan-2017].

[12] S. Fulda, A. M. Gorman, O. Hori, and A. Samali, "Cellular stress responses: cell survival and cell death.," *Int. J. Cell Biol.*, vol. 2010, p. 214074, 2010.

[13] B. Poljšak and I. Milisav, "Clinical implications of cellular stress responses," 2012.

[14] I. Milisav, "Cellular Stress Responses," in *Advances in Regenerative Medicine*, InTech, 2011.

[15] J. Kieninger *et al.*, "Sensor Access to the Cellular Microenvironment Using the Sensing Cell Culture Flask," *Biosensors*, vol. 8, no. 2, p. 44, Apr. 2018.

[16] R. G. Harrison, M. J. Greenman, F. P. Mall, and C. M. Jackson, "Observations of the living developing nerve fiber," *Anat. Rec.*, vol. 1, no. 5, pp. 116–128, Jun. 1907.

[17] B. Jiang, W. Zheng, W. Zhang, and X. Jiang, "Organs on microfluidic chips: A mini review," *Sci. China Chem.*, vol. 57, no. 3, pp. 356–364, Mar. 2014.

[18] S. Petronis, M. Stangegaard, C. Bovöge Christensen, and M. Dufva, "Transparent polymeric cell culture chip with integrated temperature control and uniform media perfusion," *Biotechniques*, vol. 40, no. 3, pp. 368–376, Mar. 2006.

[19] T. J. Nelson, A. Martinez-Fernandez, S. Yamada, Y. Ikeda, C. Perez-Terzic, and A. Terzic, "Induced pluripotent stem cells: advances to applications.," *Stem Cells Cloning*, vol. 3, pp. 29–37, Jan. 2010.

[20] G. Pasirayi *et al.*, "Microfluidic Bioreactors for Cell Culturing: A Review," *Micro Nanosyst.*, vol. 3, no. 2, pp. 137–160, Jul. 2011.

[21] K. Yum, S. G. Hong, K. E. Healy, and L. P. Lee, "Physiologically relevant organs on chips.," *Biotechnol. J.*, vol. 9, no. 1, pp. 16–27, Jan. 2014.

[22] J. M. (John M. . Davis, *Basic cell culture : a practical approach*. Oxford ;;New York : IRL Press, 1994.

[23] J. Blain Christen and A. G. Andreou, "Design, Fabrication, and Testing of a Hybrid CMOS/PDMS Microsystem for Cell Culture and Incubation," *IEEE Trans. Biomed. Circuits Syst.*, vol. 1, no. 1, pp. 3–18, Mar. 2007.

[24] D. Dutta, I. Heo, and H. Clevers, "Disease Modeling in Stem Cell-Derived 3D Organoid Systems," *Trends in Molecular Medicine*. pp. 393–410, 2017.

[25] J. L. Sterneckert, P. Reinhardt, and H. R. Schöler, "Investigating human disease using stem cell models," *Nature Reviews Genetics*. pp. 625–639, 2014.

[26] A. Fatehullah, S. H. Tan, and N. Barker, "Organoids as an in vitro model of human development and disease," *Nature Cell Biology*. pp. 246–254, 2016.

[27] M. Mirbagheri, V. Adibnia, B. R. Hughes, S. D. Waldman, X. Banquy, and D. K. Hwang, "Advanced cell culture platforms: a growing quest for emulating natural tissues," *Mater. Horizons*, vol. 6, no. 1, pp. 45–71, 2019.

[28] J. S. Joseph, "Two-Dimensional (2D) and Three-Dimensional (3D) Cell Culturing in Drug Discovery," S. T. Malindisa, Ed. Rijeka: IntechOpen, 2019, p. Ch. 2.

[29] K. Duval *et al.*, "Modeling Physiological Events in 2D vs. 3D Cell Culture," *Physiology (Bethesda).*, vol. 32, no. 4, pp. 266–277, Jul. 2017.

[30] J. W. Haycock, "3D Cell Culture: A Review of Current Approaches and Techniques," in *3D Cell Culture: Methods and Protocols*, J. W. Haycock, Ed. Totowa, NJ: Humana Press, 2011, pp. 1–15.

[31] J. Hoarau-v, A. Rafii, and C. Touboul, "Halfway between 2D and Animal Models : Are 3D Cultures the Ideal Tool to Study Cancer-Microenvironment Interactions ?"

[32] A.-J. Mäki, *Modeling and Control of Microscale Cell Culture Environments Antti-Juhana Mäki Modeling and Control of Microscale Cell Culture Environments*, vol. 1557. Tampere University of Technology. Publication, 2018.

[33] M. M. Modena, K. Chawla, P. M. Misun, and A. Hierlemann, "Smart Cell Culture Systems: Integration of Sensors and Actuators into Microphysiological Systems.," *ACS Chem. Biol.*, vol. 13, no. 7, pp. 1767–1784, 2018.

[34] Nikon, "Live-Cell Imaging and Perfusion Chambers | MicroscopyU." [Online]. Available: https://www.microscopyu.com/references/live-cell-imaging-and-perfusion-chambers. [Accessed: 01-Aug-2017].

[35] Okolab, "Microscope enclosures." [Online]. Available: http://www.oko-lab.com/live-cell-imaging/cage-incubator/temperature-unit. [Accessed: 01-Aug-2017].

[36] S. L. Shorte and F. Frischknecht, *Imaging cellular and molecular biological functions*. Springer, 2007.

[37] J. L. Collins, B. van Knippenberg, K. Ding, and A. V. Kofman, "Time-Lapse Microscopy," in *Cell Culture*, IntechOpen, 2019.

[38] A. G. Godin, B. Lounis, and L. Cognet, "Super-resolution microscopy approaches for live cell imaging.," *Biophys. J.*, vol. 107, no. 8, pp. 1777–84, Oct. 2014.

[39] D. Jin *et al.*, "Compact Wireless Microscope for In-Situ Time Course Study of Large Scale Cell Dynamics within an Incubator," 2015.

[40] Ø. I. Helle, D. A. Coucheron, J.-C. Tinguely, C. I. Øie, and B. S. Ahluwalia, "Nanoscopy on-a-chip: super-resolution imaging on the millimeter scale," *Opt. Express*, vol. 27, no. 5, p. 6700, Mar. 2019.

[41] G. Vicidomini, P. Bianchini, and A. Diaspro, "STED super-resolved microscopy," *Nature Methods*, vol. 15, no. 3. Nature Publishing Group, pp.

173–182, 01-Mar-2018.
[42] Y. S. Kim *et al.*, "Combining three-dimensional quantitative phase imaging and fluorescence microscopy for the study of cell pathophysiology," *Yale Journal of Biology and Medicine*, vol. 91, no. 3. Yale Journal of Biology and Medicine Inc., pp. 267–277, 01-Sep-2018.
[43] H. Li *et al.*, "Fast, volumetric live-cell imaging using high-resolution light-field microscopy," *Biomed. Opt. Express*, vol. 10, no. 1, p. 29, Jan. 2019.
[44] Y. S. Zhang *et al.*, "A cost-effective fluorescence mini-microscope for biomedical applications," *Lab Chip*, vol. 15, no. 18, pp. 3661–3669, 2015.
[45] M. B. Esch, T. L. King, and M. L. Shuler, "The Role of Body-on-a-Chip Devices in Drug and Toxicity Studies," *Annu. Rev. Biomed. Eng.*, vol. 13, no. 1, pp. 55–72, Aug. 2011.
[46] N. S. Bhise *et al.*, "Organ-on-a-chip platforms for studying drug delivery systems," *J. Control. Release*, vol. 190, pp. 82–93, Sep. 2014.
[47] A. M. Ghaemmaghami, M. J. Hancock, H. Harrington, H. Kaji, and A. Khademhosseini, "Biomimetic tissues on a chip for drug discovery," *Drug Discovery Today*, vol. 17, no. 3–4. pp. 173–181, 2012.
[48] C. Moraes, G. Mehta, S. C. Lesher-Perez, and S. Takayama, "Organs-on-a-Chip: A Focus on Compartmentalized Microdevices," *Ann. Biomed. Eng.*, vol. 40, no. 6, pp. 1211–1227, Jun. 2012.
[49] D. Huh, G. A. Hamilton, and D. E. Ingber, "From 3D cell culture to organs-on-chips," *Trends Cell Biol.*, vol. 21, no. 12, pp. 745–754, Dec. 2011.
[50] S. N. Bhatia and D. E. Ingber, "Microfluidic organs-on-chips."
[51] Y. Sei, K. Justus, P. Leduc, and Y. Kim, "Engineering living systems on chips: From cells to human on chips," *Microfluid. Nanofluidics*, vol. 16, no. 5, pp. 907–920, May 2014.
[52] J. P. Wikswo, "The relevance and potential roles of microphysiological systems in biology and medicine," *Exp. Biol. Med.*, vol. 239, no. 9, pp. 1061–1072, 2014.
[53] Š. Selimović, M. R. Dokmeci, and A. Khademhosseini, "Organs-on-a-chip for drug discovery," *Curr. Opin. Pharmacol.*, vol. 13, no. 5, pp. 829–833, 2013.
[54] M. L. Moya and S. C. George, "Integrating in vitro organ-specific function with the microcirculation," *Curr. Opin. Chem. Eng.*, vol. 3, pp. 102–111, 2014.
[55] H. Välimäki *et al.*, "Fluorimetric oxygen sensor with an efficient optical read-out for in vitro cell models," *Sensors Actuators B*, vol. 249, pp. 738–746, 2017.
[56] D. Kattipparambil Rajan *et al.*, "Optical non-contact pH measurement in cell culture with sterilizable, modular parts," *Talanta*, vol. 161, pp. 755–761, Dec. 2016.

[57] I. Taurino *et al.*, "Platinum nanopetal-based potassium sensors for acute cell death monitoring," *RSC Adv.*, vol. 6, no. 46, pp. 40517–40526, 2016.

[58] I. Etaluma, "Lumascopes." [Online]. Available: http://www.etaluma.com/products/about-lumascope-fluorescent-microscopes/. [Accessed: 03-Aug-2017].

[59] E. BioScience, "Real-time, quantitative live-cell analysis,IncuCyte ZOOM System," 2016. [Online]. Available: https://www.essenbioscience.com/media/uploads/files/8000-0333-E00-IncuCyte_ZOOM_brochure.pdf. [Accessed: 03-Aug-2017].

[60] J. H. Jung, C. Han, S. A. Lee, J. Kim, and C. Yang, "Microfluidic-integrated laser-controlled microactuators with on- chip microscopy imaging functionality."

[61] C. Han, S. Pang, D. V. Bower, P. Yiu, and C. Yang, "Wide Field-of-View On-Chip Talbot Fluorescence Microscopy for Longitudinal Cell Culture Monitoring from within the Incubator," *Anal. Chem.*, vol. 85, no. 4, pp. 2356–2360, Feb. 2013.

[62] G. Zheng, S. A. Lee, Y. Antebi, M. B. Elowitz, and C. Yang, "The ePetri dish, an on-chip cell imaging platform based on subpixel perspective sweeping microscopy (SPSM).," *Proc. Natl. Acad. Sci. U. S. A.*, vol. 108, no. 41, pp. 16889–94, Oct. 2011.

[63] J. El-Ali, P. K. Sorger, and K. F. Jensen, "Cells on chips," *Nature*, vol. 442, no. 7101, pp. 403–411, Jul. 2006.

[64] W. Bishara *et al.*, "Holographic pixel super-resolution in portable lensless on-chip microscopy using a fiber-optic array," *Lab Chip*, vol. 11, no. 7, p. 1276, Apr. 2011.

[65] A. Greenbaum, U. Sikora, and A. Ozcan, "Field-portable wide-field microscopy of dense samples using multi-height pixel super-resolution based lensfree imaging," *Lab Chip*, vol. 12, no. 7, p. 1242, Apr. 2012.

[66] W. Bishara, T.-W. Su, A. F. Coskun, and A. Ozcan, "Lensfree on-chip microscopy over a wide field-of-view using pixel super-resolution.," *Opt. Express*, vol. 18, no. 11, pp. 11181–91, May 2010.

[67] Z. F. Phillips, M. Chen, L. Waller, L. Waller, C. Yang, and N. Sadras, "Single-shot quantitative phase microscopy with color-multiplexed differential phase contrast (cDPC)," *PLoS One*, vol. 12, no. 2, p. e0171228, Feb. 2017.

[68] A. Ozcan and E. McLeod, "Lensless Imaging and Sensing," *Annu. Rev. Biomed. Eng.*, vol. 18, no. 1, pp. 77–102, Jul. 2016.

[69] H. Lee *et al.*, "An endoscope with integrated transparent bioelectronics and theranostic nanoparticles for colon cancer treatment," *Nat. Commun.*, 2015.

[70] R. Singhal *et al.*, "Multifunctional carbon-nanotube cellular endoscopes,"

Nat. Nanotechnol., 2011.
[71] R. Yan *et al.*, "Nanowire-based single-cell endoscopy," 2012.
[72] B. A. Flusberg, E. D. Cocker, W. Piyawattanametha, J. C. Jung, E. L. M. Cheung, and M. J. Schnitzer, "Fiber-optic fluorescence imaging.," *Nat. Methods*, vol. 2, no. 12, pp. 941–50, Dec. 2005.
[73] M. Pierce, D. Yu, and R. Richards-Kortum, "High-resolution fiber-optic microendoscopy for in situ cellular imaging.," *J. Vis. Exp.*, no. 47, p. e2306, Jan. 2011.
[74] D. Shin, M. C. Pierce, A. M. Gillenwater, M. D. Williams, and R. R. Richards-Kortum, "A Fiber-Optic Fluorescence Microscope Using a Consumer-Grade Digital Camera for In Vivo Cellular Imaging," *PLoS One*, vol. 5, no. 6, p. e11218, Jun. 2010.
[75] F. Helmchen, "Miniaturization of Fluorescence Microscopes Using Fibre Optics," *Exp. Physiol.*, vol. 87, no. 6, pp. 737–745, Nov. 2002.
[76] K. Bin Sung, C. Liang, M. Descour, T. Collier, M. Follen, and R. Richards-Kortum, "Fiber-optic confocal reflectance microscope with miniature objective for in vivo imaging of human tissues," *IEEE Trans. Biomed. Eng.*, vol. 49, no. 10, pp. 1168–1172, Oct. 2002.
[77] Y. Ando *et al.*, "In vivo bioluminescence and reflectance imaging of multiple organs in bioluminescence reporter mice by bundled-fiber-coupled microscopy," *Biomed. Opt. Express*, vol. 7, no. 3, p. 963, 2016.
[78] X. Meng *et al.*, "Smartphone based hand-held quantitative phase microscope using the transport of intensity equation method," *Lab Chip*, vol. 17, no. 1, pp. 104–109, 2017.
[79] A. Skandarajah, C. D. Reber, N. A. Switz, and D. A. Fletcher, "Quantitative imaging with a mobile phone microscope," *PLoS One*, vol. 9, no. 5, 2014.
[80] Y. S. Zhang *et al.*, "Hybrid Microscopy: Enabling Inexpensive High-Performance Imaging through Combined Physical and Optical Magnifications.," *Sci. Rep.*, vol. 6, no. November 2015, p. 22691, 2016.
[81] M. P. Walzik *et al.*, "A portable low-cost long-term live-cell imaging platform for biomedical research and education," *Biosens. Bioelectron.*, vol. 64, pp. 639–649, Feb. 2015.
[82] G. O. F. Parikesit, M. Darmawan, and A. Faisal, "Quantitative low-cost webcam-based microscopy," *Opt. Eng.*, vol. 49, no. 11, p. 113205, Nov. 2010.
[83] Jaycar, "Jaycar, 5MP USB 2.0 Digital Microscope with Professional Stand," 2016. [Online]. Available: https://www.jaycar.com.au/5mp-usb-2-0-digital-microscope-with-professional-stand/p/QC3199. [Accessed: 17-Jul-2019].
[84] ImagingSys, "DGCUS USB 2.0 Digital Microscope 1000 x," 2016.

[Online]. Available: https://www.imagingsys.com/dgcus-usb-20-digital-microscope-1000-x-magnification-8-led-mini/. [Accessed: 31-Jul-2019].
[85] E. Laboratories, "Hybrid fluorescence microscope (upright/inverted), REVOLVE 4," 2019. [Online]. Available: https://discover-echo.com/revolve. [Accessed: 23-May-2019].
[86] A. Courtney, L. M. Alvey, G. O. T. Merces, and M. Pickering, "The Flexiscope: a Low Cost, Flexible, Convertible, and Modular Microscope with Automated Scanning and Micromanipulation," *bioRxiv*, p. 442210, Oct. 2018.
[87] S. B. Kim *et al.*, "A mini-microscope for in situ monitoring of cells.," *Lab Chip*, vol. 12, no. 20, pp. 3976–82, Oct. 2012.
[88] J. Wu *et al.*, "A compact microfluidic system for cell migration studies," *Biomed. Microdevices*, vol. 16, no. 4, pp. 521–528, 2014.
[89] J. P. Sharkey, D. C. W. Foo, A. Kabla, J. J. Baumberg, and R. W. Bowman, "A one-piece 3D printed flexure translation stage for open-source microscopy," *Rev. Sci. Instrum.*, vol. 87, no. 2, Feb. 2016.
[90] A. Maia Chagas, L. L. Prieto-Godino, A. B. Arrenberg, and T. Baden, "The €100 lab: A 3D-printable open-source platform for fluorescence microscopy, optogenetics, and accurate temperature control during behaviour of zebrafish, Drosophila, and Caenorhabditis elegans," *PLoS Biol.*, vol. 15, no. 7, p. e2002702, Jul. 2017.
[91] M. Delmans and J. Haseloff, "μCube: A Framework for 3D Printable Optomechanics," *J. Open Hardw.*, vol. 2, no. 1, pp. 1–9, May 2018.
[92] "You See Too," 2019. [Online]. Available: http://useetoo.org/home/. [Accessed: 31-Mar-2020].
[93] "Miniscope V3 WireFree — Open Ephys." [Online]. Available: https://open-ephys.org/miniscope-v3-wirefree. [Accessed: 31-Mar-2020].
[94] "Inscopix Miniature Microscope Technology." [Online]. Available: https://www.inscopix.com/technology. [Accessed: 31-Mar-2020].
[95] M. Novakova *et al.*, "Effects of voltage sensitive dye di-4-ANEPPS on guinea pig and rabbit myocardium.," *Gen. Physiol. Biophys.*, vol. 27, no. 1, pp. 45–54, Mar. 2008.
[96] D. Braeken *et al.*, "Local electrical stimulation of single adherent cells using three-dimensional electrode arrays with small interelectrode distances," in *2009 Annual International Conference of the IEEE Engineering in Medicine and Biology Society*, 2009, vol. 2009, pp. 2756–2759.
[97] A. Brüggemann, S. Stoelzle, M. George, J. C. Behrends, and N. Fertig, "Microchip Technology for Automated and Parallel Patch-Clamp Recording," *Small*, vol. 2, no. 7, pp. 840–846, Jul. 2006.
[98] T. Uchida, R. Kitora, and K. Gohara, "Temperature dependence of

synchronized beating of cultured neonatal rat heart-cell networks with increasing age measured by multi-electrode arrays," *Res. Artic. Trends Med*, vol. 18, no. 4, pp. 1–10, 2018.

[99] S. Nitsch, F. Braun, S. Ritter, M. Scholz, and I. S. Schroeder, "Functional video-based analysis of 3D cardiac structures generated from human embryonic stem cells," *Stem Cell Res.*, vol. 29, pp. 115–124, May 2018.

[100] M. Maddah *et al.*, "A Non-invasive Platform for Functional Characterization of Stem-Cell-Derived Cardiomyocytes with Applications in Cardiotoxicity Testing," *Stem Cell Reports*, vol. 4, no. 4, pp. 621–631, Apr. 2015.

[101] T. Hayakawa *et al.*, "Image-based evaluation of contraction–relaxation kinetics of human-induced pluripotent stem cell-derived cardiomyocytes: Correlation and complementarity with extracellular electrophysiology," *J. Mol. Cell. Cardiol.*, vol. 77, pp. 178–191, Dec. 2014.

[102] E. K. Lee, Y. K. Kurokawa, R. Tu, S. C. George, and M. Khine, "Machine learning plus optical flow: a simple and sensitive method to detect cardioactive drugs," *Sci. Rep.*, vol. 5, no. 1, p. 11817, Dec. 2015.

[103] C. L. Mummery *et al.*, "MUSCLEMOTION A Versatile Open Software Tool to Quantify Cardiomyocyte and Cardiac Muscle Contraction In Vitro and In Vivo," 2017.

[104] C. N. Toepfer *et al.*, "SarcTrack. An Adaptable Software Tool for Efficient Large-Scale Analysis of Sarcomere Function in hiPSC-Cardiomyocytes," *Circ. Res.*, vol. 124, no. 8, pp. 1172–1183, Apr. 2019.

[105] E. Laurila, A. Ahola, J. Hyttinen, and K. Aalto-Setälä, "Methods for in vitro functional analysis of iPSC derived cardiomyocytes — Special focus on analyzing the mechanical beating behavior," *Biochim. Biophys. Acta - Mol. Cell Res.*, vol. 1863, no. 7, pp. 1864–1872, Jul. 2016.

[106] A. Ahola, A. L. Kiviaho, K. Larsson, M. Honkanen, K. Aalto-Setälä, and J. Hyttinen, "Video image-based analysis of single human induced pluripotent stem cell derived cardiomyocyte beating dynamics using digital image correlation," *Biomed. Eng. Online*, vol. 13, no. 1, 2014.

[107] C. S. Chung and K. S. Campbell, "Temperature and transmural region influence functional measurements in unloaded left ventricular cardiomyocytes," *Physiol. Rep.*, vol. 1, no. 6, pp. 1–13, 2013.

[108] R. Madonna, "Human-Induced pluripotent stem cells: In quest of clinical applications," *Molecular Biotechnology*. 2012.

[109] V. K. Singh, M. Kalsan, N. Kumar, A. Saini, and R. Chandra, "Induced pluripotent stem cells: applications in regenerative medicine, disease modeling, and drug discovery," *Front. Cell Dev. Biol.*, 2015.

[110] D. K. Rajan *et al.*, "Monitoring pH, temperature and humidity in long-term stem cell culture in CO2 incubator," in *2017 IEEE International*

Symposium on Medical Measurements and Applications, MeMeA 2017 - Proceedings, 2017, pp. 470–474.

[111] N. Schaible, G. Arteaga, T. Tveita, G. Sieck, T. Hoang, and Y. S. Han, "Hypothermia/rewarming disrupts excitation-contraction coupling in cardiomyocytes," *Am. J. Physiol. Circ. Physiol.*, vol. 310, no. 11, pp. H1533–H1540, 2016.

[112] A.-J. Mäki *et al.*, "A Portable Microscale Cell Culture System with Indirect Temperature Control," *SLAS Technol. Transl. Life Sci. Innov.*, vol. 23, no. 6, pp. 566–579, Dec. 2018.

[113] X. Ge *et al.*, "Validation of an optical sensor-based high-throughput bioreactor system for mammalian cell culture," *J. Biotechnol.*, vol. 122, pp. 293–306, 2006.

[114] M. Bäcker *et al.*, "Concept for a solid-state multi-parameter sensor system for cell-culture monitoring," *Electrochim. Acta*, vol. 54, no. 25, pp. 6107–6112, Oct. 2009.

[115] "Research group: Sensor Technology and Biomeasurements (STB) - Tampere University of Technology." [Online]. Available: https://tutcris.tut.fi/portal/en/organisations/research-group-sensor-technology-and-biomeasurements-stb(de495645-bd27-4bd0-8f41-2ef70bd1108c).html. [Accessed: 12-Oct-2019].

[116] R. Sislian, F. V. da Silva, R. Gedraite, H. Jokinen, and D. Kattipparambil Rajan, "Development of a Low-Cost Fuzzy Gain Schedule Neutralization Control System," in *Proceedings of the World Congress on Engineering and Computer Science (WCECS 2015),San Francisco, USA*, 2015, vol. II, pp. 21–24.

[117] R. Sislian, F. V. da Silva, R. Gedraite, H. Jokinen, and D. K. Rajan, "The Use of Mathematical Modeling for the Development of a Low Cost Fuzzy Gain Schedule Neutralization Control System," in *Transactions on Engineering Technologies*, Singapore: Springer Singapore, 2017, pp. 525–539.

[118] T. Ryynänen, K. Nurminena, J. Hämäläinen, M. Leskelä, and J. Lekkala, "pH electrode based on ALD deposited iridium oxide," in *Procedia Engineering*, 2010, vol. 5, pp. 548–551.

[119] D. Kattipparambil Rajan, J.-P. Raunio, M. T. Karjalainen, T. Ryynänen, and J. Lekkala, "Novel method for intensity correction using a simple maskless lithography device," *Sensors Actuators A Phys.*, vol. 194, pp. 40–46, May 2013.

[120] D. Kattipparambil Rajan and J. Lekkala, "A maskless exposure device for rapid photolithographic prototyping of sensor and microstructure layouts," *Procedia Eng.*, vol. 5, pp. 331–334, 2010.

[121] E. B. Magnusson, S. Halldorsson, M. T. Ronan, and K. Leosson, "Real-time optical pH measurement in a standard microfluidic cell culture

system," vol. 4, no. 9, pp. 77–85, 2013.
[122] M. Naciri, D. Kuystermans, and M. Al-Rubeai, "Monitoring pH and dissolved oxygen in mammalian cell culture using optical sensors," *Cytotechnology*, vol. 57, no. 3, pp. 245–250, Jul. 2008.
[123] Jim Cooper, "CO2 concentration and pH control in the cell culture laboratory," *Public Health England - GOV.UK*. [Online]. Available: https://www.phe-culturecollections.org.uk/news/ecacc-news/co2-concentration-and-ph-control-in-the-cell-culture-laboratory.aspx. [Accessed: 01-Apr-2020].
[124] T. Salpavaara, *Timo Salpavaara Inductively Coupled Passive Resonance Sensors : Readout Methods and Applications*, vol. 1524, no. 2018. 2018.
[125] K. Jan Pruszak, Máté Döbrössy, Jochen Kieninger and and G. N. Aravindalochanan, Gerald A. Urban, "Stem Cell Differentiation and Fate Specification," in *Stem Cell Engineering: Principles and Applications*, Springer Heidelberg Dordrecht London New York, 2011, pp. 442–443.
[126] M. R. Koller, M. A. Palsson, I. Manchel, and B. O. Palsson, "Long-term culture-initiating cell expansion is dependent on frequent medium exchange combined with stromal and other accessory cell effects," *Blood*, vol. 86, no. 5, pp. 1784 LP – 1793, Sep. 1995.
[127] T. Yao and Y. Asayama, "Animal-cell culture media: History, characteristics, and current issues," *Reprod. Med. Biol.*, vol. 16, no. 2, pp. 99–117, 2017.
[128] C. G. Mackenzie, J. B. Mackenzie, and P. Beck, "The effect of pH on growth, protein synthesis, and lipid-rich particles of cultured mammalian cells," *J. Biophys. Biochem. Cytol.*, vol. 9, no. 1, pp. 141 LP – 156, Jan. 1961.
[129] D. Wencel, T. Abel, and C. McDonagh, "Optical Chemical pH Sensors (Review)," *Anal. Chem.*, vol. 86, no. 1, pp. 15–29, 2014.
[130] G. Nabovati, E. Ghafar-Zadeh, and M. Sawan, "A 64 pixel ISFET-based biosensor for extracellular pH gradient monitoring," *Proc. - IEEE Int. Symp. Circuits Syst.*, vol. 2015-July, pp. 1762–1765, 2015.
[131] V. Saucedo, B. Wolk, A. Arroyo, and C. D. Feng, "Studying the drift of in line pH measurements in cell culture," *Biotechnol. Prog.*, vol. 27, no. 3, pp. 885–890, May 2011.
[132] S. Lee, B. L. Ibey, G. L. Coté, and M. V. Pishko, "Measurement of pH and dissolved oxygen within cell culture media using a hydrogel microarray sensor," *Sensors Actuators B Chem.*, vol. 128, no. 2, pp. 388–398, 2008.
[133] M. A. Hanson, X. Ge, Y. Kostov, K. A. Brorson, A. R. Moreira, and G. Rao, "Comparisons of optical pH and dissolved oxygen sensors with traditional electrochemical probes during mammalian cell culture.," *Biotechnol. Bioeng.*, vol. 97, no. 4, pp. 833–41, Jul. 2007.

[134] G. McMillan and J. Gray, "The Essentials of pH Measurement Design , Installation , Maintenance , and Improvement," in *International Instrumentation Symposium*, 2009.
[135] K. R. Rogers and A. Mulchandani, "Biomolecular Sensing for Bioprocess and Environmental Monitoring Applications," 1995.
[136] M. Oura, H. Kubo, S. Yamamori, S. Takeda, T. Shimizu, and T. Okano, "Development of cell culture monitoring system and novel non-contact pH measurement.," *Conf. Proc. ... Annu. Int. Conf. IEEE Eng. Med. Biol. Soc. IEEE Eng. Med. Biol. Soc. Annu. Conf.*, vol. 2011, pp. 22–5, 2011.
[137] J. Ehgartner, H. Wiltsche, and S. M. Borisov, "Low cost referenced luminescent imaging of oxygen and pH with a 2-CCD colour near infrared camera," *Analyst*, vol. 139, no. 19, p. 4924, Jul. 2014.
[138] J. Jang, S.-J. Moon, S.-H. Hong, and I.-H. Kim, "Colorimetric pH measurement of animal cell culture media," *Biotechnol. Lett.*, vol. 32, no. 11, pp. 1599–1607, Nov. 2010.
[139] S. Capel-Cuevas, M. P. Cuéllar, I. de Orbe-Payá, M. C. Pegalajar, and L. F. Capitán-Vallvey, "Full-range optical pH sensor based on imaging techniques.," *Anal. Chim. Acta*, vol. 681, no. 1–2, pp. 71–81, Nov. 2010.
[140] Z. Liu, J. Liu, and T. Chen, "Phenol red immobilized PVA membrane for an optical pH sensor with two determination ranges and long-term stability," *Sensors Actuators B Chem.*, vol. 107, no. 1, pp. 311–316, May 2005.
[141] X. Xu, S. Smith, J. Urban, and Z. Cui, "An in line non-invasive optical system to monitor pH in cell and tissue culture.," *Med. Eng. Phys.*, vol. 28, no. 5, pp. 468–74, Jun. 2006.
[142] X.-D. Wang and O. S. Wolfbeis, "Fiber-Optic Chemical Sensors and Biosensors (2008–2012)," *Anal. Chem.*, vol. 85, no. 2, pp. 487–508, Jan. 2013.
[143] D. B. K. Sharma, "Ultraviolet and visible spectroscopy," in *Spectroscopy*, 12th ed., Manjula Sharma, Ed. 2007, pp. 162–163.
[144] A. S. Jeevarajan, S. Vani, T. D. Taylor, and M. M. Anderson, "Continuous pH monitoring in a perfused bioreactor system using an optical pH sensor," *Biotechnol. Bioeng.*, vol. 78, pp. 467–472, 2002.
[145] G. Hellé, S. Roberston, S. Cavadias, C. Mariet, and G. Cote, "Toward numerical prototyping of labs-on-chip: modeling for liquid–liquid microfluidic devices for radionuclide extraction," *Microfluid. Nanofluidics*, vol. 19, no. 5, pp. 1245–1257, 2015.
[146] D. K. Rajan *et al.*, "A Portable Live-Cell Imaging System With an Invert-Upright-Convertible Architecture and a Mini-Bioreactor for Long-Term Simultaneous Cell Imaging, Chemical Sensing, and Electrophysiological Recording," *IEEE Access*, vol. 6, pp. 11063–11075, 2018.
[147] D. K. Rajan *et al.*, "Cardiomyocytes: Analysis of temperature response and

signal propagation between dissociated clusters using a novel video-based movement analysis software," *IEEE Access [submitted]*, 2019.
[148] J. Kreutzer *et al.*, "Structured PDMS Chambers for Enhanced Human Neuronal Cell Activity on MEA Platforms," *J. Bionic Eng.*, vol. 9, no. 1, pp. 1–10, Mar. 2012.
[149] S. S. Beauchemin and J. L. Barron, "The computation of optical flow," *ACM Comput. Surv.*, vol. 27, no. 3, pp. 433–466, Sep. 1995.
[150] B. K. P. Horn and B. G. Schunck, "Determining Optical Flow."
[151] D. Fleet and Y. Weiss, *Optical Flow Estimation, Handbook of Mathematical Models in Computer Vision*. Springer, Heidelberg, 2005.
[152] Y. David, "Affine optic flow (version 1.3)," *MATLAB Central File Exchange*, 2010. [Online]. Available: https://se.mathworks.com/matlabcentral/fileexchange/27093-affine-optic-flow. [Accessed: 03-Mar-2017].
[153] C. Bonivento, C. Melchiorri, and H. Tolle, *Advances in robotics- The ERNET Perspective; Proceedings of the Research Workshop of ERNET-European Robotics Network, Darmstadt, Germany, 1996*. World Scientific, 1996.
[154] "How Transform (Coverage) works—Help _ ArcGIS for Desktop.pdf," *ESRI*, 2019. [Online]. Available: http://desktop.arcgis.com/en/arcmap/10.3/tools/coverage-toolbox/how-transform-works.htm. [Accessed: 25-Aug-2019].
[155] Bnordgren, "Calculating coefficients for Affine Transformation," *Postgis*, 2019. [Online]. Available: https://trac.osgeo.org/postgis/wiki/DevWikiAffineParameters. [Accessed: 25-Aug-2019].
[156] M. A. Wirth, "Texture Analysis," 2004.
[157] A. Stolzing, S. Sethe, and A. M. Scutt, "Stem cell reports," *Stem Cells Dev.*, vol. 15, no. 4, pp. 478–487, Aug. 2006.
[158] K. Purandhar, P. K. Jena, B. Prajapati, P. Rajput, and S. Seshadri, "Understanding the Role of Heat Shock Protein Isoforms in Male Fertility, Aging and Apoptosis," *World J. Mens. Health*, vol. 32, no. 3, p. 123, Dec. 2014.
[159] M. S. Choudhery *et al.*, "Mesenchymal stem cells conditioned with glucose depletion augments their ability to repair-infarcted myocardium," *J. Cell. Mol. Med.*, vol. 16, no. 10, pp. 2518–2529, Oct. 2012.
[160] C. G. Crandall and J. González-Alonso, "Cardiovascular function in the heat-stressed human," *Acta Physiol.*, vol. 199, no. 4, pp. 407–423, Aug. 2010.
[161] T. E. Wilson and C. G. Crandall, "Effect of Thermal Stress on Cardiac Function," *Exerc. Sport Sci. Rev.*, vol. 39, no. 1, pp. 12–17, Jan. 2011.
[162] D. F. Wilson, "Quantifying the role of oxygen pressure in tissue function,"

Am. J. Physiol. Circ. Physiol., vol. 294, no. 1, pp. H11–H13, Jan. 2008.
[163] H. Välimäki, J. Kreutzer, J. Verho, K. Tappura, and J. Lekkala, "Fluorimetric Oxygen Sensor for in Vitro Cell Models," in *Procedia Engineering*, 2016.
[164] L. F. Araujo, A. de Matos Soeiro, J. L. Fernandes, A. E. Pesaro, and C. V. Serrano, "Coronary artery disease in women: A review on prevention, pathophysiology, diagnosis, and treatment," *Vasc. Health Risk Manag.*, vol. 2, no. 4, pp. 465–475, 2006.
[165] "Ischemic Heart Disease by National Heart Lung and Blood Institute," 2019. [Online]. Available: https://www.nhlbi.nih.gov/health-topics/ischemic-heart-disease. [Accessed: 10-Aug-2019].
[166] N. Koitabashi *et al.*, "Pivotal role of cardiomyocyte TGF-β signaling in the murine pathological response to sustained pressure overload," *J. Clin. Invest.*, vol. 121, no. 6, pp. 2301–2312, Jun. 2011.
[167] M. S. Mozaffari, J. Y. Liu, W. Abebe, and B. Baban, "Mechanisms of load dependency of myocardial ischemia reperfusion injury.," *Am. J. Cardiovasc. Dis.*, vol. 3, no. 4, pp. 180–96, Nov. 2013.
[168] T. Ryynänen *et al.*, "Microelectrode array for noninvasive analysis of cardiomyocytes at the single-cell level," *Jpn. J. Appl. Phys.*, vol. 57, no. 11, p. 117001, Nov. 2018.
[169] A. C. Bon-Mathier, S. Rignault-Clerc, C. Bielmann, and N. Rosenblatt-Velin, "Oxygen as a key regulator of cardiomyocyte proliferation: New results about cell culture conditions!," *Biochimica et Biophysica Acta - Molecular Cell Research*, vol. 1867, no. 3. Elsevier B.V., p. 118460, 01-Mar-2020.
[170] A. Carreau, B. El Hafny-Rahbi, A. Matejuk, C. Grillon, and C. Kieda, "Why is the partial oxygen pressure of human tissues a crucial parameter? Small molecules and hypoxia," *J. Cell. Mol. Med.*, vol. 15, no. 6, pp. 1239–1253, Jun. 2011.
[171] J. Kreutzer *et al.*, "Mini-incubator for prolonged hypoxia studies on MEA: Effect of hypoxia for IPSC-derived cardiomyocytes," *Front. Cell. Neurosci.*, vol. 12, 2018.
[172] A. Skogberg, A.-J. Mäki, M. Mettänen, P. Lahtinen, and P. Kallio, "Cellulose Nanofiber Alignment Using Evaporation-Induced Droplet-Casting, and Cell Alignment on Aligned Nanocellulose Surfaces," *Biomacromolecules*, vol. 18, no. 12, pp. 3936–3953, Dec. 2017.
[173] K. Kartasalo *et al.*, "CytoSpectre: a tool for spectral analysis of oriented structures on cellular and subcellular levels," *BMC Bioinformatics*, vol. 16, no. 1, p. 344, Dec. 2015.
[174] H. N. Po and N. M. Senozan, "The Henderson-Hasselbalch Equation: Its History and Limitations," *J. Chem. Educ.*, vol. 78, no. 11, p. 1499, Nov.

2001.
[175] F. Lee, "Spectrophotometric Determination of Blood pH," *J. Biol. Chem.*, vol. 236, no. 5, pp. 1589–1595, 1961.
[176] D. D. Van Slyke, L. V Hankes, and J. J. Vitols, "Photometric determination of pH with a single standard and calculation by nomogram.," *Clin. Chem.*, vol. 12, no. 12, pp. 849–70, Dec. 1966.
[177] J. Sendroy and F. L. Rodkey, "Apparent Dissociation Constant of Phenol Red as Determined by Spectrophotometrometry and by Visual Colorimetry," *Clin. Chem.*, vol. 7, pp. 646–54, Dec. 1961.
[178] C. Z. Lai *et al.*, "Spectrophotometric measurement of freshwater pH with purified meta-cresol purple and phenol red," *Limnol. Oceanogr. Methods*, vol. 14, no. 12, pp. 864–873, Dec. 2016.
[179] U. Kragh-Hansen and J. V. Møller, "Protein binding of small molecules," *Biochim. Biophys. Acta - Protein Struct.*, vol. 295, no. 2, pp. 447–456, Feb. 1973.
[180] VWR, "Cell culture flasks non treated or treated, sterile," 2018. [Online]. Available: https://uk.vwr.com/store/product/20659258/cell-culture-flasks-non-treated-or-treated-sterile. [Accessed: 01-Aug-2019].
[181] Eppendorf, "CCCadvanced® FN1 motifs Cell Culture Flasks," 2018. [Online]. Available: https://online-shop.eppendorf.co.uk/UK-en/Cell-Culture-and-Imaging-Consumables-110320/Stem-Cell-Cultureware-438131/CCCadvanced-FN1-motifs-Cell-Culture-Flasks-PF-247102.html?_ga=2.8156466.1434366476.1564680206-1020177114.1564680206. [Accessed: 01-Aug-2019].
[182] Www.biocompare.com, "Cell Culture Flasks," 2019. [Online]. Available: https://www.biocompare.com/Lab-Equipment/6485-Cell-Culture-Flasks/. [Accessed: 14-May-2019].
[183] Invitrogen, "Cell Culture Basics Handbook Invitrogen," 2018.
[184] www.tpp.ch, "T-flask with re-closable lid," 2019. [Online]. Available: https://www.tpp.ch/page/produkte/02_a_zellkultur_flasche_wv.php. [Accessed: 14-May-2019].
[185] M. M. Frigault, J. Lacoste, J. L. Swift, and C. M. Brown, "Live-cell microscopy - tips and tools.," *J. Cell Sci.*, vol. 122, no. Pt 6, pp. 753–767, 2009.
[186] E. H. Lepper and C. J. Martin, "The Protein Error in Estimating p(H) with Neutral Red and Phenol Red," *Biochem. J.*, vol. 21, no. 2, pp. 356–361, 1927.
[187] D. L. Miller and H. P. Schedl, "Nonabsorbed Indicators: A Comparison of Phenol Red and Inulin-^{14}C and Effects of Perfusion Technique," *Gastroenterology*, vol. 62, no. 1, pp. 48–55, Jan. 1972.
[188] W. J. Gelsema, C. L. de Ligny, A. G. Remijnse, and H. A. Blijleven, "pH-

Measurements in alcohol-water mixtures, using aqueous standard buffer solutions for calibration," *Recl. des Trav. Chim. des Pays-Bas*, vol. 85, no. 7, pp. 647–660, Jan. 1966.

[189] M. Kotrba and L.-H. Schilling, "Measurement of pH in Ethanol, Distilled Water, and their Mixtures: On the Assessment of pH in Ethanol-Based Natural History Wet Collections and the Detrimental Aspects of Dilution with Distilled Water," *Collect. Forum*, vol. 31, no. 1–2, pp. 84–101, Jan. 2017.

[190] G. S. Hartley, "The effect of long-chain salts on indicators: The valence-type of indicators and the protein error," *Trans. Faraday Soc.*, vol. 30, pp. 444–450, 1934.

[191] J. C. I. Ryan, "Understanding and Managing Cell Culture Contamination," 2018.

[192] R. J. Gillies, N. Raghunand, M. L. Garcia-Martin, and R. A. Gatenby, "pH Imaging A Review of pH Measurement Methods and Applications in Cancers."

[193] R. Samadani and W. T. Tan, "Stationary video camera auto-exposure conditioning," *Proc. - Int. Conf. Image Process. ICIP*, pp. 3453–3456, 2009.

[194] Y.-R. N. M. H. A. H. S. Levoy, "Correction of Distributed Optical Aberrations," vol. 2, no. 12, pp. 1–6, 2006.

[195] G. O. F. Parikesit, "Quantitative low-cost webcam-based microscopy," *Opt. Eng.*, vol. 49, no. 11, p. 113205, 2010.

[196] S. Schwamb, R. Puskeiler, and P. Wiedemann, "Monitoring of Cell Culture," Springer, Cham, 2015, pp. 185–221.

[197] R. Gustavsson, C. F. Mandenius, S. Löfgren, T. Scheper, and P. Lindner, "In situ microscopy as online tool for detecting microbial contaminations in cell culture," *J. Biotechnol.*, vol. 296, pp. 53–60, Apr. 2019.

PUBLICATIONS

Publication I Rajan DK, Kreutzer J, Välimäki H, Pekkanen-Mattila M, Ahola A, Skogberg A, Aalto-Setälä K, Ihalainen H, Kallio P, Lekkala J. A portable live-cell imaging system with an invert-upright-convertible architecture and a mini-bioreactor for long-term simultaneous cell imaging, chemical sensing, and electrophysiological recording. IEEE Access, vol. 6: pp. 11063–11075, 2018. (https://doi.org/10.1109/ACCESS.2018.2804378)

Publication II Rajan DK, Mäki, AJ, Pekkanen-Mattila M, Kreutzer J, Ryynänen T, Välimäki H, V Jarmo, Koivumäki JT, Ihalainen H, Aalto-Setälä K, Kallio P, Lekkala J. Cardiomyocytes: Analysis of temperature response and signal propagation between dissociated clusters using a novel video-based movement analysis software. IEEE Access [submitted].

Publication III Rajan DK, Patrikoski M, Verho J, Sivula J, Ihalainen H, Miettinen S, Lekkala J. Optical non-contact pH measurement in cell culture with sterilizable, modular parts. Talanta vol. 161, pp.755–761, 2016. (https://doi.org/10.1016/j.talanta.2016.09.021)

Publication IV Rajan DK, Verho J, Kreutzer J, Valimaki H, Ihalainen H, Lekkala J, Patrikoski M, Miettinen S. Monitoring pH, temperature and humidity in long-term stem cell culture in CO_2 incubator. 2017 IEEE International Symposium on Medical Measurements and Applications, MeMeA 2017 - Proceedings. IEEE, pp. 470–474. (https://doi.org/10.1109/MeMeA.2017.7985922)

PUBLICATION I

A portable live-cell imaging system with an invert-upright-convertible architecture and a mini-bioreactor for long-term simultaneous cell imaging, chemical sensing, and electrophysiological recording

Rajan DK, Kreutzer J, Välimäki H, Pekkanen-Mattila M, Ahola A, Skogberg A, Aalto-Setälä K, Ihalainen H, Kallio P, Lekkala J.

Journal IEEE Access, vol. 6, pp.11063–11075, 2018
https://doi.org/10.1109/ACCESS.2018.2804378

Access
Review | Open Access Journal

A Portable Live-Cell Imaging System With an Invert-Upright-Convertible Architecture and a Mini-Bioreactor for Long-Term Simultaneous Cell Imaging, Chemical Sensing, and Electrophysiological Recording

DHANESH KATTIPPARAMBIL RAJAN[1], (Student Member, IEEE), JOOSE KREUTZER[1], HANNU VÄLIMÄKI[1], MARI PEKKANEN-MATTILA[2], ANTTI AHOLA[1], ANNE SKOGBERG[1], KATRIINA AALTO-SETÄLÄ[2,3], HEIMO IHALAINEN[1], PASI KALLIO[1], AND JUKKA LEKKALA[1]

[1]BioMediTech Institute and Faculty of Biomedical Sciences and Engineering, Tampere University of Technology, FI-33720 Tampere, Finland
[2]BioMediTech, Faculty of Medicine and Life Sciences, University of Tampere, FI-33100 Tampere, Finland
[3]Heart Hospital, Tampere University Hospital, FI-33521 Tampere, Finland

Corresponding author: Dhanesh Kattipparambil Rajan (dhanesh.kr@tut.fi)

This work was supported by the Finnish Funding Agency for Technology and Innovation (TEKES) through Human Spare Parts 2 Project under Grant 40332/14.

ABSTRACT Cell culture *in-vitro* is a well-known method to develop cell and disease models for studying physiologically relevant mechanisms and responses for various applications in life sciences. Conventional methods for instance, using static culture flasks or well plates, have limitations, as these cannot provide accurate tractable models for advanced studies. However, microscale systems can overcome this since they mimic the cells' natural microenvironment adequately. We have developed a portable live-cell imaging system with an invert-upright-convertible architecture and a mini-bioreactor for long-term simultaneous cell imaging and analysis, chemical sensing and electrophysiological recording. Our system integrates biocompatible cell-friendly materials with modular measurement schemes and precise environment control and can be automated. High quality time-lapse cell imaging is hugely useful in cell/disease models. However, integration of advanced *in-vitro* systems into benchtop microscopes for *in-situ* imaging is tricky and challenging. This is especially true with device based biological systems, such as lab/organ/body-on-chips, or mini-bioreactors/microfluidic systems. They face issues ranging from optical and physical geometry incompatibilities to difficulties in connectivity of flow and perfusion systems. However, the novel modular system we have developed either as an inverted or as an upright system can easily accommodate virtually any *in-vitro* devices. Furthermore, it can accept additional sensor or measurement devices quite freely. Cell characterization, differentiation, chemical sensing, drug screening, microelectrode-array-electrophysiological recordings, and cell stimulation can be carried out with simultaneous *in-situ* imaging and analysis. Moreover, our system can be configured to capture images from regions that are otherwise inaccessible by conventional microscopes, for example, cells cultured on physical or biochemical sensor systems. We demonstrate the system for video-based beating analysis of cardiomyocytes, cell orientation analysis on nanocellulose, and simultaneous long-term *in-situ* microscopy with pO_2 and temperature sensing. The compact microscope as such is comparable to standard phase-contrast-microscopes without any detectable aberrations and is useful practically for any *in-situ* microscopy demands.

INDEX TERMS Portable compact microscope, label-free long-term live-cell imaging, modular portable microscope for *in-situ in-vitro* cell imaging, portable cell culture system, portable cell culture and measurement system, low-cost biosensor technology.

I. INTRODUCTION

Live-cell microscopy is a tool used commonly in various research applications and, is instrumental in investigating numerous intra and extra cellular dynamic processes and their environmental interactions. Traditional approaches to live-cell imaging are often based on short or long- term time-lapse microscopy (TLM) using high quality biological microscopes [1], [2]. The growing interest in this area is perhaps best evidenced by the dramatic increase in the number of papers reporting numerous TLM studies in life sciences. In most TLMs, the cellular activity is imaged for durations ranging from milliseconds to hours in a specimen chamber with special environment control [3], [4]. A TLM system for biological specimens is typically equipped with a contrast enhancement technique such as, differential interference contrast (DIC) or Hoffman modulation contrast (HMC), or fluorescence or phase contrast [1]. They can capture images at defined time points to produce a TLM montage or movie to unveil dynamic biological processes. High-end systems coupled with dedicated TLM softwares often support high frame rate movie recordings, and if desired, timely analysis of captured images during the TLM. The State-of-the-art TLM systems employ imaging modalities such as confocal and super resolution procedures in order to improve the contrast, to reduce the photo-cytotoxicity and to capture images at resolutions higher than Abbe's classical diffraction-limited resolution [5]. The quality of TLM images by these systems is high, however, it comes with a price; high costs and often the hardware involves fairly complicated settings with large form factors and high upkeep [6]. These systems oftentimes cannot satisfy the need for high throughput observations due to their bulky volume and limited flexibility [7]. Besides, in several device based biological systems, for example, lab/organ/body-on-chips, reaction chambers, bioreactors, and microfluidic culture systems, the real time processes need to be timely imaged in *in-situ*. They can experience tremendous challenges while being embedded into an off-the-shelf TLM system, due to issues ranging from optical and physical geometry incompatibility to difficulties in connectivity of flow and perfusion systems [8]–[17]. Several recent developments in physical, chemical and biological sensors for cell culturing and cellular-tissue models are steadily being integrated into systems for drug screening, regenerative medicine and stem cell engineering [18]–[20]. These sensors are efficient candidates for process monitoring and environment regulation, however, most of them, unfortunately, are not compatible with conventional TLM hardware for synchronised imaging. Despite various TLM systems with remarkable specifications being continually available in the market, still adapting steadily developing technologies into them is difficult and laborious.

Breaking the barriers of achievable spatial resolution in microscopy is obviously important, but at the same time, the demand for miniaturized versions of biological microscopes with uncompromising imaging quality is also continually increasing. Compact microscopes instead of high-end, large-form-factor microscopes, are unavoidable in several instances, for obvious reasons, like following the biological events *in-situ* in real time inside or outside of an incubator. Over the last years, several compact microscopes, have been developed and some have been commercialised [21], [22]. A number of compact systems, based on the emerging microscope modalities have been reported recently. The on-chip brightfield - fluorescent microscopes [23]–[26] have successfully demonstrated high resolution, large field-of-view (FOV) and incubator compatibility. However, the cells need to be plated on the imaging chip, making them less attractive for conventional cell culturing workflow. On the contrary, digital holographic microscopy (DHM) is an excellent choice for widefield lensless 2D/3D imaging, and numerous compact systems have been recently reported [27]–[29]. DHM, in general, can be implemented as a shadow or fluorescent imaging modality either by quantitative or qualitative means, but in all cases, the image of the object must be reconstructed numerically from the diffraction pattern of the specimen recorded [30], [31]. DHM, being a computational microscopy, thus typically lacks the immediate visualization of the specimen, which can be cumbersome in certain biomedical procedures [32]. Another imaging modality – the optical projection tomography, that developed notably in the last decade can produce 3D cell images, but apparently is not directly suitable for live-cell imaging. On the other hand, nonlinear optical imaging methods are suitable for live-cell imaging, but the miniaturization – from the instrumentation point of view- is tricky. On the contrary, fiber optic microscopy has remarkable advantages, but integrating fibers into cell chambers can be sometimes severely chaotic [33]–[38]. In addition to downsizing the newly emerging microscope modalities, modifying existing microscopy modalities to construct portable compact microscopes have unprecedented potential, especially when they are equipped with features for wireless communication, web interfacing and smart phone compatibility. They can have widespread applications in remote cell microscopy, mobile healthcare and on-field medical diagnosis [39], [40]. Though several compact microscopes have been reported, most of them, except for a few are either bright-field or fluorescent systems [23]–[26], [39]–[41]. As live-cells are highly transparent for visible wavelengths, the image contrast is extremely poor in bright-field systems. The contrast is greater in fluorescent systems, but staining with fluorescent markers is inevitable, which can sometimes be toxic and unacceptable. While chromatic aberration is visible in some of the reported cost-effective systems [7], controlling all the camera features in webcam based systems is not straight-forward or is sometimes impossible [7], [42], [43]. Besides, the maximum frame rate in web-cam systems might be insufficient for fast dynamic recordings.

Almost all the compact microscopes reported are intended to be used with a specific system or for a specific purpose and not necessarily modular for extended applications. They have been explicitly designed to be used either in the inverted or in

the upright configuration and are mutually exclusive. In this context, we present a compact portable live-cell imaging system with a novel modular architecture, configurable either as an inverted or as an upright system, and with a mini bioreactor for simultaneous long-term live-cell imaging, chemical sensing and electrophysiological recording. The system consists of a digital microscope module, an illumination module, positioning and a motorized focusing stage, mini-incubator with biocompatible and cell-friendly materials, fluorometric pO_2 sensor and microelectrode array (MEA) amplifier. We put forward a design where the illumination and microscope modules can be swapped, i.e. the system can be converted between inverted and upright configurations. This architecture enables the system to be useful not only for conventional inverted spatiotemporal cell imaging, but also as an upright system when the room below the cell platform is unavailable for inverted microscopy. When sensors such as opto-chemical sensors [18], [19] need to be integrated into cell platforms, ideally, they must operate in close proximity of the cells, i.e typically just under the cell platform, and resultantly, simultaneous uninterrupted inverted microscopy is practically impossible. In our design, the system can then be switched into an upright configuration, therefore, biochemical measurements conjointly with live-cell imaging becomes possible. The microscope module consists of mainly three optical components - a machine vision camera, a mirror cube and a phase contrast objective. The illumination module comprises primarily of a white LED, a LED lens, a ground glass diffuser and a projection lens. It provides a stable and reasonably safe illumination in bright-field or dark-field or phase contrast schemes. The manual xyz-stage module enables sample xy-positioning and coarse focusing. Fine focusing is accomplished with a motorized linear stage. The magnification can be adjusted, primarily by changing the objective lenses and additionally by using lensless extension tubes. We employ highly corrected phase contrast objectives to produce high quality cell images with minimal halo, distortion and aberration. The bioreactor assembly comprises of a transparent ITO cell heater, a mini-incubator with polydimethylsiloxane (PDMS) cell chamber [44], [45] and gas supply for CO_2 buffering.

In the following, we first present a detailed construction of the developed modular microscopy system. Then the microscopy characterization and system performance results, based on studies with a resolution test-target and stained histology specimens, are shown. In the live-cell microscopy section, we study the system performance in different configurations when imaging a set of unstained cells. Then we show the results from orientation analysis of fibroblasts, long term video-based beating analysis of cardiomyocytes and an excerpt from simultaneous pO_2 sensing and TLM study. We complete the paper by experimenting the z-stack capabilities of the system and, finally we discuss the results.

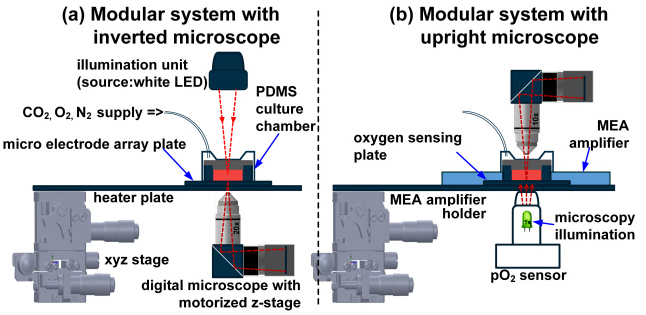

FIGURE 1. Modular microscopy schematic arrangement for (a) inverted microscopy and (b) upright microscopy with optical fluorometric oxygen sensor and MEA amplifier.

II. MODULAR CELL CULTURING SYSTEM ASSEMBLY

The modular system is schemed in FIGURE 1. The whole system was designed utilizing 3D computer-aided design (CAD) in Solidworks®. Firstly, the 3D models of suitable commercially available opto-mechanical parts were imported into the design, and the remaining parts were custom designed (anodised aluminium). The sub-assemblies of the final interchangeable assembly (see FIGURE 2) are: a camera module, an illumination module, a manual xyz-stage module, a motorized focus stage, PDMS mini-incubator, pO_2 sensor as well as a MEA amplifier with its holder. An original photograph of the final assembly is shown in FIGURE 2e. The details of each module are separately described in the following paragraphs. Check the supplementary materials section for system design CAD files.

A. CAMERA MODULE

A high quality digital microscope is constructed using an achromat phase contrast objective, a mirror cube (CCM1-E02/M-Thorlabs) and a machine vision camera. The microscope assembly is illustrated in FIGURE 3a. Two adapters (SM1A10-Thorlabs) and a coupler (CMT2-Thorlabs) are used for coupling the parts in the assembly. A camera with internal C or CS mount in the front aperture is required in the design. In the experiments discussed later, monochrome (>40 frames-per-second) or colour camera was used depending on the nature of application and intended analysis. The machine vision camera and the objective lens are mounted perpendicular to each other through the mirror cube. This geometry keeps the digital microscope very compact and facilitates a fixed mounting hole for objectives in the imaging plane. Moreover, it provides a great deal of space perpendicular to the imaging plane for additional optics. The mirror cube can be locked in its holder (FIGURE 2), either in upward or downward direction, respectively for inverted or upright microscopy. The cube holder's rail carrier head (dovetail RC2-Thorlabs, FIGURE 2a) allows upward or downward wobble-free translation of the holder and allows to lock it securely at any place along the length of the corresponding dovetail rail (RLA1200-Thorlabs, FIGURE 2a). Further, with this mechanism, the camera

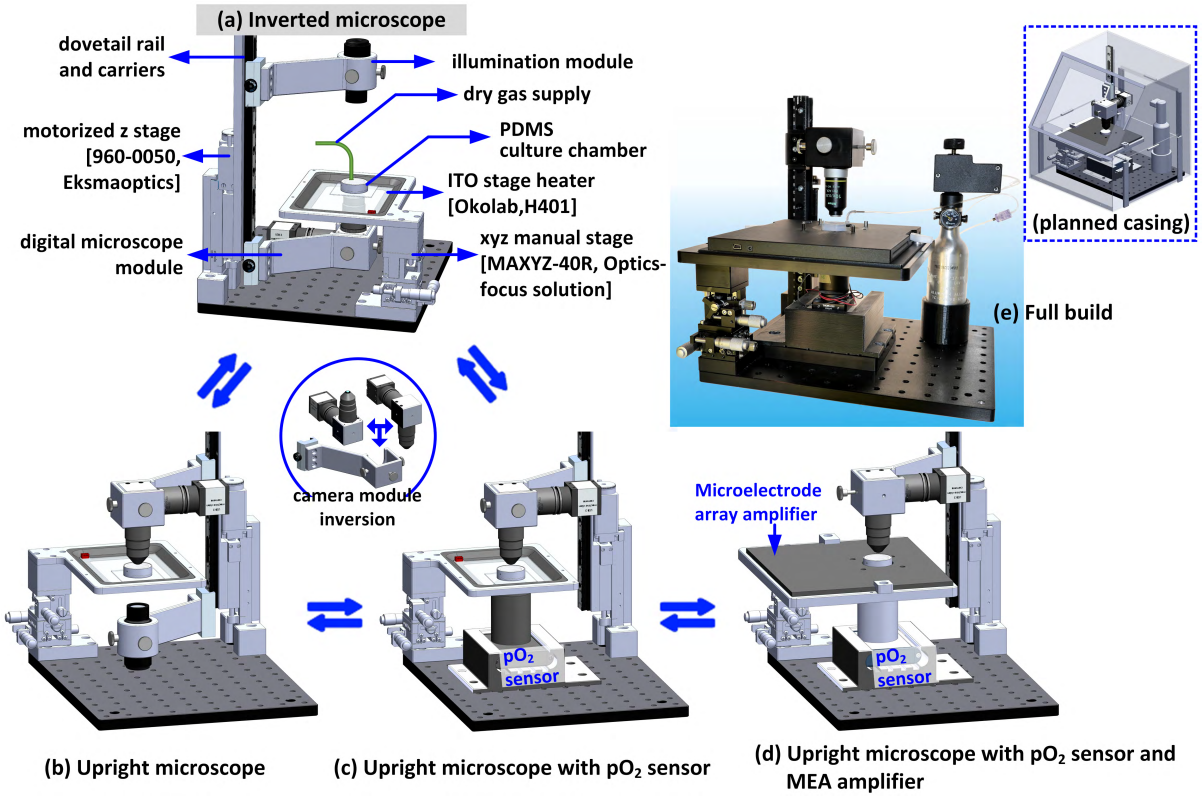

FIGURE 2. **Modular system in different configurations. Microscope assembly for (a) inverted configuration and (b) upright configuration. (c) Upright configuration with oxygen sensor. (d) Upright configuration with MEA amplifier (MEA1060-Up, Multichannel System) and oxygen sensor. (e) Original photograph of the final assembly.**

module can be easily taken out or snapped onto the rail anywhere along its length, even without accessing the rail ends.

B. OBJECTIVES

We utilize phase contrast objectives (Nikon CFI Achromat ADL 10XF, 20XF and 40XF) to produce cell images with unsurpassed details with little or negligible phase contrast halo. These objectives, in principle, transform the differences in the relative phase between the surround-un-deviated wave and the diffracted wave (by the specimen) into amplitude differences in the image [46]. An appropriate illumination (light manipulation through an annular ring) and objective placement (keeping the objective phase plate in conjugate to the illumination annular ring) are essential to achieve the maximum contrast ratio. See section '*Illumination module*' for the details of our illumination arrangement. TABLE 1 in the experimental section shows the technical specifications (measured and formula calculated) corresponding to the implementation of the select objectives. In addition to using high magnification objectives, the overall system magnification for a select objective can be improved, to a certain extent, by mounting stackable extension tubes of varying lengths in the light path (FIGURE 3a). Extension tubes are lensless hollow cylinders that stay between the objective and the camera, causing the camera sensor to move further from the objective and focus more closely, which in turn increases the overall magnification. The extension distance divided by the objective lens's focal length ultimately decides the amount of overall magnification (see TABLE 1).

C. ILLUMINATION MODULE

The anatomy of the compact illumination module is illustrated in FIGURE 3b. It consists of two separate stackable sub-assemblies, where the bottom sub-assembly can be stacked onto the main-assembly with or without an appropriate annular ring suitable for dark-field or phase contrast scheme. The optical train of the main-assembly comprises of a LED (3w-cool white, spectrum ~410-750nm, LXHL-LW3C-Lumileds), a bowl-shaped PMMA-LED collimator lens (FA10696 LN2-RS-LEDiL), a ground glass diffuser (DG05-1500-MD-Thorlabs) and spacers (stainless steel retaining rings (SM1RR, SM1RRC-Thorlabs) and 3D printed ones). All components are packed in Ø1" lens tube (SM1M20). Components can be accessed from both ends of the lens tube. A threaded adapter (S1LEDM-Thorlabs) serves as the LED lock at the top of the tube, and helps one to replace the LED without disturbing other components in the main assembly. The other sub-assembly has just two optical components, a 3D printed condenser annular ring and a plano-convex lens (L12224/L8080/L11388-SurplusShed) enclosed in an adapter (AD15F-SM1-Thorlabs) in a 3D printed casing.

TABLE 1. Modular microscope optical performance specifications, measured and estimated in air (at wavelength 550nm).

Objective lens	Extension tube length (mm)	WD[Δ] (mm)	NA[†]	Resolution[σ] (μm)	DOF (μm)	Field of View (μm)	True magnification
10X	0	12.74	0.12	2.69	17.62	1580.25	4.54
"	15	12.20	0.13	2.58	16.18	1347.37	5.33
"	25	11.74	0.14	2.48	15.00	1219.05	5.89
"	40	11.41	0.14	2.42	14.18	1075.63	6.68
"	80	10.60	0.15	2.25	12.27	820.51	8.75
20X	0	5.91	0.22	1.55	5.80	691.89	10.38
"	15	5.61	0.23	1.47	5.24	600.94	11.95
"	40	5.48	0.23	1.44	5.01	490.42	14.64
40X	0	5.75	0.23	1.43	4.96	190.48	37.70
"	15	5.70	0.24	1.42	4.88	162.44	44.20

[Δ]WD=working distance, [†]NA=numerical aperture= ref.index*sin (tan^{-1}(aperture radius/WD)), [σ]Resolution = 0.61*wavelength/NA, DOF=depth of focus[55]

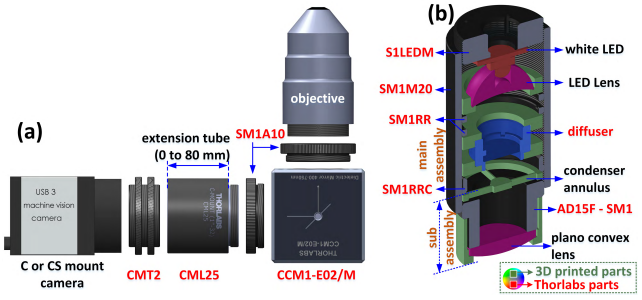

FIGURE 3. Compact microscopy parts. (a) Component assembly of the digital microscope. (b) anatomy of the illumination module. Here, the bottom sub-assembly is stackable onto the main assembly. This enables easy replacement of the condenser annule while the objective lens is changed. The S1LEDM-adapter functions as a lock for testing or replacing of LEDs (prefer star type or 5mm through hole-LEDs).

The diffuser in the light path is critical for a highly homogenous illumination for high contrast imaging. A diffuser with 1500 grits was specifically selected after several cell-imaging trials to accomplish the greatest possible contrast. The illumination module has a variable NA (0.08 - 0.27) and a matching annule needs to be inserted into the sub-assembly once the objective is changed. The illumination module to the specimen distance is adjusted freely to take full advantage of the NA.

D. STAGE MODULE AND MOTORIZED FOCUSING STAGE

A manual xyz-stage (MAXYZ-40R, Optics-focus solution, see FIGURE 2a) with micrometer head screws, is included in the set-up for coarse focusing and sample positioning (x, y $= \pm 6.5$mm, z $=$ 10mm, resolution $=$ 10 μm). A custom machined metallic frame with a rectangular slot is mounted onto the xyz-stage where, a standard k-frame transparent stage heater (Okolab, H401) can be loaded and locked. Once the camera and illumination modules are appropriately positioned on the dovetail rail and is coarsely focused, the motorized fine focusing is carried out from the software side. The narrow motorized translation stage (960-0050, Eksma Optics, see FIGURE 2a) enables fine focusing (z $=$ 50 mm, resolution $=$ 1.25 μm [full steps]) at a maximum speed of 5 mm/s. Furthermore, a specific stepper controller (980-0045-USB-Eksmaoptics), is also capable of dividing the full steps upto 1/256 step/div for sub-micron stack acquisitions. The mechanical limit switches on the translation stage establish reference positions with an accuracy of several motor steps and assists emergency stopping.

E. FLUOROMETRIC pO_2 SENSOR AND MEA AMPLIFIER

The pO_2 sensing is based on phase-fluorimetric detection, where oxygen sensitive dyes, such as platinum(II) octaethylporphyrinketone are embedded in a thin, gas permeable polymer film (polystyrene) and then the pO_2 sensitive phase difference between the fluorescence emission and excitation signal are read [47]. For this purpose, we applied a super critical angle read-out scheme based on an in-contact parabolic lens [18], which has a high emission collection efficiency and, moreover, facilitates efficient total internal reflection excitation. These features make the detection insensitive to biofouling or other optical changes in the sensing surface and, more importantly, greatly reduces the amount of optical power radiated into the cell culture chamber. In addition, the set-up leaves room for microscopy illumination in the centre of the cell chamber.

The MEA amplifier (bandwidth: 1Hz-3 kHz, gain: 100-5000) is suitable for 49 mm $\times$ 49 mm MEA plates with 8x8 grid configuration for multisite, parallel electrophysiological recording. When the amplifier lid is closed, the contact pins are pressed onto the MEA contact pads which establishes the signal connectivity. The selected MEA amplifier ensures very high signal-to-noise ratio since the amplifier electronics stays very close to the MEA plate. External ITO heater can be avoided in MEA measurements as its integrated heating element and temperature sensor serves the purpose. Electrophysiological measurements combined with morphological or chemical sensing or fluorescence readouts and multisite stimulations can be efficiently carried out in the modular system.

F. INTERCHANGING BETWEEN INVERT AND UPRIGHT MICROSCOPY CONFIGURATIONS

The procedures involved in changing the microscope from invert to upright scheme are illustrated in the FIGURE 2a-c. Firstly, the digital microscope mirror cube is reversed in the

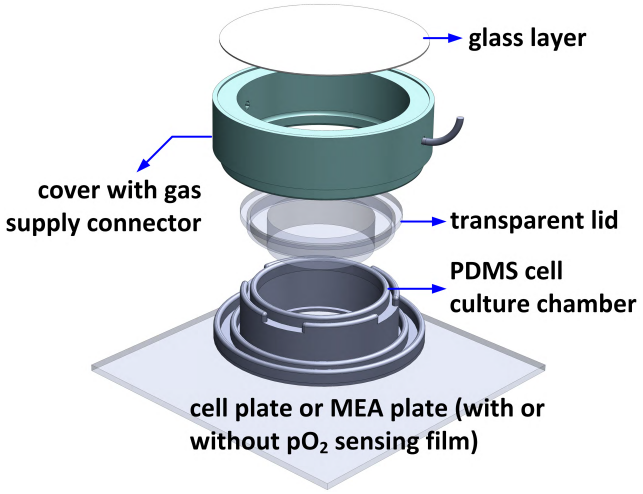

FIGURE 4. Schematic of the mini incubator that consists of PDMS cell culture chamber, transparent lid to seal the cell culture, and cover to enclose the environment to maintain the culture conditions utilizing dry gas supply from the side of the cover.

camera module and the illumination and camera modules are swapped vertically on the dovetail rail. Maintaining a gap of few mm between the objective and cell plate (or the outer layer of a culture chamber in upright microscopy) ensures safety and smooth motorized focusing. For upright microscopy, long working distance objectives are often necessary depending on the height of the culture chamber, which forces one to usually opt for low magnification objectives. In general, for most of the highly corrected series of plan fluorite and plan apochromatic-infinity objectives, the working distance decreases as both the magnification and numerical aperture increases. Therefore, out of the three objectives selected (TABLE 1), only 10X objective is particularly useful for upright microscopy where the cells are imaged from the top of the mini incubator having a height of 11mm. However, once the 10X objective is mounted, one can adjust the overall magnification by making use of extension tubes in the light path (TABLE 1).

III. MATERIALS AND METHODS

A. PDMS CULTURE CHAMBER (MINI INCUBATOR)

The schematic of the mini incubator is shown in FIGURE 4. A controlled gas supply (5% CO_2, 19% O_2, 76% N_2) during the long-term TLM is critical to maintain the pH of the culture medium for live and healthy specimens. The technique - providing gas supply surrounding the PDMS structure - is described previously [45] and is directly adapted here. Briefly, the structure of the cell culture device consists of three main parts: a cover, a lid, and a PDMS cell culture chamber. The cover and the lid were made from UV curable acrylic plastic (Shapeways, Eindhoven, The Netherlands) and polycarbonate (PC) (Saloteam Oy, Salo, Finland), respectively. The cell culture chamber was house–made and cast from PDMS (Sylgard 184, Dow Corning, USA) using standard soft–lithography techniques as explained in the previous study [44].

The lid seals the cell culture chamber watertight that prevents evaporation. The lid is highly transparent to facilitate a good optical path for microscopy. A small boss in the middle of the lid is immersed into the culture medium, which avoids empty space for water to condensate, and thus ensures undisturbed imaging during the entire TLM. The cover with glass window seals the environment around the cell culture chamber. A continuous supply (5ml/min) of dry gas mixture is provided (FIGURE 1, FIGURE 2) through the cover.

B. SOFTWARE INTERFACE AND CONTROL

Currently, a custom written Matlab (ver:R2016b)-UI (user interface) software is implemented for controlling the illumination, stage heater and time-lapse data logging (image or movie, sensors). A low-cost microcontroller (Arduino UNO R2) with a motor add-on board (Adafruit motor shield V2) enables controlling the LED illumination and focusing (stepper motor) translation stage. LED intensity can be regulated 0-100% (at 8-bit resolution) through a custom hardware-controlled LED dimmer using pulse-width-modulation (PWM) signal from Arduino. Matlab's image acquisition tool-box in conjunction with Arduino and PointGray third-party Matlab packages facilitate a two-way control of Arduino and PointGray machine vision cameras from the UI [48]–[50] During TLM, the camera is configured to write directly into the PC disk, either as independent images when slow temporal changes are monitored or directly as an uncompressed high fps (frames-per-second) movie when fast dynamics, for instance, cardiomyocyte beating, is captured. Check the supplementary materials section for an exemplary Matlab script for illumination, camera and motorized focusing control and time-lapse image or video acquisition.

C. CELL CULTURING

Fibroblast culture: All chemicals and supplements for fibroblast culture, including Dulbecco's modified eagle medium (DMEM) high glucose, w/o L-glutamine, w/o sodium pyruvate (Biowest, L0101), Dulbecco's phosphate buffered saline (PBS) w/o calcium, w/o magnesium (Biowest, L0615), Trypsin-EDTA 1x w/o Calcium, w/o Magnesium, w/phenol Red (Biowest, L0930), L-Glutamine 100x, 200 mM (Biowest, X0550), Fetal bovine serum (FBS) USA (Biowest S1520), Penicillin-streptomycin solution 100x (Biowest L0022) were purchased from VWR and used as received or reconstituted according to manufacturer's instructions. Mouse embryonic fibroblasts (MEF) originally obtained from Wolfgang H. Ziegler (Hannover medical school, Hannover, Germany) were cultured in DMEM high glucose medium supplemented with 10% (v/v) fetal bovine serum (FBS), 1% L-glutamine, 1% P/S (100 IU mL^{-1} penicillin, 100 μg mL^{-1} streptomycin) in a standard incubator. Cells were harvested using trypsin-EDTA treatment and counted using a Bruker's chamber. For the studies of MEF alignment on nanocellulose surfaces, cationic cellulose nanofibers (c-CNF) were produced and coated on cul-

ture plates. Production, surface preparation and alignment mechanism of c-CNF is described in more detail in [51]. Glass plates (49 × 49mm) and PDMS-well culture chambers were cleaned by several immersions in 70% ethanol before coatings. After mounting PDMS-well culture chambers on the sterilized plates, eight sample plates were coated with c-CNF as described in [51] and three plates without c-CNF were used as reference for alignment analysis. For each well, cell suspension was seeded in a density of approximately 1.5×10^5 cells/mL. After seeding, the MEFs were allowed to adhere in a standard cell-culturing incubator for 30 to 120 minutes before filling the PDMS-well with culture medium (1 mL). Filled PDMS-well culture plates were either directly imaged in our system or cells were allowed to adjust and proliferate up to 24 h in the incubator before imaging.

iPS-CM culture: Cardiomyocytes were derived from human iPS-cell line UTA.04602.WT as previously described in [52]. Glass plates were first sterilized with 70% ethanol and dried properly before the PDMS ring was applied to the plates creating the well for the cells, subsequent to which ăthe beating iPS-CM aggregates were plated. Plates were hydrophilized with FBS and coated with 0.1% gelatin type A (Sigma-Aldrich, St Louis, MO, USA). For each plate, 3-4 beating iPS-CM aggregates were plated. The iPS-CMs were cultured in KO-DMEM-media (Lonza, Basel, Switzerland) with 20% FBS (Lonza), 1% non-essential amino acids (NEAA) (Cambrex, East Rutherford, NJ), 2 mM Glutamax (Invitrogen, Carlsbad, CA) and 50 U/ml penicillin/streptomycin (Lonza). After plating, the iPS-CM aggregates were cultured in an incubator overnight before imaging (inverted/upright). In all prolonged cell culturing, the medium in the PDMS culture chamber was replaced (twice a week) by fresh medium.

D. CYTOSPECTRE CELL ORIENTATION ANALYSIS AND VIDEO BASED BEATING SIGNAL ANALYSIS

A spectral orientation analysis tool (CytoSpectre[1.2]) [53] was used to analyse the images and characterize the degree of alignment of the cells on the c-CNF compared to control surfaces. Cytospectre analyses the orientation and wavelength distributions by performing Fourier transform to estimate the power spectrum of an image and, based on the spectrum, computes parameter values describing, among others, the mean orientation and anisotropy. From this, the circular variance (CV) – the measure of the shape distribution – is computed to describe the degree of cell orientation. The value of CV can range from 0 (isotropy i.e. perfect alignment of all oriented structures along a single line) to 1 (lack of isotropy).

Cardiomyocyte mechanobiological function was assessed using video microscopy based contraction measurement [54]. It uses digital image correlation methods on consecutive video frames to calculate a velocity vector field, based on which a directional signal characterizing the beating is obtained.

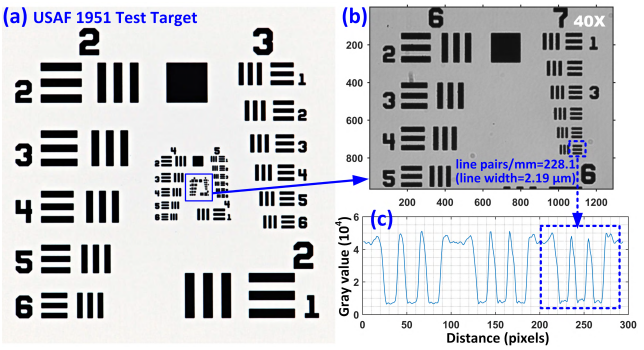

FIGURE 5. Microscopy characterisation. The USAF 1951 resolution test-target (a) original photograph and (b) microscopy image (40X, no extension tube). (c) intensity profile from three line groups ([4,7], [5,7], [6,7]). The dotted box corresponds to group [6,7] with 2.19 μm wide lines.

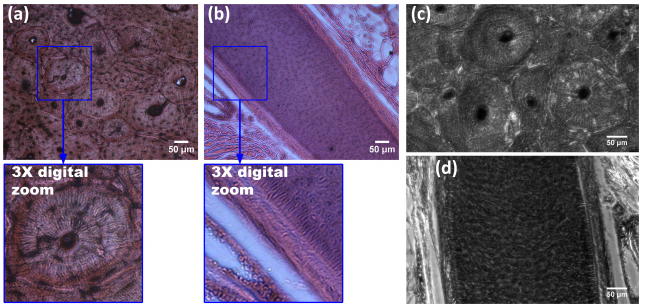

FIGURE 6. Modular microscope (inverted, 20X) images of stained histological samples. Human (a) hard bone grinding section and (b) skin section through hair follicle imaged using modular microscope. (c,d) reference images of the same samples with a benchtop-phase contrast microscope (Zeiss Axio observer z1).

IV. EXPERIMENTAL RESULTS

A. MICROSCOPY CHARACTERISATION

A standard positive resolution test-target (R1DS1P-Thorlabs) was used for measuring the resolution, FOV and true magnification. See FIGURE 5. for the example image of the resolution target captured with the 40x objective and a monochrome camera (PointGray, BFLY-U3-13S2M-CS, 1.3 MP, pixel size = 3.75 μm in 1/3" sensor). All the technical specifications for the three selected objectives with various extension tube lengths are summarised in TABLE 1. Because the objective lenses are implemented differently unlike in a recommended bench top microscope, the NA of the objectives had to be recalculated. We calculated this from the modified working distances.

B. PERFORMANCE COMPARISON WITH STAINED HISTOLOGICAL SAMPLES

Two stained human histological (Euromex PB.5221-Jaso Oy) specimens, 1) hard bone grinding section and 2) human skin section through a hair follicle were imaged with the proposed system (FIGURE 6a,b), and with a bench top biological phase contrast microscope for reference (FIGURE 6c,d). Microscopy images with the proposed system are notably comparable with the reference images, though the FOV and true magnification are slightly different in both the cases.

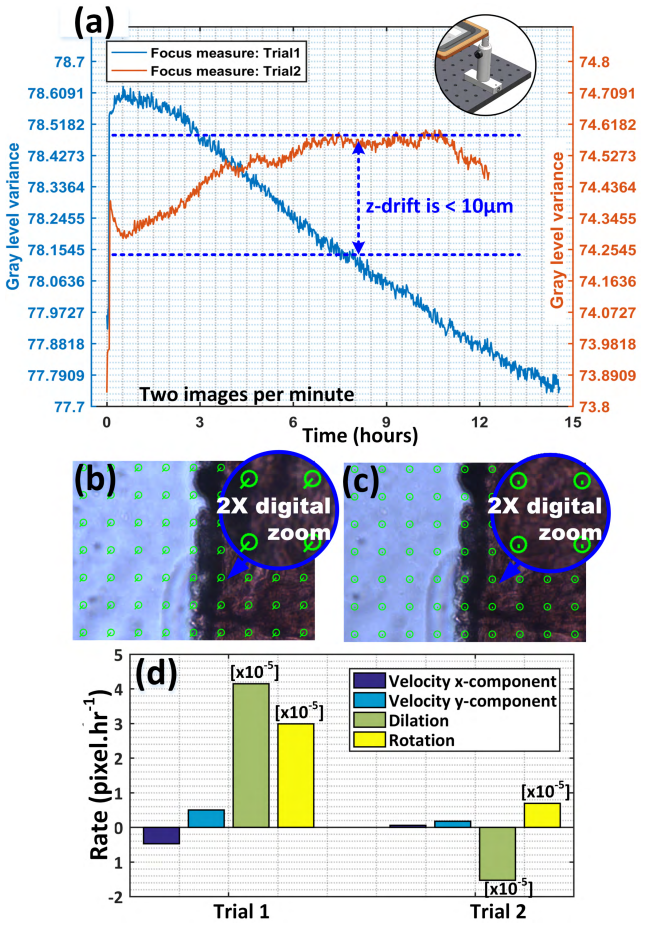

FIGURE 7. Long-term imaging performance measurements with a fixed specimen. (a) numerical estimation of focus [56]. Trial 1: measurement in room temperature. Trial 2: measurement at constant 37°C with a support pillar (inset). Ideally, a horizontal line would describe 0 focus drift. In our system, a slight focus drift is visible in Trial 2, but it is as low as 0.2% compared to 0.9% (Trial 1) in >12 hours period. (b, c) optical flow (overall relative physical movement of the specimen) in xy plane in Trial 1 and Trial 2 estimated as described in [57]. The flow vector (green line extending from the circles) indicates the xy movements were extremely small in Trial 2. (d) estimated flow field parameters [Note: -Vx indicates a shift of the last frame to the left compared to the first frame. Dilation and rotation quantify the overall expansion (or shrinking) and twisting (about z-axis) respectively of the measurement area].

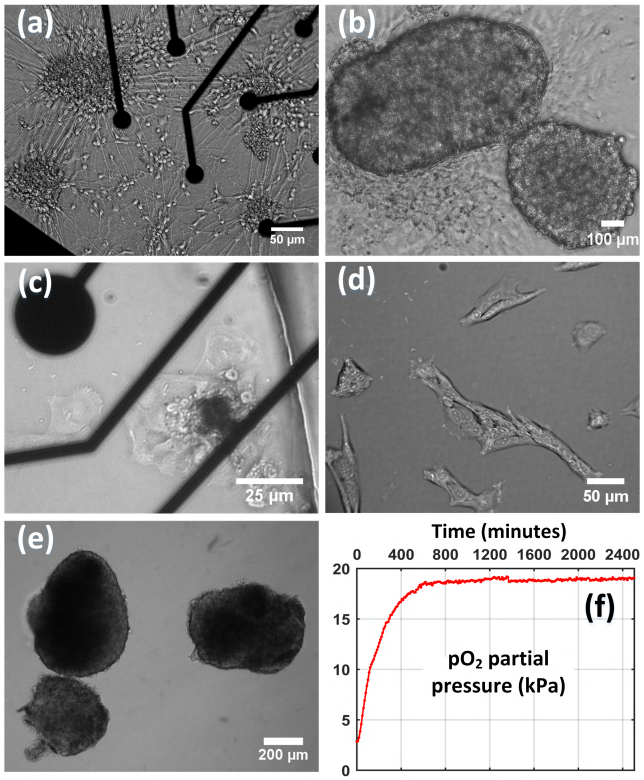

FIGURE 8. Modular microscopy images of live-cells captured on different occasions of corresponding cell culture. (a) neurons on micro electrode array (MEA) plate. (b,c) movie snapshots of a large and small (few cells) cluster of beating cardiomyocytes respectively on glass and MEA plate. (d) cropped view of MEF on glass. (e) beating cardiomyocytes on fluorescent pO_2 sensing film in simultaneous hypoxia and TLM study (upright configuration). (f) an excerpt from the corresponding pO_2 measurement log [18].

C. LONG-TERM PERFORMANCE AND STABILITY

In order to determine the focus consistency, TLM images (16 bit, 2 images/minute, camera: FL3-U3-13E4C-C) of the fixed specimen (FIGURE 6a) was captured for >12 hours and the focus was numerically computed (FIGURE 7a), as previously described in [56]. In Trial 1, images were captured at room temperature without ITO heating and the frame support pillar (FIGURE 7a inset). In Trial 2, the frame support was provided and the plate was set to 37°C for the whole duration. The mean focus drift is ∼0.9 % in Trial 1 but it is as low as only 0.2 % in Trial 2 in over 12 hours TLM. Additionally, the optical flow - the overall physical deformation between the first and last images in TLM image series - was estimated using Lucas-Kanade method based on the spatial and temporal image gradients [57]. In FIGURE 7b and FIGURE 7c the optical flow velocity vectors estimated are illustrated in corresponding images. Here, the green circles illustrate the points where the flow (movement) is computed, while the green lines represent the flow vector magnitude and direction. Additionally, the flow field parameters estimated are plotted in FIGURE 7d. Lucas-Kanade method is efficient to track apparent pixel translations in xy-plane which in turn helps to numerically estimate the xy drift of the imaging system. With a constant temperature supply and platform support, the x,y velocity components, though not zero, are much smaller (FIGURE 7d).

D. LIVE-CELL MICROSCOPY

Unstained living cells (neurons, fibroblasts and cardiomyocytes) were imaged independently on different occasions of cell culturing and the example snapshots are shown in (FIGURE 8). These trials were designed to iteratively fine-tune the optical performance of the microscopy module and, the suitability of the system for live-cell imaging was subsequently confirmed. The system, in different configurations, is reproducible and has been successfully utilized for long-term TLM observations. For example, the inverted configuration was implemented in order to study A) the alignment and

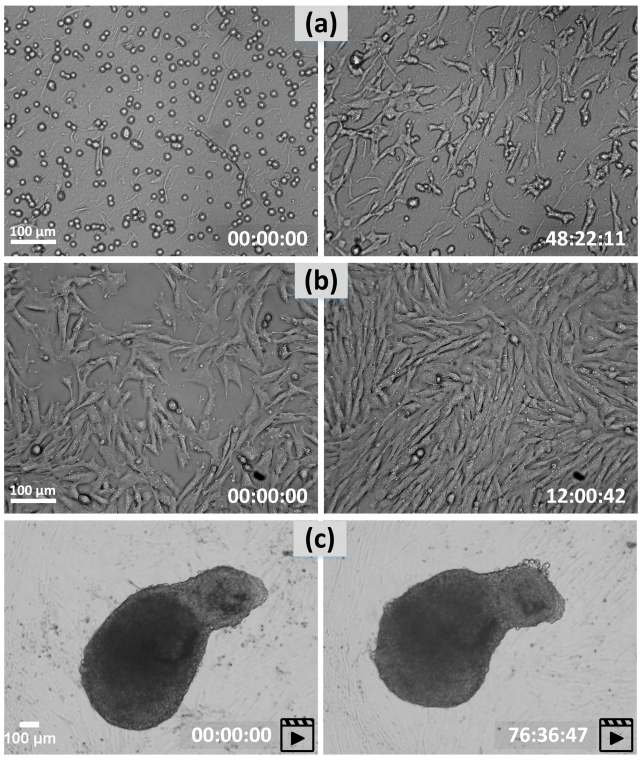

FIGURE 9. **Long-term image and video TLM (time- lapse microscopy) with modular microscope in inverted configuration in different contexts. (a) studying the alignment and proliferation capacity of fibroblasts (MEF) on nanocellulose (see Video 1) (b) the spatial and temporal expansion dynamics of fibroblast on glass at various conditions (see Video 2). (c) extended beating monitoring of cardiomyocytes.**

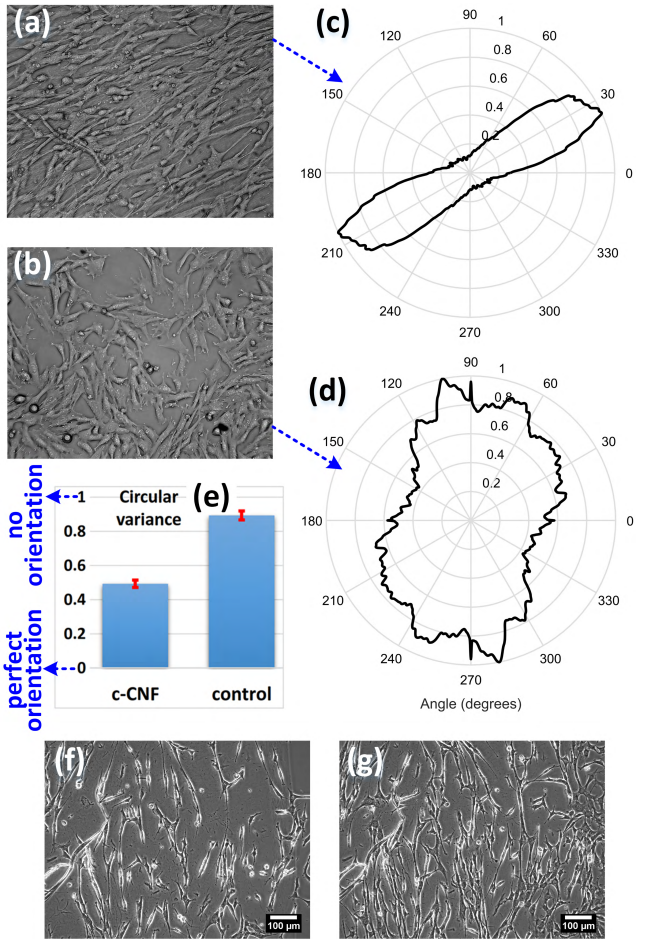

FIGURE 10. **Image based orientation analysis of fibroblast (MEF) on cellulose (c-CNF) surfaces using Cytospectre (a,b) Example images of oriented MEF on c-CNF and on control glass surface (showing no dominant orientation). (c,d) Cell orientation plots analysed with Cytospectre. (e) Average circular variance (CV) describing the degree of orientation of cells on cellulose and control plate (f,g) Reference images (20X) captured with a commercial device (Cell-IQ, CM Technologies, Finland) comparable to our system after 24 h and 48 h incubations. With our system, both the cells and cellulose fibres are equally visible and the cell boundaries are comparatively well identifiable.**

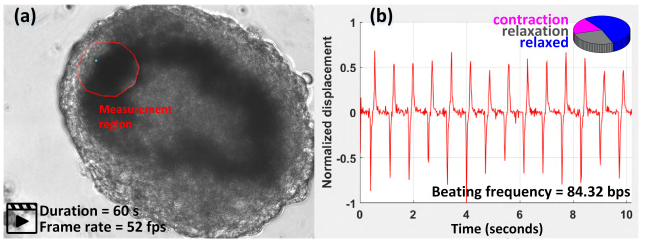

FIGURE 11. **(a) Snapshot from the movie of the beating cardiomyocytes on MEA. (b) a 10 s directional beating signal analysed [54] from the region marked by the red polygon with the light blue dot showing the point of reference. The downward peak signifies contraction velocity and the upward peak the relaxation velocity. The inset pie chart: percentage distribution of mechanobiological timing [ms] from the movie analysis. [see also the Video 3 for the full beating profile].**

proliferation capacity of MEF on nanocellulose (FIGURE 9a, Video 1), B) the spatial and temporal expansion dynamics of fibroblast on glass at various conditions (FIGURE 9b, Video 2) C) cardiomyocyte (CM) beating behaviour under normal incubation (FIGURE 9c) and hypothermic stressing conditions. The analysis results of A and C are presented in the next two chapters. With the upright microscopy, several simultaneous TLM and sensor logging (cell area temperature, pO_2) were performed. FIGURE 8e shows an example snapshot of a beating cluster on fluorescent pO_2 sensing film from a cardiac hypoxic stressing study. An excerpt from the corresponding pO_2 data log is shown in FIGURE 8f. See [18] for simultaneous pO_2 sensing and CM beating signal analysis from recorded videos using the developed modular system.

1) FIBROBLAST ON CATIONIC CELLULOSE NANOFIBER

In the MEF – TLM study, images were saved in RAW or PNG format (16 bit, camera full resolution [no binning]) and typically at a rate of two images per minute. The TLM program keeps the Illumination off at all times except at times of microscopy logging and during a few seconds of LED stabilization time. The TLM snapshots were later combined into a movie (See Video 1), which showed the temporal and spatial evolution of cells and their alignment in line with the structures of nanocellulose. TLM images (eg. FIGURE 10a) collected at the end of the orientation procedures were analysed with CytoSpectre. No dominating orientation was detected on the control glass surface (FIGURE 10b), and the

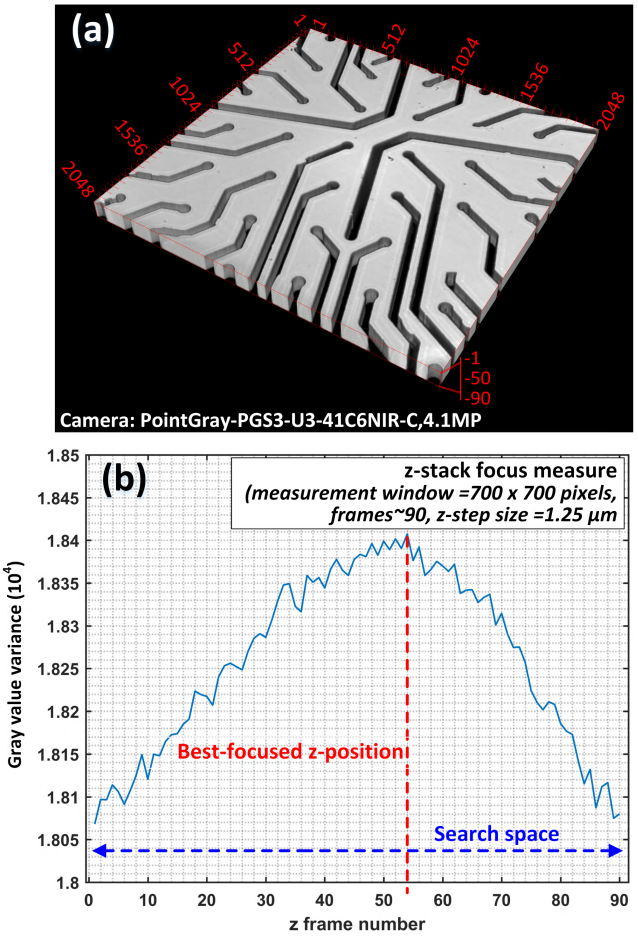

FIGURE 12. Z-stack images (upright) of MEA microelectrode array. (a) A pseudo 3D volume visualization of the stack created with imageJ 3D viewer (b) measurement of focus in the z-stack frames. The red dotted line position shows the best-focused plane where the gray level variance is the highest.

average (three samples) CV computed is 0.92 (FIGURE 10d). On the c-CNF surface (FIGURE 10a), the orientation is clearly visible and the average (eight samples) CV is 0.49 (FIGURE 10c). A similar cell experiment was performed in a commercial long-term live-cell imaging system providing stable incubation at 37°C and 5% CO_2 (Cell-IQ, CM Technologies, Finland). Cells were incubated in Cell-IQ for 48 ± 2 h, while images were recorded. Example images recorded with Cell IQ after 24 h and 48 h are presented for comparison in FIGURE 10f,g. On the contrary, microscopy images with our system show cell boundaries reasonably well and the cells and c-CNF fibres can be visualized better simultaneously.

2) CARDIOMYOCYTES AND VIDEO BASED SIGNAL ANALYSIS

Movies of the beating cardiomyocytes were recorded for TLM durations ranging from a few hours to several days, depending on the objective of the experimental study. Typically, 1-minute movies were recorded once per hour in an 8 bit uncompressed avi format (40-60 fps, 644x480 pixels) and the mechanobiological properties were analysed. A 10-second beating signal analysed from a movie of a CM cluster on MEA (FIGURE 11a) as part of a temperature stressing experiment is shown in FIGURE 11b (see also Video 3). The beating rate is estimated to be 84 beats per minute with average mechanobiological timings 19 ms, 27 ms, 54 ms for contraction, relaxation and relaxed state respectively.

E. Z-STACK ACQUISITION

The z-stack acquisition scheme is also being tested. An example stack of microelectrode array as a pseudo 3D volume (3D viewer/imageJ) is shown in FIGURE 12a. Around 90 frames, each in 1.25 μm step was captured with upright configuration using the 4.1MP camera. In FIGURE 12b, the numerically computed focus from each frame is plotted [56]. The red dotted line indicates the frame with the highest gray level variance corresponding to the best-focused plane in the z search space.

V. DISCUSSION AND CONCLUSION

We present a compact portable live-cell imaging system with a novel architecture and modular sub-assemblies for simultaneous long-term cell imaging, chemical sensing, multisite electrophysiological recording and stimulation. The system has been characterised and tested with histological (stained) and biological live (unstained) specimens. The microscopy performance (resolution and contrast) is comparable to that of traditional phase contrast biological microscopes. Several short and long-term TLM recordings have been performed with neurons, cardiomyocytes and fibroblasts. Successfully completed long-term TLM studies include monitoring the alignment and proliferation of mouse embryonic fibroblasts on nanocellulose, the beating behaviour of human based cardiomyocytes under normal and stressed (hypothermic) environments, and the evaluation of stability and suitability of sensors (temperature sensitive plates, optical pO_2, and pH). Although the imaging unit was developed primarily for our benchtop modular bioreactor, the digital microscope design as such can be used for building custom in-situ microscopes for various applications, where a traditional microscope is not acceptable or affordable. The system is fully functional, and supported with custom software allowing one to control the camera settings and TLM parameters and save the data as independent images or high-fps movies. Further, the software also supports logging data from sensors (temperature, pO_2, pH etc.) connecting via USB and adjusting the ITO-cell heater temperature in real time or in future time points. One major attribute of our system is its invert - upright convertibility, which facilitates a unique set-up for conventional spatiotemporal cell imaging in two directions, and provides flexibility to integrate subassemblies or systems for additional measurement tasks.

Notably, the image plane is reasonably planar without barrel or pincushion distortions. The microscope does not suffer from focusing issues nor display colour halos, evidently owing to the existence of a well-defined image plane without noticeable chromatic and spherical aberrations. This was

partly expected when highly corrected objectives were chosen. Nevertheless, vignetting - the peripheral image darkening [58]- could be a concern, if a camera with a large (>2/3 -inch) sensor is selected or the flange distance is too short in the assembly. For the used cameras', the pixel size (3.75-5 um) is adequate (Nyquist sampling) to preserve the spatial resolution of the objectives since the diffraction Airy disk size of objectives are 23.54 μm (=10X $\times$ 0.61 $\times$ 546 nm/0.1415NA), 23.84 μm and 43 μm for 10X, 20X and 40X, respectively. Enhancing magnification using extension tubes is inexpensive, as it requires no extra optics. They can be mounted without disturbing the objectives, either independently or as a stack of several tubes to produce higher magnification. However, the maximum usable magnification by this approach has a limit, depending on the objective type and NA, beyond which the image looks bigger but the contrast and quality are poor [59]. Calibration of magnification/FOV for each objective - extension tube combination is also necessary, as magnification cannot be directly deduced. This is especially true if the actual scale is to be marked on the captured images. As the objective lenses are implemented slightly differently than in a benchtop microscope, the full advantage of original NA of the objectives gets compromised. However, this enhances the working distance in our system which is advantageous in many instances. Measurements of focus stability and optical flow suggest the system is mechanically stable over tens of hours with a frame support pillar and with a constant heater temperature. However, addressing the focus drift during cell culturing even at a constant temperature is not easy and straightforward especially when the viscosity and refractive index of the culture medium are prone to variations due to evaporation and biochemical changes by the growth and expansion of cells. Currently, manual focus correction is carried out once a day, but it could be automated in future by including a dedicated hardware. A basic z-stack acquisition scheme has been tested, but more experiments using live specimens, and further coding of the data acquisition program is needed for controlling the camera module in the right increments and to synchronize the camera acquisition. If the z-stack acquisition is implemented efficiently with the TLM, it could also be useful for periodically correcting the focus drift as described in [60] without using any dedicated hardware.

Cell culture experiments with integrated MEA amplifier for simultaneous pO_2, electrophysiological recording and TLM are scheduled for later this year. At present, the system is not equipped with vibration mitigation measures. Integrating a benchtop vibration isolation platform would be certainly advantageous for reducing noise and vibrations in high fps movie recordings. The long-term objective of this research is to develop a versatile incubator-independent benchtop bioreactor to automate cell-culture experiments and simultaneously expand its range of possibilities for combined electrical, optical and electrophysiological measurements. Intended applications include *in-vitro* characterization and differentiation of various cell types, chemical measurements and drug screening. A high quality TLM with these studies can undeniably yield an absolute or a more holistic view of the dynamic activity in complex cellular microenvironment.

The ergonomic future-proof system design brings about a further customizable platform for testing diverse optical components and measurement systems. Integration of a non-contact pH measurement module as previously described in [19] and [61] as part of the forthcoming perfusion module or as a completely new CMOS module for 2D pH maps is also under consideration. We envision a widespread application of our digital microscope assembly and portable modular system for long-term *in-vitro* monitoring in various fields of life sciences.

ACKNOWLEDGMENT

We gratefully acknowledge Olli Tanhuanpää, Verho Jarmo, Jouni Niemelä and Antti-Juhana Mäki, Tampere University of Technology, for technical assistance, Panu Lahtinen, VTT Technical Research Centre of Finland Ltd, for providing nanocellulose and Tanja Paavilainen, University of Tampere, for providing neurons for trial imaging.

REFERENCES

[1] S. L. Shorte and F. Frischknecht, *Imaging cellular and molecular biological functions*. Berlin, Germany: Springer-Verlag, 2007.

[2] M. M. Frigault, J. Lacoste, J. L. Swift, and C. M. Brown, "Live-cell microscopy—Tips and tools," *J. Cell Sci.*, vol. 122, no. 6, pp. 753–767, 2009.

[3] Nikon. *Live-Cell Imaging and Perfusion Chambers MicroscopyU*. Accessed: Aug. 1, 2017. [Online]. Available: https://www.microscopyu.com/references/live-cell-imaging-and-perfusion-chambers

[4] Okolab. *Microscope Enclosures*. Accessed: Aug. 1, 2017. [Online]. Available: http://www.oko-lab.com/live-cell-imaging/cage-incubator/temperature-unit

[5] A. G. Godin, B. Lounis, and L. Cognet, "Super-resolution microscopy approaches for live cell imaging," *Biophys. J.*, vol. 107, no. 8, pp. 1777–1784, Oct. 2014.

[6] D. Jin *et al.*, "Compact wireless microscope for *in-situ* time course study of large scale cell dynamics within an incubator," *Sci. Rep.*, vol. 5, Dec. 2015, Art. no. 18483.

[7] Y. S. Zhang *et al.*, "A cost-effective fluorescence mini-microscope for biomedical applications," *Lab Chip*, vol. 15, no. 18, pp. 3661–3669, 2015.

[8] M. B. Esch, T. L. King, and M. L. Shuler, "The role of body-on-a-chip devices in drug and toxicity studies," *Annu. Rev. Biomed. Eng.*, vol. 13, no. 1, pp. 55–72, Aug. 2011.

[9] N. S. Bhise *et al.*, "Organ-on-a-chip platforms for studying drug delivery systems," *J. Control. Release*, vol. 190, pp. 82–93, Sep. 2014.

[10] A. M. Ghaemmaghami, M. J. Hancock, H. Harrington, H. Kaji, and A. Khademhosseini, "Biomimetic tissues on a chip for drug discovery," *Drug Discovery Today*, vol. 17, nos. 3–4, pp. 173–181, 2012.

[11] C. Moraes, G. Mehta, S. C. Lesher-Perez, and S. Takayama, "Organs-on-a-Chip: A focus on compartmentalized microdevices," *Ann. Biomed. Eng.*, vol. 40, no. 6, pp. 1211–1227, Jun. 2012.

[12] D. Huh, G. A. Hamilton, and D. E. Ingber, "From 3D cell culture to organs-on-chips," *Trends Cell Biol.*, vol. 21, no. 12, pp. 745–754, Dec. 2011.

[13] S. N. Bhatia and D. E. Ingber, "Microfluidic organs-on-chips," *Nature Biotechnol.*, vol. 32, no. 8, p. 760, 2014.

[14] Y. Sei, K. Justus, P. LeDuc, and Y. Kim, "Engineering living systems on chips: From cells to human on chips," *Microfluidics Nanofluidics*, vol. 16, no. 5, pp. 907–920, May 2014.

[15] J. P. Wikswo, "The relevance and potential roles of microphysiological systems in biology and medicine," *Exp. Biol. Med.*, vol. 239, no. 9, pp. 1061–1072, 2014.

[16] Š. Selimović, M. R. Dokmeci, and A. Khademhosseini, "Organs-on-a-chip for drug discovery," *Current Opinion Pharmacol.*, vol. 13, no. 5, pp. 829–833, 2013.
[17] M. L. Moya and S. C. George, "Integrating *in vitro* organ-specific function with the microcirculation," *Current Opinion Chem. Eng.*, vol. 3, pp. 102–111, Mar. 2014.
[18] H. Välimäki *et al.*, "Fluorimetric oxygen sensor with an efficient optical read-out for *in vitro* cell models," *Sensors Actuators B, Chem.*, vol. 249, pp. 738–746, Oct. 2017.
[19] D. K. Rajan *et al.*, "Optical non-contact pH measurement in cell culture with sterilizable, modular parts," *Talanta*, vol. 161, pp. 755–761, Dec. 2016.
[20] I. Taurino *et al.*, "Platinum nanopetal-based potassium sensors for acute cell death monitoring," *RCS Adv.*, vol. 6, no. 46, pp. 40517–40526, 2016.
[21] I. Etaluma. *Lumascopes*. Accessed: Aug. 3, 2017. [Online]. Available: http://www.etaluma.com/products/about-lumascope-fluorescent-microscopes/
[22] E. BioScience. (2016). Real-time, quantitative live-cell analysis. IncuCyte ZOOM System. Accessed: Aug. 3, 2017. [Online]. Available: https://www.essenbioscience.com/media/uploads/files/8000-0333-E00-IncuCyte_ZOOM_brochure.pdf
[23] J. H. Jung, C. Han, S. A. Lee, J. Kim, and C. Yang, "Microfluidic-integrated laser-controlled microactuators with on-chip microscopy imaging functionality," *Lab Chip*, vol. 14, no. 19, pp. 3781–3789, 2014.
[24] C. Han, S. Pang, D. V. Bower, P. Yiu, and C. Yang, "Wide field-of-view on-chip Talbot fluorescence microscopy for longitudinal cell culture monitoring from within the incubator," *Anal. Chem.*, vol. 85, no. 4, pp. 2356–2360, Feb. 2013.
[25] G. Zheng, S. A. Lee, Y. Antebi, M. B. Elowitz, and C. Yang, "The ePetri dish, an on-chip cell imaging platform based on subpixel perspective sweeping microscopy (SPSM)," *Proc. Nat. Acad. Sci. USA*, vol. 108, no. 41, pp. 16889–16894, Oct. 2011.
[26] J. El-Ali, P. K. Sorger, and K. F. Jensen, "Cells on chips," *Nature*, vol. 442, no. 7101, pp. 403–411, Jul. 2006.
[27] W. Bishara *et al.*, "Holographic pixel super-resolution in portable lensless on-chip microscopy using a fiber-optic array," *Lab Chip*, vol. 11, no. 7, pp. 1276–1279, Apr. 2011.
[28] A. Greenbaum, U. Sikora, and A. Ozcan, "Field-portable wide-field microscopy of dense samples using multi-height pixel super-resolution based lensfree imaging," *Lab Chip*, vol. 12, no. 7, pp. 1242–1245, Apr. 2012.
[29] W. Bishara, T.-W. Su, A. F. Coskun, and A. Ozcan, "Lensfree on-chip microscopy over a wide field-of-view using pixel super-resolution," *Opt. Exp.*, vol. 18, no. 11, pp. 11181–11191, May 2010.
[30] Z. F. Phillips, M. Chen, and L. Waller, "Single-shot quantitative phase microscopy with color-multiplexed differential phase contrast (cDPC)," *PLoS ONE*, vol. 12, no. 2, p. e0171228, Feb. 2017.
[31] A. Ozcan and E. McLeod, "Lensless imaging and sensing," *Annu. Rev. Biomed. Eng.*, vol. 18, no. 1, pp. 77–102, Jul. 2016.
[32] A. Greenbaum *et al.*, "Imaging without lenses: achievements and remaining challenges of wide-field on-chip microscopy," *Nature Methods*, vol. 9, no. 9, pp. 889–895, 2012.
[33] B. A. Flusberg, E. D. Cocker, W. Piyawattanametha, J. C. Jung, E. L. M. Cheung, and M. J. Schnitzer, "Fiber-optic fluorescence imaging," *Nature Methods*, vol. 2, no. 12, pp. 941–950, Dec. 2005.
[34] M. Pierce, D. Yu, and R. Richards-Kortum, "High-resolution fiber-optic microendoscopy for *in situ* cellular imaging," *J. Vis. Exp.*, vol. 47, p. e2306, Jan. 2011.
[35] D. Shin, M. C. Pierce, A. M. Gillenwater, M. D. Williams, and R. R. Richards-Kortum, "A fiber-optic fluorescence microscope using a consumer-grade digital camera for *in vivo* cellular imaging," *PLoS ONE*, vol. 5, no. 6, p. e11218, Jun. 2010.
[36] F. Helmchen, "Miniaturization of fluorescence microscopes using fibre optics," *Experim. Physiol.*, vol. 87, no. 6, pp. 737–745, Nov. 2002.
[37] K.-B. Sung, C. Liang, M. Descour, T. Collier, M. Follen, and R. Richards-Kortum, "Fiber-optic confocal reflectance microscope with miniature objective for *in vivo* imaging of human tissues," *IEEE Trans. Biomed. Eng.*, vol. 49, no. 10, pp. 1168–1172, Oct. 2002.
[38] Y. Ando *et al.*, "*In vivo* bioluminescence and reflectance imaging of multiple organs in bioluminescence reporter mice by bundled-fiber-coupled microscopy," *Biomed. Opt. Exp.*, vol. 7, no. 3, pp. 963–978, 2016.
[39] X. Meng *et al.*, "Smartphone based hand-held quantitative phase microscope using the transport of intensity equation method," *Lab Chip*, vol. 17, no. 1, pp. 104–109, 2017.
[40] A. Skandarajah, C. D. Reber, N. A. Switz, and D. A. Fletcher, "Quantitative imaging with a mobile phone microscope," *PLoS ONE*, vol. 9, no. 5, p. e96906, 2014.
[41] Y. S. Zhang *et al.*, "Hybrid microscopy: Enabling inexpensive high-performance imaging through combined physical and optical magnifications," *Sci. Rep.*, vol. 6, Mar. 2016, Art. no. 22691.
[42] M. P. Walzik *et al.*, "A portable low-cost long-term live-cell imaging platform for biomedical research and education," *Biosens. Bioelectron.*, vol. 64, pp. 639–649, Feb. 2015.
[43] G. O. F. Parikesit, M. Darmawan, and A. Faisal, "Quantitative low-cost webcam-based microscopy," *Opt. Eng.*, vol. 49, no. 11, p. 113205, Nov. 2010.
[44] J. Kreutzer *et al.*, "Structured PDMS chambers for enhanced human neuronal cell activity on MEA platforms," *J. Bionic Eng.*, vol. 9, no. 1, pp. 1–10, Mar. 2012.
[45] J. Kreutzer, L. Ylä-Outinen, A. J. Mäki, M. Ristola, S. Narkilahti, and P. Kallio, "Cell culture chamber with gas supply for prolonged recording of human neuronal cells on microelectrode array," *J. Neurosci. Methods*, vol. 280, pp. 27–35, Mar. 2017.
[46] D. B. Murphy, *Fundamentals of Light Microscopy and Electronic Imaging*, vol. 53. Hoboken, NJ, USA: Wiley, 2012.
[47] J. R. Lakowicz, *Principles of Fluorescence Spectroscopy*, 3rd ed. New York, NY, USA: Springer, 2006.
[48] D. Georg. *Camera GUI (Version 1.0)*. Accessed: Aug. 1, 2017. [Online]. Available: https://se.mathworks.com/matlabcentral/fileexchange/35919-cameragui
[49] MathWorks MATLAB Hardware Team. (2014). *MATLAB Support Package for Arduino Hardware (Version 1.1), MATLAB Central File Exchange*. Accessed: Apr. 1, 2014. [Online]. Available: https://se.mathworks.com/matlabcentral/fileexchange/47522-matlab-support-package-for-arduino-hardware
[50] MathWorks Image Acquisition Toolbox Team. *Image Acquisition Toolbox Support Package for Point Grey Hardware (Version 1.1)*. Accessed: Aug. 1, 2017. [Online]. Available: https://se.mathworks.com/matlabcentral/fileexchange/45178-image-acquisition-toolbox-support-package-for-point-grey-hardware
[51] A. Skogberg, A.-J. Mäki, P. Lahtinen, and P. Kallio, "Cellulose nanofiber alignment using evaporation-induced droplet-casting, and cell alignment on aligned nanocellulose surfaces," *Biomacromolecules*, vol. 18, no. 12, pp. 3936–3953, 2017.
[52] A. L. Lahti *et al.*, "Model for long QT syndrome type 2 using human iPS cells demonstrates arrhythmogenic characteristics in cell culture," *Disease Models Mech.*, vol. 5, no. 2, pp. 220–230, Mar. 2012.
[53] K. Kartasalo *et al.*, "CytoSpectre: A tool for spectral analysis of oriented structures on cellular and subcellular levels," *BMC Bioinf.*, vol. 16, no. 1, p. 344, Dec. 2015.
[54] A. Ahola, A. Kiviaho, K. Larsson, M. Honkanen, K. Aalto-Setälä, and J.Hyttinen, "Video image-based analysis of single human induced pluripotent stem cell derived cardiomyocyte beating dynamics using digital image correlation," *Biomed. Eng. Online*, vol. 13, no. 1, p. 39, 2014.
[55] I. T. Young, R. Zagers, L. J. van Vliet, J. Mullikin, F. Boddeke, and H. Netten, "Depth-of-focus in microscopy," in *Proc. 8th Scandin. Conf. Image Anal.*, 1993, pp. 493–498.
[56] S. Pertuz, D. Puig, and M. A. Garcia, "Analysis of focus measure operators for shape-from-focus," *Pattern Recognit.*, vol. 46, no. 5, pp. 1415–1432, 2013.
[57] Y. David. (2010). *Affine Optic Flow (Version 1.3), MATLAB Central File Exchange*. Accessed: Mar. 3, 2017. [Online]. Available: https://se.mathworks.com/matlabcentral/fileexchange/27093-affine-optic-flow?focused=6019470&tab=example
[58] F. J. W.-M. Leong, M. Brady, and J. O. D. McGee, "Correction of uneven illumination (vignetting) in digital microscopy images," *J. Clin. Pathol.*, vol. 56, no. 8, pp. 619–621, Aug. 2003.
[59] Nikon. *Useful Magnification Range MicroscopyU*.Accessed: Aug. 10, 2017. https://www.microscopyu.com/microscopy-basics/useful-magnification-range
[60] M. Kreft, M. Stenovec, and R. Zorec, "Focus-drift correction in time-lapse confocal imaging," *Ann. New York Acad. Sci.*, vol. 1048, no. 1, pp. 321–330, Jun. 2005.
[61] D. K. Rajan *et al.*, "Monitoring pH, temperature and humidity in long-term stem cell culture in CO2 incubator," in *Proc. IEEE Int. Symp. Med. Meas. Appl. (MeMeA)*, May 2017, pp. 470–474.

DHANESH KATTIPPARAMBIL RAJAN received the M.Sc. degree (Tech.) in biomedical engineering from the Tampere University of Technology (TUT), Finland, in 2008, where he is currently pursuing the D.Sc. degree with BioMediTech Institute. He was with the photolithography facility at TUT for four years. He is currently a Research Scientist with BioMediTech Institute and the Faculty of Biomedical Sciences and Engineering, TUT, where he develops compact-modular imaging and optical measurement techniques and systems.

JOOSE KREUTZER received the B.Eng. degree in electrical and electronic engineering from the University of Sunderland, Sunderland, U.K., in 2003, and the M.Sc. degree in electrical engineering from the Tampere University of Technology (TUT), Tampere, Finland, in 2005. He is currently a Research Scientist with the Micro and Nanosystems Research Group, BioMediTech Institute, and the Faculty of Biomedical Sciences and Engineering, TUT. His current research interests include microfabrication, microfluidics, and their applications in biomedical engineering, especially for stem cell-based bioengineering.

HANNU VÄLIMÄKI received the M.Sc. degree in electrical engineering from the Tampere University of Technology (TUT), Tampere, Finland, in 1996. He was a Research Scientist in the field of acoustical and optical sensors with the VTT Technical Research Centre of Finland, Tampere, until 2013. He is currently with the BioMediTech Institute and Faculty of Biomedical Sciences and Engineering, TUT, where he develops optical sensing technologies for cell culturing applications.

MARI PEKKANEN-MATTILA received the Ph.D. degree in stem cell and tissue engineering from the University of Tampere, Finland, in 2011. Her research interests include human induced pluripotent stem cells, cell differentiation, and disease modeling of human genetic cardiac diseases.

ANTTI AHOLA received the master's degree in biomedical engineering from the Tampere University of Technology, Finland, in 2010. He is currently pursuing the D.Sc. degree. His research interests include cardiomyocyte biomechanics, video microscopy, and image analysis.

ANNE SKOGBERG received the master's degree in cell and tissue engineering from the University of Tampere, Finland, in 2010. She is currently pursuing the Ph.D. degree with the Tampere University of Technology, Finland. Her research interests include nanocellulose and its utilization in biomedical applications.

KATRIINA AALTO-SETÄLÄ received the M.D. degree. She is currently a Professor of physiology with the Faculty of Medicine and Life Sciences, University of Tampere, and a Cardiologist with the Heart Hospital, Tampere University Hospital, Finland. She is an Invasive Cardiologist and is in charge of the Genetic Cardiac Outpatient Clinic, Heart Hospital. She was involved in human genetic cardiac diseases, such as genetic arrhythmias and atherosclerosis with the help of induced pluripotent stem cell technology. The main aim of the research group is to learn more about the basic pathology of the genetic diseases as well as to test current and new pharmaceutical agents to correct the abnormalities. Her research group in collaboration with researchers at the Tampere University of Technology has also invented new methods to monitor and analyze the maturity and functionality of cardiomyocytes.

HEIMO IHALAINEN started teaching measurement technology at the Tampere University of Technology in 1974, and conducted research in multivariate signals in the 1990s. In 2000, he was involved in a new topic, measurement based on images, and though he is officially retired now, the topic motivates him to continue in the field.

PASI KALLIO received the M.S. degree in electrical engineering and the D.Tech. degree in automation engineering from the Tampere University of Technology (TUT), Tampere, Finland, in 1994 and 2002, respectively. Since 2008, he has been a Professor of automation engineering at TUT. He is currently the Vice Director of the Faculty of Biomedical Sciences and Engineering. He has authored over 130 articles and has over ten patent applications. His current research interests include microrobotics, microfluidics, and their automation in cell and tissue engineering, medical diagnostics, and soft material testing applications. He was a recipient of the Finnish Automation Society Award in 2009. He was the Chair of the IEEE Finland Section from 2012 to 2013.

JUKKA LEKKALA received the M.Sc. degree in electronics and the D.Sc. (Tech.) degree in biomedical engineering from the Tampere University of Technology (TUT), Tampere, Finland, in 1979 and 1984, respectively. From 1985 to 2001, he was a Senior Research Scientist with the VTT Technical Research Centre of Finland in different research units developing biosensor technology and sensor materials. In 1991, he was appointed as a Docent of bioelectronics with the University of Oulu and a Docent of biomedical engineering at TUT. Since 2002, he has been a Professor of automation engineering at TUT. He is currently a Professor Emeritus with the Faculty of Biomedical Sciences and Engineering (TUT-BMT). He has over 170 scientific publications and ten patents. His research interests include sensors, measurement systems, and biosensing.

PUBLICATION II

Cardiomyocytes: Analysis of temperature response and signal propagation between dissociated clusters using a novel video-based movement analysis software.

Rajan DK, Mäki, AJ, Pekkanen-Mattila M, Kreutzer J, Ryynänen T, Välimäki H, V Jarmo, Koivumäki JT, Ihalainen H, Aalto-Setälä K, Kallio P, Lekkala J.

Unpublished manuscript (Submitted to Journal IEEE Access in Nov. 2019**)**

'Date of publication xxxx 00, 0000, date of current version xxxx 00, 0000.

Digital Object Identifier 10.1109/ACCESS.2017.Doi Number

Cardiomyocytes: Analysis of temperature response and signal propagation between dissociated clusters using a novel video-based movement analysis software

Dhanesh Kattipparambil Rajan [1], Antti-Juhana Mäki [1], Mari Pekkanen-Mattila [2], Joose Kreutzer [1], Tomi Ryynänen [1], Hannu Välimäki [1], Jarmo Verho [1], Jussi T Koivumäki [3], Heimo Ihalainen [1], Katriina Aalto-Setälä [2,3,4,5], Pasi Kallio [1], Jukka Lekkala [1]

[1]Micro- and nanosystems research group, Faculty of Medicine and Health Technology, Tampere University, 33720 Tampere, Finland
[2]Heart group, Faculty of Medicine and Health Technology, Tampere University, 33520 Tampere, Finland
[3]Computational Biophysics and Imaging Group, Faculty of Medicine and Health Technology, Tampere University, 33520 Tampere, Finland
[4]Heart Hospital, Tampere University Hospital, 33520 Tampere, Finland
[5]Clinical Medicine, Faculty of Medicine and Health Science, Tampere University, 33520 Tampere, Finland

Corresponding author: Dhanesh K. Rajan (e-mail: dhanesh.kr@tuni.fi)

This work was supported by the Business Finland (former Finnish Funding Agency for Technology and Innovation (TEKES)) through Human Spare Parts 2 Project.

ABSTRACT Human induced pluripotent stem cell-derived cardiomyocytes (hiPSC-CMs) provide a great resource for functional cell and tissue models that can be applied in the heart research, pharmaceutical industry and the future regenerative medicine. While experimenting with the cell models, the precise control of the environmental parameters is important. Temperature is a fundamental parameter, and the acute effect of temperature on hiPSC-CM functions has previously been studied. This paper reports on long-term, systematic temperature response studies of hiPSC-CM cultures. The studies are carried out outside an incubator in a modular cell culturing system, combined with a temperature sensor plate (TSP) and a new beating analysis software (CMaN—cardiomyocyte function analysis tool). Temperature sensing at the actual cell location is challenging with bulky external sensors, but a TSP with resistive microsensors provides an effortless solution. Experimental results showed that temperature affects the hiPSC-CM beating frequency nonlinearly with a Q_{10} temperature coefficient value of ~2.2. Both the active (contraction) and passive (relaxation) movements are influenced by temperature, while the changes in relaxation times are larger than the contraction times. The contraction amplitudes, however, exhibited a greater spread of variation. We also present novel results of the visualization of hiPSC-CM contractile networking and a non-invasive image-based measurement of signal propagation between dissociated CM clusters. Compared to previously reported tools, CMaN is an advanced, easy-to-use robust software. It is faster, more sensitive, computationally less expensive and extracts six different signals of the contractile motion per processing, allowing typically at least one useful beating signal even in complex cases. The software also supports movement center detection and independent computation of the relaxation and contraction features.

INDEX TERMS Cardiomyocytes beating analysis software, Movement center detection, Cardiomyocytes temperature response, Nonlinear temperature dependency, Signal propagation between clusters

I. INTRODUCTION

The limited availability of primary human cardiomyocytes (CMs) poses challenges for basic and translational research. However, human induced pluripotent stem cells (hiPSC) can be differentiated into cardiomyocytes (hiPSC-CMs), providing an unlimited source of human CMs from healthy individuals, as well as from patients with genetic cardiac diseases. The hiPSC-CMs are a promising tool to study the

development of the heart and CMs, cardiac disease modelling, and future regenerative medicine applications [1], [2]. Furthermore, due to their human origins, they overcome the limitations of animal models in drug screening and toxicology [3]. In hiPSC-CM experimental models, levels of O_2, CO_2, pH, and osmolarity are crucial to maintain the functionalities of CMs. Temperature is another vital parameter, and it needs to be regulated carefully for maintaining normal cardiac activity without hyper/hypothermia [4], [5]. Hypothermia, in hibernation experiments, has been shown to cause metabolic injuries and damage to mammalian hearts [6]. Functional and cellular injuries and field potential alterations have also been reported in cultured CMs in hypothermia [7], [8]. In general, both hypo- and hyperthermia induce stress for the cells, which can generate various stress reactions [9]. Typical stress reactions are the expression of cold or heat shock proteins, which can adversely affect vital cell functions [10]–[12]. Hypothermia/rewarming (H/R) cycles are known to reduce myofilament Ca^{2+} sensitivity and affect cardiac action potentials (AP) and contractility [13], [14]. It has also been shown to affect the sarcomere length and cardiac muscle force generation in animal models [14]–[16]. H/R, in general, is poorly tolerated by the myocardium, and a complete picture of the underlying mechanism of H/R induced abnormalities is still elusive [14]. In laboratory settings, cells often experience temperature shock when moved outside the incubator or sometimes even inside the incubator. This can affect the cell attachment [17], pH [18], and the evaporation rate, all of which can generate undesired stimulations and experimental variations [18]–[21]. In extreme cases, temperature shocks can trigger oxidative damages [10] and initiate cell death [22]. Therefore, it is important that the temperature-related stress responses of hiPSC-CMs are recognised and carefully evaluated.

The temperature responses can be studied in different ways, e.g. by using standard electrophysiological methods, traction/atomic force microscopy, or video microscopy [23]. The decline in beating frequency has often been observed when CMs are taken from the incubator or studied at low temperatures [23]. However, precise temperature sensing from the cell area is usually challenging with bulky external sensors [24], and the temperatures reported in many earlier studies might correspond only approximately to the real temperatures experienced by the CMs, due to difficulties in attaching temperature sensors closely to the cells. Furthermore, to our knowledge, a systematic automated H/R temperature stressing and concurrent hiPSC-CM mechanobiological measurements have not been described yet. A few recent reports have described the excitation-contraction coupling in H/R and temperature-dependent beating synchronization [14], [25]. However, these studies were not conducted using hiPSC-CMs but with animal CMs. In this study, a long-term automated hiPSC-CM mechanobiological response to temperature is evaluated using a previously reported apparatus [26] and two new add-ons: 1) a temperature sensor plate (TSP) patterned with micro temperature sensors and 2) novel video-based mechanobiology analysis software (CMaN - cardiomyocyte function analysis tool). By integrating the TSP, traditional bulky thermometers are avoided; instead, CMs are directly cultured on the TSP. This enables accurate temperature sensing from the exact cell area. In our experimental data analysis, we found that the temperature dependence on hiPSC-CM beating frequency is nonlinear, which has not been reported earlier. We also computed the Q_{10} temperature coefficients [27] of hiPSC-CMs. Furthermore, we observed the contractile networking and beating synchronization of dissociated clusters and measured the propagation of action potential (AP) signal between them. This is the first paper reporting these events in hiPSC-CM cultures and their non-invasive measurements by image processing.

The new software CMaN is an easy-to-use tool and available as Supplementary material 1. Compared to conventional function analysis methods, such as Ca^{2+} transients, electrophysiology, sarcomere length profiling or AFM approaches [25], [28]–[31], CMaN is a non-invasive and robust tool. Properties of several similar tools have been compared elsewhere [23] and CMaN was tested against [32]–[34]. CMaN is faster, more sensitive, computationally less expensive and allows ROI (region of interest) selection. It can process videos from single cells or large clusters individually or batchwise and compared to [32]–[38], CMaN extracts six separate signals of the contractile motion per processing. The separate signals are especially advantageous when analysing videos with complex features, such as weak movements, overexposure and gamma variations due to uneven backgrounds. In addition, the signals from CMaN represent the contractile phenomena more exactly with both positive (upstroke) and negative (downstroke) segments, allowing one to compute not only the beating frequency but also the contraction and relaxation features separately. Further, the optional features to detect the movement area (cluster location) and movement center (region of the largest contractile motion) are also integrated.

II. MATERIALS AND METHODS

A. DEVICE

The portable cell culture system [26] and in-house microfabricated temperature sensor plate [24] are shown in FIGURE 1. The temperature sensor plate contains independently calibrated resistive micro temperature sensors, patterned with copper on glass plate, which act as the sensing transducers for localized temperature measurements from the cell area. The culture temperature is regulated with a programmable transparent indium tin oxide (ITO) heater [24]. Out of two microscopy options [26], inverted microscopy was utilized for recording the beating videos (camera: FL3-U3-13E4C-C (PointGray-FLIR

Systems). The culture was illuminated only during actual video recordings. The hiPSC-CMs were cultured in a mini incubator (FIGURE 1 b,c) made of a polydimethylsiloxane (PDMS) cell culture chamber [35] sealed with a transparent polycarbonate lid and polypropylene outer cover [39][40]. A gas mixture (5 % CO_2, 19 % O_2, 76 % N_2) supply around the PDMS chamber facilitated the stable gas environment [21]. The data flow and all the automated operations were controlled from a custom user interface scripted with MATLAB R2016B (MathWorks, Inc., Natick, MA, USA).

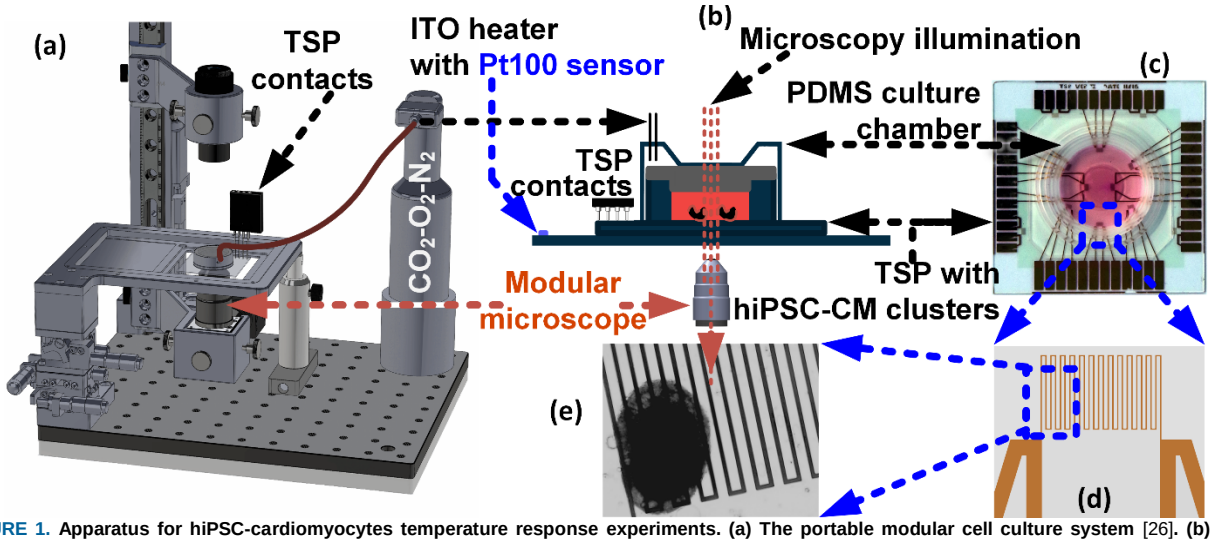

FIGURE 1. Apparatus for hiPSC-cardiomyocytes temperature response experiments. (a) The portable modular cell culture system [26]**. (b) Mini incubator. (c) Temperature sensor plate (TSP). The mini incubator is fixed on the TSP and the ITO heater stays underneath. (d, e) A beating hiPSC-CM cluster on one of the resistive temperature sensors on the TSP. Beating signals were analyzed non-invasively from the recorded cell videos using CMaN software.**

B. CELL CULTURING

The hiPSC-CMs were differentiated [41] by co-culturing iPS-cells with END-2 cells [42] from the healthy control in-house iPS-cell line (UTA.04602.WT). The beating hiPSC-CM clusters were mechanically excised from the differentiation cultures 20–30 days after differentiation initiation and plated on the TSP. Before plating, TSPs were first sterilized with 70 % ethanol and dried thoroughly before the mini incubator was attached to the plate. Plates were hydrophilized with fetal bovine serum (FBS, Lonza) and coated with 0.1 % gelatin type A (Sigma-Aldrich). For each plate, 3–4 beating hiPSC-CM clusters were plated. After plating, the hiPSC-CM clusters were cultured in a conventional incubator overnight in KnockOut Dulbecco's Modified Eagle Medium (KO-DMEM, Lonza) with 20 % FBS, 1 % nonessential amino acids (NEAA, Cambrex), 2 mM Glutamax (Invitrogen), and 50 U/ml penicillin/streptomycin (Lonza) before transferring them onto the modular system. In all prolonged cell culturing, the exhausted culture medium was replaced by fresh medium twice a week.

C. ANALYSIS SOFTWARE

A new video-based contractile movement analysis software (CMaN) was scripted (in MATLAB), evaluated, and utilized in this study. It is available as Supplementary material 1 with this article. In CMaN, the movement analysis is based on a novel approach of the computation of affine optic flow, which is an improved version of the classical Lucas-Kanade optical flow method that estimates the velocity of objects in consecutive images [43]. In affine optic flow, the flow field is parameterized [44], [45] by a six-dimensional vector to describe the x and y translation velocities (V_x, V_y); dilation i.e. the rate of expansion/shrinking (d); the rate of rotation around z axis (r); and the shear rates along x axis (s1) and y axis (s2, called as diagonal shear rate in [44]). These six parameters are estimated by computing the least squares on the spatial and temporal gray-level gradients in consecutive video frames [43], [44]. FIGURE 2a shows a screenshot from CMaN. The six signal components analyzed from an example single cell are shown in FIGURE 2c. Several mechanobiological [32], [37], [46] parameters—namely the beating frequency, relaxation time, contraction time, amplitude of beating, and beat-to-beat interval—can be estimated using one or more of the six signals. FIGURE 2b shows the table of these parameters analyzed from the single cell. Beating of both single cells and large clusters can be analyzed independently or batchwise. TABLE 1 summarizes the performance of CMaN in comparison with MUSCLEMOTION (v1-1beta.ijm) and SarcTrack (v 2019). See [47] and also FIGURE 4 for the measurement sensitivity. CMaN has already been applied elsewhere [48] for CM tracking in conductive hyaluronic acid hydrogels. An example case of beat rate increasing and decreasing drug response analyzed with CMaN is provided as Supplementary material 4 [49], [50].

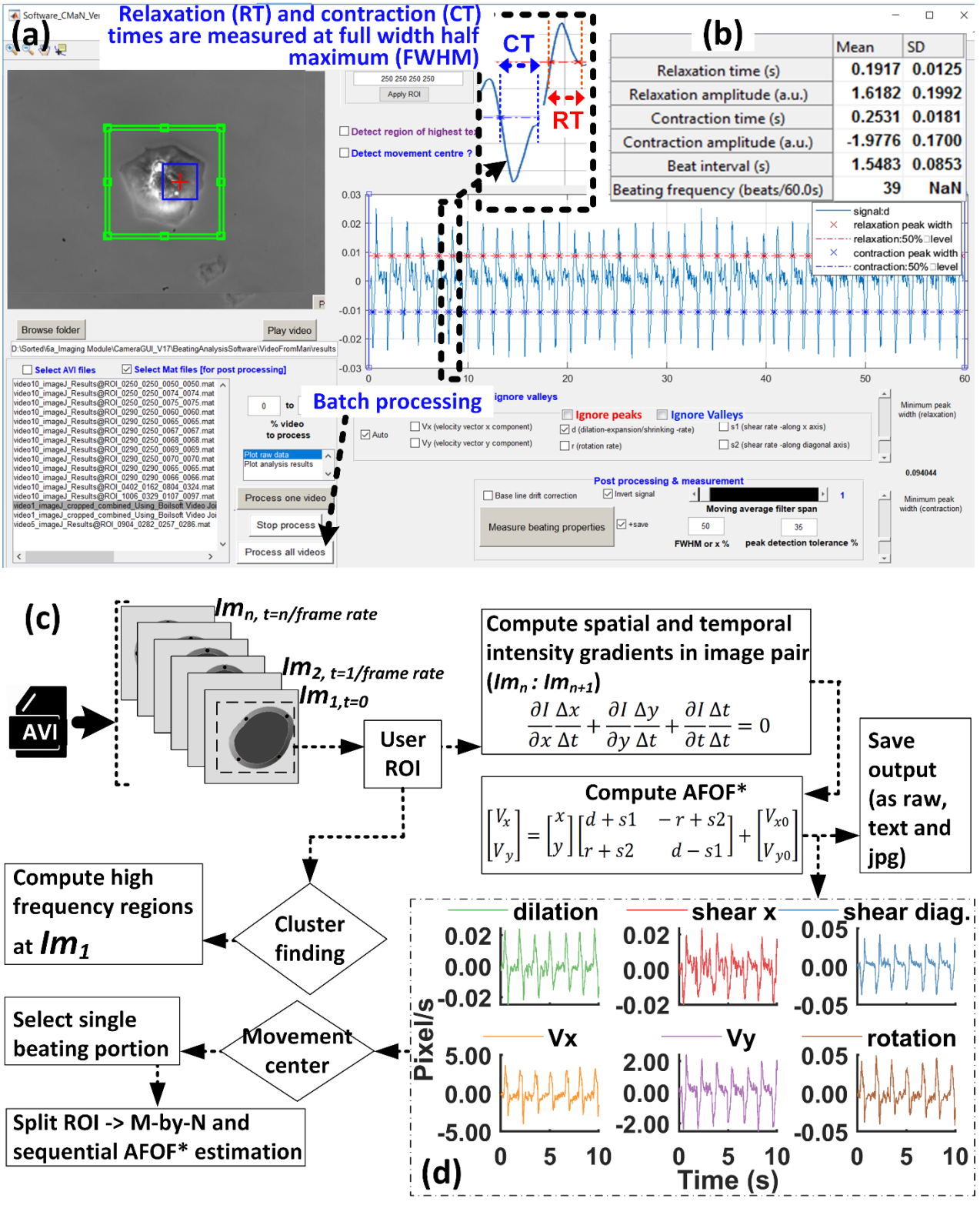

FIGURE 2. An advanced video-based movement analysis software CMaN (Cardiomyocyte function analysis tool). (a) Screenshot from the software user interface. In the upper left corner, the blue rectangle shows the movement center of a single cell cardiomyocyte whereas the green rectangle is the user-selected ROI. (b) The table of mechanobiology parameters estimated. (c) A schematic overview of the algorithm flow and the principle behind the *AFOF (affine optical flow) computation from image pairs. (d) The six signal components of the contractile motion extracted from the single cell beating video.

D. MOVEMENT CENTER DETECTION AND CLUSTER FINDING

One novel feature of CMaN is the movement center detection, which identifies the location of the most energetic movement area by detecting the region of the highest affine flow signal amplitude. This feature is illustrated in FIGURE 3a-b. The computation is started with a short portion of the beating signal containing at least one contraction-relaxation segment. Each image (either full frame or ROI) in the selected portion is first spatially sampled into M-by-N tiles (FIGURE 3b, where M and N are even). Then the affine flow is sequentially computed in all the tiles, and the tile with the highest signal amplitude (movement center) is identified. In FIGURE 3a, the blue dashed rectangle shows the movement center identified over the user-selected ROI (green rectangle). An example of beating signals from the ROI, and separately from the identified movement center and its neighborhoods, are shown in Supplementary material 5.One of the advantages of the movement center detection is that once the movement center is known, the best beating signal can be extracted by analyzing an area around the center.

The CMaN software also provides tools for CM cluster finding, based on identifying the locations of the highest textures (high frequency regions), which is illustrated in FIGURE 3c. The cells in the CM cluster generate high frequency textures (FIGURE 3c, left). First, the image is gamma corrected, smoothed and low pass filtered, which results in bright cluster boards against a black background (FIGURE 3c, middle). This is followed by an image convolution using a large area template on the whole frame (full frame/ROI). This way, multiple clusters can be distinguished from the surroundings. In FIGURE 3c, the blue rectangles show the three clusters identified. This feature provides means to automate both the cluster detection and beating analysis.

E. EXPERIMENTAL PROTOCOLS

The culturing temperature was programmatically adjusted from 37 ºC to 25 ºC and back to 37 ºC in 3 ºC steps, and beating videos were recorded. Overall, twelve CM clusters were studied in five separate cultures, see TABLE 2 for the experimental summary. The temperature was logged in every 60 s while the video was logged every 2 hours. When a new temperature was set, the culture was let to stabilize for 30 minutes before the video logging. Results are provided in the section **Automated temperature stressing**. The contractile synchronization measurements were carried out using cultures containing dissociated clusters, and the results from a six cluster case are provided in the section **Contractile synchronization of dissociated hiPSC-CM clusters.** Further, the plots of temporal reduction in beating frequency in cases of two long-term cultures are provided in the section **Temporal changes in beating at a constant**

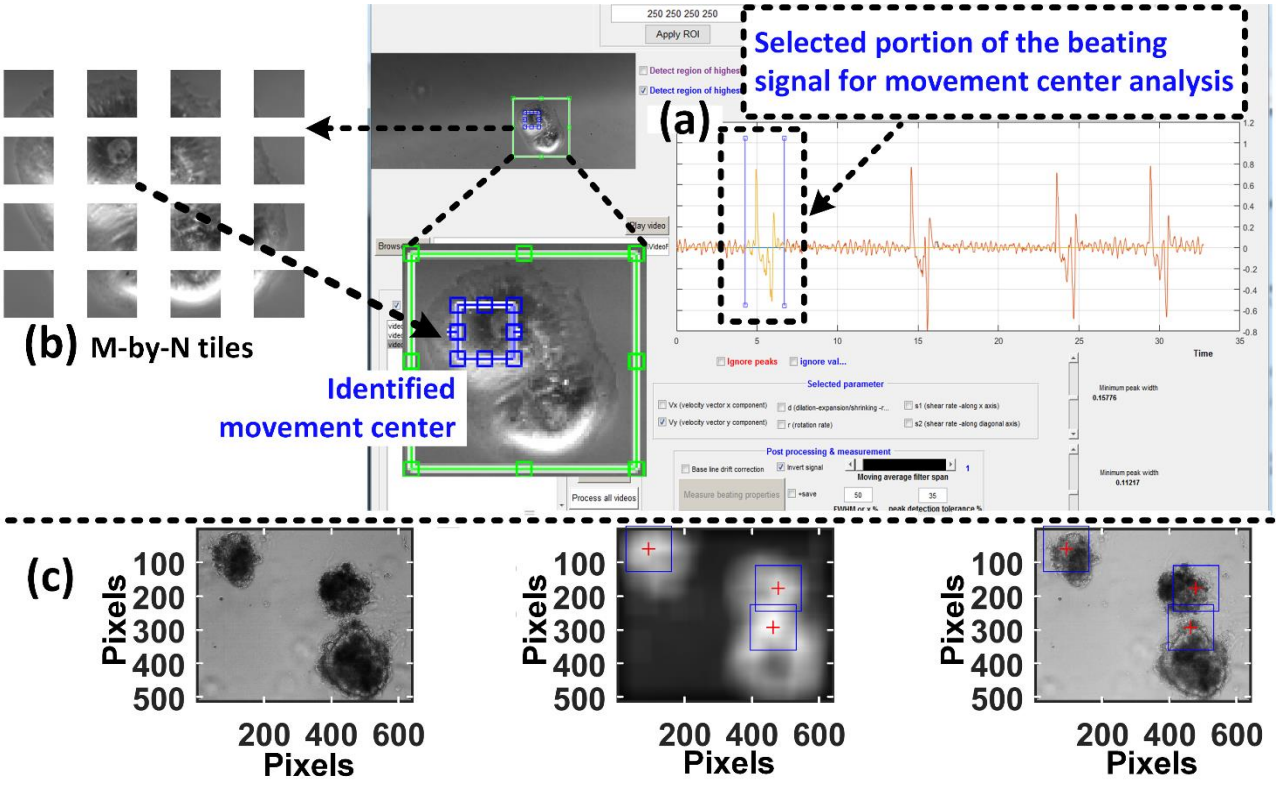

FIGURE 3. Movement center detection and cluster finding. (a-b) The signal portion of a contraction-relaxation region of a single cell selected for the movement center analysis. The frames from this portion are spatially split into M-by-N tiles for sequential affine flow processing. The detected movement center is marked with a dashed blue rectangle. (c) Three images (first frame, smoothed, and with identified clusters) from the cluster-finding feature. The blue rectangles show the identified clusters in the *whole frame*. *See also the* Supplementary material 5

TABLE 1. CMaN performance comparison against MUSCLEMOTION and SarcTrack using two computers (System1: 2.6 GHz processor and 32 GB RAM, System2: 2.7 GHz processor and 8GB RAM). †30 s long avi (60 fps, 640 x 512 pixels, 32 bit RGB, 1.64 GB size on SSD hard drive). †220 avi files (33 GB size on external SSD drive).

	MUSCLEMOTION	SarcTrack	CMaN	
Platform	Image J	MATLAB	MATLAB	
Algorithm principle	pixel intensity difference	fluorescent tag tracking	affine flow	
User ROI	no	no	yes	
Minimum ROI (pixels)	NA	NA	78 x 78	
Number of signals/processing	1	1	6	
Sensitivity	see FIGURE 4	NA	see FIGURE 4	
Processing time (~ minutes)			**System1**	**System2**
1 video†	3 (6 in dynamic mode)	350	1	1.3
Batch†2 of videos	129	7390	25	28

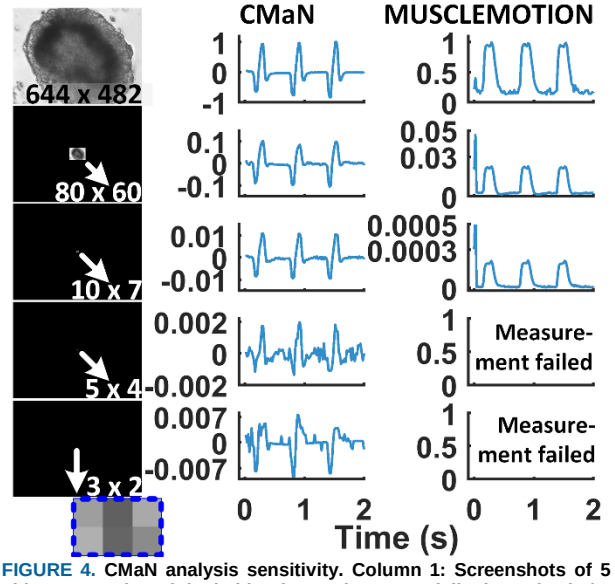

FIGURE 4. CMaN analysis sensitivity. Column 1: Screenshots of 5 videos. Here the original video (1st one) was spatially downsized 1/8, 1/64, 1/128 and 1/256 times to produce subsequent videos with reduced movement area. Columns 2 &3: Normalized signals (referenced to original signal, ROI: full frame which includes also black area in downsized videos) analyzed with CMaN and MUSCLEMOTION. CMaN apparently displayed better sensitivity.

temperature. The Q_{10} temperature coefficients were calculated using an exponential model, as $(BF_1/BF_2)*\exp(10/[T_1 - T_2])$ where BF_1 and BF_2 are beating frequencies at temperatures T_1 and T_2 [27]. **Statistical analysis:** Pairwise comparisons of mean parameter values at different temperatures were performed by one sided parametric t-test and $p < 0.05$ was regarded as statistically significant.

III. RESULTS

A. AUTOMATED TEMPERATURE STRESSING

The beating signals (V_y) analyzed from a representative cluster (C12, RNo-2) at three selected temperatures (37 °C, 31 °C, and 25 °C) as an overlay on corresponding beating

TABLE 2. Summary of temperature response experimentation

Cluster code	Temperature (range, step, [°C])	Number of replication cycles (code: RNo)	Logging interval TSP (minutes)	Logging interval Video (hours)
C1	37-25-37, 3	5	1	2
C2	37-25-37, 3	5	1	2
C3	37-25-37, 3	8	1	2
C4	37-25-37, 3	8	1	2
C5	37-25-37, 3	8	1	2
C6	37-25-37, 3	8	1	2
C7	37-25-37, 3	8	1	2
C8	37-25-37, 3	8	1	2
C9	37-25-37, 3	6	1	2
C10	37-25-37, 3	6	1	2
C11	37-25-37, 3	4	1	2
C12	37-25-37, 3	2	1	2
C11	constant 37	-	1	4
C9	constant 37	-	1	18

videos are shown in FIGURE 6. In addition, the figure displays the calculated values for the beating frequency (BF), contraction time (CT), relaxation time (RT), and relaxed time (RxT, the time between relaxation and contraction). The results show that lowering the temperature decreases BF, increases RT and RxT, while CT remains relatively constant here. The full video is provided as Supplementary material 2. FIGURE 5a-e shows the temperature induced changes in the beating frequency (BF), contraction time (CT), relaxation time (RT), and amplitude of contraction for two representative clusters (C9, C10, RNo-1:4). The data is from four consecutive stressing cycles lasting for approximately 60 hours. The results show that hiPSC-CM contractility responds strongly to the temperature changes: the beating frequency (FIGURE 5b) changes, as expected, directly proportionally to temperature and also declines over time (see also FIGURE 7b, C9 and C10, ~100 hours). In a single representative stressing cycle (FIGURE 7a, C12, RNo-1), the linear temperature coefficient is approximately 5 BPM/°C (the coefficient of determination, R^2=0.97). Remarkably, nonlinear functions provide better fits, for

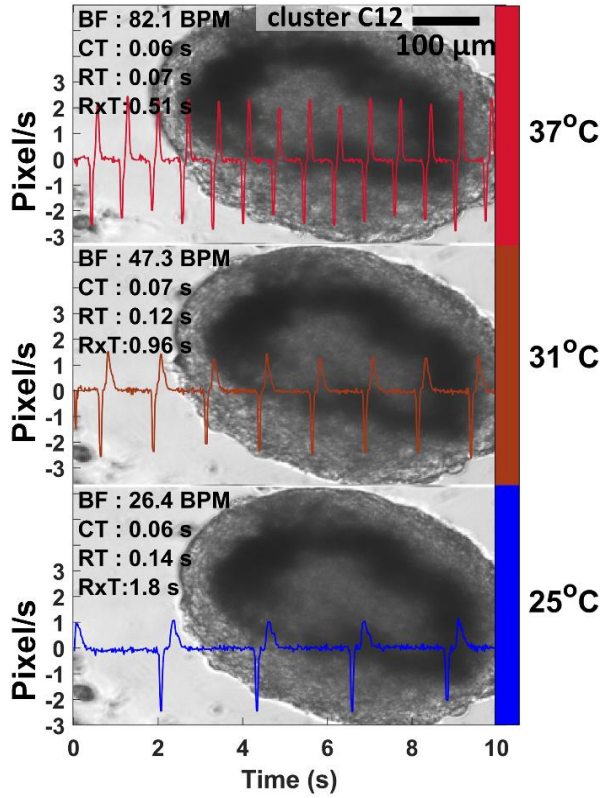

FIGURE 6. Effect of temperature on hiPSC-cardiomyocyte function. Analyzed beating signals (C12, RNo-1) at three selected temperatures as an overlay on the corresponding videos. See Supplementary material 2 for the full video. Calculated values are shown for the beating frequency (BF), contraction time (CT), relaxation time (RT), and relaxed time (RxT-the time between relaxation and contraction)

example, a 2nd degree polynomial and a monoexponential function yielded $R^2 = 0.9999$ and $R^2 = 0.9996$ respectively. FIGURE 7c shows the beating frequency (C9, C10) together with their nonlinear fits for 75 hours of culture. Here, the Q_{10} temperature coefficients (see plots) are larger than 2 (up to 60 hours), implying strong temperature dependence. Here also the R^2 of nonlinear fits (FIGURE 7d) are usually larger than that of linear (poly1) fits.

Further, the nonlinear temperature dependence was confirmed in the case of all the 12 clusters, and its significance was statistically verified with t-test on the R^2 values. There, the nonlinear R^2 > linear R^2 in 0-15 hours (means 93 % and 90 %, $p < 0.05$) and 0-30 hours (means 91 % and 88 %, $p < 0.05$). But, for durations > 30 hours, several clusters show a reduction in spontaneous contractility by factors other than temperature too, hence the statistical analysis becomes complex.

Similarly, the contraction and relaxation times also vary, but inversely (see FIGURE 5c,d) with the temperature, so their magnitudes are larger at lower temperatures. In addition, the relaxation times were often found to be larger than the contraction times. In TABLE 3, the relaxation and contraction times at low (T=25.0±0.1 °C) and high (T=37.1 ± 0.1 °C) temperatures are listed. The numbers show that a

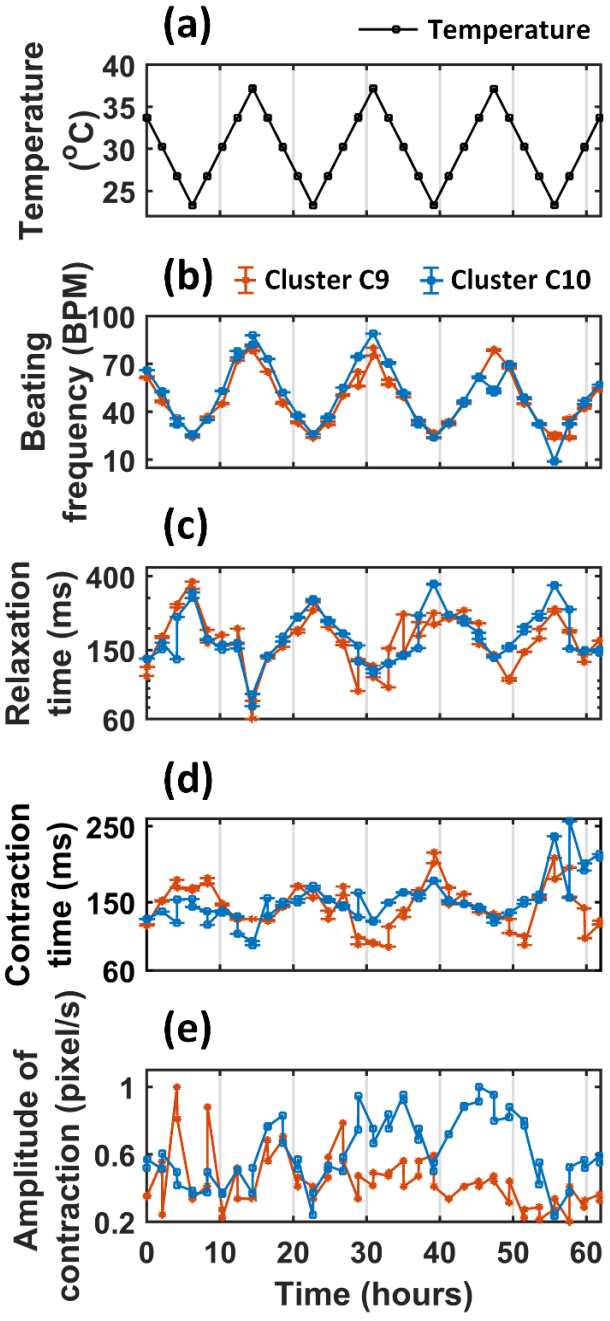

FIGURE 5. Temperature response plots of the two representative hiPSC-CM clusters (C9 and C10). Experimental data from approximately 60 hours of mechanobiological measurements where (a) Cell area temperature, (b) Beating frequency, (c) Contraction time, (d) Relaxation time, and (e) Amplitude of contraction. The temperature was precisely measured using the temperature sensitive plate and the plotted parameters were non-invasively analyzed with the video-based beating analysis software CMaN.

12 °C decline in temperature causes a 80 % increase in the contraction time and a 115 % increase in the relaxation time. Likewise, the amplitude of contraction (FIGURE 5e), calculated as the geometric mean of the amplitudes of V_x and V_y signals also shows a strong temperature dependence

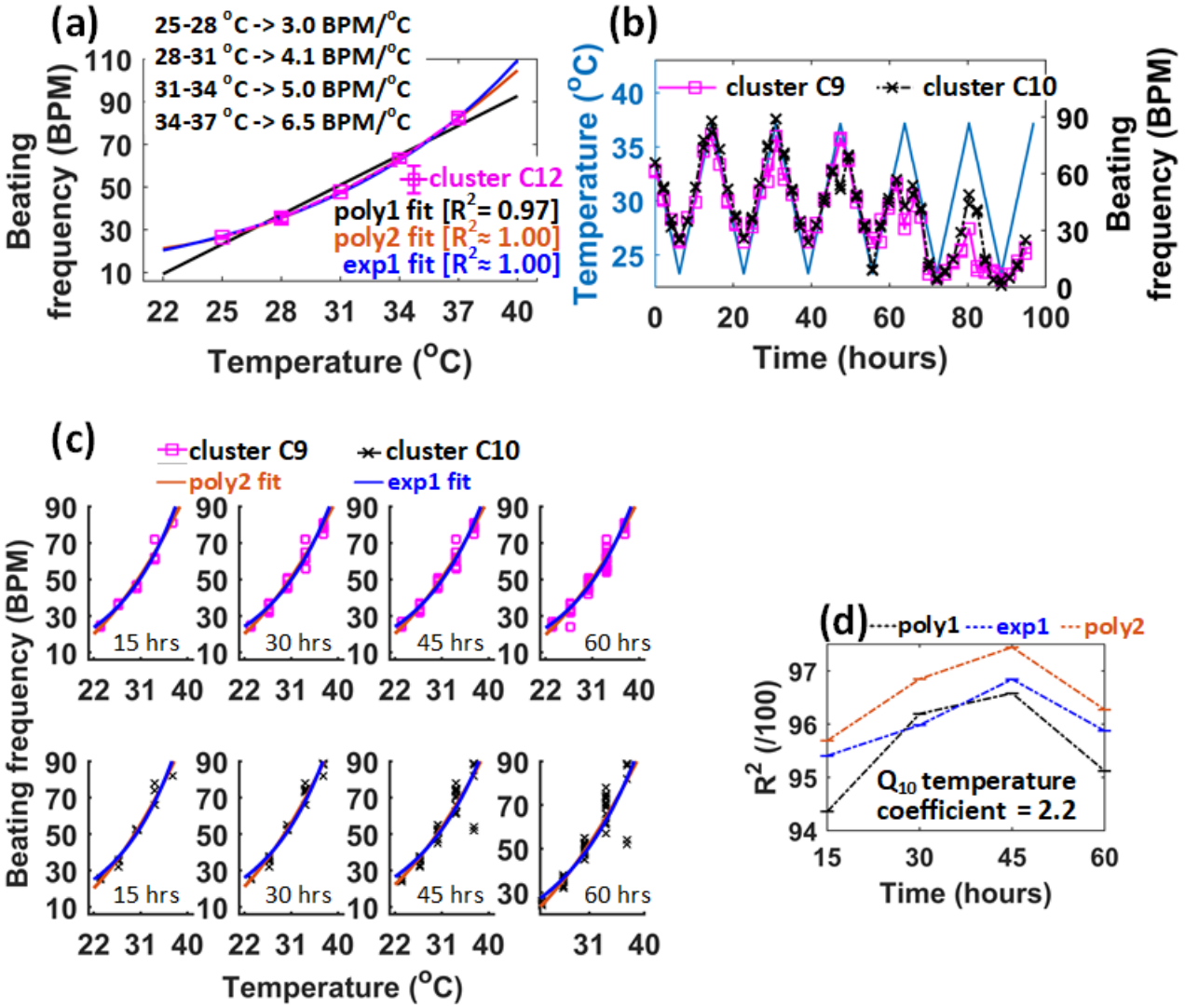

FIGURE 7. The hiPSC cardiomyocytes beating frequency in long-term temperature stressing experiments. The data are from automated temperature cycles of decreasing (37 °C to 25 °C) and increasing (25 °C to 37 °C) temperatures in 3 °C steps. (a) C12 data from a representative single stressing cycle (RNo-1) with linear and nonlinear (polynomial 2 and monoexponetial) fits. Compared to linear fit, the nonlinear functions showed nearly perfect (R^2 ≈1) fits. (b) Beating frequencies of two clusters (C9 and C10, RNo-1:4) in about 60 hours of experiment. (c) Data (shown in upper right figure) rearranged into different time segments, with 2nd degree polynomial and monoexponential fits. The computed Q_{10} temperature coefficients are shown in each figure, showing a strong temperature dependence on hiPSC-CM function. However the coefficient of determination drops significantly in extended cultures.

similar to beating frequency. However, the beat-to-beat amplitude variation in the 60 s videos, especially at low temperatures, is large.

Further, the beating frequency from four stressing cycles of all twelve clusters (from five different cell cultures) is shown in FIGURE 9. The span of beating frequency varied from culture to culture, so for statistical comparison, frequencies are scaled between 1 and 0 using a normalization function (BF-min(BF))/(max(BF)-min(BF)), where BF is the beating frequency. Despite the normalization, the error bars show relatively large variations, which presumably stems from a biological variability between the individual clusters.

TABLE 3. The mean relaxation and contraction time of all clusters (C1-C12) at two temperatures. Results are presented in terms of mean and standard deviation. Statistical analysis according to t-test (one-tailed). Statistical significances are denoted as * p < 0.05; ** p < 0.01.

Temperature (°C)	Contraction time (CT, ms)		Relaxation time(RT, ms)		RT to CT ratio
37.1 ± 0.1	152 ± 21.6	**	177.3 ± 55.6	*	1.1
25.0 ± 0.1	274.1 ± 93.4		367.0 ± 110		1.3

B. CONTRACTILE SYNCHRONIZATION OF DISSOCIATED hiPSC-CM CLUSTERS

We also quantified the electrical activation (AP propagation) between dissociated clusters by measuring the time delay between their beatings. FIGURE 10a shows six beating clusters (C3-C8) whose movement centers are marked with blue rectangles. Their beating signals are shown in FIGURE 10c, where the AP propagation time delay between contractions is clear. The signal propagation is also made

visually detectable in the original video by image processing; an example video is provided as Supplementary material 3. FIGURE 10b shows selected frames from this video. The dynamic sequence of cluster networking starts at cluster (FIGURE 10b(i)), passes through other clusters up until the cluster 6 (FIGURE 10b(vi)). Here, each frame is produced as the absolute difference in intensity between the actual frame and the first frame. As a result, a brighter passing halo becomes visible to describe the AP propagation delay. In FIGURE 10d, this time delay is plotted as a function of the cluster distance (cluster C8/ C7/ C6/ C5/ C4/C3- cluster C3), and the corresponding AP propagation velocities (slope) are calculated to be v = 3.88, 2.76, 2.34 and 1.98 mm/s at T = 37, 34, 31, and 28 °C, respectively.

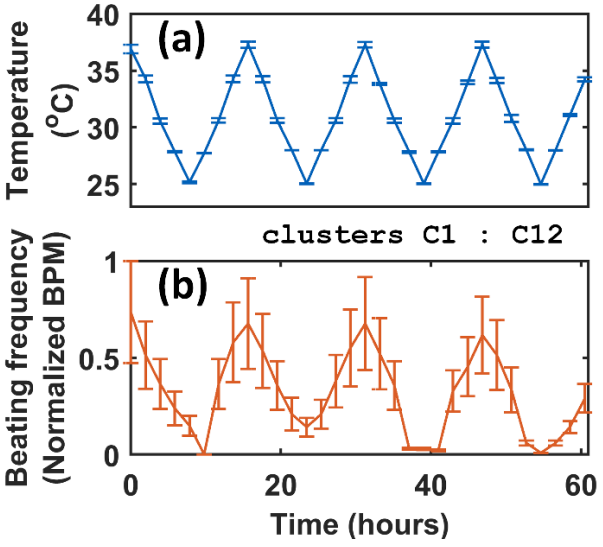

FIGURE 9. Beating frequency of twelve spontaneously beating hiPSC-cardiomyocyte clusters in four stressing cycles. The clusters are from five different cell cultures where the range of beating frequency varied from culture to culture. Thus, the error bars also account for the biological variability.

C. TEMPORAL CHANGES IN BEATING AT A CONSTANT TEMPERATURE

It has also been observed that the contractility slowly decreases over extended periods of time even at a constant temperature. The beating frequency plots from two long-term measurements at constant 37 °C with 2 clusters (C11, C9) are shown in FIGURE 8. The measured slope (dBF/dt [BPM/hrs]) values are -0.22 and -0.74, respectively, indicating a 68–85 % decline in beating frequency in 70–100 hours. The rate of the decline probably depends on many factors, including the cell density, secretory/metabolic conditions, and medium ageing (exhaustion of accessory food factors).

IV. DISCUSSION

In this paper, we have demonstrated the applicability of a previously reported modular cell culturing system [26] with two new add-ons: 1) temperature sensor plates [24] and 2) a

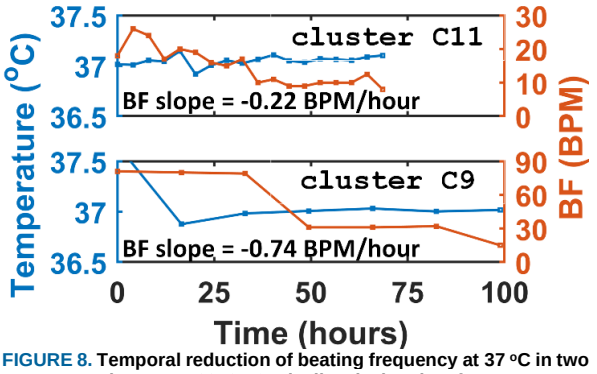

FIGURE 8. Temporal reduction of beating frequency at 37 °C in two separate cultures. A 68–85 % decline in beating frequency was observed in 70–100 hours.

novel video-based mechanobiology analysis software, CMaN, to study the temperature response of hiPSC-CMs. Experiments were conducted outside a conventional incubator, and to the best of our knowledge, this is the first report describing a systematic automated temperature stressing and concurrent hiPSC-CM function analysis. The results show that the hiPSC-CM contractile function is strongly temperature dependent, and that typically temperature coefficient Q_{10}> 2. Further, the beating frequency –temperature relationship was found to be well described by nonlinear (2nd order polynomial and monoexponential) functions. In the statistical analysis, the R^2 values were always higher for the nonlinear models than for the linear ones, and some clusters showed nearly perfect (R^2 ~1) nonlinear fits. Thus, maintaining a stable temperature in hiPSC-CMs experiments is of utmost important in order to minimize undesired stimulation of the cells and to avoid experimental errors. Further, we noticed that in continuous measurements, the contractility of hiPSC-CMs decreases over time even at fixed temperatures, which is also an important factor to consider in experimental designs. The medium ageing, evaporation, and related changes in the medium composition as well as exhaustion of essential nutrients are likely contributing to slowing the contractile kinetics temporally [19]. The combined beating frequency plot (FIGURE 9) contains the data from twelve beating clusters from five different cell cultures, hence the error bars also account for the biological variability. As the hiPSC-CMs are known to exhibit high phenotype variability, the variability of the temperature dependency between different myocytes/culture preparations also needs to be recognized. In contrast to beating frequency, the contraction and relaxation times vary inversely with temperature. The relaxation times are typically longer than the contraction times. The amplitude of the contraction, on the other hand, displayed more beat-to-beat variability (standard deviation) in almost all recorded videos. Intriguingly, some clusters ceased the beating function occasionally, but regained the function in due course and exhibited the temperature dependence in continued stressing cycles.

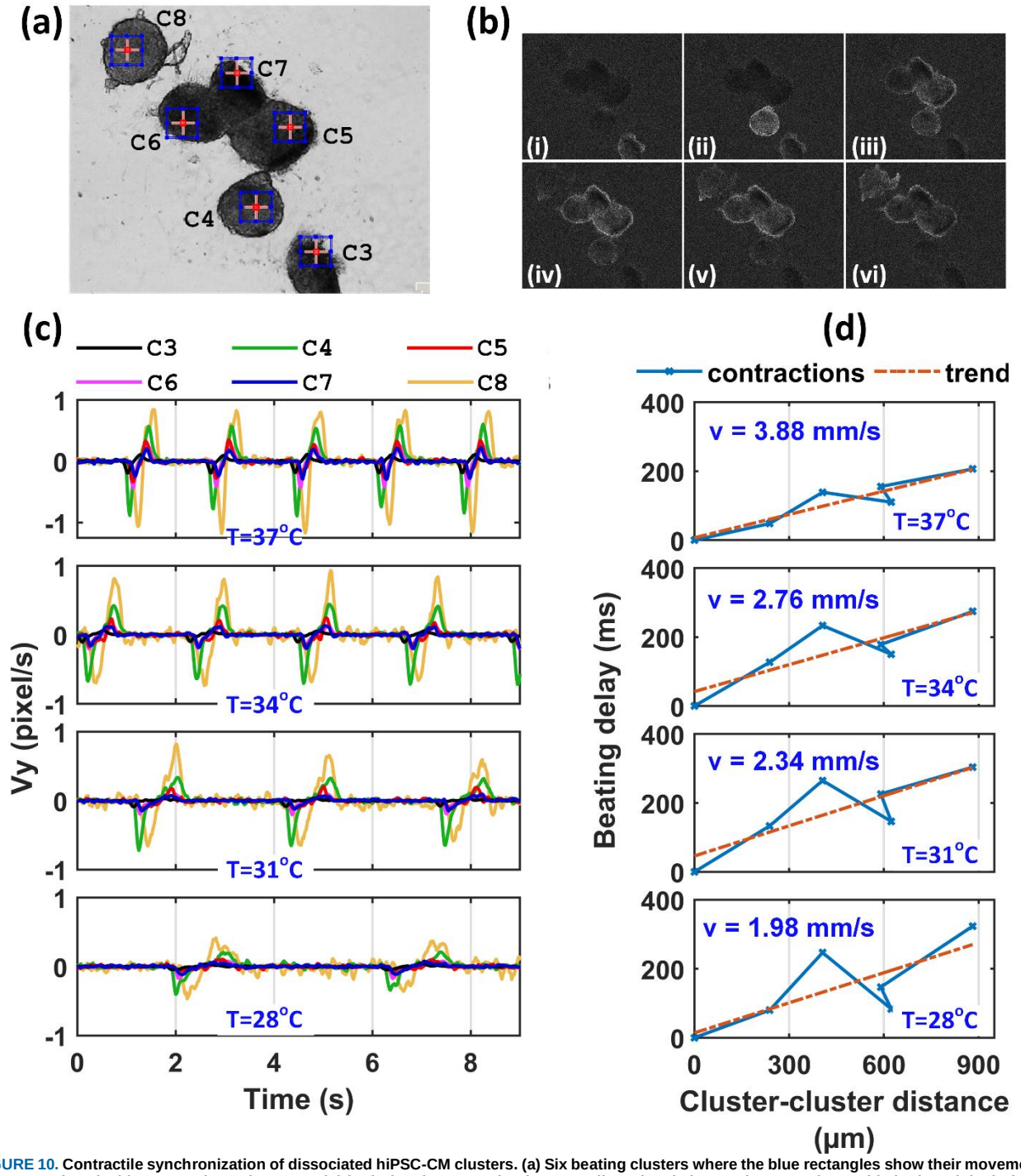

FIGURE 10. **Contractile synchronization of dissociated hiPSC-CM clusters. (a) Six beating clusters where the blue rectangles show their movement centers analyzed with CMaN. The action potential (AP) signal propagation between dissociated clusters became observable in the original video by image processing. See Supplementary material 3 for an example video. (b) Selected frames from Supplementary material 3, where a passing brighter halo displays the AP propagation. The networking dynamic sequence starts from cluster 1 and advances up to cluster 6. (c) Beating signals from the six clusters where the time delay between the signals is clear. (d) The time delay versus the cluster separation distance (cluster C8/ C7/ C6/ C5/ C4/C3 – cluster C3) plots and the computed AP propagation velocities.**

Biologically, the temperature dependence of the hiPSC-CMs can be multifactorial. A more general explanation is the prolongation of APs at lower temperatures due to slower kinetics of underlying ion channels, exchangers, and intracellular pumps [51]. The hiPSC-CMs, similar to their native human counterparts, have most of the basic underlying excitation-contraction coupling components including membrane voltage regulation and signaling cascades [52]–[54]. However, reduced inward rectifier K^+ (potassium) currents and the presence of prominent pacemaker currents collectively produce AP waveforms that make the hiPSC-CMs significantly different and facilitate spontaneous automaticity that is not observed in matured human ventricular myocytes [53]. Temperature dependence

of AP prolongation has been previously studied in animal models [55], [56]. Guinea pig ventricular myocytes have shown 115 % prolongation of AP with a 10 ºC temperature drop [56]. The acute effect of temperature on the relaxation time and pacemaker firing rate of Sprague-Dawley rat CMs has also been reported [3]. In our study, we measured the prolongation of the hiPSC-CM relaxation (analogue to the AP repolarization) and contraction times systematically. Multiple voltage-gated ion channels are presumably contributing to this; however, the exact quantification schemes of the dependence of most of the underlying mechanisms on environmental parameters (e.g. temperature, pO_2, pH, pCO_2) are ambiguous, and accurate models have not yet been developed.

We also measured the propagation of electrical activation between dissociated hiPSC-CM clusters by optical means. The clusters, even though physically separated, are possibly connected to each other through cells (non-CMs) underneath, that act as a cardiac skeleton for mechanical scaffolding. A few studies using animal cells have confirmed the electrophysiological coupling of fibroblasts (of cardiac origin) with CMs to propagate contractions over finite distances [57]–[59]. Recently, some studies quantified the AP propagation distance and the beating synchronization of certain CM types [7], [60], [61]. In our study, we quantified the synchronization delay for hiPSC-CMs by non-invasive image-based measurements and measured the AP propagation velocities (v = 1.98-3.88 mm/s at 28-37 ºC). The AP propagation velocities can obviously be a function of cell density, configuration (single cells, cell sheets, etc.), age, and maturation state.

The software, CMaN, is freely available and in contrast to compared software programs, it is several times faster, more robust and sensitive, computationally less expensive and allows easy ROI selection. This allows processing of specific areas/cells carefully, for instance when frames contain multiple cells/clusters. More importantly, CMaN extracts six components of contractile motion per processing, which enables a minimum of one useful beating signal even in complex scenarios such as weak movements, or overexposure/gamma by uneven background illumination. Signal from CMaN is analogues to ECG with both positive (upstroke) and negative (downstroke) segments to represent the contractile phenomena more exactly. This helps to compute the beating frequency and contraction and relaxation phenomena separately. Additionally, CMaN has supplemental features for cluster finding and movement center detection. One limitation of the CMaN is that it can currently only process avi files. If the input comes as a sequence of images, those have to be first converted into an avi file (for example using ImageJ or the script provided in the CMaN user manual). Currently the mechanobiological analysis is carried out in two stages; first stage is the automatic signal extraction, and in the second stage, a fine tuning (adjusting thresholds with the sliders in the GUI) may be required in case of heavily noisy or complex beating scenarios. The software is an offline tool, but the basic script for the affine flow computation is provided (see CMaN user manual) which can be edited for online automated beating analysis or other extended applications. One future direction is the measurement of contractile forces with beating signals by integrating a micro-displacement actuator (e.g. fluorescent beads/magnetic beads/micro-cantilevers). We are also developing cell and disease models where the platform described in this paper is directly applied.

V. CONCLUSIONS

We have described a system and software that allows the assessment of hiPSC derived CM contractions with changing temperatures. The highlights of the paper are the first time reporting of 1) the nonlinear temperature dependence on the beating frequency of hiPSC-CMs; 2) the visualization of hiPSC-CM contractile networking and the non-invasive measurement of signal propagation between dissociated clusters; 3) the release of an advanced and robust software that tracks multiple signals from CM beating videos. The system and software are useful additions in assay development and organ-on-chip experimentations.

CONFLICT OF INTERESTS

The authors report no conflicts of interest.

ELECTRONIC SUPPLEMENTARY MATERIAL

This article contains supplementary materials, which are available to authorized users.

Supplementary material 1. CMaN- a video-based cardiomyocyte functional analysis software:
https://figshare.com/s/3402bca86fe93f29a73f

Supplementary material 2. Temperature response characteristics of a beating hiPSC-CM cluster at three selected temperatures:
https://figshare.com/s/0ae47cd47234b93afb21

Supplementary material 3. Visualization of AP propagation between dissociated clusters. For better visualization the video speed is reduced to one third of the original speed:
https://figshare.com/s/46d03767284ba2d32a1d

Supplementary material 4. An example beat rate increasing and decreasing drug response analysis with CMaN:
https://figshare.com/s/09cebfe5fbed9762f058

Supplementary material 5. Movement center analysis. Beating signals at the movement center and at different locations of a contracting hiPSC-CM:
https://figshare.com/s/9bf68f0707a4e64a4a78

REFERENCES

[1] R. Madonna, "Human-Induced pluripotent stem cells: In quest of clinical applications," *Molecular Biotechnology*. 2012.
[2] V. K. Singh, M. Kalsan, N. Kumar, A. Saini, and R. Chandra,

"Induced pluripotent stem cells: applications in regenerative medicine, disease modeling, and drug discovery," *Front. Cell Dev. Biol.*, 2015.

[3] C. S. Chung and K. S. Campbell, "Temperature and transmural region influence functional measurements in unloaded left ventricular cardiomyocytes," *Physiol. Rep.*, vol. 1, no. 6, pp. 1–13, 2013.

[4] C. G. Crandall and J. González-Alonso, "Cardiovascular function in the heat-stressed human," *Acta Physiol.*, vol. 199, no. 4, pp. 407–423, Aug. 2010.

[5] T. E. Wilson and C. G. Crandall, "Effect of Thermal Stress on Cardiac Function," *Exerc. Sport Sci. Rev.*, vol. 39, no. 1, pp. 12–17, Jan. 2011.

[6] K. B. Storey and J. M. Storey, "Mammalian Hibernation: Biochemical Adaptation and Gene Expression," in *Functional Metabolism*, Hoboken, NJ, USA: John Wiley & Sons, Inc., 2005, pp. 443–471.

[7] R. Kienast, M. Stöger, M. Handler, F. Hanser, and C. Baumgartner, "Alterations of field potentials in isotropic cardiomyocyte cell layers induced by multiple endogenous pacemakers under normal and hypothermal conditions.," *Am. J. Physiol. Heart Circ. Physiol.*, vol. 307, no. 7, pp. H1013-23, Oct. 2014.

[8] H. Orita, M. Fukasawa, S. Hirooka, K. Fukui, M. Kohi, and M. Washio, "A cardiac myocyte culture system as an in vitro experimental model for the evaluation of hypothermic preservation," *Surg. Today*, vol. 23, no. 5, pp. 439–443, May 1993.

[9] K. E. Cullen and K. D. Sarge, "Characterization of hypothermia-induced cellular stress response in mouse tissues.," *J. Biol. Chem.*, vol. 272, no. 3, pp. 1742–6, Jan. 1997.

[10] A. Stolzing, S. Sethe, and A. M. Scutt, "Stem cell reports," *Stem Cells Dev.*, vol. 15, no. 4, pp. 478–487, Aug. 2006.

[11] K. Purandhar, P. K. Jena, B. Prajapati, P. Rajput, and S. Seshadri, "Understanding the Role of Heat Shock Protein Isoforms in Male Fertility, Aging and Apoptosis," *World J. Mens. Health*, vol. 32, no. 3, p. 123, Dec. 2014.

[12] M. S. Choudhery *et al.*, "Mesenchymal stem cells conditioned with glucose depletion augments their ability to repair-infarcted myocardium," *J. Cell. Mol. Med.*, vol. 16, no. 10, pp. 2518–2529, Oct. 2012.

[13] J. Kockskämper, "Excitation–Contraction Coupling of Cardiomyocytes," in *Cardiomyocytes – Active Players in Cardiac Disease*, Cham: Springer International Publishing, 2016, pp. 67–96.

[14] N. Schaible, G. Arteaga, T. Tveita, G. Sieck, T. Hoang, and Y. S. Han, "Hypothermia/rewarming disrupts excitation-contraction coupling in cardiomyocytes," *Am. J. Physiol. Circ. Physiol.*, vol. 310, no. 11, pp. H1533–H1540, 2016.

[15] B. D. Stuyvers, A. D. McCulloch, J. Guo, H. J. Duff, and H. E. D. J. Ter Keurs, "Effect of stimulation rate, sarcomere length and Ca2+ on force generation by mouse cardiac muscle," *J. Physiol.*, vol. 544, no. 3, pp. 817–830, 2002.

[16] T. Tveita, M. Skandfer, H. Refsum, and K. Ytrehus, "Experimental hypothermia and rewarming: changes in mechanical function and metabolism of rat hearts," *J. Appl. Physiol.*, vol. 80, no. 1, pp. 291–297, Jan. 1996.

[17] J. A. Ryan, "Corning Guide for Identifying and Correcting Common Cell Growth Problems," *Corning Incorporated Life Sciences*, 2019. [Online]. Available: https://beta-static.fishersci.com/content/dam/fishersci/en_US/documents/programs/scientific/technical-documents/technical-bulletins/corning-guide-identifying-cell-growth-problems-technical-bulletin.pdf. [Accessed: 12-Jan-2017].

[18] D. K. Rajan *et al.*, "Monitoring pH, temperature and humidity in long-term stem cell culture in CO2 incubator," in *2017 IEEE International Symposium on Medical Measurements and Applications, MeMeA 2017 - Proceedings*, 2017, pp. 470–474.

[19] F. Wang, "Culture of animal cells: A manual of basic technique, fifth edition," *Vitr. Cell. Dev. Biol. - Anim.*, vol. 42, no. 5, p. 169, 2006.

[20] D. Kattipparambil Rajan *et al.*, "Optical non-contact pH measurement in cell culture with sterilizable, modular parts," *Talanta*, vol. 161, pp. 755–761, Dec. 2016.

[21] J. Kreutzer, L. Ylä-Outinen, A. J. Mäki, M. Ristola, S. Narkilahti, and P. Kallio, "Cell culture chamber with gas supply for prolonged recording of human neuronal cells on microelectrode array," *J. Neurosci. Methods*, vol. 280, pp. 27–35, Mar. 2017.

[22] S. Fulda, A. M. Gorman, O. Hori, and A. Samali, "Cellular stress responses: cell survival and cell death.," *Int. J. Cell Biol.*, vol. 2010, p. 214074, 2010.

[23] E. Laurila, A. Ahola, J. Hyttinen, and K. Aalto-Setälä, "Methods for in vitro functional analysis of iPSC derived cardiomyocytes — Special focus on analyzing the mechanical beating behavior," *Biochim. Biophys. Acta - Mol. Cell Res.*, vol. 1863, no. 7, pp. 1864–1872, Jul. 2016.

[24] A.-J. Mäki *et al.*, "A Portable Microscale Cell Culture System with Indirect Temperature Control," *SLAS Technol. Transl. Life Sci. Innov.*, vol. 23, no. 6, pp. 566–579, Dec. 2018.

[25] T. Uchida, R. Kitora, and K. Gohara, "Temperature dependence of synchronized beating of cultured neonatal rat heart-cell networks with increasing age measured by multi-electrode arrays," *Res. Artic. Trends Med*, vol. 18, no. 4, pp. 1–10, 2018.

[26] D. K. Rajan *et al.*, "A Portable Live-Cell Imaging System With an Invert-Upright-Convertible Architecture and a Mini-Bioreactor for Long-Term Simultaneous Cell Imaging, Chemical Sensing, and Electrophysiological Recording," *IEEE Access*, vol. 6, pp. 11063–11075, 2018.

[27] M. K. Worden, C. M. Clark, M. Conaway, and S. A. Qadri, "Temperature dependence of cardiac performance in the lobster Homarus americanus.," *J. Exp. Biol.*, vol. 209, no. Pt 6, pp. 1024–34, Mar. 2006.

[28] G. Caluori *et al.*, "Simultaneous study of mechanobiology and calcium dynamics on hESC-derived cardiomyocytes clusters," *J. Mol. Recognit.*, vol. 32, no. 2, p. e2760, Feb. 2019.

[29] S. Dinarelli *et al.*, "AFM nano-mechanical study of the beating profile of hiPSC-derived cardiomyocytes beating bodies WT and DM1," *J. Mol. Recognit.*, vol. 31, no. 10, p. e2725, Oct. 2018.

[30] M. Pesl *et al.*, "Phenotypic assays for analyses of pluripotent stem cell-derived cardiomyocytes," *J. Mol. Recognit.*, vol. 30, no. 6, p. e2602, Jun. 2017.

[31] P. Spitalieri *et al.*, "Modelling the pathogenesis of Myotonic Dystrophy type 1 cardiac phenotype through human iPSC-derived cardiomyocytes," *J. Mol. Cell. Cardiol.*, vol. 118, pp. 95–109, May 2018.

[32] A. Ahola, A. L. Kiviaho, K. Larsson, M. Honkanen, K. Aalto-Setälä, and J. Hyttinen, "Video image-based analysis of single human induced pluripotent stem cell derived cardiomyocyte beating dynamics using digital image correlation," *Biomed. Eng. Online*, vol. 13, no. 1, 2014.

[33] C. L. Mummery *et al.*, "MUSCLEMOTION A Versatile Open Software Tool to Quantify Cardiomyocyte and Cardiac Muscle Contraction In Vitro and In Vivo," 2017.

[34] C. N. Toepfer *et al.*, "SarcTrack. An Adaptable Software Tool for Efficient Large-Scale Analysis of Sarcomere Function in hiPSC-Cardiomyocytes," *Circ. Res.*, vol. 124, no. 8, pp. 1172–1183, Apr. 2019.

[35] S. Nitsch, F. Braun, S. Ritter, M. Scholz, and I. S. Schroeder, "Functional video-based analysis of 3D cardiac structures generated from human embryonic stem cells," *Stem Cell Res.*, vol. 29, pp. 115–124, May 2018.

[36] M. Maddah *et al.*, "A Non-invasive Platform for Functional Characterization of Stem-Cell-Derived Cardiomyocytes with Applications in Cardiotoxicity Testing," *Stem Cell Reports*, vol. 4, no. 4, pp. 621–631, Apr. 2015.

[37] T. Hayakawa *et al.*, "Image-based evaluation of contraction–relaxation kinetics of human-induced pluripotent stem cell-derived cardiomyocytes: Correlation and complementarity with extracellular electrophysiology," *J. Mol. Cell. Cardiol.*, vol. 77, pp. 178–191, Dec. 2014.

[38] E. K. Lee, Y. K. Kurokawa, R. Tu, S. C. George, and M. Khine, "Machine learning plus optical flow: a simple and sensitive method to detect cardioactive drugs," *Sci. Rep.*, vol. 5, no. 1, p. 11817, Dec. 2015.

[39] J. Kreutzer *et al.*, "Structured PDMS Chambers for Enhanced Human Neuronal Cell Activity on MEA Platforms," *J. Bionic Eng.*, vol. 9, no. 1, pp. 1–10, Mar. 2012.

[40] O. Metsälä, J. Kreutzer, H. Högel, P. Miikkulainen, P. Kallio, and P. M. Jaakkola, "Transportable system enabling multiple irradiation studies under simultaneous hypoxia in vitro," *Radiat. Oncol.*, vol. 13, no. 1, p. 220, Nov. 2018.

[41] A. L. Lahti *et al.*, "Model for long QT syndrome type 2 using human iPS cells demonstrates arrhythmogenic characteristics in cell culture.," *Dis. Model. Mech.*, vol. 5, no. 2, pp. 220–30, Mar. 2012.

[42] C. Mummery *et al.*, "Differentiation of Human Embryonic Stem Cells to Cardiomyocytes," *Circulation*, vol. 107, no. 21, pp. 2733–2740, Jun. 2003.

[43] S. S. Beauchemin and J. L. Barron, "The computation of optical flow," *ACM Comput. Surv.*, vol. 27, no. 3, pp. 433–466, Sep. 1995.

[44] Y. David, "Affine optic flow (version 1.3)," *MATLAB Central File Exchange*, 2010. [Online]. Available: https://se.mathworks.com/matlabcentral/fileexchange/27093-affine-optic-flow. [Accessed: 03-Mar-2017].

[45] C. Bonivento, C. Melchiorri, and H. Tolle, *Advances in robotics-The ERNET Perspective; Proceedings of the Research Workshop of ERNET-European Robotics Network, Darmstadt, Germany, 1996*. World Scientific, 1996.

[46] J. Liu, N. Sun, M. A. Bruce, J. C. Wu, and M. J. Butte, "Atomic Force Mechanobiology of Pluripotent Stem Cell-Derived Cardiomyocytes," *PLoS One*, vol. 7, no. 5, p. e37559, May 2012.

[47] D. Rajan, "Modular instrumentation for controlling and monitoring in-vitro cultivation environment and image-based functionality measurements of human stem cells," *Tampere Univ. DSc-Tech thesis*, vol. 256, pp. 1–150, 2020.

[48] H. Kemppi, "Gold nanoparticle crosslinked conductive hyaluronan and chondroitin sulfate hydrogels for culturing embryonic stem cells derived human cardiomyocytes," *Master's thesis, Tampere University*, 2018. .

[49] D. Shah *et al.*, "Modeling of LMNA-Related Dilated Cardiomyopathy Using Human Induced Pluripotent Stem Cells," *Cells*, vol. 8, no. 6, p. 594, Jun. 2019.

[50] J. Kim, D. Shah, I. Potapov, J. Latukka, K. Aalto-Setälä, and E. Räsänen, "Scaling and correlation properties of RR and QT intervals at the cellular level," *Sci. Rep.*, vol. 9, no. 1, pp. 1–9, Dec. 2019.

[51] K. Wang, A. Climent, D. Gavaghan, P. Kohl, and C. Bollensdorff, "Room Temperature vs Ice Cold - Temperature Effects on Cardiac Cell Action Potential," *Biophys. J.*, vol. 110, no. 3, p. 587a, Feb. 2016.

[52] C. Y. Ivashchenko *et al.*, "Human-induced pluripotent stem cell-derived cardiomyocytes exhibit temporal changes in phenotype," *Am J Physiol Hear. Circ Physiol*, vol. 305, pp. 913–922, 2013.

[53] I. Karakikes, M. Ameen, V. Termglinchan, and J. C. Wu, "Human induced pluripotent stem cell-derived cardiomyocytes: insights into molecular, cellular, and functional phenotypes.," *Circ. Res.*, vol. 117, no. 1, pp. 80–8, Jun. 2015.

[54] J. T. Koivumäki *et al.*, "Structural Immaturity of Human iPSC-Derived Cardiomyocytes: In Silico Investigation of Effects on Function and Disease Modeling.," *Front. Physiol.*, vol. 9, p. 80, 2018.

[55] M. Laursen, S.-P. Olesen, M. Grunnet, T. Mow, and T. Jespersen, "Characterization of cardiac repolarization in the Göttingen minipig," *J. Pharmacol. Toxicol. Methods*, vol. 63, no. 2, pp. 186–195, Mar. 2011.

[56] T. Kiyosue, M. Arita, H. Muramatsu, A. J. Spindler, and D. Noble, "Ionic mechanisms of action potential prolongation at low temperature in guinea-pig ventricular myocytes," 1993.

[57] T. Kaneko, F. Nomura, and K. Yasuda, "On-chip constructive cell-network study (I): contribution of cardiac fibroblasts to cardiomyocyte beating synchronization and community effect.," *J. Nanobiotechnology*, vol. 9, p. 21, May 2011.

[58] P. Kohl, "Heterogeneous Cell Coupling in the Heart," *Circ. Res.*, vol. 93, no. 5, pp. 381–383, Sep. 2003.

[59] G. Gaudesius, M. Miragoli, S. P. Thomas, and S. Rohr, "Coupling of Cardiac Electrical Activity Over Extended Distances by Fibroblasts of Cardiac Origin," *Circ. Res.*, vol. 93, no. 5, pp. 421–428, Sep. 2003.

[60] M. Miragoli, G. Gaudesius, and S. Rohr, "Electrotonic Modulation of Cardiac Impulse Conduction by Myofibroblasts," *Circ. Res.*, vol. 98, no. 6, pp. 801–810, Mar. 2006.

[61] J. P. Fahrenbach, R. Mejia-Alvarez, and K. Banach, "The relevance of non-excitable cells for cardiac pacemaker function," *J. Physiol.*, vol. 585, no. 2, pp. 565–578, Dec. 2007.

PUBLICATION III

Optical non-contact pH measurement in cell culture with sterilizable, modular parts

Rajan DK, Patrikoski M, Verho J, Sivula J, Ihalainen H, Miettinen S, Lekkala J.

Journal of Pure and Applied Analytical Chemistry, Talanta, vol. 161, pp. 755–761, 2016 (https://doi.org/10.1016/j.talanta.2016.09.021)

Talanta 161 (2016) 755–761

Contents lists available at ScienceDirect

Talanta

journal homepage: www.elsevier.com/locate/talanta

Optical non-contact pH measurement in cell culture with sterilizable, modular parts

Dhanesh Kattipparambil Rajan [a,*], Mimmi Patrikoski [b,c], Jarmo Verho [a], Jyrki Sivula [b,c], Heimo Ihalainen [a], Susanna Miettinen [b,c], Jukka Lekkala [a]

[a] Department of Automation Science and Engineering, Tampere University of Technology, Tampere, Finland
[b] Adult Stem Cell Group, BioMediTech, Institute of Biosciences and Medical Technology, University of Tampere, Tampere, Finland
[c] Science Center, Tampere University Hospital, Tampere, Finland

ARTICLE INFO

Article history:
Received 16 June 2016
Received in revised form
2 September 2016
Accepted 5 September 2016
Available online 8 September 2016

Keywords:
Cell culture pH measurement
Cell culture non-contact pH measurement
Phenol red medium pH measurement
Cell culture optical pH measurement
Long term pH measurement

ABSTRACT

A non-contact real time pH measurement using fully modular optical parts is described for phenol-red medium cell cultures. The modular parts can be sterilized, and once the measurement is started at the beginning of culture, no recalibration or maintenance is needed till the end of the culture. Measurements can be carried out without any special manual attention. The modular assembly of LED and sensor cassettes is unique, robust, reusable and reproducible.

pH is measured in an intact closed flow system, without wasting any culture medium. A special pump encapsulation enables the system to be effortlessly functional in extremely humid incubator environments. This avoids lengthy sample tubings in and out of the incubator, associated large temperature changes and CO_2 buffering issues.

A new correction model to compensate errors caused e.g. by biolayers in spectrometric pH measurement is put-forward, which improves the accuracy of pH estimation significantly. The method provides resolution down to 0.1 pH unit in physiological pH range with mean absolute error 0.02.

1. Introduction

pH monitoring in adult stem cell culture provides valuable information on cell metabolic processes and overall growth environment [1]. Cell viability and tissue functions in vivo are strongly correlated to pH. Changes in extracellular pH from optimal can have substantial impact on cell metabolism and proliferation [2,3]. Most mammalian cells typically grow at pH 7.0–7.5 [4,5]. For example, a fully prepared medium for human adipose stem cells is typically at $\approx$7.2 pH at 37 °C with sodium bicarbonate buffering. However, when cells proliferate and metabolize nutrients in the culture medium, they secrete CO_2 and acid products (lactic, carbonic etc.), causing the pH to invariably decrease over time [1,4,5]. Extremely dense versus sparse plating confluency and rate of evaporation can also affect pH levels [6]. For monitoring cellular environment, it is therefore important to have an accurate, rapid pH monitoring in real time. Conventionally, to measure pH reliably, electrochemical sensors or field effect transistor (ISFET) sensors are used [2,6–8]. Electrochemical sensors are precise, fast and reversible, but bulky, require large sample volume and physical contact [4,8]. ISFETs, having non-metallic gates with pH selective membranes, can provide precise measurements for small volumes, but still requires physical contact [7,9]. Moreover, both of them show significant signal drift in long term continuous operation and require periodic recalibration and maintenance which restricts them as good candidates mainly for short term applications [6,8,10–13]. A pH sensor in cell culture has to be operated in an extreme sterile condition where the increased risk of contamination by periodic recalibration and maintenance, biolayer formation, and glass membrane cell clogging are all problematic. In contrast to the aforementioned sensors, optical pH sensors have received widespread attention during the last decade in cell culture applications [14–18]. A few optical pH sensors are commercially available as of Wavepod II-pHOPT from GE Healthcare, iTube pH Bioreactor from PreSens, TruFluor® pH from Finesse and OptiSens pH from Sartorius. Optical pH sensors, in general, are based on indicator dyes, typically immobilized on a planar light guide or on an optical fiber, forming an optode. H^+ ions induce changes in the molecular structure or orbital energy levels of optodes, which are translated into changes in spectroscopic phenomena such as absorption or reflectance or luminescence or fluorescence [8,17,18]. Most of these sensors require sample

* Corresponding author.
E-mail addresses: dhanesh.kr@tut.fi (D. Kattipparambil Rajan), mimmi.patrikoski@staff.uta.fi (M. Patrikoski), jarmo.verho@tut.fi (J. Verho), jyrki.sivula@outlook.com (J. Sivula), heimo.ihalainen@tut.fi (H. Ihalainen), susanna.miettinen@staff.uta.fi (S. Miettinen), jukka.lekkala@tut.fi (J. Lekkala).

http://dx.doi.org/10.1016/j.talanta.2016.09.021
0039-9140/

physical contact. Signal drift due to immobilized indicator decay (photobleaching/leaching) is also a concern [8,18–20]. Therefore, non-contact, real time pH monitoring is desired in several areas including cell therapy experiments. A true non-contact pH measurement is made possible, for example, when a pH indicator is dissolved in the culture medium, whose spectral changes by H^+ ions are measured by spectroscopic means [8]. pH sensitive smart cuvette (Ocean optics) is an attractive option, but it is designed to be used with a spectrometer, normally not cost effective. Most of the standard stem cell culture media contain phenol red, a stable biocompatible pH indicator, allowing the quick visual inspection of pH changes. Changes in the characteristic absorptions of phenol red medium in accordance with pH can also be exploited for quantitative spectroscopic non-contact pH estimation. This technique has been tested also in pH measurements in some cell cultures [2,14,16,19,21]. In phenol red systems, the core idea is to measure light intensities at two wavelengths, one at the pH sensitive wavelength and other at a neutral reference wavelength. However, there are a few practical issues for adapting the reported methods to stem cell cultures. Sample extraction from culture dishes is inevitable though keeping the flow pump or the measurement cell out of the incubator with sample tubings in and out of the incubator is somewhat unappealing. Lengthy sample tubings, associated large temperature changes, need for large sample volume and more culture supplements, and extra tubing for buffering CO_2 are all challenging. Lengthy tubings also impose sterilization issues and necessitate to use a high flow rate for the fast response, which in turn can be uncomfortable for stem cells. When two beams of dissimilar wavelengths operate in close proximity, the possible light cross talk due to the scattering of light by detached cells or debris is also to be addressed electronically or optically. Moreover, the formulations that translate absorption ratios into pH, lack parameters to account the effect of temperature and biolayer formations in continuous long term cell culture. In an effort to overcome the above challenges, we have tested a robust, reusable non-contact pH measurement system. Almost all parts are 3D printed, fully modular, can be sterilized and placed inside the incubator. No sample extraction from the incubator or any special sample treatment is needed. Temperature dependencies are continuously compensated. A new absorption correction model to compensate non-specific absorptions (eg. by biolayer in continuous long term culture) is proposed and tested which improves the pH accuracy significantly.

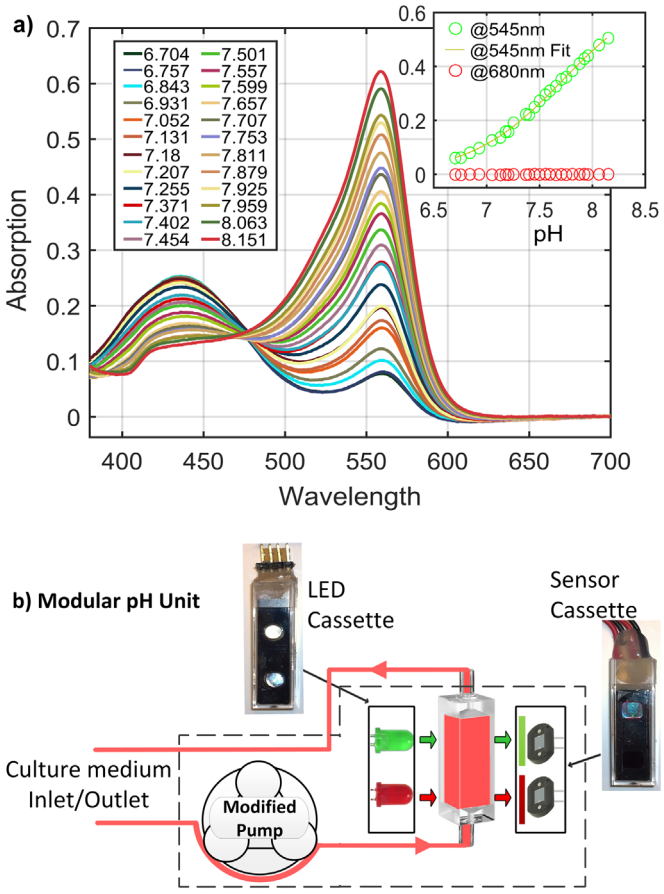

Fig. 1. a) Absorption spectra of DMEM/-F12 based BM measured with spectrometer (JAZ, Ocean optics) at different pHs. Figure inset: Absorption at 545 nm and 680 nm as a function of pH. Continuous line: Textbook equation (Eq. (4)) fitted at 545 nm. b) Modular non-contact pH unit with modules of LED cassette, sensor cassette, sample holder and peristaltic pump. LED cassette: Green and red LEDs (545-03, 680–02 AU/Roithner Laser Technik) with PLA support inside a transparent cuvette (PS, SE-202295, Spectrecology). Sensor cassette: Two photodiodes (VTB8441BH/ Excelitas-tech) with filters green (dielectric shortpass FES0600/Thorlabs) and red (Dichroic red 647 nm LWP/Opticalfiltershop). Flow through cuvette: 10 mm quartz cuvette (Z804983/Sigma Aldrich), Pump: ISM 596/REGLO Digital MS-2/12/IDEX). Additional: Silicon sensors (TSic™ 506F/ IST-AG and HiH-5031/Honeywell) to monitor humidity and temperature in the proximity of cuvette and pump enclosure throughout the culture.

2. Materials and methods

2.1. Theory

Indicator Phenol red (8.1 mg/L, CAS number 34487-61-1) responds to pH by changing the colour from red to yellow as the culture medium pH changes from 8.2 to 6.8 (~1.5 pH units). Absorption spectra (Fig. 1a, measured with Ocean optics' JAZ spectrometer) of fully prepared cell culture medium (Dulbecco modified Eagle medium, DMEM/F-12 1:1; Life Technologies, Gibco, Carlsbad, CA, USA), show characteristic peaks at 434 nm and 558 nm with an isosbestic point at 470 nm. Characteristic peaks are due to structural isomerism, meaning the existence of phenol red molecules either in its acidic ([HIn] – yellow) or alkaline ([In^-]- red) forms. Consequently, at a given temperature and acidity (or basicity), the concentration ratio [In^-]/[HIn] determines the bulk colour of the host medium. Spectroscopically, Henderson–Hasselbalch equation connects the concentration ratio and host medium pH as,

$$pH = pKa^{In} + \log 10\left(\frac{[In^-]}{[HIn]}\right) \quad (1)$$

where pKa^{In} – indicator dissociation constant [22,23].

By applying Beer-Lambert's law, Eq. (1) can be approximated in terms of absorption ratio as,

$$pH = pKa^{In} + \log 10\left(\frac{\varepsilon_{HIn} A_{560}}{\varepsilon_{In} A_{430}}\right) \quad (2)$$

where ε_{HIn}, ε_{In} - molar absorptivity of indicator acidic and alkaline forms, A_{560}, A_{430} – absorptions at 560 and 430 nm.

At any pH, the bulk indicator concentration (C_t), is a constant as the sum of acid and alkaline concentrations,

$$C_t = [In^-] + [HIn] \quad (3)$$

In highly acidic solutions, essentially the whole indicator is in the acidic form, meaning, C_t=[HIn] conversely, C_t=[In^-] in highly alkaline solutions. With this concept Eq. (2) can be simplified into,

$$pH = pKa^{In} + \log 10\left(\frac{A_{560}}{A_{mx} - A_{560}}\right) \quad (4)$$

where A_{mx} is the maximum absorption of highly alkaline state at 560 nm [23,24].

Absorption as a function of pH at 545 nm (suitable LED nearest to 558 nm wavelength) at ambient temperature is shown in Fig. 1a inset. For fresh medium without any cells Eq. (4) is found to be accurate enough. However, it was not accurate enough for real time pH estimation in active cell culture. This is mainly due to the formation of proteins in the medium and protein coating or biolayer on the cuvette wall leading to non-specific scattering and absorption losses, which in turn induce error in A_{545}. Consequently, an integrated reference transmission measurement at a pH insensitive wavelength (eg. 680 nm, see Fig. 1) became inevitable, for compensating the contributions of other species than the indicator molecules in the light path. We put forward an absorption correction model (hereafter GR model) where the reference channel data is also included in the pH computation with certain approximations, so that the accuracy of pH estimation improved radically. The core objective of the GR model is to separate indicator absorption unequivocally from all other non-specific contributions arising out of detached entities (cells/cell debris/particles), biolayer, and protein binding in progressing culture [3,21,25]. Since absorption in a multicomponent system is cumulative in nature, the total absorption measured by 545 nm and 680 nm sensors can be expressed as

$$A^{545}_{total} = A^{545}_{indicator} + A^{545}_{dm} + t_{545}k_{545} \quad (5)$$

$$A^{680}_{total} = A^{680}_{indicator} + A^{680}_{dm} + t_{680}k_{680} \quad (6)$$

where A_{dm} – absorption due to detached non-indicator molecules in the medium, t, k – biolayer thickness and light loss constant in coated biolayer.

Since indicator molecules do not absorb light at 680 nm,

$$A^{680}_{indicator} = 0 \quad (7)$$

$$\text{Also } A^{680}_{dm} = b\left[dm\right]\varepsilon_{680} \quad (8)$$

Eqs. (7) and (8) in Eq. (6) yields $[dm]$. Additionally

$$A^{545}_{dm} = b[dm]\varepsilon_{545} \quad (9)$$

Now Eq. (5) can be reconstructed as,

$$A^{545}_{indicator} = A^{545}_{total} - \frac{\varepsilon_{545}}{\varepsilon_{680}}A^{680}_{total} - \left[t_{545}k_{545} - \frac{\varepsilon_{545}}{\varepsilon_{680}}t_{680}k_{680}\right] \quad (10)$$

Eq. (10) represents the explicit indicator absorption in terms of measured total absorptions and all other artifacts. However, since many of the artifact terms are practically immeasurable in the context of cell culture, a perfect artifact free measurement is virtually impossible. Nevertheless, the situation can be handled mathematically, with these approximations,

$$\frac{\varepsilon_{545}}{\varepsilon_{680}} = k_{dm} \text{ (absolute constant)}, \quad (11)$$

$$\left[t_{545}k_{545} - \frac{\varepsilon_{545}}{\varepsilon_{680}}t_{680}k_{680}\right] \approx k_{bm} \quad (12)$$

Now Eq. (10) can be simplified into an empirical formula as,

$$A^{545}_{indicator} = A^{545}_{total} - k_{dm}A^{680}_{total} - k_{bl} \quad (13)$$

The glass electrode reference pH data at times of start, medium change and end days of culture, can be used with Eqs. (4) and (13) to extract approximate values of k_{dm} and k_{bl} by means of non-linear least square fit. The approach seems to be straight forward and has been effectively applied for real time pH measurements in 4 long term cell cultures.

Integrated temperature measurements indicate several fluctuations though the temperature is expected to be constant throughout the culture since cells and measurement setup are in the incubator. This can be due to inherent incubator variabilities, heating caused by the measurement electronics and major drops at times of incubator door openings. Door openings affect the temperature and CO_2 levels, which directly affect pH levels of the culture medium. Effect of temperature can be compensated in Eq. (4) with integrated temperature sensor readings by applying Van't Hoff's equilibrium constant correction as,

$$pKa_{T_2} = pKa_{T_1} + \log\left[e^{-7.5\left(\frac{1}{T2} - \frac{1}{T1}\right)}\right] \quad (14)$$

where T_1 - initial temperature, T_2 - new temperature.

2.2. Apparatus

Modular system schematic is shown in Fig. 1b. It consists of LED and sensor modules (cassettes), a sample cuvette, peristaltic pump, and their support structure. Transmitted light from the LED module through the sample is measured with a sensor module. Optical filters in the sensor module eliminate measurement errors resulting from the cross talk due to the scattering of light in culture media by detached cells and debris. Spectra of LED's emission and filter's transmission are shown in Fig. 2a. All the support structures are 3D printed (TAZ 3/LulzBot PLA(Polylactic acid)) and modular cassettes are sealed using hot melt glue. Sealing efficacy was tested by keeping them in DI water bath for around 50 h at 38° celsius. The cassettes can be sterilized with 90% ethanol quite easily. Culture medium flows through the cuvette at a very stable rate (5 ml/min) with the peristaltic pump. Placing commercial peristaltic pumps inside the incubator is usually not possible due to their size, sterilization difficulties, and incompatibility in high humidity (> 90% RH). Commercial pumps are typically rated for 60–80% RH environment mainly due to associated electrical and electronics parts. However, we separated the pump rotatory mechanism from its electronics and casing and encapsulated it in a separate 3D printed PLA casing. The whole pump can now be thoroughly sterilized with relative ease. Two short (< 30 cm) silicone tubes (228–0704AU/VWR International) establish the flow through the cuvette and peristaltic pump. Silicon temperature sensor and humidity sensors continually monitor humidity and temperature in the proximity of cuvette and pump enclosure throughout the culture. The entire modular unit goes into an incubator after sterilization. Once the measurement commences at the start of culture, no further parts replacement, recalibration is needed till the end of culture. Measurements are carried out without any special manual attention or maintenance, exempting the medium changing days.

The LEDs are powered with constant current sources and their light output stability is mainly limited by the LEDs themselves. The LEDs relative radiant intensity as a function of temperature is shown in Fig. 2b. The spectral stability of LEDs emission during long term operation measured with spectrometer is shown in Fig. 2c. The photodiodes are reverse biased for a linear light response and the photocurrent to voltage conversion is done with resistors. All the sensors are powered by a regulated 5 V power supply. LEDs, photodiodes, temperature and humidity sensors are controlled with a microcontroller board (Arduino Uno). A 16 bit 8 channel data acquisition board of our own design is used for

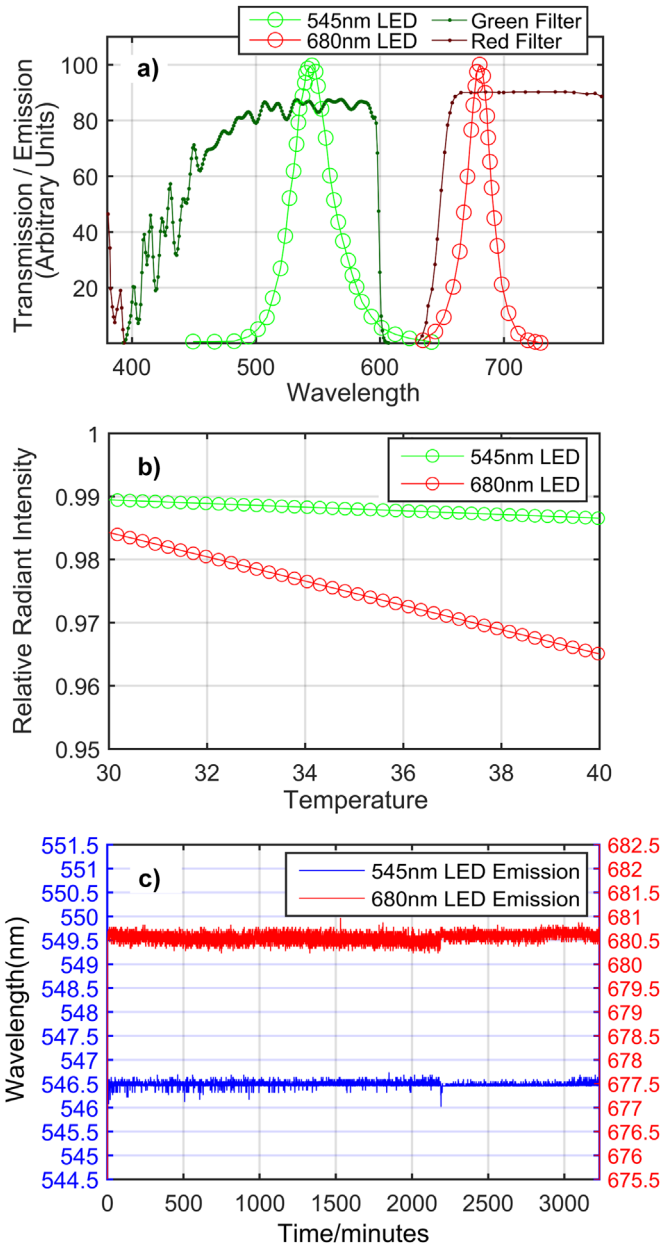

Fig. 2. a) Emission and transmission spectra of green and red LEDs (545-03, 680-02AU/Roithner Laser Technik) and green (Dielectric shortpass FES0600/Thorlabs) and red (Dichroic Red 647 nm LWP/Opticalfiltershop) filter. b) Relative radiant intensity as a function of the temperature for the green and red LEDs in the cassette module. An intensity change of $\pm 0.15\%$ and $\pm 1\%$ need to be expected in green and red channels respectively for ± 5 °C change around the incubator temperature. c) Spectral stability of the green and red LEDs measured with a spectrometer. The jump seen at ~2200 min is when the LEDs were restarted after 2 min pause. Nevertheless, wavelength standard deviation computed is 0.1340 nm and 0.2398 nm for green and red LED, respectively, indicating relatively stable emissive spectral consistency over time.

digitizing the voltage signals from the sensors. The measurement data is sent to the PC via USB and the PC stores the received data in Matlab's file format. A 5 s (2500 samples) average of data in 60 s intervals at 500 Hz sampling rate was used in real time measurements. The used method stored all the measured samples. The standard deviations based on these values was also computed and, based on mean and standard deviation the main features of the noise distribution were observed. In future more features of the distribution can be computed and used to get better estimates of the results. Some error removal and signal modeling methods are planned. Data logging, sensor control (via microcontroller), data processing and pH computation are carried out with Mathworks, Matlab (vR2015b) in conjunction with Arduino Matlab support package.

2.3. Isolation and culture of adipose stem cells and fibroblasts

The study was conducted in accordance with the ethics committee of the Pirkanmaa Hospital District, Tampere, Finland (R03058). Adipose stem cells (ASCs) were isolated from an adipose tissue sample obtained with written informed consent from one female donor (age 53 years) undergoing elective surgical procedures at the Department of Plastic Surgery, Tampere University Hospital, Tampere, Finland. Human ASCs were isolated by mechanical and enzymatic procedure as previously described [26]. In addition to ASCs, commercial fibroblast cell line (ATCC® CRL-2429™; ATCC, Manassas, VA, USA) was used in the first measurements.

Isolated ASCs and commercial fibroblasts were cultured in DMEM/F-12 1:1 medium (CO_2 independent and dependent measurements) supplemented with 1% L-analyl-L-glutamine (GlutaMAX I; Life Technologies, Gibco), 1% antibiotics (p/s; 100 U/ml penicillin, 0.1 mg/ml streptomycin; Lonza, BioWittaker, Verviers, Belgium) and 5% human serum (Human Serum AB Male HIV tested; Biowest, Nuaillé, France). This medium composition is referred to as basic medium (BM) in this article. The cells were seeded into T75 nunclon™ flasks in 40 ml of BM (the first three measurements) or in 25 ml of BM (the fourth measurement). Cell seeding density was sparse at the beginning of the culture but the flasks became fully confluent during (the) two week culture period. At time of medium change, 10 ml of used BM was removed and replaced by 10 ml of fresh BM. Medium was changed once a week.

3. Results and discussion

3.1. pH measurements at room temperature (no cells)

pH values measured optically from several pH samples with a calibrated sensor are shown in Fig. 3. All the reference measurements were carried out with a pH glass electrode (WTW Multi 340i with SenTix 41-3 electrode, Weilheim, Germany).

3.2. Real time pH measurement during cell culture

Online measurements were carried out in two CO_2 independent and two CO_2 dependent culture media. Measured Green, red and GR model absorptions throughout the culture and glass electrode reference pHs Vs. various absorptions at times of 1) culture start 2) medium change 3) culture end can be found in Appendix A, Supplementary material. Optical pHs measured with GR model continuously from 14 days culture is shown in Fig. 4. The constants extracted for Eqs. (4) and (13) from 4 cultures are given in Table 1. At the end of cultures, the used BM was microbial tested but no contamination was identified. Light microscope images of ASC culture (4th measurement) before and after the two-week culture period are shown in Fig. 5. Cell proliferation was efficient during the measurements and the flasks became fully confluent during the two-week culture period.

The large spikes seen in the pH data (Fig. 4) occur mainly at times of medium change due to drop in incubator temperature and CO_2 levels and addition of a fresh unbuffered medium (pH~8.3). Drop in temperature and CO_2 levels shoot-up the pH within minutes, but on the other hand gaining the stable pH back takes hours even in incubator conditions. Microscopy examination

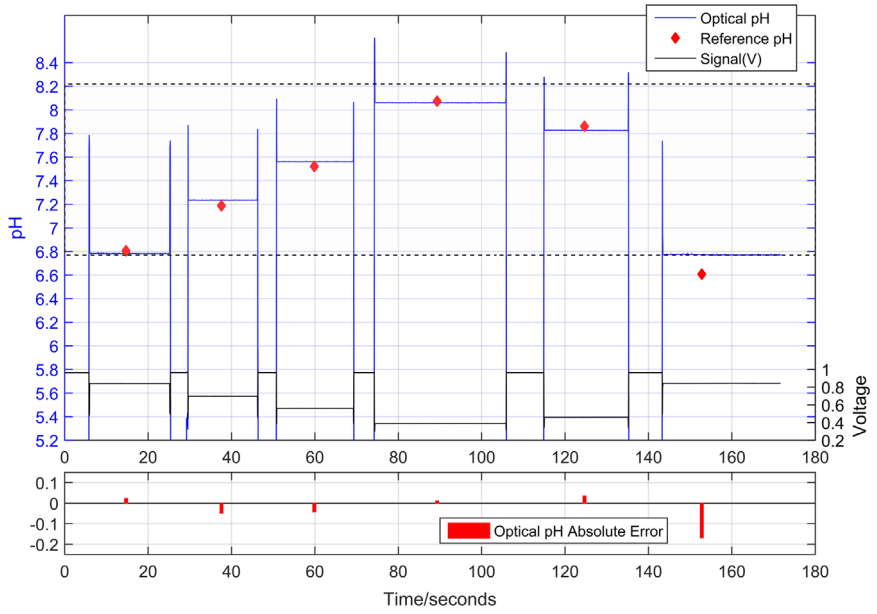

Fig. 3. Signal voltage and optically measured pH values for several culture medium samples at room temperature after three point calibration. Textbook equation (Eq. (4)) was used for pH computation. pKa is estimated to be 7.723 with RMS error of 0.0274. Reference pHs measured with glass electrode are also shown. Dashed box represents the reliable pH range with indicator phenol red [pH 6.7–8.3].

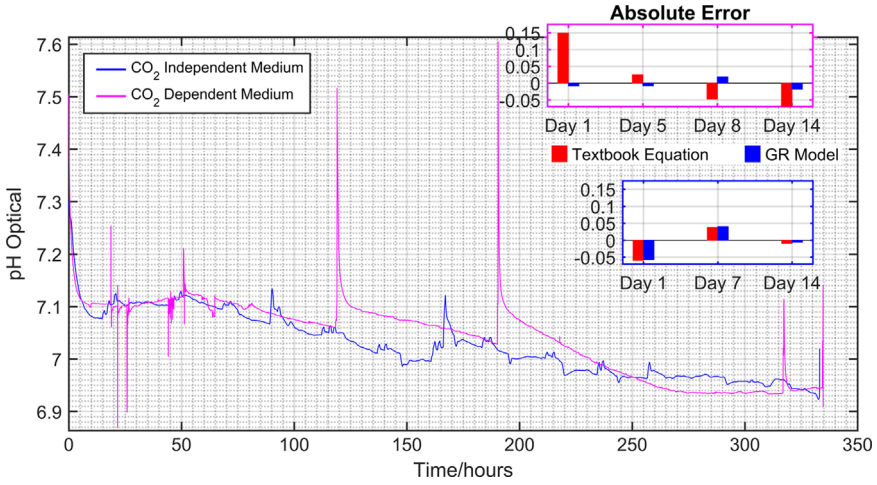

Fig. 4. Optical non-contact pH in adipose stem cell culture in CO_2 dependent and independent cultures. Real time 24/7 measurement for 14 days continuously with 1 min measurement interval. A 2500 samples, 5 s worth, was averaged in every minute. The large spikes are at times of medium change predominantly due to drop in incubator temperature and CO2 levels and addition of a fresh unbuffered medium (pH∼8.3). Figure inset: Absolute error with text book pH formula (Eq. (4)) and GR model (Eq. (13)). Reference glass electrode pHs were collected at the days of culture start, medium change(s) and culture end.

Table 1
Values of absolute constants extracted for Eq. (4) and Eq. (13) for online pH measurements in 4 cultures.

Culture/Type of medium	pKa	k_{dm}	k_{bl}	Mean pH Error	Number of Calibration samples
CO_2 dependent	7.6272	1.3063	0.0615	0.0131	4
CO_2 dependent	7.5952	1.7291	0.0870	0.0344	3
CO_2 independent	7.9500	0.0109	0.0015	0.0269	3
CO_2 independent	7.8556	0.0011	0.0003	−0.0101	3

of the cuvette at the end of cell culture confirmed the existence of biolayers on all internal walls. See Fig. 6 for the macro and micro images of biolayer on cuvette wall after the 4th culture.

4. Conclusions

Phenol red indicator molecules are relatively stable, enabling high degree of inherent measurement accuracy. Rapid measurements are possible since the indicator chemical equilibration is fairly fast. Change in absorption per pH (dA/dpH) at 545 nm is 3.2 times higher than that at 434 nm, therefore, together with 16-bit data acquisition resolution down to 0.1 pH became possible. No special optics or lenses are used, enabling reliable measurements in a highly humid environment (> 90% RH) where moisture or droplets can alter the properties of optical systems unless special heating or hot lenses are used. A circular 5 mm light beam, instead of a focused narrow one, delivers more area for light- liquid interaction enabling enhanced responsivity/sensitivity. Furthermore, the small particles then would not have any significant signature in the transmission measurement. Light measurements at a small distance from the cell growth location have limitations though it maintains cell viability and avoids practically all instances of phototoxicity due to the oxygen dependent reactions of free radical species by photon absorption [27]. The 3D printed modular arrangements and pump mechanism for measurement are unique,

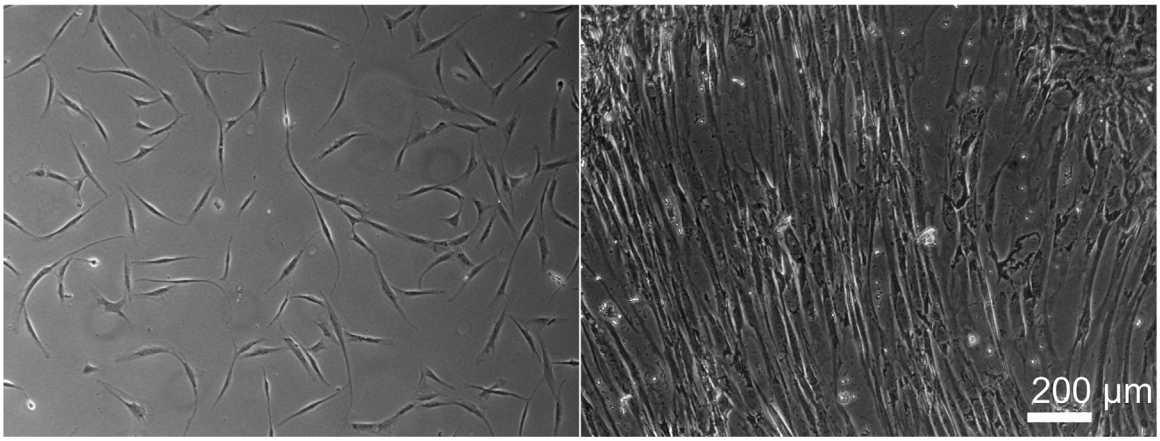

Fig. 5. Adipose stem cells images a) at the start and b) at the end of 4th measurement taken with Zeiss AXIO Vert.A1 microscope, Axio Cam ERc5s with 5 × objective. Cells showed efficient proliferation during the measurement and became fully confluent during the two week culture.

robust and reproducible. Though the sealed PS (polystyrene) cassette modules work fine, careful handling is essential at the time of sterilization and initial installation to avoid scratches. Cassettes, using glass or scratch free transparent materials could be even better and robuster.

Closed sample looping neither wastes nor extracts any sample off the incubator avoiding lengthy sampling lines, drastic temperature changes, and associated cell shock. Integrated temperature compensation seemed to be very important. Addition of a CO_2 sensor could be even interesting to realize bicarbonate buffering phenomena precisely in culture with CO_2 dependent medium.

With Arduino, a low cost software control of LEDs, sensors, and data acquisition is straight forward and convenient. Measurement channels can be kept constantly 'ON' throughout the culture, or programmatically evoked in predefined intervals for measurement. Sensor calibration was carried out with known pH buffers made from fresh cell culture medium. Alternatively, optical pH buffers can be prepared with dissolving phenol red in commercial standard pH buffers.

Effect of non-indicator absorptions and biolayer artifacts are reasonably compensated with the GR model. This improved the pH computation accuracy dramatically which seems to be an adequate step in long term 24/7 real time measurements. Likelihood of molecular or structural heterogeneity of non-indicator error species and possible changes in biolayer thickness during culture is likely to correspond to non-singular values for k_{dm} and k_{bl} in GR model. However, error estimation in four cultures confirmed unique values derived from non-linear least square fit are sufficient enough to compute pH with high accuracy.

In addition to the aforementioned errors, other errors that could be present in colorimetric indicator pH analysis include, salt error (ionic strength changes), protein error (indicator-protein binding), and alcohol error. Since the total inorganic salts in the medium is only 142 mM, salt error is relatively insignificant. Alcohol error can also be fully neglected in an alcohol free culture. But protein error (see: Fig. 6) could have some effect on our measurements. However, addressing it specifically is practically impossible due to complexity of the medium and the long culture

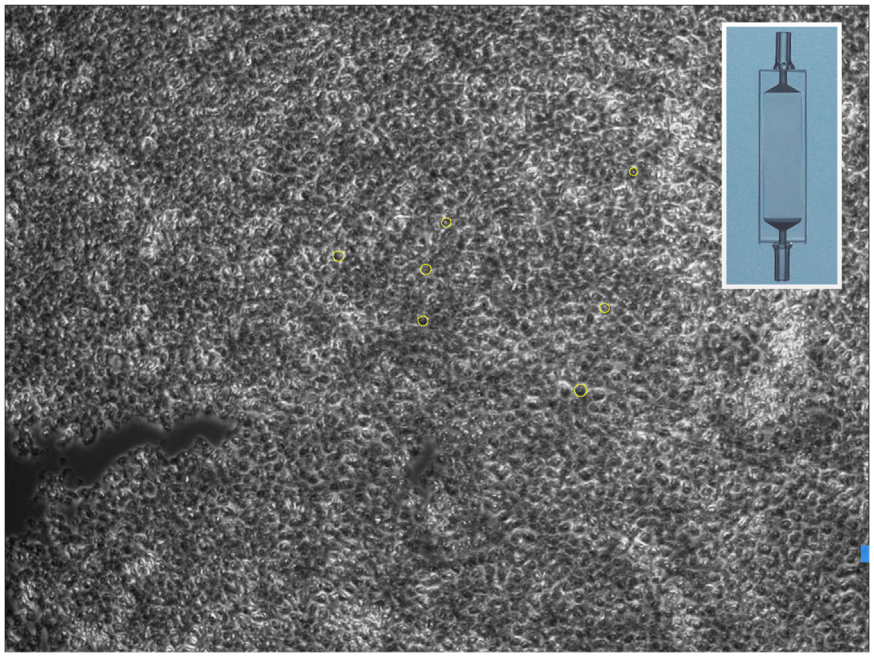

Fig. 6. Biolayer on the internal cuvette wall imaged with phase contrast microscope (Zeiss Axio observer z1-20 × objective). Approximate average grain size: 8 µm. Inset: Dry cuvette after 4th culture where difference in light transmission through measurement region and surrounding areas of the cuvette is recognizable with slightly varying colors.

process. Nevertheless in general, GR model performs artifact compensation effectively. Measurement repeatability has been tested successfully both in room temperature and incubator conditions. Needless to say, catastrophic events such as contamination (bacterial, yeast etc.) can affect the light measurement undesirably. However, such instances can be easily identified from unexpected signal drop (intensity loss) due to elevated absorptions by the cloudiness of intruder colonies. Turbidity arising from particles or cell debris in culture can have different optical effects at different wavelengths. Together with pH, a 90° scattering measurement channel is also to be incorporated to collect information about the turbidity in general, and also the colour of the topic that causes the turbidity. The plan is to approximately measure the turbidity and to compensate the colour effects of turbidity in pH computation if there is any.

The modular arrangement of 3D printed parts, though exclusively intended for non-contact cell culture pH measurements, the technique can have applications in many sensing situations in analytical chemistry.

Funding

This study was funded by Human Spare Parts 2 project (40332/14) granted by Finnish Funding Agency for Technology and Innovation (TEKES).

Acknowledgements

We thank Jouni Niemelä, Department of Automation Science & Engineering, Tampere University of Technology and Anna-Maija Honkala, BioMediTech, Tampere for their valuable technical assistance.

Appendix A. Supporting information

Supplementary data associated with this article can be found in the online version at http://dx.doi.org/10.1016/j.talanta.2016.09.021

References

[1] A. Sarkar, Bio Instrumentation, in: Stem Cell Culture, Discovery Publishing House, Pvt. Ltd., 2009, pp. 29–33.
[2] E.B. Magnusson, S. Halldorsson, M.T. Ronan, K. Leosson, Real-time optical pH measurement in a standard microfluidic cell culture system, Biomed. Opt. Express 4 (9) (2013) 1749–1758.
[3] M. Naciri, D. Kuystermans, M. Al-Rubeai, Monitoring pH and dissolved oxygen in mammalian cell culture using optical sensors, Cytotechnology 57 (3) (2008) 245–250.
[4] J.P. Mather, M. Tsao, Expression of cloned proteins in the mammalian cells: Regulation of Cell-Associated Parameters, in: A.S. Lubiniecki (Ed.), Large-Scale Mammalian Cell Culture Technology, 10, Marcel Dekker, Inc, 1990, p. 164.
[5] A. Allaire, M.X. Luong, K.P. Smith, Basic cell culture growth conditions in: Human Stem Cell Technology and Biology, in: G.S. Stein, M. Borowski, M. X. Luong, M.-J. Shi, K.P. Smith, P. Vazquez (Eds.), A Research Guide and Laboratory Manual, Wiley-Blackwell, 2011, pp. 34–35.
[6] J. Pruszak, M. Döbrössy, J. Kieninger, K. Aravindalochanan, G.A. Urban, G. Nikkhah, Neural Stem Cells, in: G.M. Artmann, S. Minger, J. Hescheler (Eds.), From Cell Fate and Metabolic Monitoring Toward Clinical Applications in: Stem Cell Engineering Principles and Applications, Springer, Heidelberg, Dordrecht, London, New York, 2011, pp. 442–443.
[7] G. Nabovati, E. Ghafar-Zadeh, M. Sawan, A 64 pixel ISFET-based biosensor for extracellular pH gradient monitoring, in: International Symposium on Circuits and Systems, vol. 2015-July, 2015, pp. 1762–1765.
[8] D. Wencel, T. Abel, C. McDonagh, Optical Chemical pH Sensors (review), Anal. Chem. 86 (1) (2014) 15–29.
[9] W. Baumann, M. Lehmann, A. Schwinde, R. Ehret, M. Brischwein, B. Wolf, Microelectronic sensor system for microphysiological application on living cells, Sens. Actuators B Chem. 55 (1) (1999) 77–89.
[10] V. Saucedo, B. Wolk, A. Arroyo, C.D. Feng, Studying the drift of in line pH measurements in cell culture, Biotechnol. Prog. 27 (3) (2011) 885–890.
[11] S. Lee, B.L. Ibey, G.L. Coté, M.V. Pishko, Measurement of pH and dissolved oxygen within cell culture media using a hydrogel microarray sensor, Sens. Actuators B Chem. 128 (2) (2008) 388–398.
[12] M.A. Hanson, X. Ge, Y. Kostov, K.A. Brorson, A.R. Moreira, G. Rao, Comparisons of optical pH and dissolved oxygen sensors with traditional electrochemical probes during mammalian cell culture, Biotechnol. Bioeng. 97 (4) (2007) 833–841.
[13] G. McMillan, J. Gray, The essentials of pH measurement design, installation, maintenance, and improvement, in: International Instrumentation Symposium, 2009.
[14] M. Oura, H. Kubo, S. Yamamori, S. Takeda, T. Shimizu, T. Okano, Development of cell culture monitoring system and novel non-contact ph measurement, in: Conference Proceedings: Annual International Conference of the IEEE Engineering in Medicine and Biology Society, vol. 2011, 2011, pp. 22–25.
[15] J. Ehgartner, H. Wiltsche, S.M. Borisov, Low cost referenced luminescent imaging of oxygen and pH with a 2-CCD colour near infrared camera, Analyst 139 (19) (2014) 4924.
[16] J. Jang, S.-J. Moon, S.-H. Hong, I.-H. Kim, Colorimetric pH measurement of animal cell culture media, Biotechnol. Lett. 32 (11) (2010) 1599–1607.
[17] S. Capel-Cuevas, M.P. Cuéllar, I. de Orbe-Payá, M.C. Pegalajar, L.F. Capitán-Vallvey, Full-range optical pH sensor based on imaging techniques, Anal. Chim. Acta 681 (1–2) (2010) 71–81.
[18] Z. Liu, J. Liu, T. Chen, Phenol red immobilized PVA membrane for an optical pH sensor with two determination ranges and long-term stability, Sens. Actuators B Chem. 107 (1) (2005) 311–316.
[19] X. Xu, S. Smith, J. Urban, Z. Cui, An in line non-invasive optical system to monitor pH in cell and tissue culture, Med. Eng. Phys. 28 (5) (2006) 468–474.
[20] X.-D. Wang, O.S. Wolfbeis, Fiber-optic chemical sensors and biosensors (2008–2012), Anal. Chem. 85 (2) (2013) 487–508.
[21] A.S. Jeevarajan, S. Vani, T.D. Taylor, M.M. Anderson, Continuous pH monitoring in a perfused bioreactor system using an optical pH sensor, Biotechnol. Bioeng. 78 (2002) 467–472.
[22] F. Lee, Spectrophotometric determination of blood pH, J. Biol. Chem. 236 (5) (1961) 1589–1595.
[23] D.D. Van Slyke, L.V. Hankes, J.J. Vitols, Photometric determination of pH with a single standard and calculation by nomogram, Clin. Chem. 12 (12) (1966) 849–870.
[24] J. Sendroy, F.L. Rodkey, Apparent dissociation constant of phenol red as determined by spectrophotometrometry and by visual colorimetry, Clin. Chem 7 (1961) 646–654.
[25] U. Kragh-Hansen, J.V. Møller, Protein binding of small molecules, Biochim. Biophys. Acta Protein Struct. 295 (2) (1973) 447–456.
[26] M. Patrikoski, M. Juntunen, S. Boucher, A. Campbell, M.C. Vemuri, B. Mannerström, S. Miettinen, Development of fully defined xeno-free culture system for the preparation and propagation of cell therapy-compliant human adipose stem cells, Stem Cell Res. Ther. 4 (2) (2013) 27.
[27] M.M. Frigault, J. Lacoste, J.L. Swift, C.M. Brown, Live-cell microscopy - tips and tools, J. Cell Sci. 122 (Pt 6) (2009) 753–767.

PUBLICATION IV

Monitoring pH, temperature and humidity in long-term stem cell culture in CO_2 incubator

Rajan DK, Verho J, Kreutzer J, Valimaki H, Ihalainen H, Lekkala J, Patrikoski M, Miettinen S.

IEEE International Symposium on Medical Measurements and Applications, MeMeA 2017 - Proceedings. IEEE, pp. 470–474.
https://doi.org/10.1109/MeMeA.2017.7985922

Monitoring pH, temperature and humidity in long-term stem cell culture in CO_2 incubator

Dhanesh Kattipparambil Rajan,
Jarmo Verho, Joose Kreutzer, Hannu Välimäki,
Heimo Ihalainen, Jukka Lekkala
BioMediTech Institute and Faculty of Biomedical Sciences and Engineering, Tampere University of Technology
Tampere, Finland
dhanesh.kr@tut.fi

Mimmi Patrikoski, Susanna Miettinen
Adult Stem Cell Group, BioMediTech
Institute of Biosciences and Medical Technology
University of Tampere
Science Center, Tampere University Hospital
Tampere, Finland

***Abstract*—Cell culture in stem cell research is on the rise, not only for basic research but also for its potential medical and therapeutic applications. Monitoring culture process using sensors throughout the culture helps to optimize culture conditions for optimal growth and maximize yield from the cells. Further, the sensor data gives insight into developing better cell culture systems. Typical stem cell culture platforms, e.g. well plates or flasks, cannot be easily equipped with sensors and impose many challenges in periodic process measurements in a CO_2 incubator. We present an incubator compatible modular measurement system with three sensors, to monitor pH, temperature and humidity continuously throughout the culture. Sensors are assembled around a flow through cuvette for highly sterile non-contact measurements. No sample preparation or sample extraction from the incubator is needed and the measurements are carried out in a closed flow loop without wasting any medium. The modular assembly is novel, reusable and feasible for humid incubator environments. The system has been tested, validated and used in mesenchymal stem cell expansion and differentiation, for periods ranging from two to three weeks. Once the measurement has commenced at the beginning of culture, continuous measurements without sensor recalibration or special manual attention are carried out till the end of the culture. Measurement data clearly show the interplay between measured parameters, indicating a few stress sources present all through the culture. Additionally, it gives an overall picture of behavior of critical control parameters in an incubator and points out the need for bioprocess systems with automatic process monitoring and smart control for maximum yield, optimal growth and maintenance of the cells.**

Keywords— incubator compatible sensors, cell culture incubator environmental monitoring, non-contact cell culture measurements, long-term cell culture measurements, long-term optical cell culture pH measurements

I. INTRODUCTION

Stem cell research is a rapidly expanding field to develop therapeutic agents to treat diseases as well as to study disease development from early stages[1–3]. Cell culture is a critical part in stem cell research and culture parameters need to be refined according to the final purpose of the culture. Monitoring culture parameters using sensors throughout the culture helps to optimize culture conditions for optimal growth and maximum productivity. Further, the sensor data helps to visualize necessary control schemes to be considered in designing optimized compact cell culture systems. Small-scale upstream cell culture for bioprocess development often occurs in flasks and multi-well plates kept in CO_2 incubators. Incubators regulate temperature (~37°C), humidity (~95%RH) and gaseous atmosphere (CO_2,/O_2) around the cells, and also indirectly the pH of the culture medium with a bicarbonate buffer system. These parameters, ideally should be constant and not a source of experimental variations[4]. However, variations do occur, which create stress, and cells can respond, depending on the cell type, nature and duration of the stress, in various ways ranging from the activation of survival pathways to the initiation of cell death [5]. It can also adversely affect the cell attachment on culture platforms [6]. There is often an interplay between these parameters, for instance, the pH set-point, can be influenced not only by CO_2 levels, but also by fluctuations in temperature and medium evaporation. Therefore, the incubator door opening conditions (duration and frequency), the nature of the fresh medium (preheated/pre-buffered) added at times of medium change, are also external stressors, resulting in undesirable experimental variations. When cells proliferate and metabolize nutrients, the byproducts (CO_2, pyruvic, lactic acids etc.) tend to lower the pH, but the active bicarbonate buffer system, in principle, should counteract and stabilize the pH set-point. However our previous studies indicate a drop in pH in prolonged cultures which has been verified with electrochemical sensors as well [7]. In this study, we measured the pH, temperature, and humidity continuously in prolonged cultures in a water-jacketed incubator. Conventionally, sensor matrix chips or the combination of electrochemical and optical sensors are widely used in multi-analyte sensing, which usually requires large sample volume and physical contact with the measurand [8–16]. Electrochemical sensors, generally, are precise, fast and reversible, but signal drift, need for periodic calibration and maintenance are drawbacks in long-term biomedical applications. Several reported optical sensors also require sampling, physical contact or culture vessel modification and further, signal drift by photobleaching/leaching is also a concern in long term measurements[11,16–18]. On the other hand, non-contact measurement techniques are highly advantageous since they reduce instances of sterilization, minimize the risks of contamination and can be implemented without wasting any culture medium. Non-contact, real time pH monitoring is

This study was funded by Human Spare Parts 2 project (40332/14) granted by Finnish Funding Agency for Technology and Innovation (TEKES).

desired in several areas, including cell therapy experiments. When the culture medium contains phenol red, changes in its characteristic light absorptions as a function of pH can also be exploited for non-contact pH estimation[14,15,17,19,20]. One basic method is measuring light intensities at a pH sensitive wavelength and at a neutral reference wavelength. However, there are a few practical issues for adapting the reported methods directly into the stem cell culture environment. Extracting the culture sample to be measured out of the incubator using length tubings and external pumps is somewhat unappealing. Lengthy sampling lines in and out of the incubator impose large temperature differences, and demand large sample volume and more culture supplements. Further, it creates sterilization issues and necessitate high flow rates for fast sensor response, which in turn can be stressful for the cells. The cross talk between light measurement channels, when light beams of two wavelengths operate in close proximity, due to scattering of light by detached cells or debris also needs to be addressed electronically or optically. Moreover, the effect of possible biolayer (on the internal wall of the measurement cell) on the pH and the effect of temperature on the pH are left untreated [14,15,17,19,20]. In our multisensor modular measurement system, for pH, the previously reported optical non-contact pH sensor employing a dual wavelength measurement is utilized [7]. The system parts are 3D printed, robust and fully modular. It can be easily sterilized and placed inside the incubator, therefore, no special sampling or sample extraction from the incubator is needed. Effect of temperature on absorption is also compensated continuously. The proposed absorption correction model [7] compensates non-specific absorptions (eg. by biolayers) which improves the pH accuracy significantly. The temperature sensor which is a platinum resistance thermometer in a stainless steel housing is highly precise and suitable for medical process measurements. The thermoset polymer based capacitive humidity sensor is fast, linear and has excellent long term stability. All the sensors are incubator compatible, and are tightly attached to the measurement cuvette for continuous long term cell culture measurements.

II. MATERIALS AND METHOD

A) Experimental

The modular measurement arrangement is shown in Fig.**1**. Mostly all support parts are 3D printed using PLA material. The flow through cuvette (Z804983/Sigma Aldrich) and silicon tubes are autoclave sterilized preceding the culture. Resistance thermometer (Heraeus-30500109/with stainless steel housing), humidity sensor (HIH-5031/Honeywell/factory calibrated), and pH sensor module are sterilized with 70-90% ethanol. Temperature and humidity sensors stay in contact with the external wall of the flow through cuvette. During measurements, medium is pumped through the flow through cuvette at ~ 3-5ml/min with the help of a modified peristaltic pump (ISM 596/REGLO/Digital MS-2/12/IDEX) encapsulated in a 3D printed airtight box. The measurement system is placed next to the culture bottle inside the incubator and the medium is constantly circulated through the flow through cuvette during the culture. No sample preparation or external sample

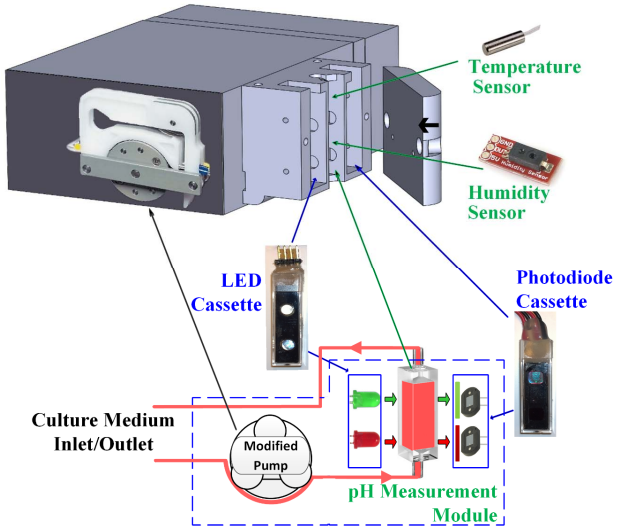

Fig.1. Modular incubator compatible measurement system. Check [7] for pH sensor module details. Measurement cuvette: 10mm Quartz flow through cuvette (Z804983/Sigma Aldrich). Pump: Modified peristaltic pump (ISM 596/REGLO Digital MS-2/12/IDEX). Temperature sensor: Platinum resistive thermometer (Heraeus 30500109/PT100 in stainless steel housing). Humidity sensor: Thermoset polymer capacitive sensor (HIH-5030/5031/Honeywell-factory calibrated).

extraction outside of the incubator is needed. A CO_2 sensor (GC-0016-COZIR/ Factory calibrated) was also used for collecting CO_2 data for short-term characterization measurements. A 16 bit 8 channel data acquisition board of our own design is used for digitizing the voltage signals from the sensors. The measurement data is sent to the PC via USB and, the PC stores the received data in Mathworks, Matlab's file format. A 5 s (2500 samples) average of data in 60 s intervals at 500 Hz sampling rate was used in real time measurements. Data logging, sensor control (via microcontroller), data processing and pH computation are carried out with Matlab (vR2015b). Once the measurement has begun, no recalibration or maintenance is needed and measurements can be carried out without any special manual attention till the end of the culture.

B) Cells and Culture Medium

The cell expansion and osteogenic differentiation experiments described in this study were conducted in accordance with the ethics committee of the Pirkanmaa Hospital District, Tampere, Finland (R15161). Mesenchymal stem cells were isolated from adipose tissue samples (adipose stem cells, ASCs) obtained with written consent from donors undergoing elective surgical procedures at the Department of Plastic Surgery, Tampere University Hospital, Finland. Human ASCs were isolated by mechanical and enzymatic procedure as previously described [21]. In addition to ASCs, commercial fibroblast cell line (ATCC® CRL-2429™; ATCC, Manassas, VA, USA) was used in the initial trial measurements.

The pH, temperature and humidity were monitored during cell expansion and osteogenic differentiation. For cell

expansion, ASCs were cultured in DMEM/F-12 1:1 medium supplemented with 1% l-analyl-l-glutamine (GlutaMAX I; Life Technologies, Gibco), 1% antibiotics (p/s; 100 U/ml penicillin, 0.1 mg/ml streptomycin; Lonza, BioWittaker, Verviers, Belgium) and 5% human serum (Human Serum AB Male HIV tested; Biowest, Nuaillé, France). This medium composition is referred to as basic medium (BM) in this article. The cells were seeded into T75 nunclon™ flasks in 25 ml of BM in the first test (Fig.3). Cell seeding density was sparse at the beginning of the culture but the flasks became fully confluent during the two-week culture period. At the time of medium change, 10ml of used BM was removed and replaced by 10 ml of fresh BM. Medium was changed once a week.

For the osteogenic differentiation, cells were cultured in T150 flasks in osteogenic medium containing DMEM/F-12 1:1 medium (Life Technologies, Gibco, Rockville, MD) supplemented with 5% human serum (Biowest), 1% GlutaMAX I (Life Technologies), 1% p/s (p/s; 100 U/mL penicillin, 0.1 mg/mL streptomycin; Lonza), 200 µM L-ascorbic acid 2-phosphate (Sigma), 10mM beta-glycerophosphate (Sigma) and 5 nM dexamethasone (Sigma)]. Medium was changed twice a week during the three weeks' induction period.

III. RESULTS AND DISCUSSION

A) System Characterization

In an effort to understand the effect of CO_2 and temperature separately on pH, we measured the pH of the culture medium (without cells) as a function of temperature in the absence and presence of CO_2. The measurement results are shown in Fig. **2**a and Fig. **2**b. The pH decreases with increase in the temperature as expected [22]. A decrease of ~ 0.2 pH unit in the absence of CO_2 and a decrease of ~1.0 pH unit in the presence of CO_2 were observed for ~10°C temperature rise. Culture medium with the bicarbonate buffer system is typically alkaline in the absence of CO_2 due to sodium bicarbonate ($NaHCO_3$) in the medium (Equation 1). Inside the incubator, CO_2 dissolves in the medium to form carbonic acid (Equation 2). The carbonic acid to $NaHCO_3$ ratio at 37°C regulates the pH (Equation 2). Since the $NaHCO_3$ concentration is set by the media manufacturer, typically, a 5-10% CO_2 environment is necessary to establish a

$$NaHCO_3 \leftrightarrow Na^+ + HCO_3^- \quad (1)$$

$$CO_2 + H_2O \leftrightarrow H_2CO_3 \leftrightarrow HCO_3^- + H^+ \quad (2)$$

Carbonic acid — Bicarbonate (conjugate base)

stable physiological pH [6,20-21]. The stabilization of pH, both in the absence and presence of CO_2 (Fig. **2**a and Fig. **2**b) is seemingly, not a fast process, therefore medium pre-conditioning (pre-heating and pre-buffering) preceding the use

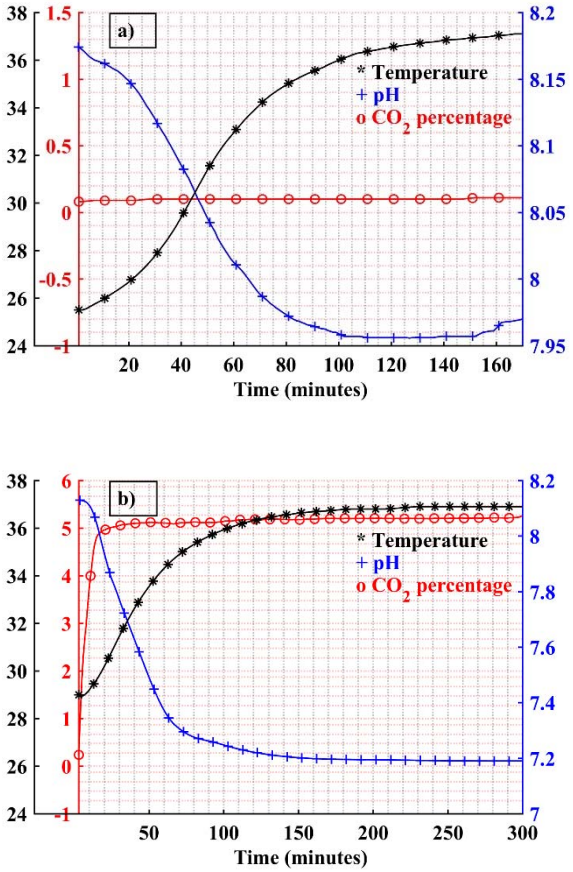

Fig. 2. pH of the culture medium (without cells) as a function of temperature. a) Measurement in the absence of CO_2. The CO_2 sensor showed 0.0995% mean base value though the incubator CO_2 was set to zero. Around ~0.2 pH unit drop is seen with around 10°C temperature rise b) Measurement in the presence of CO_2. It took ~30 minutes to reach a stable 5% CO_2 environment after CO_2 was turned on. Relatively large pH drop (~1.0 pH units) is seen in the presence of CO_2 over ~10°C temperature rise. The effect is presumably due to combined influence of temperature and CO_2. Noticeably, the pH stabilization time is in the order of hours in both the cases in the studied typical culture flask arrangement in the incubator.

of any fresh medium is recommended to reduce the pH shock to cells.

B) Cell Culture pH Measurements.

Measurement results from cell expansion and osteogenic differentiation are shown in Fig.3 and Fig.4 respectively. The sudden large transients (spikes) in the data are mainly at times of medium change. Addition of fresh medium and drop in temperature and CO_2 by incubator door openings at the time of medium change, shifts the chemical equilibrium (Equation 1&2) and shoots-up the pH. Further, the overall drop in solution H^+ ionization due to drop in temperature also contributes to slight pH variations. Small pH changes e.g. from 7.3 to 7.2 is a seemingly small deviation, but it brings about actually large

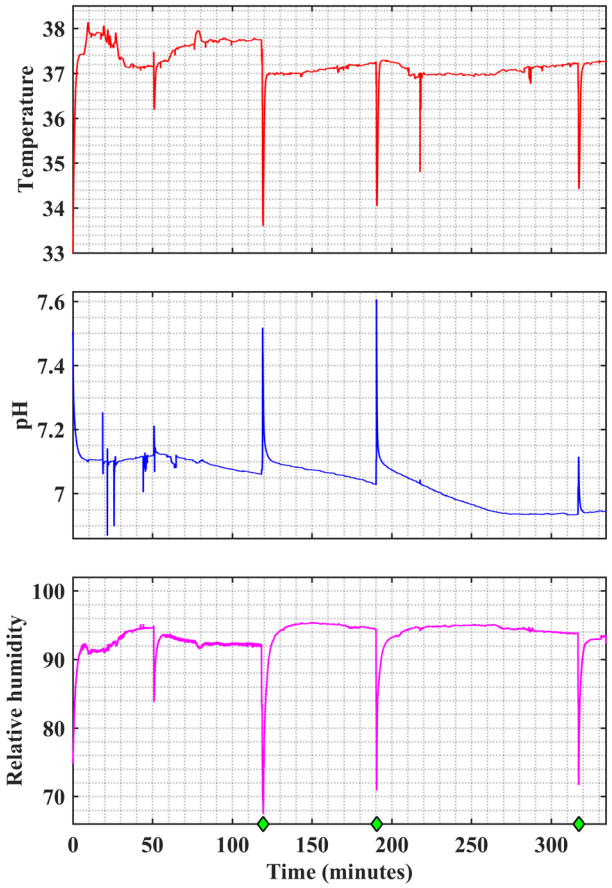

Fig.3. Temperature, pH and humidity measured during adipose stem cell expansion of ~15 days. The large spikes are at times (green marker) of medium change, predominantly due to drop in incubator temperature and CO_2 levels and addition of fresh medium (pH~8.3) [7].

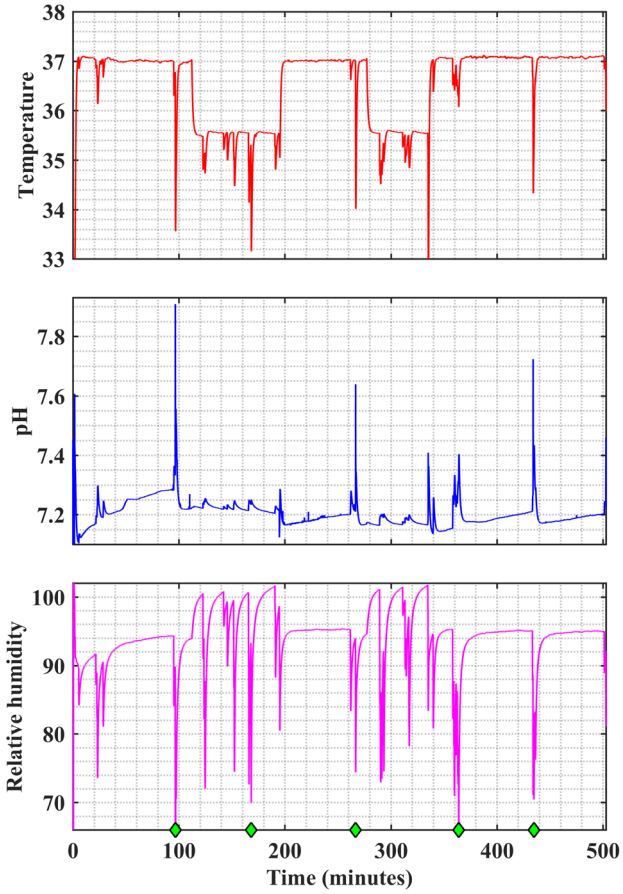

Fig.4. Temperature, pH, and humidity measured during osteogenic differentiation of human adipose stem cells for ~21 days. The large spikes are at times (green marker) of medium change, predominantly due to drop in incubator temperature and CO_2 levels and addition of fresh unbuffered medium (pH ~ 8.4).

(~40%) changes in the H^+ concentration. After the medium change, once the temperature and CO_2 levels are re-established, the buffer system re-establishes the pH, in principle back to the set-point. As the cells constantly metabolize glucose and other nutrients, the waste products (pyruvic, lactic acids, CO_2 etc.) can however, slow down the pH stabilization and decrease the pH over time. pH curves in Fig.3 and Fig.4 reflect the combined influences of CO_2, temperature and cell metabolism. One possible reason for the clipping in humidity data (Fig.4), though its actual reason is unclear, is a tiny leakage through the incubator door sealing. Several hours shift seen in the simultaneous temperature measurement also might be due to the same issue. The expected maximum error due to the temperature sensor itself and measurement inaccuracies is 232mK with 2.3mKrms noise (averaging 625 samples/data acquisition). With temperature compensation, the maximum error of the humidity sensor is ~13.1% of RH. The mean absolute error in pH measurement is ~ 0.032 pH units in the physiological pH range.

IV. CONCLUSIONS

In this work, we have implemented an incubator compatible modular measurement system and measured the pH, temperature and humidity in long term mesenchymal stem cell expansion and differentiation. Non-invasive unattended measurements were carried out in a closed flow loop without wasting any medium. The humidity sensor (HIH-5031) is a condensation-resistant, pre-calibrated sensor with a hydrophobic filter that allows it to be used in condensing environments including medical applications. However, some care is needed not to physically damage the filter during installation. Wiping it with an alcohol wetted paper instead of direct alcohol spray is preferred for sterilization before placing the system into the incubator. A sensor with a better housing similar to that of the temperature sensor can be better from the installation and handling point of view. Interplay between measured parameters shows a few possible stress sources present in cell culture in a CO_2 incubator. The system provides a comprehensive picture of behavior of critical control

parameters in incubator based cell culture, and points out the need for bioprocess systems with automatic monitoring and smart control for the optimal growth and maintenance of the cells and maximum productivity. Our continued future research, planned in this direction will aid this.

V. Acknowledgment

We thank Jouni Niemelä and Antti-Juhana Mäki, Department of Automation Science and Engineering, Tampere University of Technology and Anna-Maija Honkala, BioMediTech, Tampere for their valuable technical assistance.

References

[1] M. Borowski, M. Giovino-Doherty, L. Ji, M.-J. Shi, K. P. Smith, and J. Laning, *Basic pluripotent stem cell culture protocols*. Harvard Stem Cell Institute, 2008.

[2] B. Van Der Sanden, M. Dhobb, F. Berger, and D. Wion, "Optimizing stem cell culture," *J. Cell. Biochem.*, vol. 111, no. August, pp. 801–807, 2010.

[3] G. Maguire, "Therapeutics from Adult Stem Cells and the Hype Curve," *ACS Med. Chem. Lett.*, vol. 7, no. 5, pp. 441–443, May 2016.

[4] R. I. Freshney, *Culture of animal cells : a manual of basic technique*. Wiley-Liss, 1994.

[5] S. Fulda, A. M. Gorman, O. Hori, and A. Samali, "Cellular stress responses: cell survival and cell death.," *Int. J. Cell Biol.*, vol. 2010, p. 214074, 2010.

[6] J. A. Ryan, "Corning Guide for Identifying and Correcting Common Cell Growth Problems." Corning Incorporated.

[7] D. Kattipparambil Rajan *et al.*, "Optical non-contact pH measurement in cell culture with sterilizable, modular parts," *Talanta*, vol. 161, pp. 755–761, 2016.

[8] E. Y. Hwang, D. Pappas, A. S. Jeevarajan, and M. M. Anderson, "Evaluation of the Paratrend Multi-Analyte Sensor for Potential Utilization in Long-Duration Automated Cell Culture Monitoring," *Biomed. Microdevices*, vol. 63, no. 241, 2004.

[9] M. S. Wilson and W. Nie, "Electrochemical Multianalyte Immunoassays Using an Array-Based Sensor," 2006.

[10] G. Nabovati, E. Ghafar-Zadeh, and M. Sawan, "A 64 pixel ISFET-based biosensor for extracellular pH gradient monitoring," *Proc. - IEEE Int. Symp. Circuits Syst.*, vol. 2015–July, pp. 1762–1765, 2015.

[11] D. Wencel, T. Abel, and C. McDonagh, "Optical Chemical pH Sensors (Review)," *Anal. Chem.*, vol. 86, no. 1, pp. 15–29, 2014.

[12] W. Honda, S. Harada, T. Arie, S. Akita, and K. Takei, "Printed wearable temperature sensor for health monitoring," *IEEE SENSORS 2014 Proc.*, pp. 2227–2229, 2014.

[13] W. Baumann, M. Lehmann, A. Schwinde, R. Ehret, M. Brischwein, and B. Wolf, "Microelectronic sensor system for microphysiological application on living cells," *Sensors Actuators B Chem.*, vol. 55, no. 1, pp. 77–89, 1999.

[14] M. Oura, H. Kubo, S. Yamamori, S. Takeda, T. Shimizu, and T. Okano, "Development of cell culture monitoring system and novel non-contact pH measurement.," *Conf. Proc. ... Annu. Int. Conf. IEEE Eng. Med. Biol. Soc. IEEE Eng. Med. Biol. Soc. Annu. Conf.*, vol. 2011, pp. 22–5, 2011.

[15] J. Jang, S.-J. Moon, S.-H. Hong, and I.-H. Kim, "Colorimetric pH measurement of animal cell culture media," *Biotechnol. Lett.*, vol. 32, no. 11, pp. 1599–1607, Nov. 2010.

[16] Z. Liu, J. Liu, and T. Chen, "Phenol red immobilized PVA membrane for an optical pH sensor with two determination ranges and long-term stability," *Sensors Actuators B Chem.*, vol. 107, no. 1, pp. 311–316, May 2005.

[17] X. Xu, S. Smith, J. Urban, and Z. Cui, "An in line non-invasive optical system to monitor pH in cell and tissue culture.," *Med. Eng. Phys.*, vol. 28, no. 5, pp. 468–74, Jun. 2006.

[18] X.-D. Wang and O. S. Wolfbeis, "Fiber-Optic Chemical Sensors and Biosensors (2008–2012)," *Anal. Chem.*, vol. 85, no. 2, pp. 487–508, Jan. 2013.

[19] E. B. Magnusson, S. Halldorsson, M. T. Ronan, and K. Leosson, "Real-time optical pH measurement in a standard microfluidic cell culture system," vol. 4, no. 9, pp. 77–85, 2013.

[20] A. S. Jeevarajan, S. Vani, T. D. Taylor, and M. M. Anderson, "Continuous pH monitoring in a perfused bioreactor system using an optical pH sensor," *Biotechnol. Bioeng.*, vol. 78, pp. 467–472, 2002.

[21] M. Patrikoski *et al.*, "Development of fully defined xeno-free culture system for the preparation and propagation of cell therapy-compliant human adipose stem cells.," *Stem Cell Res. Ther.*, vol. 4, no. 2, p. 27, 2013.

[22] A. Cooper and C. M. Johnson, "Introduction to Microcalorimetry and Biomolecular Energetics," in *Microscopy, Optical Spectroscopy, and Macroscopic Techniques*, New Jersey: Humana Press, pp. 109–124.

[23] M. J. Gramer and T. Ogorzalek, "A semi-empirical mathematical model useful for describing the relationship between carbon dioxide, pH, lactate and base in a bicarbonate-buffered cell-culture process," *Biotechnol. Appl. Biochem*, vol. 47, pp. 197–204, 2007.

[24] J. E. Swain, "Optimizing the culture environment in the IVF laboratory: impact of pH and buffer capacity on gamete and embryo quality," *Reprod. Biomed. Online*, vol. 21, pp. 6–16, 2010.